University College London

Forming Next-Generation Antibody-Nanoparticle Conjugates through the Oriented Installation of Antibody Fragments

By

João Carlos Faria Nogueira

Submitted in partial fulfilment of the requirements for the degree of

Doctor of Philosophy

Declaration

I, João Carlos Faria Nogueira, confirm that the work presented in this thesis is my own. Where information has been derived from other sources, I confirm that this has been indicated in the thesis.

João Carlos Faria Nogueira

July, 5, 2019

Abstract

Use of antibody-nanoparticle conjugates (ANCs) has emerged as a multi-disciplinary strategy for combating cancer - they combine the versatility of nanoparticles and the potential to deliver cargo to cancer cells with the high targeting specificity of surface antibodies to recognise specific biomarkers that are expressed in cancer cells. Several strategies have been employed to graft nanoparticles to antibodies, however, most of them rely on fragile non-covalent interactions or on methods that do not exert control on antibody paratope orientation (*e.g.* random modification of multiple lysine residues on antibodies). These issues greatly limit ANCs antigen binding capability, reproducibility and, thus, overall efficacy. In this thesis, alternatives strategies of generating ANCs are proposed, regarding antibody orientation on the nanoparticles' surface through the use of pyridazinedione-based linkers that site-selectively modify disulfide(s) on antibodies. The overall aim is to achieve highly-controlled ANC construction so that these next-generation ANCs can be employed in future cancer treatments.

In Chapter 1, an introduction to current protein modification techniques is presented and, in a more biological context, the structure and use of full antibodies and antibody fragments is described. Additionally, an overview of the current biomedical applications of numerous different types of inorganic and organic nanoparticles is introduced. In Chapter 2, the creation of antibody fragment Fab targeted PEG-PLGA nanoparticles is reported. In particular, the generation of Trastuzumab Fab fragments *via* digestion techniques and a new approach for their attachment to PEG-PLGA nanoparticles and the consequent results of improved antigen binding are described. In Chapters 3 and 4, different proteins are employed for the generation of ANCs, namely Cetuximab Fab (in which cell studies are also performed) and considerably smaller proteins such as variable new antigen receptors (V_{NARs}) *via* a similar methodology to that employed in Chapter 2. Concluding, an overview of achieved results and future work are covered.

Impact Statement

The research mission of this work was to identify current flaws within the field of critical care medicine and attempt to develop more efficient platforms to overcome these flaws, in view of further medical applications. More specifically, this thesis presents a new approach for the generation of specialised nanoparticles (NPs) for the treatment of diseases, with particular focus on cancer. Cancer is becoming the leading cause of mortality in most developed countries, with an estimated number of new cancer cases being above 300,000 every year, just in the UK. Surgery, when possible, along with radiation and chemotherapy continue to remain the most regular form of cancer treatment. However, in the past decades, using nanoparticles (NPs) to get drugs into tumours has been exhaustively explored, since they provide a novel way to deliver combination therapy with special and temporal control over drug release. Furthermore, nanoparticles' combination with monoclonal antibodies (mAbs) is thought to bring an unmet specificity to the platform since mAbs and their fragments have demonstrated unprecedented affinity profiles to overexpressed cell cancer biomarkers in clinical and preclinical trials. Moreover, the proposed method of grafting antibodies to the surface of nanoparticles, that will be described throughout this thesis, demonstrates an improvement when compared to methods employed in many particle-based formulations described in literature. Remarkably, resultant Antibody-Nanoparticle Conjugates (ANCs) were tested in cancer cell-based assays, where they demonstrated superior therapeutic effect when compared to other nanoparticle-based formulations or even to common chemotherapy methods. These highly promising preliminary results resulted in two ANC-related publications in high impact papers (*Chem. Sci.* and *Chem. Comm.*) demonstrating the acceptance of scientific community.

As such, it is suggested the future exploration and further assessment of these newly developed ANCs (described throughout this thesis) in an *in vivo* setting. If, as expected, the trends show superior targeting and elimination of cancer cells whilst combined with less adverse effects on healthy cells, it is then envisioned the potentially impactful application of these ANCs to the field of cancer treatment.

Table of Contents

Acknowledgements

This PhD represents one of the biggest challenges I have ever embraced. Undeniably, I expanded my boundaries, gained a vast plethora of new skills (also learned fancy words) but, most importantly, I feel that I overcame many limitations. Thus, taking this opportunity to acknowledge some individuals who supported me through this journey.

Firstly, *Mãe* e *Pai*, I am deeply grateful for your unconditional love, support and advice, shown in infinite ways. Thank you for always encouraging me to explore out of the comfort zone, while always trusting me. Means a lot. Hope I made you proud.

Also, I am thankful to my sisters, Anocas and Lenita, and my nephews, *reguilas*: Zé, Mariana, Diogo and Leninha for making me feel genuinely happy everytime I go back home.

A very special thank you to my supervisor soon-to-be Prof Vijay Chudasama. No words to describe the amount of support given, it is the mentor one could hope to have. Most importantly, thanks for believing in me at the beginning, middle and end of my PhD. I did my best not to disappoint the trust placed.

"*If you are the smartest person in the room you are in the wrong room*" – Always felt in the right room, if that says enough of what I think of everyone in my research group: André, *o Prodígio*; Antoine, *le Mage*; Calise, *the Wise Owl*; Peter, *the Epica Magyar*; Faiza, *the Dangerous Socialite;* Marcos, *el calmo*; Richard, *the Theatrical* or Alex, *the Millionaire*. Will miss you, my friends. Also, extending my thanks to past members, particularly Dan for showing me the ropes, for happily transferring some of his knowledge and for reading my thesis. Owe you a dinner or two! Additionally, thanks to the *Epic Friday Team*, which includes Nafsika, Sabatini, Raul, Brian, Sebastian, Archie and many more – thank you all for the great times either in the lab or wandering around in London – times that I will deeply miss.

To Diana, for appearing in my life in the right timing, a huge thanks. You are a keeper.

To my best mates overseas, especially Diogo(s), Pedro, Magno and Vitor, and to my former housemates, thanks for the multiple visits and for providing the happiest distractions to rest my mind outside of work.

Finally, I wish to acknowledge Dr Chris Spicer and Dr Jon Wilden for accepting to be my examiners.

Abbreviations

AcOH	Acetic acid
ADC	Antibody-Drug Conjugate
ADIBO	Azadibenzylcyclooctyne
AFPD	Antibody Fragment Pyridazinedione
ANC	Antibody-Nanoparticle Conjugate
BARAC	Biarylazacyclooctynone
BBS	Borate buffered saline
BCA	Bicinchoninic acid assay
BCN	Bicyclononyne
CPT	Camptothecin
CTX	Cetuximab
DAR	Drug to Antibody Ratio
DCM	Dichloromethane
DIFO	Difluorinated cyclooctyne
DLL4	Delta like canonical Notch ligand 4
DMF	Dimethylformamide
DNA	Deoxyribonucleic Acid
EDC	(1-Ethyl-3-(3-dimethylaminopropyl)carbodiimide)
EDTA	Ethylenediamine Tetraacetic Acid
EGFR	Epidermal Growth Factor Receptor
ELISA	Enzime-linked Immunosorbent assay
EPR	Enhanced Permeability and Retention
FAR	Fluorophore to Antibody Ratio
FDA	Food and Drug Administration
FITC	Fluorescein Isothiocyanate
FLISA	Fluorescence-linked immunosorbent assay
HCAb	Heavy chain Antibody
HER2	Human Epidermal growth factor Receptor 2
HIV	Human Immunodeficiency Virus
Hz	Hertz
Ig	Immunoglobulin

IONPs	Iron Oxide Nanoparticles
IR	Infra-Red
LC-MS	Liquid Chromatography – Mass Spectrometry
mAb	Monoclonal Antibody
MMAE	Monomethyl auristatin E
MS	Mass Spectroscopy
MSN	Mesoporous Silica Nanoparticles
NAA	Natural Amino Acid
NEt_3	Triethylamine
NHS	*N*-Hydroxysuccinimide
NP	Nanoparticle
PAR	Pyridazinedione to Antibody Ratio
PBS	Phosphate buffered saline
PD	Pyridazinedione
PDI	Polidispersity index
PEG	Polyethylene Glycol
PK	Pharmacokinetic
PLGA	Polylactic-*co*-glycolic acid
PVA	Polyvinyl Acetate
QD	Quantum Dots
RNA	Ribonucleic Acid
SDS-PAGE	Sodium dodecyl Sulfate-polyacrylamide Gel Electrophoresis
SEM	Standard error of mean
SPAAC	Strain-promoted Azide-alkyne Cycloaddition
SPR	Surface Plasma Resonance
TCEP	(Tris(2-carboxyethyl)phosphine)
TCO	Trans-cyclooctene
TFA	Trifluoroacetic acid
THF	Tetrahydrofuran
TRAZ	Trastuzumab
uAA	Unnatural Amino Acid
UV/Vis	Ultraviolet-Visible Spectroscopy
V_{NAR}	Variable new antigen receptors

Chapter 1 Introduction

1.1 Protein modification

Nowadays, proteins are seen as the pinnacle of the chemical biology research field: these macromolecules perform a vast array of functions within organisms such as providing structure to cells, regulating organism processes or transporting materials throughout the body.[1] Moreover, the tertiary folded structure of proteins makes them ideal candidates for analysing natural systems and creating novel biological tools.[2] In order to enhance the potential of such tools, over the past decades proteins have been chemically modified with diagnostic and/or therapeutic probes. Ideally, these modifications should be highly controllable in order to yield highly homogeneous constructs that can be well-characterised, easily reproduced and have predictable pharmacokinetic (PK) profiles.[3,4] For this reason, there has been a lot of work into achieving highly selective modification of amino acids, despite the many challenges (*e.g.* attempting to modify a single amino acid in the presence of other reactive functional groups such as carboxylic acids, amides, amines, alcohols or thiols).[5,6] Additional challenges lie in finding discriminatory chemical reactions which are also biorthogonal, *i.e.* reactions which do not disrupt the structure and/or function of the protein, are able to proceed under mild temperatures, at near physiological pH, and in aqueous media. In addition, protein modification reactions need to be compatible with various buffer additives used to stabilise proteins, *e.g.* EDTA, sodium azide, salts, and other surfactants, which are often required for protein stability.[7] Over the years, several techniques have been successfully developed to overcome these challenges, resulting in an extensive library of protein conjugation strategies. These are now applied in various fields, such as diagnostics (*e.g.* fluorescent tagged proteins)[8] and therapeutic agents (*e.g.* as protein-drug conjugates[9] for the treatment of diseases such as HIV,[10] cancer[11] or malaria[12]).

1.1.1 Modification of natural amino acids

There is now a vast ‘toolkit’ for the modification of natural and unnatural amino acids (uAAs),[3] however, as the modification of proteinogenic natural amino acids (NAAs) is of greatest relevance to this thesis only this will be discussed in detail below. As

NAAs are naturally present in all proteins, they can be targeted without the need to further alter a protein's natural backbone. Also, NAAs can be incorporated into proteins using site-directed mutagenesis to provide chemical handles at particular sites of interest. However, the degree of selectivity offered by this method is reliant on the reactivity and natural abundance of the NAA that is being introduced, *i.e.* either it is the only amino acid of a certain category being introduced, or it is the only amino acid of that category that is available for bioconjugation (other residues of the same type may be buried in the protein structure and, therefore, not accessible). Out of the 20 existent natural amino acids cysteine and lysine are within the most utilised for selective protein modification as they possess two of the most nucleophilic side-chains, a thiol and an amine respectively (Figure 1).[4] That being said, other amino acids, albeit with less nucleophilic side-chains, have also been exploited for this purpose (*e.g.* histidine, tyrosine, serine – Figure 1).

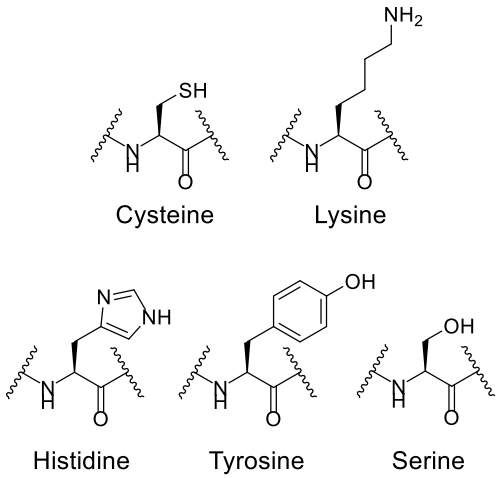

Figure 1. Some of the natural amino acids side chains targeted for chemical modification of proteins.

1.1.1.1 Modification of lysine residues

One of the most common protein modification methods is through bioconjugation to lysine residues.[13] Primary amines are located in the side-chain of lysine amino acid residues and, being positively charged at physiological pH, they are usually situated on the outside surfaces of native proteins to maximise protein solubility. This factor also means that many lysine residue side-chain amino acids are solvent accessible and available for reaction with bioconjugation reagents. In addition, the nucleophilic

behaviour of the amino group makes it a desirable target for conjugation with several well-established chemistries, generally *via* acylation or alkylation. The most commonly used reagents for their modification are sulfonyl chlorides,[14] isothiocyanates[15] or activated esters[16], amongst others (*vide infra*, Scheme 1).

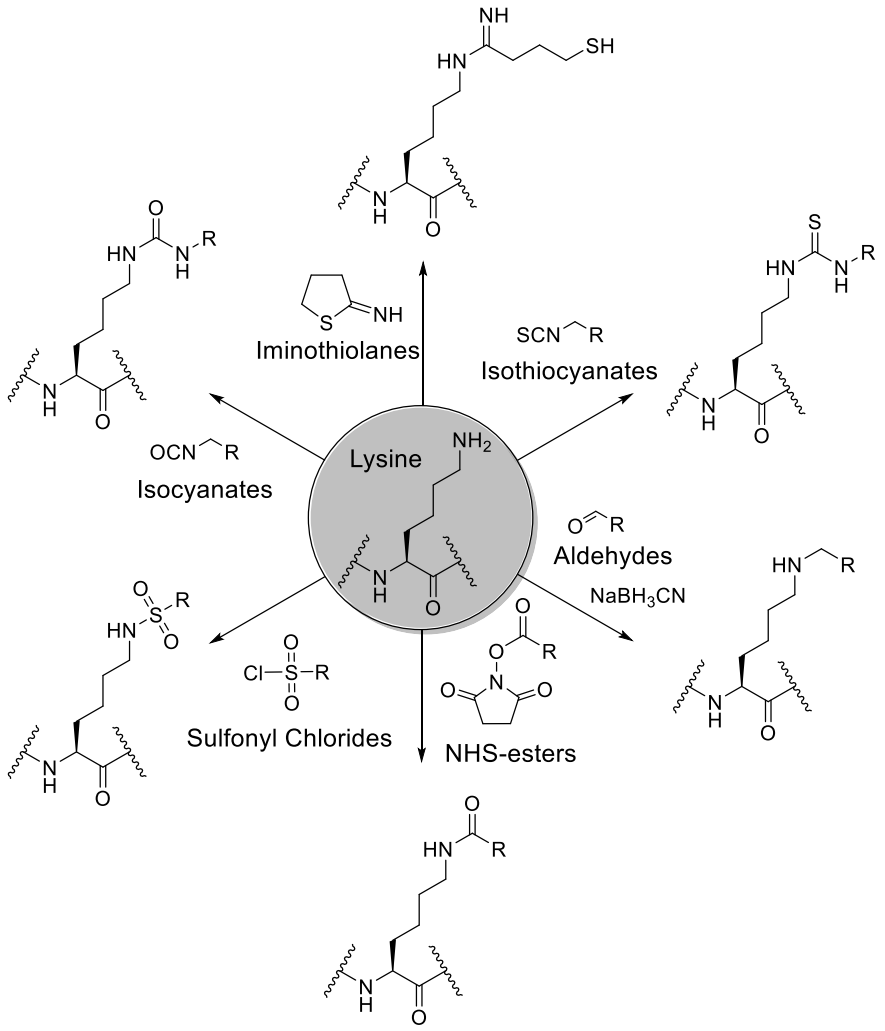

Scheme 1. Commonly used strategies for lysine modification.

Most FDA approved chemically modified proteins have been generated *via* lysine modification protocols, typically through amine-reactive succinimidyl esters.[17] However, due to the high natural abundance and solvent accessibility of this amino acid, the modification of lysines results in the formation of heterogeneous products when targeting modifications, where the average degree of conjugation is lower than the number of accessible lysine residues (this is typically the case); this presents challenges for characterisation, batch-to-batch variability, unpredictable pharmacokinetics, and analysis. Owing to the nature of the conjugation method, in the

plethora of species formed there will be conjugates with high to no modification, both of which are undesirable. For high modification, conjugates may have issues of poor pharmacokinetics (for conjugates where many lysines are modified and the molecule that is introduced is relatively hydrophobic), and the protein's natural activity may be reduced if an accessible lysine residue is proximal to the active site. If there is a large number of biomolecules unmodified (*i.e.* no modification), this can lead to high concentrations of competitive target binders that elicit no desired response. It also for these reasons why high and low level of lysine modification are not targeted, *i.e.* too high means too many highly modified conjugates and too low means a high risk of too many non-modified conjugates, making the correct level of conjugation a difficult task/balance. Nonetheless, there are a few clinically relevant protein conjugates generated by lysine modification (*e.g.* Kadcyla®)[18] and there are currently being developed technologies which allow site-selective lysine modification.[19]

1.1.1.2 Modification of cysteine residues

Cysteine-targeting chemistry is a very well recognised strategy in protein modification, and its benefits have been reported in the literature for more than 40 years.[20] This methodology has been widely employed to create versatile bioconjugates,[21,22] multiply labelled proteins[23] or even to obtain structural information about a protein.[24] They provide a unique reactive handle in proteins and they are a convenient target for alkylation, disulfide formation and oxidation reactions (Scheme 2).

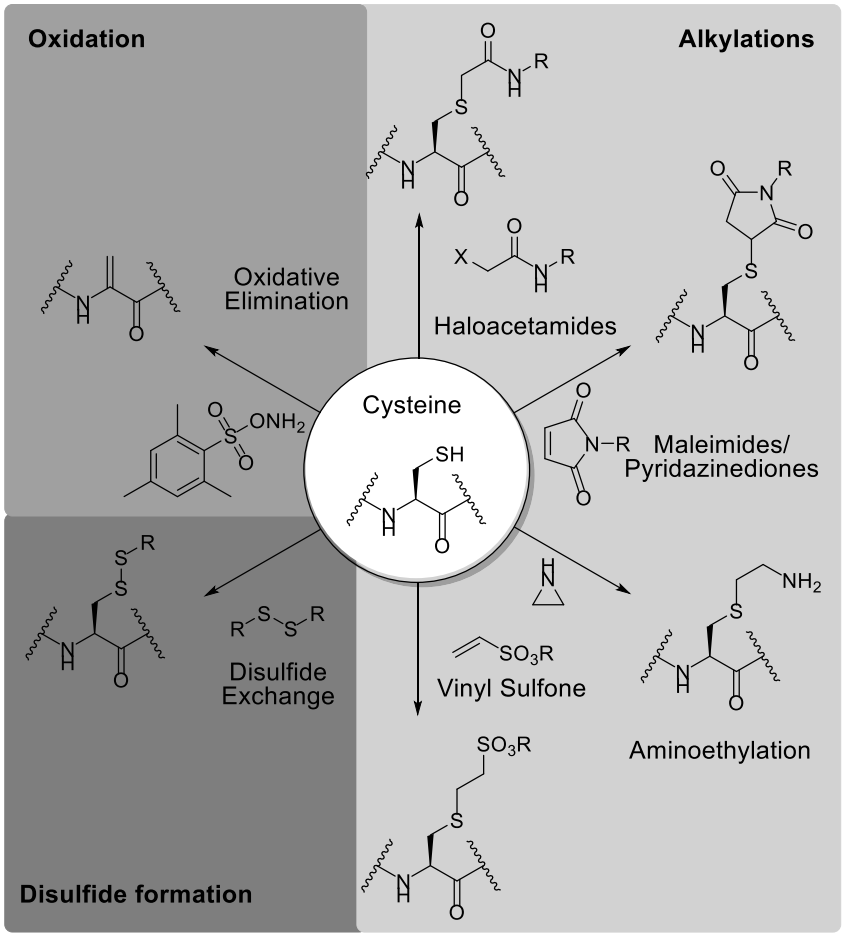

Scheme 2. Some of the most commonly used strategies for Cysteine modification.

Considerably more reactive than lysine at physiological pH, cysteine reacts rapidly in a chemoselective manner through its 'soft' nucleophilic thiolate side chain; Thiolates have lower charge density than other nucleophiles, favouring the formation of thermodynamically stable products.[25] Whilst total cysteine abundance is at 1.7% in the human proteome, the majority of cysteine residues exist in their oxidised form, disulfide bridges, and just 0.2% occur as free cysteine residues. This is especially attractive for two reasons: i) often, if a protein contains cysteine(s), it only contains one (or few) free solvent accessible cysteine(s) (*e.g.* albumin), allowing for relatively facile site-specific modification with a cysteine-only reactive reagent; ii) if a protein contain(s) no solvent accessible cysteine(s), as cysteines can be introduced into a protein sequence in a facile manner using well established site-directed mutagenesis, cysteine(s) can be introduced at positions of interest on a protein and reacted specifically.[26,27]

1.5% of total amino acids are cysteine residues which are paired in a unique cross-linked fashion; disulfide bridges. These bridges are often known to give covalent support to a protein's tertiary structure and preserve desirable conformations. When unpaired or reduced, there is the possibility of protein clustering due to non-native thiol-thiol interactions, which often results in protein precipitation.[28] Thus, if single cysteine thiols are liberated from a disulfide, usually under reducing conditions, a correct pairing or functional re-bridging strategy is often required to retain structural integrity. To this end, strategies for the insertion of non-natural moieties, *e.g.* next-generation maleimides or pyridazinediones (PDs) (*vide infra*, Scheme 3), into disulfide bonds have been developed. The newly formed bridge usually includes a functional group of interest or a chemical handle for further functionalisation, acting as a useful bioconjugation linker. Moreover, it is already described in literature that highly controlled functional disulfide re-bridging techniques show no significant decrease in protein stability.[29,30] For instance, Chudasama *et al.* recently reported that reagents based on pyridazinediones could be used as a disulfide re-bridging platform, without affecting protein structure, activity or stability *in vivo*.[26,31,32]

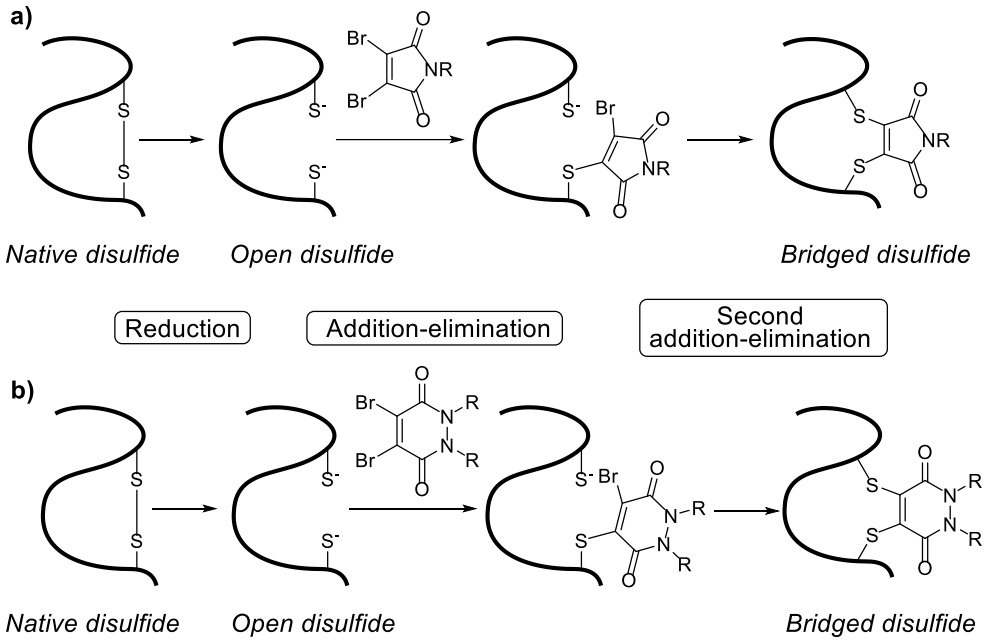

Scheme 3. Mechanism of correct re-bridging disulfide through **a)** next-generation maleimide chemistry **b)** pyridazinedione chemistry.

Despite the aforementioned advantages of modifying disulfide bonds by functionally re-bridging them, in cases where the protein is heavily templated, researchers have

simply reduced disulfides and alkylated the liberated free cysteines, for instance in the formulation of Adcetris® **2**, an engineered antibody currently employed in the treatment of Hodgkin Lymphoma.

1.2 Antibodies as therapeutic agents

In the past few decades, and owing to medical research development, phenotypic and genotypic expression patterns on patients led scientists to identify several disease markers, resulting in the development of various targeting agents.[33] Although there have been several improvements/new considerations, the main goal for scientists during these past decades remained the same: finding the best disease marker (regarding selectivity and best expression in all types of unhealthy cells) and developing the optimal targeting efficiency, whilst having a stable construct that is recognised by the cell environment. As natural biocompatible proteins, monoclonal antibodies (mAbs) or immunoglobulins (Ig) have been widely explored platforms for this purpose.

Extensively used in biochemistry, molecular biology, medical research and therapeutics, mAbs are immunoproteins capable of recognising and binding to specific disease antigens, triggering immunological activity.[34] They represent a versatile therapeutic solution for several diseases such as cancer, HIV, Crohn's disease, rheumatoid arthritis, bronchopulmonary dysplasia, amongst others.[35] Of these, using specific antibodies for cancer treatment is a promising strategy in oncological medicine, albeit with some limitation in efficacy.[36,37] That being said, antibody targeted therapy is reported to maximise successfully killing tumour cells and reduce undesired side effects when compared to other traditional chemical therapies.[38]

Monoclonal antibodies have a Y-shaped structure, a molecular weight of approximately 150 kDa, are produced by B blood cells and recruited to biological systems when immunological activity is required.[26] These immunoproteins are effective through different mechanisms either inducing apoptosis, or blocking key receptors or growth factors that are vital for cells to reproduce, or even binding to cellular targets and recruiting cytotoxic agents, amongst other strategies.[35] In addition, their selectivity ensures that toxic contamination is minimised on healthy cells, compared to traditional chemotherapy methods.[34,39]

Antibodies are divided into different isotypes as they are classified according to their heavy chain constant domain structure/shape in placental mammals (*vide infra*, Table 1).

	Location	Proportion	Valency	Function
IgG*(γ)*	Blood	70-75%	2	Immunity against invading pathogens
IgA*(α)*	Mucosal areas, gland secretions	10-15%	2-4[a]	Agglutination, immunity against invading pathogens
IgM *(μ)*	B cells, blood	10%	10[b]	Agglutination, immunity against pathogens
IgE *(ε)*	Mast cells, basophils	≤ 1%	2	Allergy, protection against parasitic worms
IgD *(δ)*	B cells	≤ 1%	2	Activation of B cells

Table 1. Properties of the different isotypes of placental mammals. [a] IgAs can be released as dimers. [b] The value 10 is theoretical since IgMs are mostly pentameric, however, steric hindrance is generated when IgMs are bound to antigen epitopes, resulting in a value closer to 5.

1.2.1 Antibody fragments

Since the biological properties of antibodies are so varied and promising, their functional abilities have been studied in detail. Therefore, it is known that the antibody can be divided or digested into smaller fragments and still retain antigen-binding capability.[40] Several techniques using specific enzymatic or chemical cleavage are currently used, deriving different fragments (Figure 2) which will be discussed in turn below.

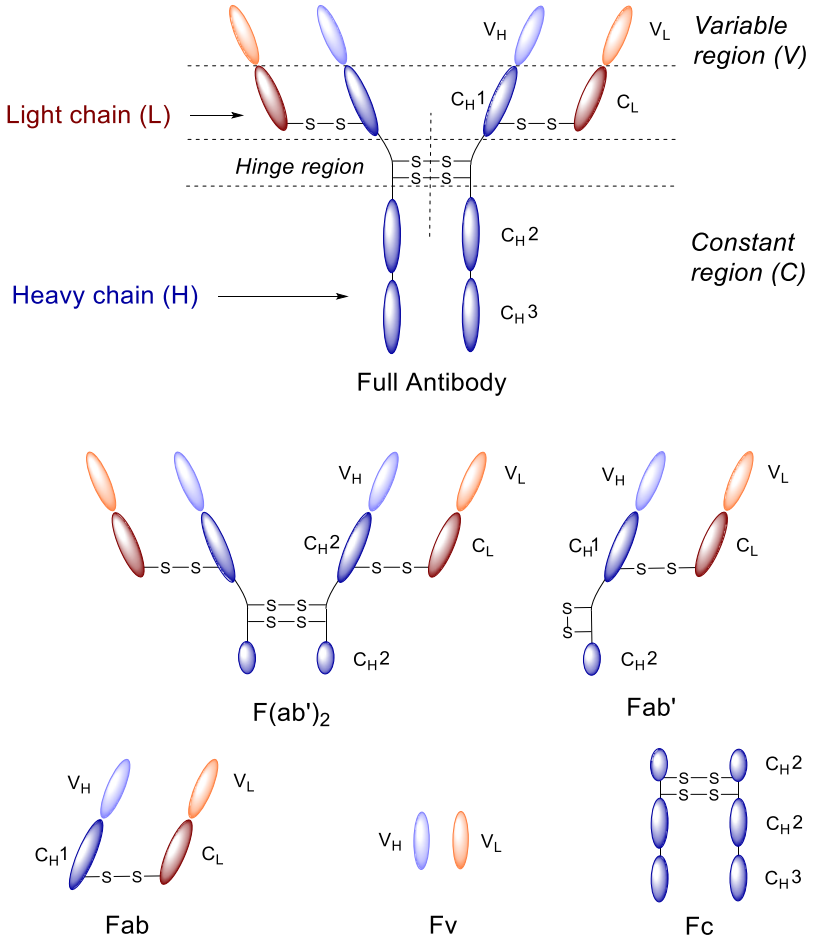

Figure 2. General structure of an immunoglobulin G1 (IgG1) highlighting cleavable regions through digestion and most commonly used fragments.

Fv

The variable fragment is the smallest region that still retains the binding capability to antigen epitopes. It is composed of the upper regions in the Y arms (V_L and V_H) and, in most common IgGs, has a molecular weight of *ca*. 25 kDa. This fragment also finds its application as a single chain variable fragment (ScFv), in which the variable regions of V_H and V_L are connected *via* a short peptide of 10-25 amino acids.

Fab

The antigen binding fragment or Fab is the responsible region for antigen epitope binding through the paratope present in Fv region. It integrates part of the heavy chain (C_H1 and V_H1) and the whole light chain (V_L and C_L), which are linked together by a single disulfide. These fragments are monovalent and usually have a molecular weight of *ca*. 47 kDa.

Fab'

This fragment integrates the Fab region and an extended portion of the heavy chain that contains two cysteine residues which belong to the denominated *hinge region* amongst other amino acids. Thus, its molecular weight is slightly bigger than Fab (*ca.* 48 kDa).

F(ab')$_2$

This fragment corresponds to the association of two Fab' fragments, linked together by the *hinge region* disulfides, in the same fashion as the native full antibody. As a consequence, F(ab')$_2$ fragments possess a molecular weight of *ca*. 96 kDa.

Fc

The crystallisable fragment, or Fc, region forms the antibody tail of the Y shaped structure and interacts with cell surface receptors (Fc receptors), allowing immune system activation. Consequently, it behaves as an important mediator of antibody physiological effects detecting opsonized particles, and degranulating mast cells, basophils and eosinophils. However, this fragment is unable to recognise antigen epitopes. They have a molecular weight of *ca.* 50 kDa.

These fragments have been attracting more and more interest recently since their altered physico-chemical properties can bring versatility to cancer research. For instance, their smaller size facilitates greater tissue penetration whilst retaining desired immunologic properties in certain cases.[41] Also, their less complex structure enables more controlled and orientated antigen-binding strategies.[42] In addition, undesired non-specific binding from certain antibody regions, *e.g.* unspecific Fc-binding, is reduced.[43]

1.3 Antibody Conjugates

As described previously, crucial advances in the past decades in the biomedical field led to the first generation of therapeutic antibodies for cancer treatment. However, there remained a large margin to improve in antibody engineering, safety and efficacy, as reflected by the limited number of antibodies or antibody fragments showing clinical efficiency as single agents.[36] As a consequence, and in order to enhance the therapeutic potential of antibodies, their conjugation with small molecule cytotoxic

drugs was attempted, creating a new generation of constructs for the treatment of human diseases, antibody-drug conjugates (ADCs).

ADCs are a promising class of biotherapeutic constructs that are primarily aimed at cancer treatment.[44] They combine the cell-killing potency of a cytotoxic drug with the high selectivity of an antibody towards overexpressed receptors on cancer cell membranes. Creating a successful antibody-drug conjugate requires careful selection of an antibody, drug and linker (Figure 3).[45]

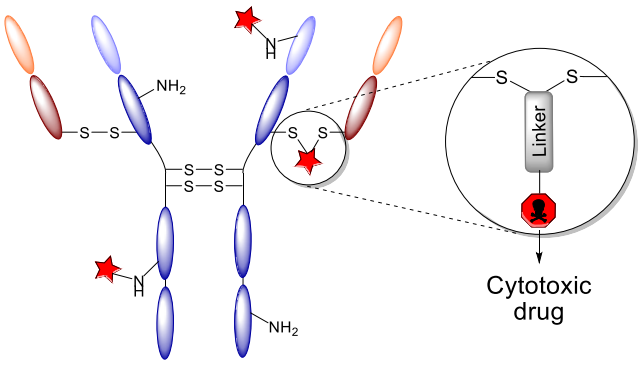

Figure 3. An ADC model highlighting different strategies for modification (cysteines and lysines).

Utilizing proteins to deliver small molecule payloads *in vivo* is already a well-recognized strategy[20] as is shown by the approvals of ado-trastuzumab emtansine (Kadcyla® **1** (T-DM1); Roche/Genentech, Figure 4), brentuximab vedotin (Adcetris® **2**; Seattle Genetics/Millennium Pharmaceuticals, Figure 4) and, more recently, of inotuzumab ozogamicin (Besponsa™). Also, gemtuzumab ozogamicin (Mylotarg™) was re-approved by the FDA after being temporarily withdrawn from the market, between 2010 and 2017.

ADCs are now a validated drug class and, due to the improved technology and appropriate targeting, their application is growing rapidly.[46] However, due to an evolving understanding of ADCs, the current marketed products are considered suboptimal. For instance, Kadcyla® **1** is generated by modifying accessible lysine residues. As described previously, lysine modification is not considered a selective method, and especially for modification on antibodies since there are *ca.* 90 accessible lysines on an antibody's surface, producing *ca.* 10^6 possible species in the heterogeneous mixture when targeting typically tolerated drug loadings are of 2-4

drugs per antibody. This results in poor reproducibility, a lack of efficacy for low drug loaded conjugates and rapid clearance of high drug loaded conjugates.[47] Consequently, Kadcyla® **1** heterogeneity and batch-to-batch variability is reported to deliver random-effect results in clinic.[48] In Adcetris® **2**, there is site-selective modification, as only the reduced interstrand disulfides (of which there are 4) are modified. However, the mono-alkylation strategy means that the disulfides are not functionally re-bridged, which can affect structure integrity and stability *in vivo* (Figure 4).[27] Also, as only a drug loading of 2-4 is desired and there are 8 released cysteines, a statistical mixture will again be formed with conjugates ranging from 0 to 8 drugs loaded. In addition, the use of classical maleimides for cysteine conjugates is undesirable as multiple reports have shown the resultant bioconjugates to be unstable in serum due to retro-Michael deconjugation and subsequent reaction with albumin.[49] As with Kadcyla® **1**, the existence of high drug to antibody ratio (DAR) species (>4) has been recognized to lead to physical instability, faster clearance, a lower therapeutic index, whilst low loading conjugates (<2) has diminished efficacy.[50]

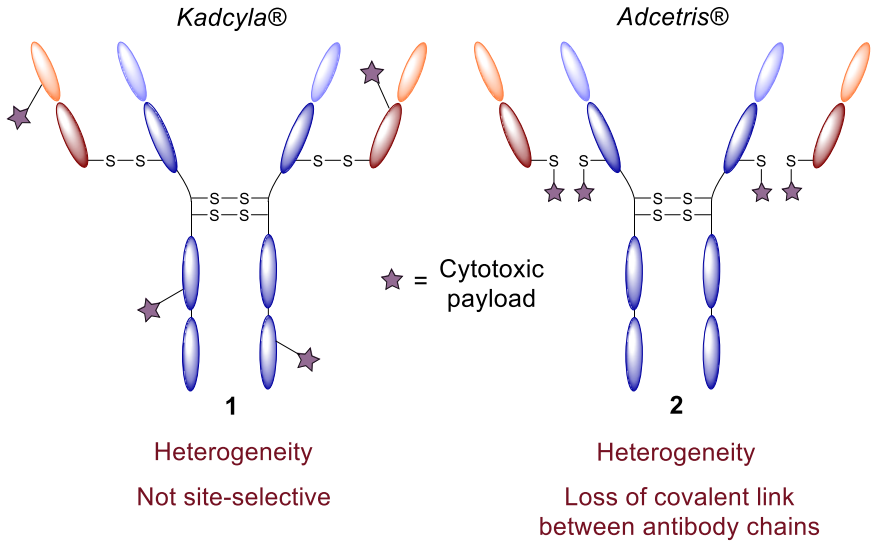

Figure 4. Schematic representations of Kadcyla® **1** and Adcetris® **2** highlighting the drawbacks of each technology.

To overcome heterogeneity issues, site-directed mutagenesis was one of the strategies that was employed to customise antibody properties, leading to the generation of near-homogeneous ADCs. However, this route is not considered ideal since such procedures are expensive and non-trivial, *e.g.* if a cysteine is introduced there is the possibility of disulfide scrambling at the precise site at which mutagenesis is carried

out. Also, this engineering procedure is antibody specific and needs to be optimised on each antibody it is applied, which is costly and time consuming. Consequently, there has been a drive towards site-selectively modifying native antibodies/fragments to generate homogeneous constructs.[51]

1.3.1 Site-selectively modified conjugates

Several bioconjugation strategies have been developed to improve ADC construction and homogeneity whilst trying to avoid expensive and time-consuming engineering strategies. For instance, *N*-glycolisation is an oligosaccharide modification of the multiple naturally-occurring glycan chains present in most antibodies and it is an often-used approach for antibody-drug conjugation (Scheme 4).[52]

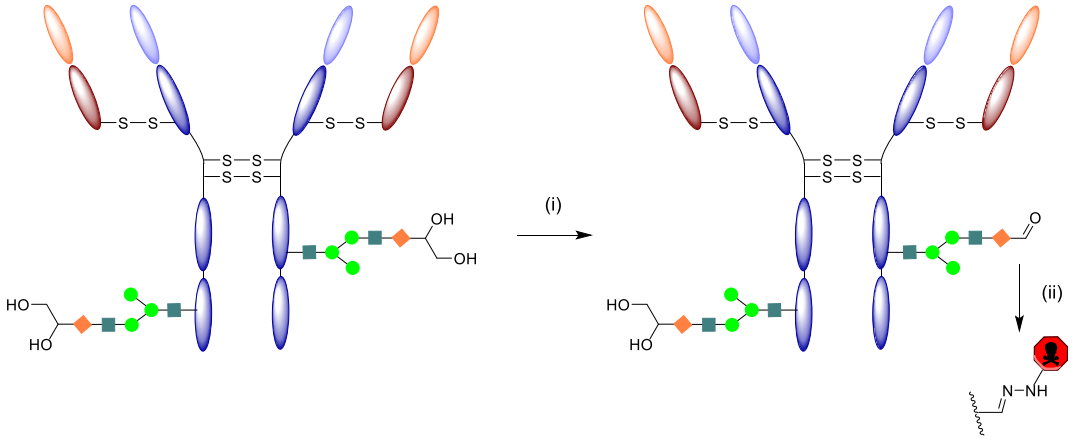

Scheme 4. Example of N-glycolisation reaction: oxidation and functionalisation with cytotoxic drug.

Reagent and conditions: (i) $NaIO_4$, acetate buffer pH 5.5, 4 °C, 30 min; (ii) cytotoxic moiety (*e.g.* Calicheamicin derivative), acetate buffer pH 5.5, 3 h.

For instance, the biotechnology company Synaffix explored these glycan properties to generate homogeneous ADCs, through GlycoConnect™ technology. This innovative conjugation method is achieved *via* a controlled two-step enzyme digestion treatment; the first enzyme trims the glycan to a desired extent and the second enzyme installs a small molecule substrate bearing a reactive functional group – a tag substrate. Following the implementation of a tag, a payload can be subsequently attached in a chemoselective manner.[53] Contrastingly, other techniques simply rely on amino acid abundance or differential accessibility to generate selectivity, avoiding extensive

engineering processes. For that reason, one of the most valuable conjugation methods for generating ADCs is *via* functionally re-bridging the thiols of reduced inter-chain disulfide bonds that are native to antibodies, to create stable, near homogeneous conjugates.[44]

1.3.2 Use of Pyridazinediones (PDs) for site-selective bioconjugation

Besides pyridazinedione scaffolds being noted as intermediates in the synthesis of insecticides, acaricides and ectoparasites, they have found their main application in chemical biology.[54] They are considered an excellent platform for functional re-bridging disulfides due to their stability profile and ability to attach multiple modalities *via* their structural core backbone (Scheme 5). Moreover, and unlike many classical cysteine modification reagents, they are exclusively specific for thiol modification; even when 100 equivalents of reagent is used no lysine modification is observed – under analogous conditions, classical maleimides often react with multiple lysine residues.[54] Also, PD conjugates possess exceptional resistance to hydrolysis as opposed to other cysteine-modified conjugates, particularly maleimide-based conjugates.[55]

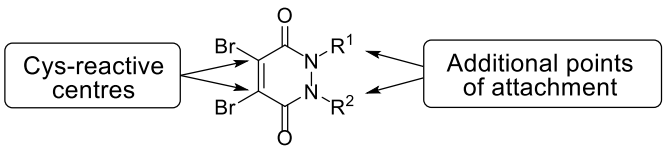

3

Scheme 5. 3,6-Dibromopyridazinedione **3** structure – two cysteine reactive centres which are responsible for disulfide re-bridging and two additional reactive handles.

Consequently, a lot of work has been carried out in the ADC field to incorporate PDs as bioconjugation linkers into the four native interchain disulfide bonds of an antibody, especially by the Caddick and Chudasama groups.[55,56] For instance, Lee *et al*. managed to incorporate four PD moieties in one single multi-disulfide system (*i.e.* trastuzumab antibody) with native configuration functional re-bridging, generating the homogeneous antibody-conjugate **4** (Figure 5).[32]

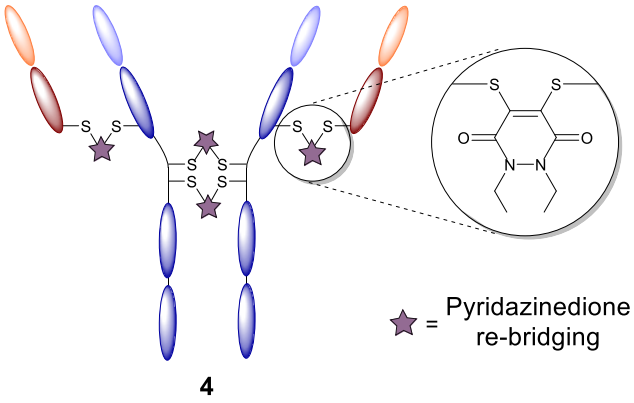

Figure 5. Functionally re-bridged native antibody *via* a PD platform, arranged in the native configuration.

Furthermore, Eifion *et al.* reported the use of PDs to functionalise a trastuzumab antibody with a controlled loading of 4 monomethyl auristatin E (MMAE) drug molecules - a potent, selective and efficacious drug against cancer cells *in vitro* and *in vivo*.[27]

1.3.2.1 'Click' chemistry in antibody modification

A common strategy when antibodies are site-selectively modified with PDs is that a PD with a functional handle is attached to the antibody and then the formed conjugate is derivatised by reaction of the functional handle. This functional handle must therefore be biorthogonal and stable to conjugation conditions, and able to react selectively when on the protein.[54] To this end, functional handles from the 'click' chemistry toolbox have been explored. 'Click' chemistry is defined as a class of biorthogonal reactions that are easy to perform, stable to oxygen and water, high yielding, and take place with minimum (or no) by-products.[57] Also, as the use of the antibody conjugate is in an *in vivo* setting, it is essential that the employed chemistry is free of toxic reagents.[58] For this reason, a biorthogonal strained alkyne functional 'click' handle **6** is used, as it engages in a copper-free strain-promoted azide-alkyne cycloaddition (SPAAC) (Scheme 6).[58]

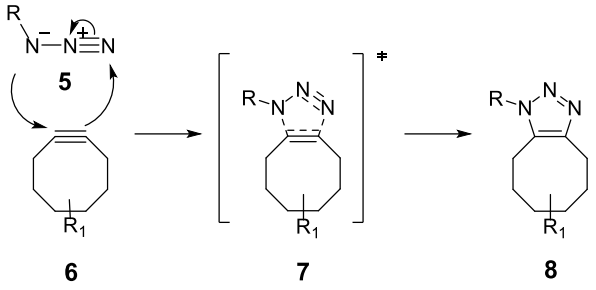

Scheme 6. Copper free SPAAC 'click' reaction.

SPAAC reactions are remarkably popular within the chemical science field due to their ease of operation, broad solvent compatibility and 100% atom efficiency resulting in the formation of a highly stable triazole **8**. SPAAC reactions happen spontaneously, simply by mixing and stirring a cyclic alkyne **6** with an organic azide **5**, without the necessity of other reagents or catalysts (*e.g.* copper catalyst), avoiding future live cell toxicity.[59] While SPAAC reactions are not only applicable to cyclooctynes, they are the smallest cyclic alkynes that can be isolated in a facile manner and stored in their pure form. However, due to the strained alkyne reactive nature, careful exclusion of air from cyclooctynes is encouraged in order to avoid rapid decomposition.[60]

The reactivity of cyclic alkynes is directly correlated with ring size: the bigger the cyclic ring, the smaller is the alkyne straining effect (*i.e.* this effect induces a deviation from the typical acetylene 180 º bond angle). Gratifyingly, in the case of a cyclooctyne, the straining effect on the acetylene bond angle is still significant (163 º), hence, a lower activation energy is required for reaction when compared to a strain-free alkyne.[59] Thus, there is currently a wide toolbox of engineered cyclooctynes available such as DIFO **9**, ADIBO **10**, BARAC **11** or BCN **12** (Figure 6).

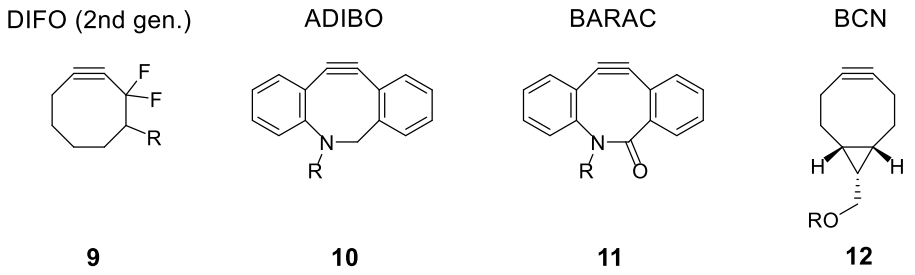

Figure 6. Structures of some of the most commonly employed cyclooctynes for SPAAC reactions.

Whilst DIFO **9** depends on the two electron-withdrawing fluorine atoms to further increase the rate of strain-promoted cycloaddition, ADIBO **10** and BARAC **11** rely on the (di)benzoannulated conformation to enhance cyclooctyne reactivity, as aryl rings are reported to increase the ring strain (*i.e.* this effect is conferred by the sp^2-hybridized carbons) and acetylene angle values can go down to 153 °.[61,62] However, the broad application of the aforementioned cyclooctynes is limited, as they are associated with time-consuming and expensive synthetic routes. For instance, seven synthetic steps are required for the formation of BARAC **11**, eight steps for DIFO **9**, and nine steps for ADIBO **10**, while yields are usually low (*e.g.* 16% for BARAC **11**).[63] Additionally, highly reactive probes such as BARAC **11** often suffer from poor stability and rapid degradation.[59] Consequently, ring-strained alkynes such as BCN **12** have attracted more attention as they are reported to be more stable than most cyclooctynes and can be synthesised in a facile manner, over 4 steps and with a 46% yield, as reported by Dommerholt *et al.*[63] Although less reactive than ADIBO **10** or BARAC **11,** BCN **12** derivatives are still amongst the most reactive cyclooctynes that are commercially available because they induce additional ring strain through the fusion with cyclopropane, enabling a superior reaction rate when compared to plain cyclooctynes.[64] Additionally, it is reported that a cyclooctyne with a single fused aryl ring provides an optimal balance between strain enhancement and minimisation of steric hindrance, especially if the aryl ring is at a distal site to the alkyne.[65,66] Therefore, BCN **12** derivatives are considered to finely balance high reactivity with relative stability forming a class of versatile cyclooctynes for bioconjugation with proteins. Additionally, and due to the inherent disadvantages of size and hydrophobicity of cyclooctynes, a PEG spacer is often necessary to allow SPAAC reaction to occur in aqueous conditions.[67] Particularly, van Delft's commercially available bicyclononyne BCN(endo)-PEG_2-NH_2 **13** (Figure 7)[63] attracted attention as a potential 'clickable' handle, as it comprises a useful terminal primary amine, allowing amide formation strategies in view of BCN integration in a pyridazinedione scaffold.

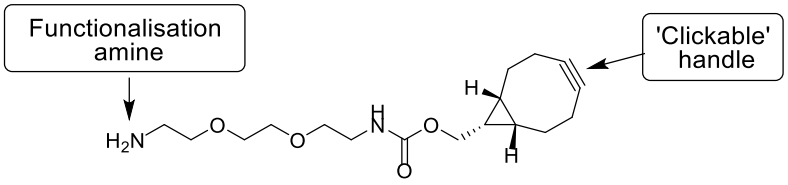

13

Figure 7. Structure of BCN **13**, highlighting relevant reactive centres.

Thus, BCN **13** will be the preferred substrate for the inclusion of azide-reactive 'clickable' handles on PDs throughout this thesis.

1.4 Nanotechnology for Biomedical Applications

Nanotechnology (from *nano*, 'dwarf' in Greek) is the manipulation or creation of materials at the atomic and molecular level, usually at a scale between 1 and 100 nanometres.[68] It is applied to diverse fields such as computational science, physics, material engineering and, with most relevance for this work, biomedical sciences. The science that merges nanotechnology with the biomedical field, also known as nanomedicine, consists in using formulations like nanoparticles (NPs) or nanodevices to cure, diagnose or prevent numerous diseases. One of its major attractive features is the fact that this scale of sizes overlaps with most biologically relevant substances such as proteins, enzymes, antibodies, receptors, amongst others (Figure 8). Also, nanoscale materials are inherently small compared to the size of major cell organelles (usually between 1-10 μm)[68] and, due to this feature, they can cross biological barriers including the blood-brain barrier[69] or transit in and out blood vessels[70] enabling them to interact with a wide panel of biological entities. Thus, the application of nanotechnology for biomedical applications has exponentially grown during the last few years.[71]

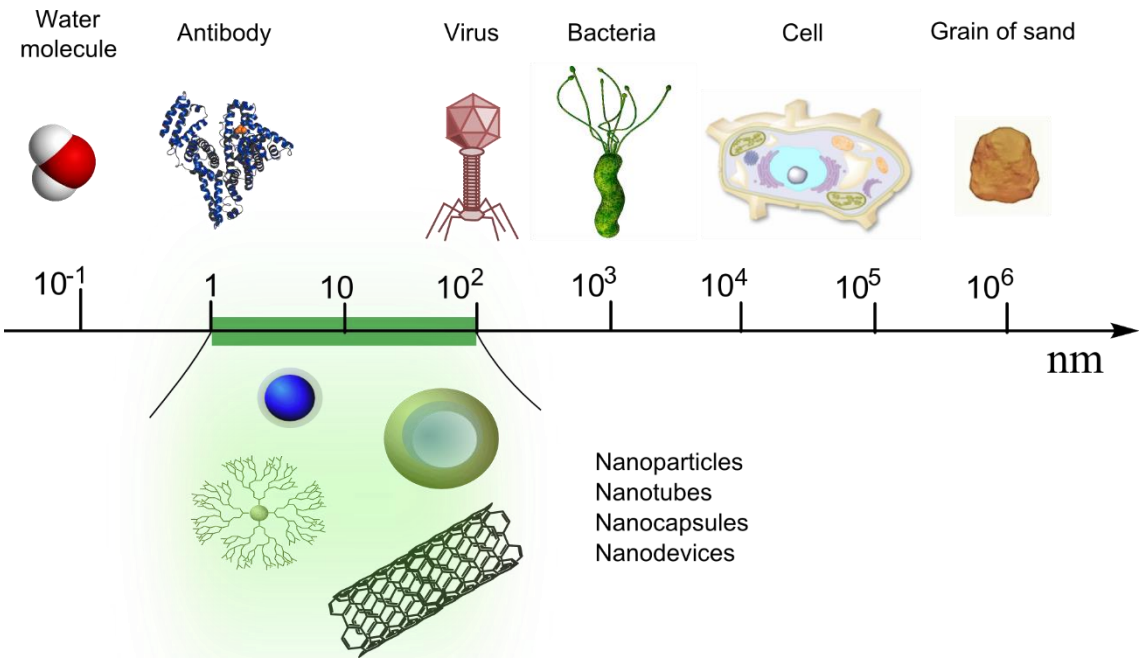

Figure 8. Size comparison between nanomaterials (1-100 nm) and other references.

1.4.1 Nanoparticle formulations

This thesis combines the art of protein modification to that of nanoparticle functionalisation. As such, this part of the thesis introduction focuses on the formation and properties of various nanoparticles.

Nanoparticles tend to be categorised in two major groups: inorganic and organic, although there has been also considerable effort in developing procedures for the controlled synthesis of organic nanobeads encapsulating inorganic nanoparticles.[72] Herein in this section will be presented a summary for the most widely used inorganic and organic nanoparticles for biomedical applications and their main advantages and drawbacks.

1.4.1.1 Inorganic Nanoparticles

Iron oxide nanoparticles

Iron Oxide Nanoparticles (IONPs) consist of an iron oxide ferromagnetic core (typically Fe_3O_4) and are usually coated with moieties such as dextran to enhance its biocompatibility with biological systems, allowing further chemical modification on their surfaces.[73] IONPs have been used in a vast plethora of applications, for instance, they have been applied as magnetic resonance imaging agents (usually as a T2 weighted contrast agent),[74] drug-delivery probes[75] or even as therapeutics (*e.g.* magnetic hypothermia).[76] For instance, van Kasteren *et al.* developed iron oxide nanoparticles decorated with carbohydrates that target endothelial markers, usually over-expressed in acute inflammation, associated with diseases such as multiple sclerosis, ischemic stroke or HIV-related dementia.[77] However, most methods to synthesise IONPs (*e.g.* co-precipitation) generate batches with large size distribution, aggregation and poor crystallinity.[78] Additionally, the absence of porous cavities in the inner, rigid core impedes cargo loading, turning them into poor candidates for drug-delivery applications.

Gold nanoparticles

Gold nanoparticles have attracted a wide interest due to their exquisite chemical, physical and biological properties. For instance, their ability to produce heat upon absorbance of near-infrared light is currently used in photothermal therapy.[79] Recently, Xiaoping Yang *et al.* demonstrated that Epidermal Growth Factor Receptor (EGFR) directed gold nanorods could be heated via near infrared light, inducing tumour ablation in mice models with urinary bladder cancer.[80] Also, gold optical properties such as localised surface plasmon resonance (LSPR) lead to its wide use in biosensing applications, particularly in point of care lateral flow assays for the detection of diseases (*e.g.* acute pancreatitis).[81] Even though, their solid core does not provide a suitable platform for cargo delivery and their inner inorganic characteristics still present obstacles to biocompatibility, due to their high toxicity.[82]

Mesoporous silica nanoparticles

Mesoporous silica nanoparticles (MSNs) are typically generated by the reaction of tetraethyl orthosilicate with a template made of micellar rods.[83] This process often yields sphere shaped silica nanoparticles with a regular arrangement of pores usually between 2 and 50 nm (*vide infra*, Figure 9), providing them with a high surface area to volume ratio, thus, a high loading capacity.[84] Hence, MSNs are highly desirable in the biomedical field as they can encapsulate high amounts of cargo while still being more biocompatible than most inorganic particles.[83] However, it is reported that MSNs' treatment often leads to severe metabolic changes, which are believed to be related to melanoma promotion. Additionally, the high density of silanol groups present in the nanoparticles surface promotes the interaction with the phospholipids of the red blood cell membrane, resulting in hemolysis.[85] These fundamental disadvantages limit their immediate applications as drug-delivery systems for treatment of diseases.

Quantum dots

Quantum dots (QDs), usually smaller than other inorganic nanoparticles, are semiconducting crystals which have been attracting attention since their discovery over 30 years ago.[86] There is a plethora of different combinations for QD formulations, the most common being a cadmium selenide core with a zinc selenide cap.[87] These particles possess exquisite optical properties as they emit bright colours and display size dependent optical properties (*i.e.* the emission wavelength can be tuned with slight changes in particle size and composition), making them one of the favourite candidates for biosensing and imaging technologies.[88] However, their small size limits their application for drug delivery systems. Moreover, their high toxicity remains a hurdle for human *in vivo* applications.[89]

Carbon nanoparticles

Carbon nanoparticles are mainly composed of carbon, the second most abundant element by mass in human (after oxygen) and one of the four most abundant in the universe. For those reasons, it has a low toxicity profile in biological tissues and has low synthetic costs.[90] Although these particles can assume a spherical shape, they are usually assembled in a cylindrical or tubular structure (*vide infra*, Figure 9) possessing unusual properties such as exceptional strength and stiffness, when compared to other

materials, enhancing the structural rigidity of a potential nanoconstruct. It is reported that carbon nanoparticles can have an important role in cancer treatment, as they can be heated by radio waves to eradicate tumours or even metastasised cancer.[91] However, they have a tendency to accumulate in human organs and consequently cause organ damage (*e.g.* pulmonary damage).[92] This drawback, allied to the poor degradability profile,[93] has hindered the adoption of these nanoparticles for *in vivo* applications.

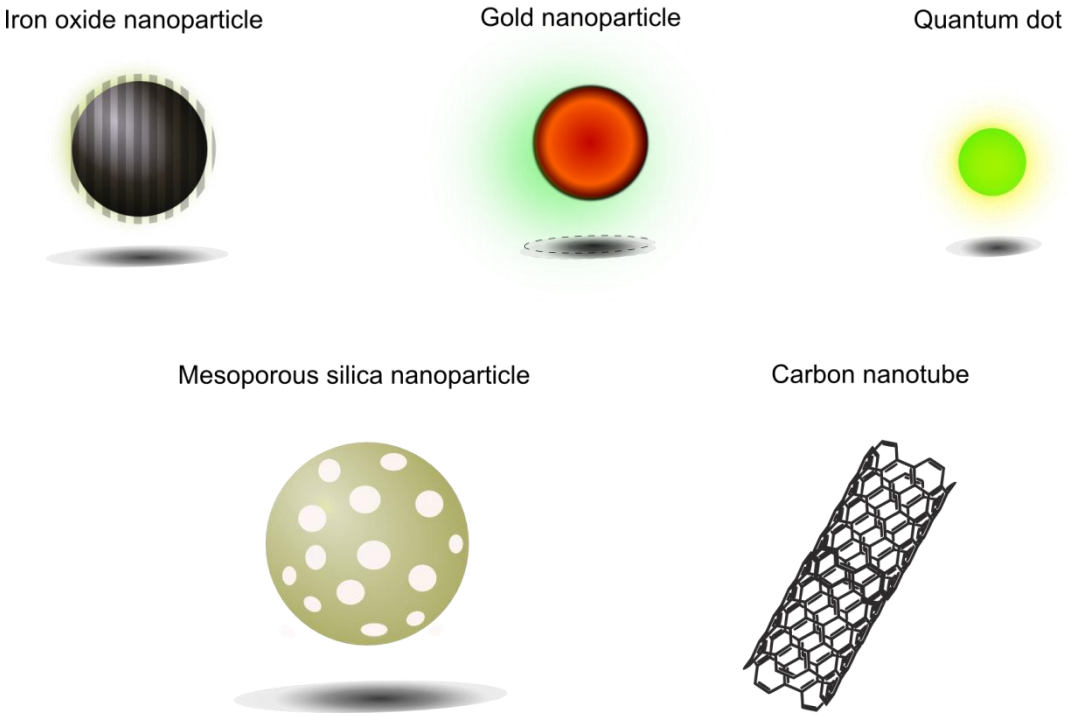

Figure 9. Representation of different types of inorganic nanoparticles.

1.4.1.2 Organic Nanoparticles

Liposomes

Liposomal nanoparticles are amongst the most utilised nanoparticles in nanomedicine, with several formulations FDA approved and available on the market (*e.g.* Doxil®, Ambisome® or DepoDur™).[94] These vesicles are usually synthesised by self-assembling methods (*e.g.* ultrasound treatment) due to the nature of the constituent lipids (*i.e.* their polar and non-polar components). Moreover, this spontaneous assembly enables the encapsulation of molecules/ions present in the aqueous solution, where the vesicles are generated.[95] Liposomes are considered versatile since their size, flexibility, and cargo quantity can be controlled. Thus, they are considered an excellent

vehicle for controlled drug delivery. It is reported that liposomes can exhibit enhanced pharmacological properties when compared to traditional drugs in sensible treatments such as ophthalmologic disorder therapies, antimicrobial therapy or even chemotherapy.[96]

Polymeric micelles

Polymeric micelles are nanoscopic structures formed by a core of aggregated hydrophobic polymers coated with hydrophilic polymeric chains.[97] One of their main advantages is the ability to circulate for a long time in the blood stream, avoiding uptake by the reticuloendothelial system due to their hydrophilic nature. Furthermore, the polymeric micelles ability to encapsulate poorly water-soluble anticancer drugs within their hydrophobic core is widely appreciated.[98] Nonetheless, their structural fragility could be a drawback when the end goal is encapsulation of cargo since the high porosity results in poor controlled release profiles. Also, the lack of suitable methods for large-scale production limits the applications in the near future.[99]

Dendrimers

Dendrimers (from the Greek word *dendro*, which translates to tree) are polymer complexes generated through numerous polymerisation steps that result in a highly branched construct (see representation below, Figure 10).[100] The more repeated branching cycles are performed during their synthesis, the higher generation the dendrimer is considered, as it will have more functional groups exposed on the surface. Dendrimers are characterised by their structural perfection and monodispersity which makes them useful for drug delivery systems, biosensors, blood substitutes and for the generation of capsules in inorganic nanoparticles (*e.g.* metallodendrimers).[101,102] Although promising, dendrimers use in biomedical applications is still at an early stage.

Polymeric nanoparticles

Polymeric nanoparticles can be categorised as nanocapsules or nanospheres; the primary difference being in how the desired cargo is stored. Nanocapsules contain a defined core or capsule where hydrophilic payloads (*e.g.* DNA/RNA) can be encapsulated,[103] whilst nanospheres trap hydrophobic or hydrophilic (if at an adequate

pH) drugs within their solid polymer matrix conformation.[104] These polymeric nanoparticles have shown significant therapeutic potential due to their low *in vivo* toxicity and structural rigidity (provided by the polymeric core) allied with the capacity for constant release of payloads, adjusted to clinically relevant time scales.[105] In addition, their polymer constitution allows facile surface functionalisation with targeting moieties essential for targeting specificity.[106,107]

For instance, Polylactic-*co*-glycolic acid (PLGA) has been explored as a co-polymer for biomedical applications due to its ability to self-assemble into nanostructures while entrapping small molecules like drugs. For this, PLGA ability to completely degrade is also considered a major advantage since it allows drug release into the body in a time-dependent manner.[108]

Additionally, polyethylene glycol (PEG), is one of the most employed polymers for drug delivery applications (the first PEGylated product is already on the market for over 25 years) due to its characteristics such as stealth behaviour (*i.e.* this property allows the polymer to be undetected by the immune system at early stages (opsonisation), allowing increased blood circulation time).

Also, PEG hydrophilic nature allows the nanoparticle to be stabilised in water by steric effects in detriment of ionic effects.[109]

Thus, PEG-PLGA copolymers arose as one of the most promising systems for the polymeric nanoparticles formation.[110] By combining all the good qualities of both polymers PEG and PLGA, these nanoparticles stand now amongst the preferred candidates for cancer therapy and will be widely utilised in the context of this thesis.

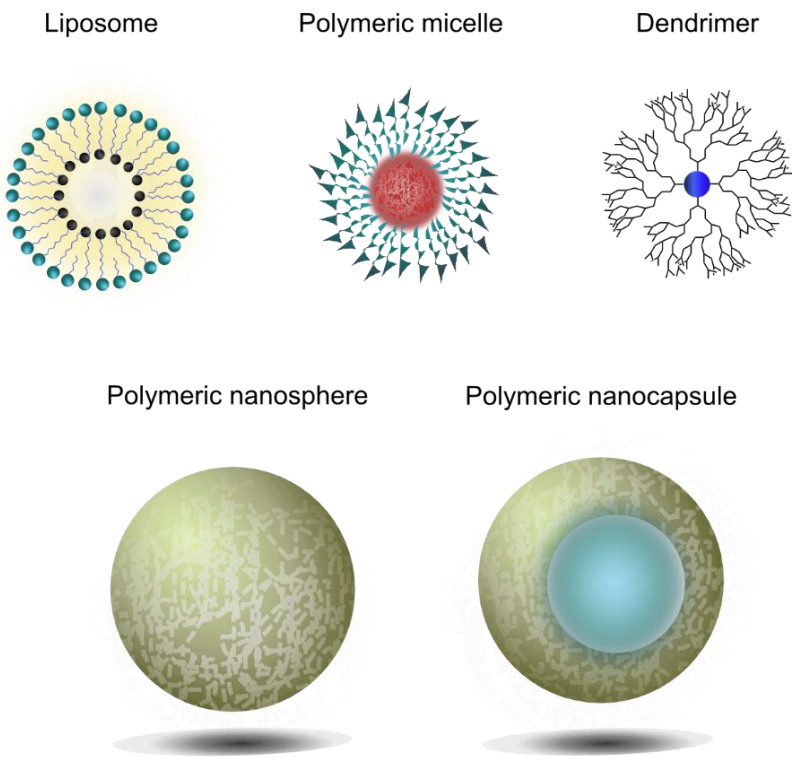

Figure 10. Representation of various formulations of organic nanoparticles.

1.4.2 Cancer therapies

Although nanoparticles are widely used for multiple purposes in the biomedical field, lately there has been a drive to use this technology within cancer research, as current technologies have proven inadequate to meet demand. In this section, nanotechnology applied to cancer for diagnostic and therapeutic purposes will be compared with conventional chemotherapy and their advantages and disadvantages highlighted.

1.4.2.1 Cancer – Facts and Figures

By definition, cancer is a group of diseases that involve abnormal cell growth, with the ability to invade and spread to other tissues and organs. Lifestyle choices (*e.g.* non-balanced diets, sedentary lifestyle, smoking, etc.) are widely considered to be the main factors for the development of cancer (90-95% of the cases), while genetic background is responsible for 5-10% of the cases.[111] Experts estimate that more than 4 in 10 cancer cases can actually be prevented through lifestyle choices. Cancer is responsible for approximately 15% of all human deaths and one of the critical factors is cancer

variability - there are more than 100 different human cancer types related to more than 500 different genes.[112] For this reason, it is unlikely that researchers will find a 'universal cure' or a single treatment for all the different types of cancer. Essentially, successful treatment depends on the type of cancer (*e.g.* pancreatic adenocarcinoma is considered more lethal than breast cancer with 1% and 78% survival rates, respectively),[113] its ability to spread or not to other organs (through a mechanism called metastasis) and the time-scale in which the cancer is detected (ideally, before anatomic anomalies are visible).

1.4.2.2 Chemotherapy and its limitations

Currently, chemotherapy is one of the most commonly employed therapeutic strategies for cancer treatment; its consists of administering small drugs, often in combination with other types of treatment (*e.g.* radiotherapy or surgical resection).[114] Chemotherapy has been proven to reduce cancer tumour sizes and, in some cases, eradicate the cancer to an extent where it cannot be detected anymore in the system (known as full remission). However, this combination of therapeutic strategies is still associated with high morbidity and mortality. Their side effects remain a hurdle since healthy body tissues are widely affected.[115] This non-specificity is notorious, especially because the affected healthy cells share many of the same characteristics of cancer cells, *i.e.* healthy cells such as hair, skin, bone marrow or the lining cells of the digestive system also grow and divide at a constant, fast pace. This also greatly limits the therapeutic window/index of chemotherapy. Additionally, the lack of capacity to overcome biological barriers and adequately respond to the disease environment often leads to poor drug delivery in the tumour sites.[114]

In conclusion, the uncontrolled injury of non-targeted tissues complicates chemotherapy in a way that limits therapeutic dosages of highly toxic drugs (*e.g.* doxorubicin) and significantly affects the quality of life of patients during and after treatment.[116]

1.4.3 Cancer Nanotechnology

Cancer nanotechnology has been developed to overcome these challenges, and it is now seen as one of the key solutions for revolutionising cancer detection, diagnosis

and treatment. With the advances in the nanotechnology field it is now possible to find a vast nanotechnology library offering a plethora of nanomaterials with different shapes, fillings, surfaces, modes of action and compositions (*vide supra*, Section 1.4.1). Also, the biocompatibility and biodegradability of these materials are now tuneable to the desired application, *i.e.* some nanoparticles are tuned to be cleared by the immune system faster than others whilst some are intended to rapidly degrade after relevant stimuli.[117] Nanoparticles are also able to safely transport different types of cargo to specific targets in the body, such as molecular imaging agents or cytotoxic drugs in high quantities – all of these new features are seen as a major breakthrough in cancer diagnosis and treatment.[118] Therefore, there are now FDA-approved nanocarriers (mostly polymeric nanoparticles and liposomes) that are used for delivery of anticancer agents such as paclitaxel,[119,120] doxurobicin[121] or 5-FU.[122]

Two general approaches have been utilised to accomplish selective or preferential delivery of nanomaterials to cancer sites: passive and active targeting.

1.4.3.1 Passive targeting

Some nanoformulations are able to 'passively' accumulate within cancerous tissues by exploiting the abnormal gap junctions (100-600 nm) in the endothelium of tumour blood vessels and impaired lymphatic drainage, a phenomenon known as the enhanced permeability and retention (EPR), an effect described in literature, although still causing debate within the scientific community.[123] EPR effect supposedly favours the accumulation of nanoparticles in tumour tissue when compared to normal tissue, since the tumour neovasculatures are underprovided in form and architecture, lacking lymphatic drainage, therefore, nanoparticles can accumulate for longer and have more chances of transposing the abnormal barriers. This effect has provided mixed results; some reports support preferential EPR-mediated accumulation of NPs in tumours whilst others show the EPR effect is highly dependent on the tumour model.[123] Nonetheless, to achieve this effect, nanoparticles are often engineered to extend their circulation half-lives (*e.g.* coating nanoparticles with hydrophilic polymer chains such as PEG) as they are expected to circulate in the body before accumulating in cancerous tissues. Generally, particle features such as shape or size are also factors as it is thought that they can be adapted to favour intratumoural extravasation.[124,125] An important consideration is that systemically administered NPs might gradually release toxic

payloads during the long circulation – not only damaging healthy cells but also holding relatively small payloads by the time they reach the tumour.[126] Although there are several reviews that cover the passive targeting approach,[127,128] the focus of this thesis will be in active targeting applications.

1.4.3.2 Active targeting

One of the key challenges when developing clinically viable cancer therapeutic protocols is the specificity of the drugs; as mentioned previously, poor targeted and non-localised delivery often damages healthy tissues. To overcome this issue, researchers are focused on developing nanoengineered materials that target the tumour sites specifically – usually by targeting specific biomarkers (*e.g.* antigens, folate, transferrin, etc.) that are overexpressed in cancer cells, as opposed to letting the often toxic nanoparticles circulate freely.[129] This concept is referred to as 'active' targeting.[130] In active targeting, nanoparticles are combined with high affinity disease-specific targeting ligands such as small molecules, sugars, fatty acids, proteins, antibodies and aptamers, resulting in a wide range of therapeutic and diagnostic applications. Thus, active targeting is considered more optimal than non-targeted approaches, delivering higher amounts of cytotoxic drugs to tumour cells and reducing the side effects.[131]

1.5 Antibody-Nanoparticle Conjugates (ANCs)

Antibody-based derivatisations are amongst the most reliable therapeutic active targeting agents due to antibodies' biocompatible *in vivo* properties along with their high targeting specificity (*vide supra*, Section 1.3).[40] Antibody-based nanoparticles used as drug carriers as chemotherapeutic agents have the potential to significantly improve the way cancer is treated. This approach can expand therapeutic indices by ensuring that potent payloads are conveniently delivered only to the tumour site, hence, reducing the side effects of traditional chemotherapy. Several candidates have entered clinical trials, namely SGT-53,[132] C225-ILs-Dox[133] and Anti-EGFR ILs-Dox,[134] amongst others. Interestingly, the majority of these constructs utilise antibody fragments rather than full mAbs as the targeting ligand. This preference is indicative of the aforementioned advantages of these fragments over full-length antibodies - smaller size permits a greater loading of nanoparticles' surface and means less

immunogenicity, while maintaining full antigen-binding capability. An early study in support of smaller antibody fragments as targeting ligands was provided by Cheng and Allen. Their study compared the effectiveness of doxorubicin-bearing liposomes decorated with mouse anti-human CD19 antibody (clone HD37) mAb and respective Fab' and ScFv to selectively target B-cell antigen CD19. Cheng and Allen were able to observe a steep improvement in antigen binding for the HD37 Fab' fragment over HD37 mAb and HD37 ScFv.[135] Drastic differences were also noticed when tested *in vivo* protocols in mice; full antibody targeted liposomes were rapidly cleared from the system, possibly due to the Fc-mediated uptake into the liver and spleen that ScFv and Fab' fragments resist. Also, the mice treated with HD37 Fab' targeted Doxorubicin liposomes had a significant improvement in survival rates when compared to the mAb and even ScFv fragment. Although it would be expected that ScFv fragments would behave similarly to Fab' fragments, ScFv fragments were found to be unstable, possibly due to the absence of the stabilising region of the parent antibody, resulting in loss of binding activity.

These findings are a key reference for the next generations of antibody-nanoparticle conjugates - it encourages the use and digestion of non-engineered antibodies, which confer compatibility with biological environments at a relatively low cost. These and other benefits of antibody fragments have been described in a recent review published by Richards *et al*.[40]

1.5.1 Nanoparticle-protein interface

Whilst nanoparticle-antibody conjugates show great promise, it is believed that the methods by which the antibody fragments are often attached to nanoparticles have significant room for improvement, especially regarding orientation of the protein.

Nanoparticle surface modifications are broadly separated in two categories: covalent and non-covalent. Non-covalent technologies are based on physisorption and/or chemisorption of the desired moiety with the particle surface. However, this method is mediated by the surface charge of antibodies, which vary significantly from antibody to antibody and there is also an issue with batch-to-batch variability of the resulting nanoconjugate.[136] Furthermore, upon antibody-nanoparticle conjugation, alterations in charge in nanoparticle and antibody may occur, resulting in undesired release of the

antibodies from the NPs, affecting the stability and therapeutic potential of nanoconjugate.[137] Thus, in order to achieve a successful surface modification with antibodies or antibody fragments, it is believed that a covalent interaction is ideal, as it involves the incorporation of a chemical function group that can be further modified with targeting ligands, providing greater *in vivo* stability.[138] Several methods of covalently incorporating functional groups onto surface of nanoparticles have been reported including azides, amines, carboxylic acids, thiols, alkynes, alcohols, aldehydes and maleimides, leading to a wide selection of functional handles that can be paired with different groups from the desired antibody ligand.

1.5.1.1 Attachment of antibodies to nanoparticles – Current approaches

Currently, one of the most common approaches to covalently attach antibodies/antibody fragments to nanoconstructs is *via* carbodiimide chemistry (see below, Scheme 7). Typically, carbodiimides such as 1-ethyl-3-(-3-dimethylaminopropyl) carbodiimide **15** (EDC) are employed, as they activate carboxylic groups present on the surface of nanoparticles **14** '*in situ*', generating an unstable o-acylisourea intermediate **16**. In order to form more stable nanoconstructs, intermediate **16** can be further functionalised with amine-reactive esters (*e.g.* NHS esters **17** or Sulfo-NHS esters), facilitating attachment *via* lysine residues.

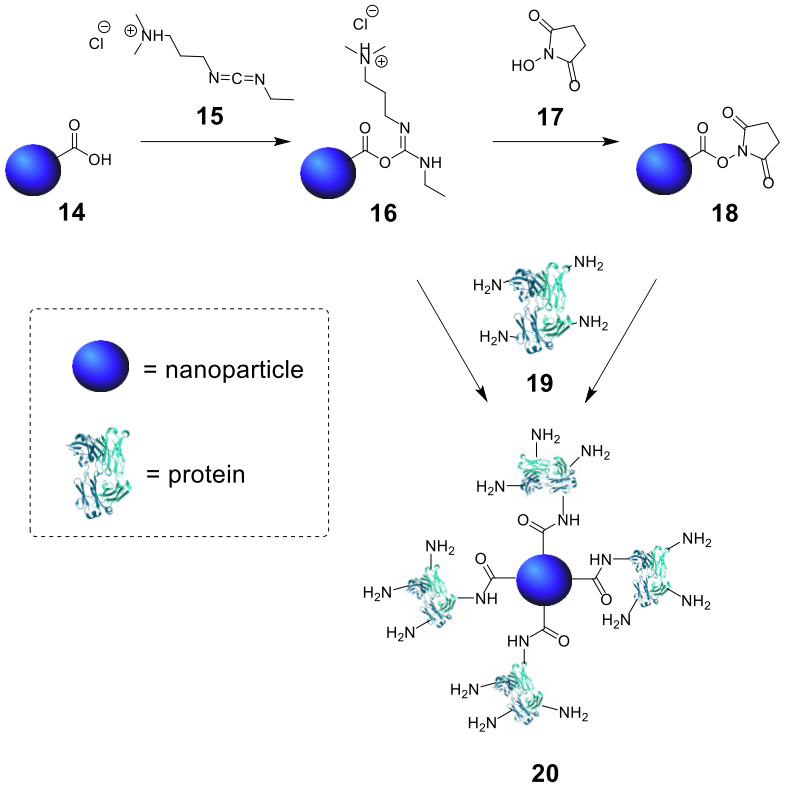

Scheme 7. EDC-mediated strategies for crosslinking reactions between nanoparticles and proteins.

However, the aforementioned approaches are not considered optimal as they usually present low reaction efficiencies in aqueous conditions *i.e.* although NHS-ester functionalised nanoparticles **18** are more stable than **16**, hydrolysis still competes with the primary amine reaction. Conjointly, it is believed that lysine amines modification affords very little control over the orientation of the antibody targeting ligands on the nanoparticles (*i.e.* the lack of paratope orientation, exerted by the random location attachment provided by lysines, which is believed to limit antigen-binding accessibility) (Scheme 8).

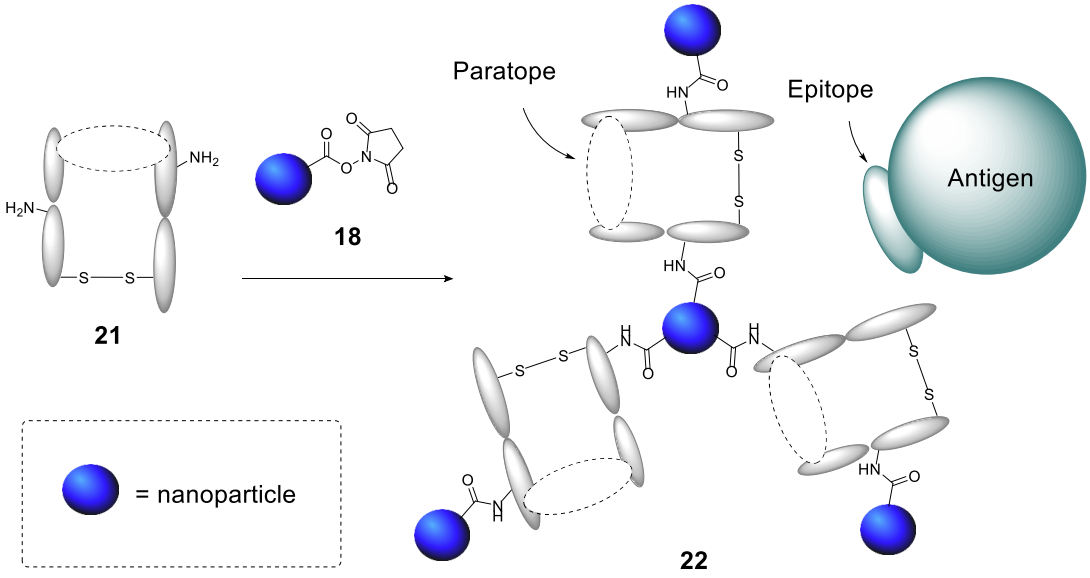

Scheme 8. Representation of the nanoconstruct **22** when NHS-ester amide formation chemistry is used to graft antibody fragments such as **21** to the surface of nanoparticles bearing NHS-esters (**18**) *via* the multiple lysine residues on the fragment.

Furthermore, it generates highly heterogeneous conjugates **22** due to the amine group's high natural abundance on antibodies. This abundance permits the conjugation of more than one NHS-ester modified nanoparticle **18** per antibody fragment, which could be related to aggregation issues in using such methodologies.

1.6 Project Aims

The aforementioned pyridazinediones (see section 1.3.2) present a novel approach for the functional re-bridging of native inter-strand disulfide bonds of antibodies or their constituent fragments and will be used as a platform for the generation of various nanoconjugates. This will enable a site-selective approach, permitting the modification of only a single site in a Fab fragment (see Fab conjugate **24**, Scheme 9), consequently preventing aggregation (*i.e.* through this approach, one Fab will only have one possible site for chemical attachment, whilst in the lysine conjugation strategy the Fab can chemically attach to more than one nanoparticle), enabling superior paratope presentation and optimal fragment packing on the nanoparticle surface.

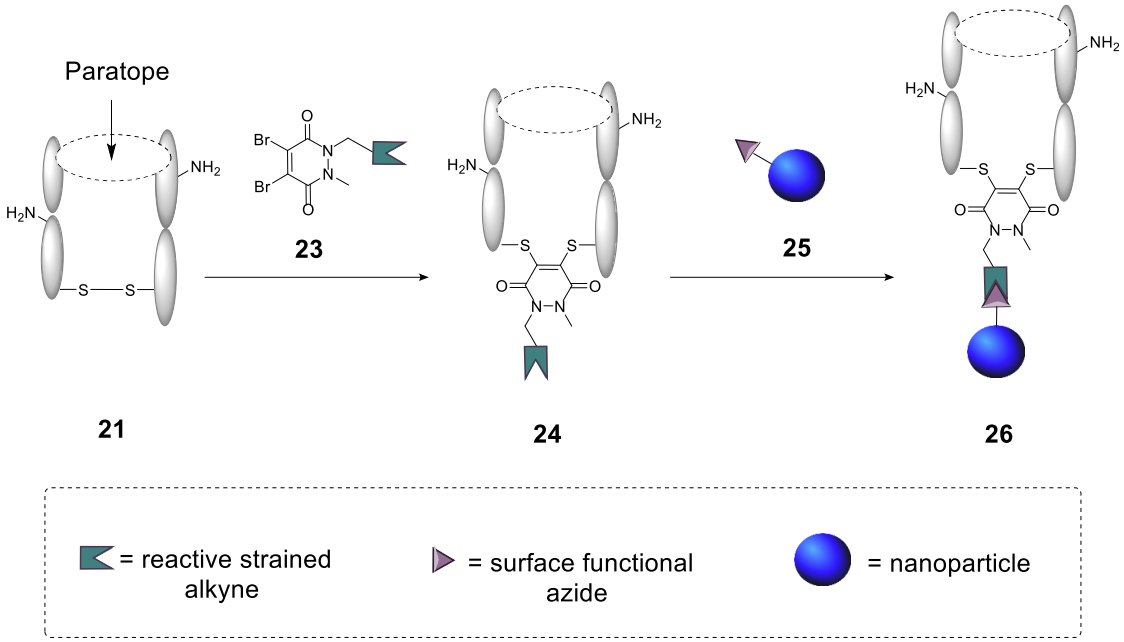

Scheme 9. Representation of the resulting nanoconjugate **26** when antibody-PD fragment **24** is attached to an azide nanoparticle **25**.

It is also aimed to demonstrate the superior chemical enhancement of chemistry 'click' strategies, compared to classical NHS-ester approaches for grafting proteins to the surface of particles. For that purpose, a strained alkyne clickable handle will be introduced in the PD scaffold, allowing further 'click' interaction with azide functionalised nanoparticles **25** (Scheme 9).

More interestingly, this disulfide re-bridging strategy occurs in a distal position from the paratope, permitting the Fab fragments to be oriented in an angle in which the paratopes are directed away from the nanoparticle; hence, they are more available to bind a potential receptor (Figure 11).

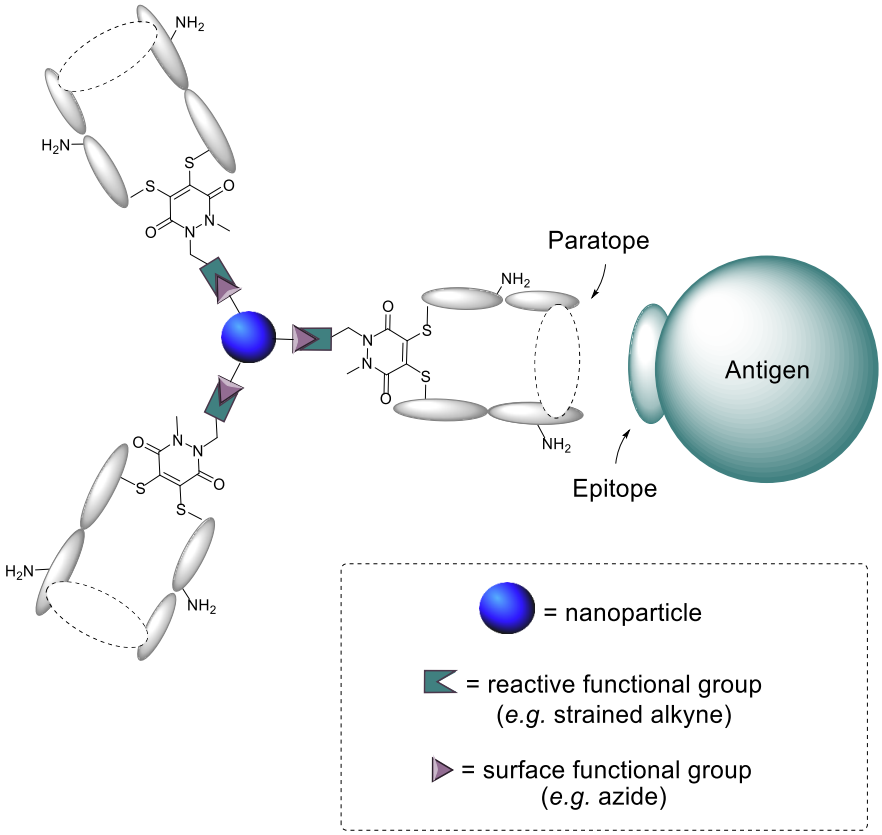

Figure 11. Representation of the potential antibody fragment display, away from the surface of particles, available for direct interaction with biological entities.

The overall aim is thus to understand whether the newly-oriented nanoconjugates possess a higher binding affinity to receptors compared to the non-oriented nanoconjugates. After this is confirmed, it will be investigated whether these nanoconjugates are specifically taken up by cancer cells.

Chapter 2 Creation of Fab protein targeted PEG-PLGA nanoparticles

As previously described, PEG-PLGA nanoparticles have been explored as drug delivery vehicles due to their potential benefits, such as good pharmacokinetic profiles and evasion of immune clearance mechanisms. However, their 'passive' activity is considered suboptimal (particularly in oncology treatment).[139] Consequently, to enhance cellular uptake and retention at tumour sites, the attachment of several targeting ligands to their surface has been explored, including aptamers, peptides, carbohydrates and antibodies - the latter being the most frequently employed.[140] However, grafting antibodies to nanoparticles is still at an early stage since most strategies do not consider the orientation of epitope, antibody size nor enhanced chemistry approaches.[40]

The aim of this chapter was to present novel strategies to refine antibody-nanoparticle conjugates with emphasis on achieving optimal presentation of the antibody for maximal interaction with the surface of nanoparticles and improved antigen-binding capability. This was examined by considering the following premises in the construction of ANPs:

1. Trastuzumab (TRAZ) (Figure 12) was chosen as the principle targeting ligand for this chapter because it is a humanised antibody that holds clinical relevance as an approved therapeutic against HER2 breast cancers. Moreover, there is significant room for refining and optimising the therapeutic efficiency of HER2-directed therapies, since relapse and mortality rates are high. [141] For this reason, promising new approaches are being developed not only in the ADC field (where cytotoxic moieties are linked to TRAZ antibodies) but also, more recently, in the ANC field, where TRAZ antibodies are being explored as targeting ligands for the formation of various nanoconjugates.[142,143]

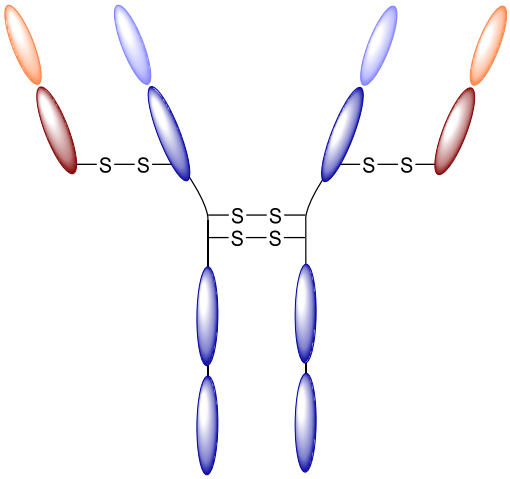

27

Figure 12. Representation of Trastuzumab Full Antibody, MW: 145532 Da.

2. TRAZ antibody fragments (*e.g.* Fab) were to be presented as an alternative to full antibodies because this would reduce surface crowding and allow maximum antibody capacity on the surface of PEG-PLGA nanoparticles (Figure 13). As previously stated, antibody fragments are reported to provide multiple benefits to the overall performance of nanoconjugates.[135] Moreover, Fab antibody fragments can be obtained from the native full antibody scaffold of TRAZ using standard enzymes, which is preferential to using costly and time-consuming protein engineering methods to obtain alternative antibody fragments.

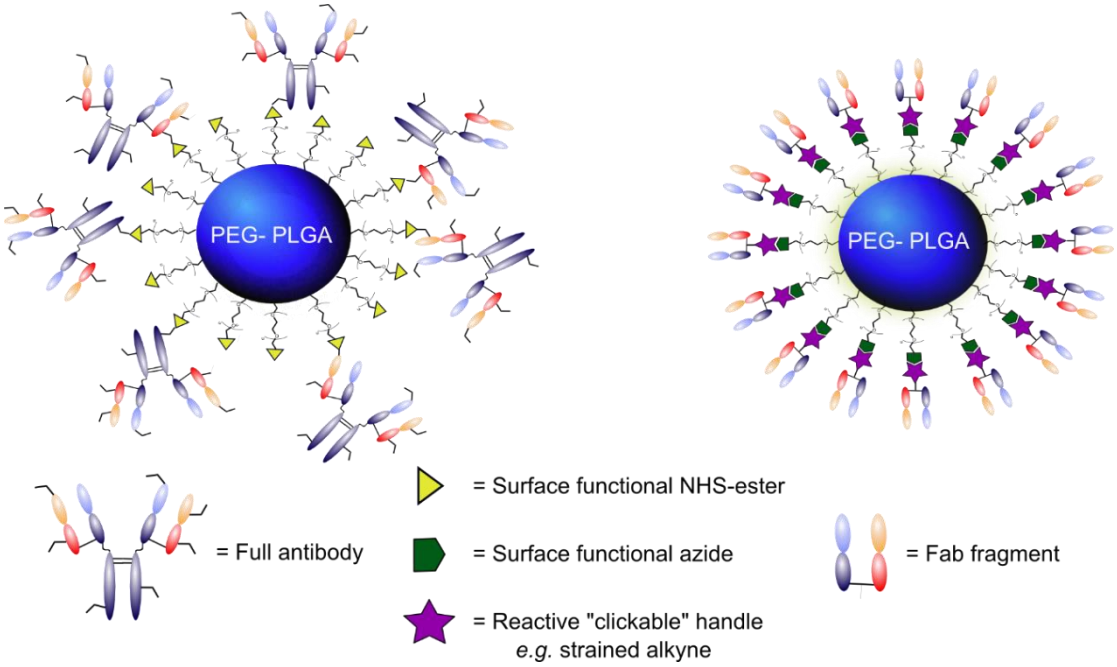

Figure 13. A comparison of differences in antibody-nanoparticle conjugates representing non-oriented attachment of native monoclonal antibodies (left) and highly oriented attachment of antibody Fab fragments (right).

The use of Fab fragments also ensures maximum complementary with the pyridazinedione scaffold since the fragment only contains one solvent accessible disulfide bond, compared to four present on a whole mAb, ensuring site-selective modification and preventing heterogeneity of further nanoconjugates (Figure 14).

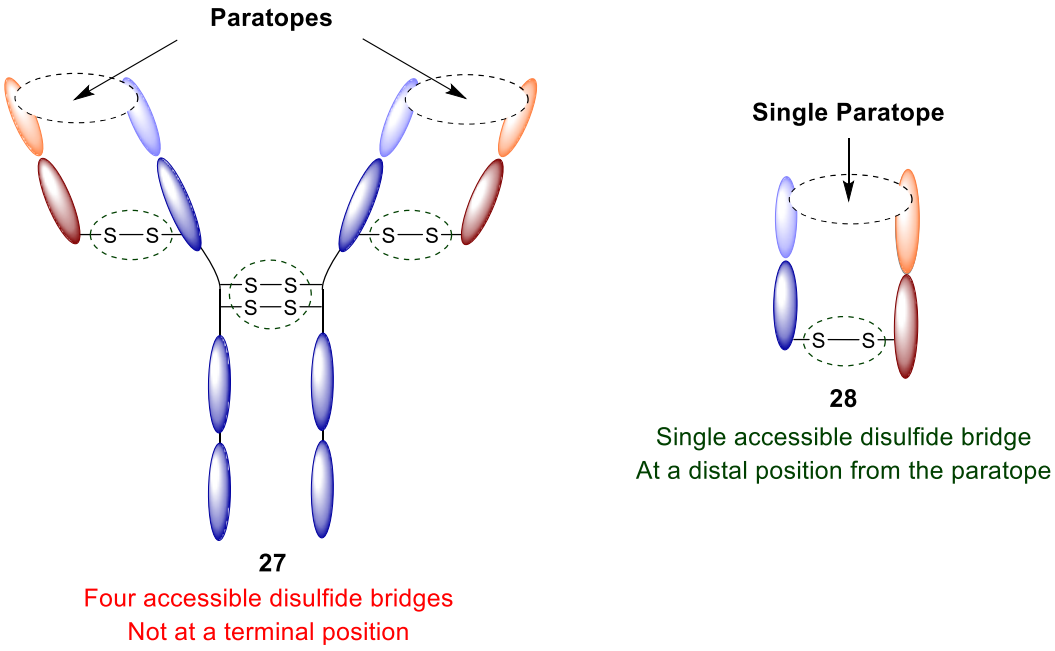

Figure 14. Comparison between whole mAb TRAZ and TRAZ Fab fragment, highlighting potential advantages of the fragment: enhanced homogeneity and orientation.

3. Site-selective Fab fragment disulfide modification was to be employed as an alternative to non-selective lysine modification through the implementation of a pyridazinedione linker (Figure 15). This would enable precise control over the location of the linker, result in no loss of covalent linkage between antibody chains and ensures modification at a single position that is distal from the antibody binding site.

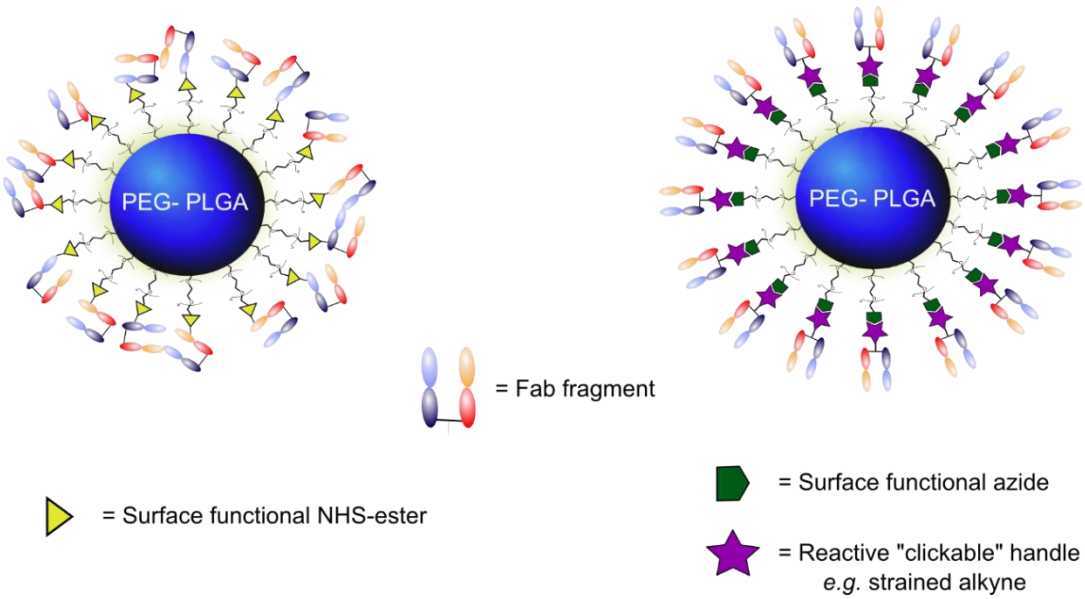

Figure 15. Representation of the differences in orientation *via* both lysine (left) and disulfide modification (right) in Fab fragments.

4. The use of ‘click’ chemistry approach to attach modified fragments to azide nanoparticles was to be implemented - it was decided to incorporate a strained alkyne BCN on the pyridazinedione moiety. In this way, and after pyridazinedione conjugation with a TRAZ Fab fragment, the newly-formed conjugate **29** could engage in a copper-free strained-promoted alkyl-azide cycloaddition (SPAAC) bio-orthogonal, simple and powerful reaction with azide derivates (Scheme 10).

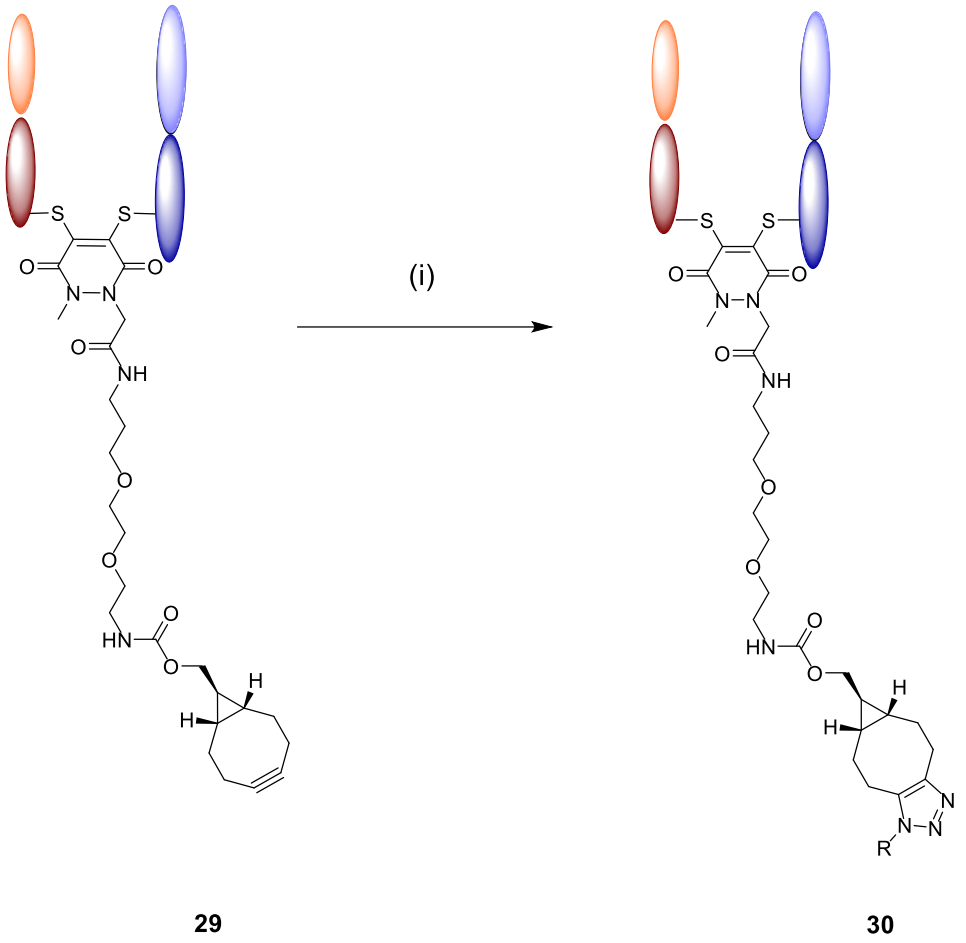

Scheme 10. Representation of method used for PD-modified TRAZ antibody fragment **29** attachment to azide moieties – a biorthogonal, copper-free ‘click’ reaction.

Reagents and conditions: (i) R-N_3, phosphate buffer pH 7.4, 21 °C, 5 h.

2.1 Generation of modified Fab fragments

Being aware of the aforementioned antibody fragment benefits over full antibodies, the study thus began with the formation of TRAZ Fab domains. These fragments were generated *via* a two-step enzyme digestion, a well-established method in literature;[40] Pepsin enzyme was used to cleave the IgG Fc region (*hinge* region, see Antibody fragments section 1.2.1, Figure 2), generating a $F(ab')_2$ fragment. Subsequently, the enzyme papain was used to cleave the monomer into two TRAZ Fab fragments. As an appropriate isotype control to evaluate the antigen target specificity of TRAZ Fab fragments, Cetuximab native antibody was also digested *via* the same route to form Cetuximab Fab fragments (Scheme 11). Cetuximab was considered an optimal control due to its structural similarities to Trastuzumab, and the fact that it binds to EGFR – a closely related but structurally distinct target to HER2.[144]

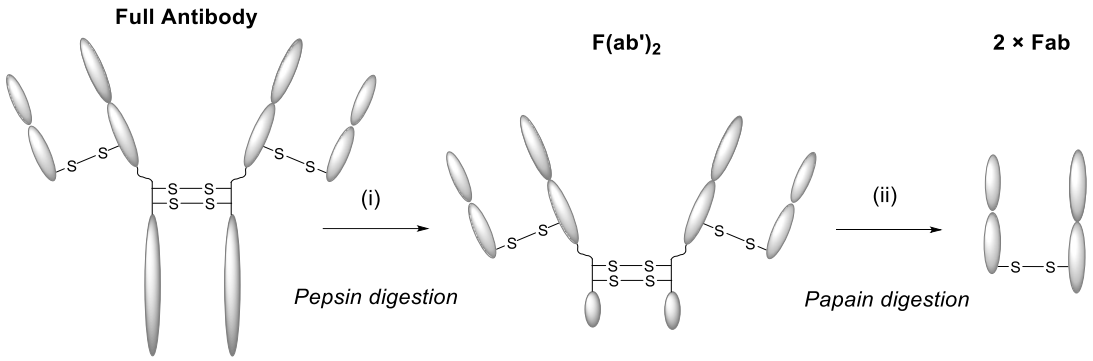

Scheme 11. Two-step digestion protocol applied to both Trastuzumab and Cetuximab antibodies, to yield Fab fragments of both.
Reagents and conditions: (i) Pepsin, acetate buffer pH 3.1, 37 °C, 5 h; (ii) Papain, digest buffer pH 6.8, 37 °C, 16 h.

Digestions of parent antibodies were optimised, yielding homogeneous species of the desired fragments. Although the procedure for Trastuzumab and Cetuximab digestion is similar, optimisation was needed to accomplish the formation of the desired Fab fragments, in good yields. For instance, Trastuzumab and Cetuximab required different amounts of each enzyme(s) to be fully digested into the fragments (see experimental for Chapter 2) Nonetheless, the current protocol for these digestions results in 54% yield of Cetuximab Fab (CTX Fab) and 84% of TRAZ Fab.

2.2 Synthesis of PD based linkers

Several chemical linkers have been explored in some extent to efficiently graft antibodies to the surface of PEG-PLGA nanoparticles, as they are known to have direct influence on drug loading capacity, and might affect several properties of the resulting construct such as potency, selectivity, stability, clearance rate and therapeutic index.[145] Also, the linker must be stable in circulation and enable drug release following internalisation into the target cell.[27] For all these requirements, the use of a pyridazinedione was chosen due to its aforementioned characteristics – its stability in circulation, exquisite selectivity to functionally re-bridge disulfide bonds presents in various antibody fragments and proven capability to bear 'clickable' handles, *e.g.* a strained alkyne, as well participate in 'click' reactions.

2.2.1 Synthesis of Methyl-Strained Alkyne PD (diBrMestra PD)

This part of the study thus began with the synthesis of a heterobifunctional linker that would facilitate conjugation to an antibody disulfide at one end (using a PD) and attachment to a azide nanoparticle at the other (strained alkyne). Synthesis of the strained alkyne functionalised pyridazinedione (diBrMestra PD **35**) proceeded from readily available starting materials in a facile manner over four steps (Scheme 12). Following mono-Boc protection of hydrazine **31**, amine **32** underwent imine formation and reduction to yield acid **33**. Following this, Boc deprotection and dehydration under acid condition afforded acid PD **34**.[27] In the final step, a PyBOP-mediated direct coupling between commercially available BCN(endo)-PEG_2-NH_2 **13** and acid PD **34** yielded diBrMestra PD **35**, albeit in low yield.

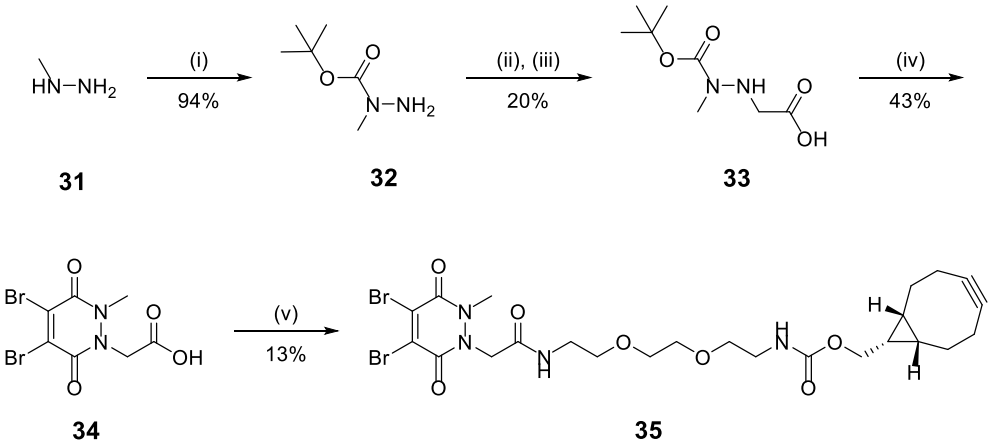

Scheme 12. Synthesis of Methyl-Strained Alkyne pyridazinedione **33** (diBrMestra PD).

Reagents and Conditions: (i) Boc anhydride, DCM, 21 °C, 4 h; (ii) Glyoxylic acid, *i*-PrOH, 21 °C, 5.5 h; (iii) Pd/C, H_2, 21 °C, 24 h; (iv) Dibromomaleic acid, AcOH, reflux, 24 h; (v) BCN(endo)-PEG_2-NH_2 **13**, PyBOP, DIPEA, DCM, 21 °C, 16 h.

2.2.2 Conjugation to TRAZ Fab and CTX Fab

Once the antibody Fab fragments and diBrMestra PD were generated, they were reacted to form Fab conjugates and complete conversion was observed. The newly-formed TRAZ bioconjugate **29**, which bears a strained alkyne for further functionalisation to particles (Scheme 13) is hereafter referred to as TRAZ Fab [disulfide]. To demonstrate the availably of the strained alkyne in this conjugate to participate in a ‘click’ reaction, the PD conjugate underwent a SPAAC reaction with Alexafluor®-488-N_3 **37**. This showed peak-to-peak conversion and confirmed the availability/reactivity of the strained alkyne.

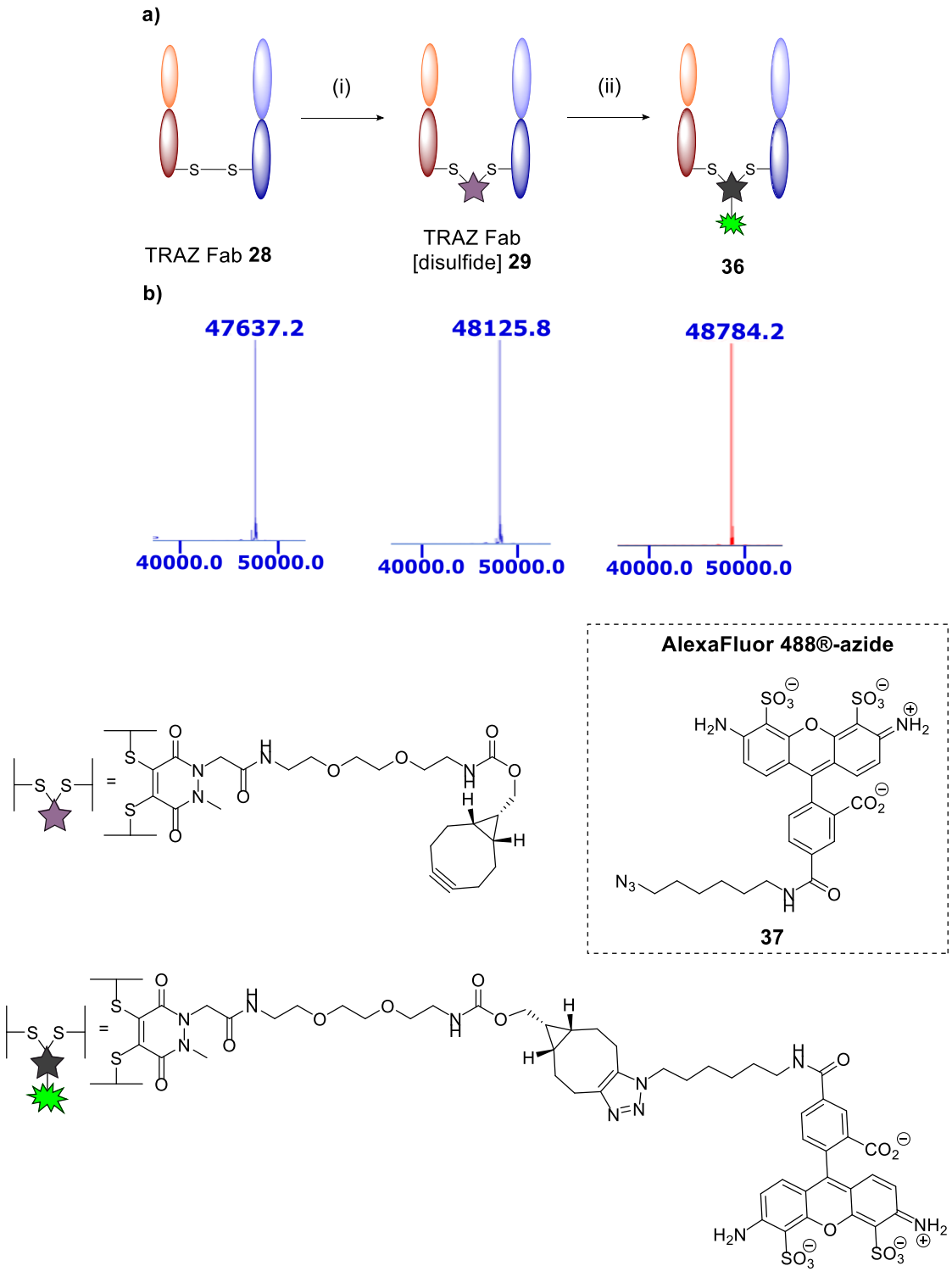

Scheme 13. a) Modification of TRAZ Fab with diBrMestra PD **35**. Calculated masses for **28**: 47629 Da; **29**: 48125 Da; **30**: 48781.

Reagents and conditions: (i) PD **35**, TCEP.HCl, borate buffer pH 8.0 (2 mM EDTA), 4 °C, 15 h; (ii) Alexafluor®-488-N_3 **37**, borate buffer pH 8.0 (2 mM EDTA), 21 °C, 2 h. **b)** LC-MS data showing successful conversion to conjugate **29** and 'clicked'

conjugate **36**. Spectra have been modified for clarity, see experimental Fig(s) 51 to 58 for full spectral data.

A cetuximab Fab bioconjugate was formulated in parallel, alongside with Alexafluor®-488-N_3 **37** 'click' reaction confirmation. This newly formed bioconjugate will from now on be referred to as CTX Fab [disulfide].

2.3 Synthesis of lysine reactive strained alkyne reagent

The synthesis of a lysine reactive strained alkyne control reagent was considered key as it would, after conjugation to TRAZ Fab **28** and attachment to an azide nanoparticle, allow us to understand if any difference in binding between this conjugate and a conjugate derived from fragment **38** was due to improved reactivity of 'click' chemistry over carbodiimide-based chemistry or if orientation plays a crucial role on antigen binding, *i.e.* having the 'clickable' handle at a distal position to the epitope compared to a 'clickable' handle on lysine residues in a random position attributed by lysine locations (Figure 16). Thus, the synthesis of such a reagent would allow for concrete appraisal of the importance of orientation as it would eliminate the possibility that greater binding was down to greater conjugation efficiency.

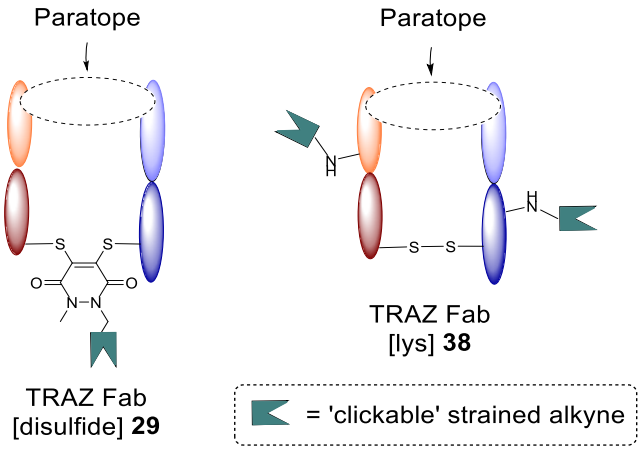

Figure 16. Representation of a TRAZ Fab fragment modification with a 'clickable' handle on the single disulfide distal position (left) compared with randomly assigned orientated 'clickable' handle through lysine residues (right).

Scheme 14 shows the structure of the required lysine reactive strained alkyne control reagent, **39**, and its preparation, developed by Dr Daniel Richards.

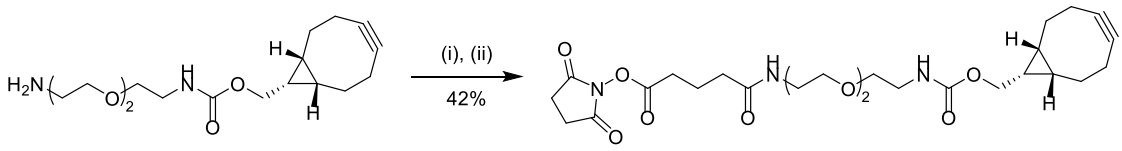

13 **39**

Scheme 14. Linker synthesised by Dr Daniel Richards that was further reacted with lysine residues *via* NHS chemistry.

Reagents and Conditions: (i) Glutaric anhydride, Et_3N, DCM, 21 °C, 2 h;
(ii) *N*-Succinimidyl carbonate, 21 °C, 2 h.

2.4 Manufacture of PEG-PLGA nanoparticles

For this study, polymeric nanospheres were utilised as they are easily formulated, relatively easy to handle, can be formulated with different reactive functional groups, and can encapsulate a variety of small molecule fluorophores to aid in characterisation and antigen binding studies. Consequently, and to enable the 'click' conjugation of TRAZ Fab [disulfide] **29** and analogous CTX Fab [disulfide], as well as control lysine modified strain alkyne bearing conjugate **38**, a novel polymeric nanoparticle incorporating a complementary azide moiety was needed. A homogeneous population of azide-terminated nanospheres (with a monodisperse size distribution of *ca.* 200 nm) was developed by Dr Michelle Greene, through a single emulsion protocol from a 25%:75% polymer blend of PLGA-PEG-azide and PLGA Resomer® RG 502 H (PLGA RG502H), in line with literature previously established methods (Scheme 15, in detail on experimental section for Chapter 2).[104]

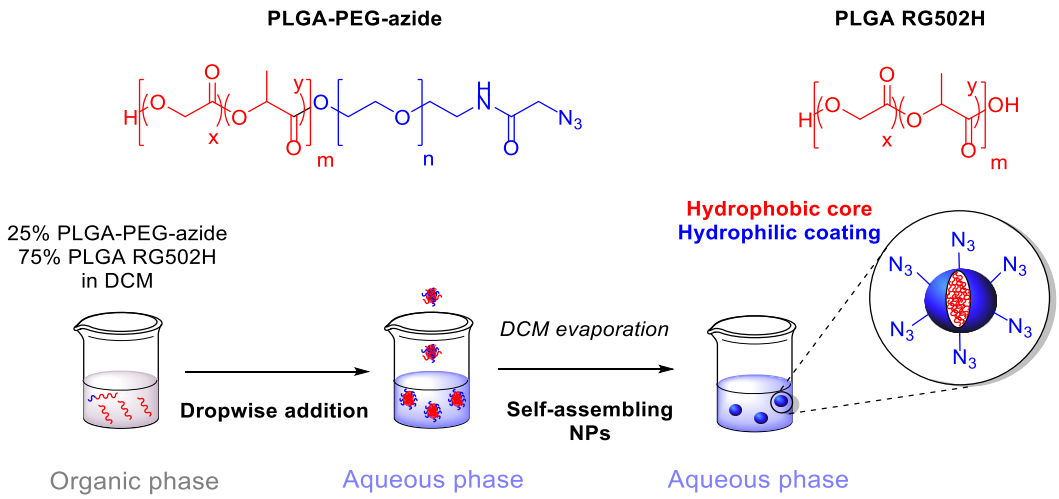

Scheme 15. Representation of azide-terminated nanospheres formation *via* hydrophobic-hydrophilic interactions; cytotoxic drugs or fluorophores can be encapsulated *via* prior addition to the organic phase.

Also, for further comparison with classical lysine-modified antibody-nanoparticle conjugates, NHS-ester terminated particles were also generated by Dr Michelle Greene. In this way, the NHS-esters coating could be further reacted with the lysines of native TRAZ Fab **28**, as is done classically. Both formulations of nanoparticles demonstrated great stability over several months, as they were monitored by Dynamic Light Scattering (DLS) and Zeta Potential, with no significant alterations in physicochemical characteristics observed upon storage at 4 °C or -20 °C (see experimental for Chapter 2). The comparison between TRAZ Fab [disulfide] **29** and TRAZ Fab [lys] **38** was considered key part of this work, as it just not clears up the differences in reactivity between NHS and 'click' chemistries but could also highlight the impact of directed chemistry against non-directed chemistry (Figure 16). It was also hypothesised that by using a pyridazinedione moiety the orientation could be enhanced, and consequently, the overall performance of the ANC improved.

2.5 Attachment of antibody fragment pyridazinediones (AFPDs) conjugates to nanoparticles

The modified fragments were sent to Queens University in Belfast (QUB), where Dr Michelle Greene proceeded with nanoparticle conjugates formation and

characterisation experiments. Bicinchoninic Acid (BCA), Surface Plasma Resonance (SPR), Fluorescence-linked immunosorbent assay (FLISA), competition and blocking assays were all performed in the QUB facilities, I shadowed Michelle Greene in doing some experiments and was also involved in doing some of the repeats. I also had input in designing of the experiments and analysing the results. Results are presented to demonstrate the efficiency of such methods of grafting antibodies to nanoparticles.

Azide-functionalised particles were incubated with TRAZ Fab [disulfide] **29** for 2 h at 21 ºC. Several equimolar controls were also formulated in parallel (Figure 17): (i) a native TRAZ Fab **28** conjugated to NHS-functionalised nanoparticles (**TRAZ Fab NP**), (ii) a modified TRAZ Fab [lys] **38** conjugated to azide-functionalised nanoparticles (a 'click' chemistry approach but with the strained alkyne introduced at the lysine residues, **TRAZ Fab [lys] NP**), (iii) a native CTX Fab conjugated to NHS-functionalised nanoparticles (**native CTX Fab NP**), (iv) a modified CTX Fab fragment conjugated to azide-functionalised nanoparticles (**CTX Fab [disulfide] NP**); (v) and finally both control azide and NHS nanoparticles (**Nude azide NP** and **Nude NHS NP**).

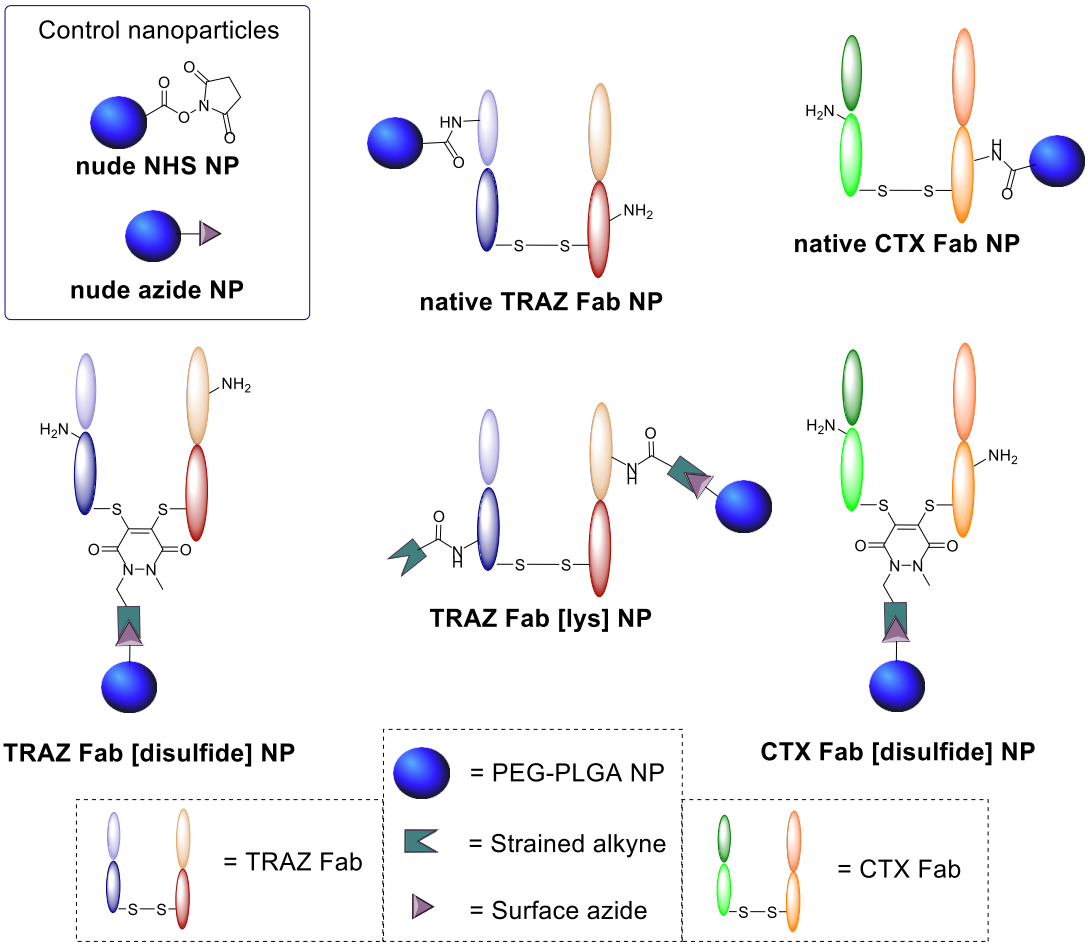

Figure 17. Representation of all nanoformulations tested: nude NHS-ester functionalised NP; nude azide functionalised NP; native TRAZ Fab NP; native CTX Fab NP; TRAZ Fab [disulfide] NP; TRAZ Fab [lys] NP; CTX Fab [disulfide] NP.

Bicinchoninic protein assay (BCA)

TRAZ Fab conjugation to the PEG-PLGA nanoparticles was then tested to determine the conjugation efficiency of the different chemistries (Table 2). This assay quantified the Fab attachment to the nanoparticles, and the concentration is determined by reference to a standard curve. This curve is prepared by spiking known amounts of native or modified Fab into nude NHS NP or nude azide NP suspensions, respectively. Fab conjugation was then calculated following the equation below:

$$Fab\ conjugation\ (\%) = \frac{\text{amount of Fab on NPs surface}}{\text{amount of Fab initially added to NPs}} * 100$$

Nanoformulation	Polymer	Diameter [a] (nm)	Zeta potential [a] (mV)	Fab conjugated (pmoles/mg polymer) [a]	Conjugation efficiency[a] (%)
Nude NHS NP	PLGA-PEG-NHS	191.1 ± 1.2	-4.6 ± 0.6	-	-
Native TRAZ Fab NP	PLGA-PEG-NHS	210.4 ± 2.7	-3.5 ± 0.1	65.3 ± 24.0	6.2 ± 2.3
Native CTX Fab NP	PLGA-PEG-NHS	191.2 ± 1.8	-3.9 ± 0.4	103.8 ± 29.1	9.9 ± 2.8
Nude azide NP	PLGA-PEG-azide	187.4 ± 1.8	-2.7 ± 0.6	-	-
TRAZ Fab [disulfide] NP	PLGA-PEG-azide	192.4 ± 1.5	-1.9 ± 0.7	193.1 ± 49.9	18.4 ± 4.7
TRAZ Fab [lys] NP	PLGA-PEG-azide	207.4 ± 0.1	-3.1 ± 0.3	475.0 ± 221.7	45.2 ± 21.1
CTX Fab[disulfide] NP	PLGA-PEG-azide	189.9 ± 0.2	-2.3 ± 0.1	208.4 ± 86.5	19.8 ± 8.2

Table 2. Characterisation of all the different nanoformulations. [a] Data expressed as mean ± SD, 3 measurements.

These results demonstrated that conjugation *via* the strained alkyne has superior efficiency over NHS-ester chemistry due to the greater reaction efficiency of copper-free 'click' chemistry in such conditions, possibly due to NHS-esters unstable hydrolytic nature in aqueous conditions.[146] This improvement is visible by the increase in conjugation efficiency values (*e.g.* TRAZ Fab [disulfide] NP shows *ca.* 3-fold more conjugation efficiency than native TRAZ Fab NP) despite the large abundance of lysine residues when compared to the single strained alkyne (Table 2). Also, perhaps as expected, TRAZ Fab [lys] NP had the greatest conjugation efficiency since many lysine residues were equipped with strained alkynes, which does further reinforce the idea that SPAAC chemistry is superior to NHS chemistry in these particular conditions.

Surface Plasmon Resonance (SPR)

Having successfully proved the enhanced formulation of the nanoconjugate, the ability of the different Fab fragments to bind to HER2 receptor was then explored through surface plasmon resonance. Binding activity was examined towards a HER2 fusion protein immobilized on a carboxymethylated dextran chip. Despite native TRAZ Fab NP being detected to some extent, the same concentration of the modified fragment TRAZ Fab [disulfide] NP led to a significantly enhanced binding profile

(measurements 3 and 6, respectively, Figure 18). Also, the expected low values of nude NP binding (both NHS and azide) or CTX Fab NP (both native and modified) confirm the necessity of TRAZ Fab for antigen binding.

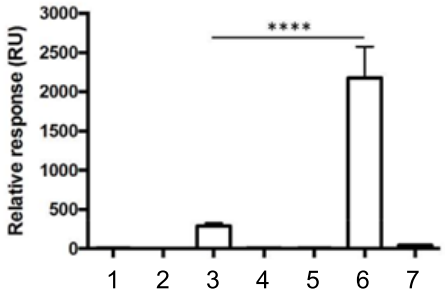

Figure 18. SPR assessment of TRAZ Fab NP and associated controls. Number of samples: 3. **1)** Nude NHS NP. **2**) Native CTX Fab NP. **3)** TRAZ Fab NP. **4)** Nude azide NP. **5)** CTX Fab [disulfide] NP. **6)** TRAZ Fab [disulfide] NP. **7)** TRAZ Fab[lys] NP. Relative response (RU) is striking on the TRAZ Fab [disulfide] PLGA-PEG azide particles. Statistical significance was established by one-way ANOVA and Tukey's post-hoc test (****$p \leq 0.0001$). I shadowed Dr Michelle Greene in doing this experiment.

Importantly, HER2 binding of modified TRAZ Fab [lys] NP was also negligible despite highly efficient coupling of the fragment to nanoparticles (*vide supra*, Table 2). This could possibly indicate aggregation issues, *i.e.* although the 'click' chemistry is shown to be more efficient, more nanoparticles will be attached to a single Fab fragment, causing a clustering effect and, consequently, reduced paratope accessibility. This comparison demonstrates that the site-selective nature of pyridazinedione conjugation to Fab plays a critical role in the observed improvements in antigen binding; this indicates improved paratope accessibility is granted by the oriented display of the fragments on the nanoparticle surface.

Fluorescence-linked immunosorbent assay (FLISA)

To exclude the possibility that the improved antigen binding of modified Fab [disulfide] NP is a consequence of free Fab complexation rather than direct coupling to nanoparticles, a fluorescence-linked immunosorbent assay (FLISA) was performed. For this, the aforementioned PEG-PLGA nanoparticles were labelled by encapsulating with them a fluorophore, *via* addition of rhodamine 6G to the organic phase prior to

the self-assembly. These particles were then incubated with modified TRAZ [disulfide] **35** and complementary controls. After this time, the well-plates were washed extensively to ensure that all free nanoformulations were washed off. In this way, the immobilised HER2 antigen-plates would only retain fluorescent nanoparticles that were bound. Following this, the nanoparticles that were bound to the plate were dissolved in organic solvent for fluorescence readout. The observed trend was in agreement with the SPR analyses, demonstrating TRAZ Fab[disulfide] NP superior binding to HER2 when compared to native TRAZ Fab NP and also to the remaining controls (Figure 19).

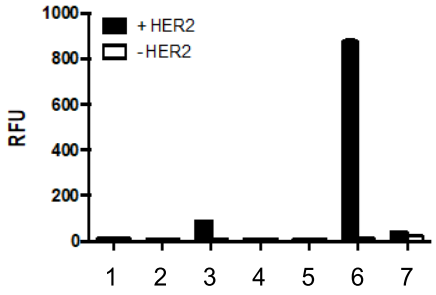

Figure 19. FLISA assessment of TRAZ Fab NP and associated controls. Number of samples: 3. **1)** Nude NHS NP. **2)** Native CTX Fab NP. **3)** Native TRAZ Fab NP. **4)** Nude azide NP. **5)** CTX Fab[disulfide] NP.**6)** TRAZ Fab[disulfide] NP. **7)** TRAZ Fab[lys] NP. I actively participated in doing this experiment.

In summary, the data indicates that the non-oriented conjugation approach limits paratope accessibility. Contrastingly, the site-selective nature of the pyridazinedione linkers enhances paratope accessibility due to the oriented configuration onto a nanoparticles surface; the single modification only allows one point of attachment, which is distal from the binding paratope.

Blocking and competition assays

Targeting specificity was further validated *via* other FLISA assessments, where HER2 coated wells are pre-incubated with an excess of TRAZ full antibody with the purpose of impeding nanoparticle binding *via* Fab fragments (Figure 20). These results demonstrated higher HER2 binding affinity for both nanoconjugates Native TRAZ Fab NP and TRAZ Fab [disulfide] NP where no TRAZ full antibody was added, albeit with a remarkable enhanced binding in the latter.

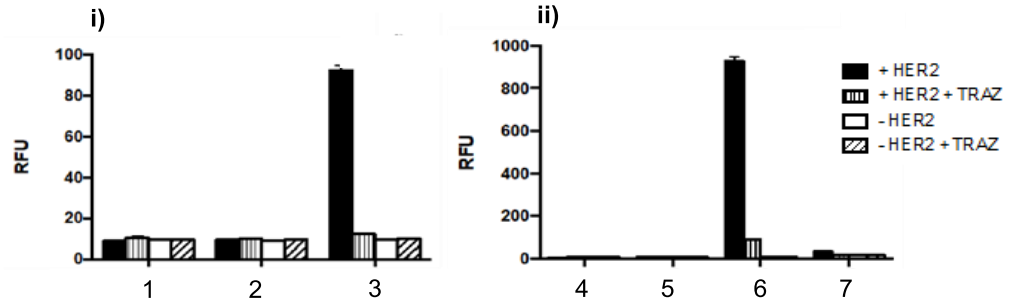

Figure 20. FLISA competition assays: HER2 binding activity of **i)** native TRAZ Fab NP **ii)** TRAZ Fab [disulfide] NP and associated controls: **1)** Nude NHS NP **2)** Native CTX Fab NP **3)** Native TRAZ Fab NP **4)** Nude azide NP **5)** CTX Fab [disulfide] NP **6)** TRAZ Fab[disulfide] NP **7)** TRAZ Fab[lysine] NP. Number of samples: 3. I actively participated in doing this experiment.

Collectively, these results show the successful coupling of native TRAZ Fab **28** and TRAZ Fab [disulfide] **29** domains to NHS- and azide-functionalised nanoparticles by different approaches, generating two active-targeted nanoconjugates with HER2 binding capability (*i.e.* these newly-formed nanoconjugates show improvement in antigen binding compared to respective nude nanoparticles' controls, nanoformulations 1 and 3; 4 and 6, Figure 20). However, there is a significantly enhanced binding profile in TRAZ Fab [disulfide] NP when compared to TRAZ Fab NP (over ten times more in both modified FLISA and competition assays, Figure 19 and 20).

Orientation influence in antigen-binding

Next, it was crucial to examine upon SPR analysis the basis for the superior HER2 binding activity of the nanoconjugate through site-selective chemistry (TRAZ Fab [disulfide] NP). It was necessary to eliminate the possibility that this effect could be simply attributed to enhanced Fab loading (*i.e.* provided by a more suitable 'click' strategy over NHS-ester chemistry for such conditions) rather than any orientation benefits. For this, both native TRAZ Fab NP and TRAZ Fab [disulfide] NP were generated where different amounts of fragments **28** and **29** were added to NHS-ester nanoparticles and azide nanoparticles, respectively (Table 3, range of 210-2100 pmoles/mg of polymer). The generated data elicited a significantly enhanced binding

profile on TRAZ Fab [disulfide] NP (Figure 21, measurements 8-12) proving that superior binding in not only attributed to enhanced protein conjugation.

Formulation	Fab added (pmoles/mg polymer)	Fab conjugated (pmoles/mg polymer)	Relative response (RU)
(1) Nude NHS NP	-	-	17.0
(2) Native TRAZ Fab NP	210.13	98.76	137.2
(3) Native TRAZ Fab NP	525.33	90.36	261.6
(4) Native TRAZ Fab NP	1050.66	52.53	267.2
(5) Native TRAZ Fab NP	1575.99	142.89	507.6
(6) Native TRAZ Fab NP	2101.33	102.96	204.5
(7) Nude azide NP	-	-	23.8
(8) TRAZ Fab [disulfide] NP	210.13	74.81	2175.4
(9) TRAZ Fab [disulfide] NP	523.33	195.32	2955.3
(10) TRAZ Fab [disulfide] NP	1050.66	214.03	2526.4
(11) TRAZ Fab [disulfide] NP	1575.99	243.12	2224.2
(12) TRAZ Fab [disulfide] NP	2101.33	292.99	1643.8

Table 3. SPR Biacore® data for the HER2 binding activity of native TRAZ Fab NP and TRAZ Fab NP [disulfide] with various protein loadings. I shadowed Dr Michelle Greene in doing this experiment.

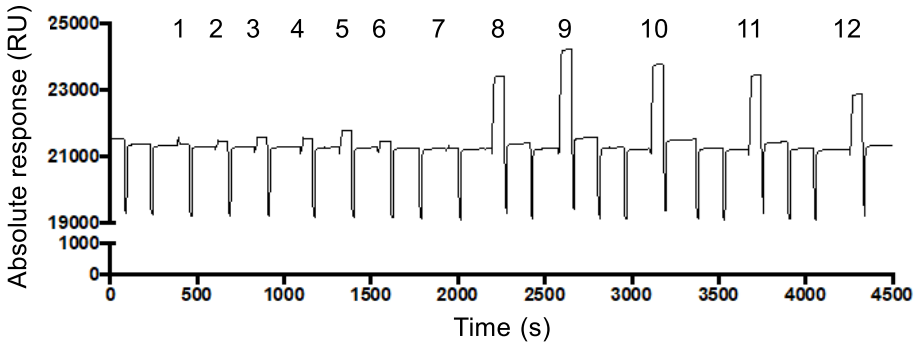

Figure 21. Representative SPR Biacore® sensorgram for Table 3.

Interestingly, enhanced binding of TRAZ Fab [disulfide] NP was observed even when the Fab loading was almost half that of native TRAZ Fab NP (Table 3, measurements 5 and 8). This suggests that significant benefits can be achieved even in the case of lower Fab loadings onto particles, establishing the positive effect of using controlled chemistries that enable orientation. These studies were replicated *via* FLISA, with comparable findings to SPR analyses (see below, Figure 22).

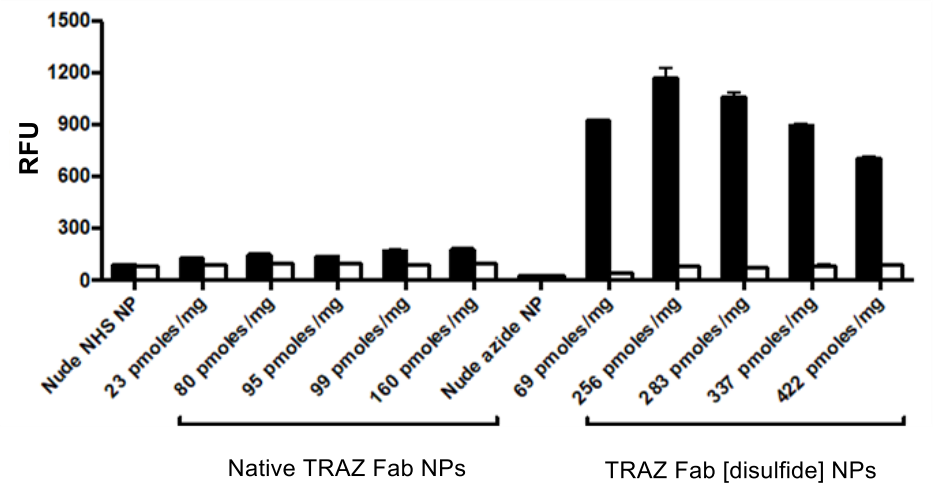

Figure 22. HER2 binding activity of native TRAZ Fab NP or TRAZ Fab [disulfide] NP (400 µg polymer/mL) with various protein loadings was assessed by modified FLISA through fluorescence readout. Protein loadings are expressed as pmoles of Fab per mg polymer. Data expressed as mean ± SEM. Number of samples: 3. Dr Michelle Greene proceeded with this set of experiments.

Curiously enough, this data also revealed that with the addition of more than 256 pmoles/mg of TRAZ Fab [disulfide] **29** the binding activity to HER2 is diminished gradually, which suggests potential steric hindrance effects that lead to suboptimal paratope display. Thus, this particular set of tests was not only crucial to identify the range of optimal loading of antibody fragment TRAZ Fab [disulfide] **29** (between 256-283 pmoles/mg), but it was also important to highlight the level of delicacy needed for an optimal decoration of antibody fragments onto the particles.

2.6 Cell-binding studies on TRAZ AFPD conjugated to PEG-PLGA nanoparticles

Through the above sets of data using BCA, SPR and FLISA analyses, it was possible to prove the superior binding of TRAZ Fab[disulfide] NP over native TRAZ Fab NPs to the receptor HER2. It was, however, felt important to further evaluate the aforementioned nanoconstructs in a more biologically relevant context through cell-based assays; Michelle Greene carried out the following cell-based assays. To this end, these nanoconjugates were labelled by encapsulation of nile red dye and incubated with the HER2-positive cell line HCC1952. This cell line was chosen as it grows in a

monolayer, permitting enhanced confocal imaging when compared to other HER2-sensitive cell lines (*e.g.* BT747 cell line, which is also used in the next set of experiments, grows in clusters, making it harder to distinguish individual cells). Confocal microscopy demonstrated an evident association of TRAZ Fab [disulfide] NP to these cells (see Figure 23). Additionally, HER2-dependent binding was also verified *via* a co-incubation test, where an excess of TRAZ full antibody and TRAZ Fab [disulfide] NP were simultaneously added, ablating significantly the fluorescence when compared to the original experiment (where only the TRAZ Fab[disulfide] NP was added).

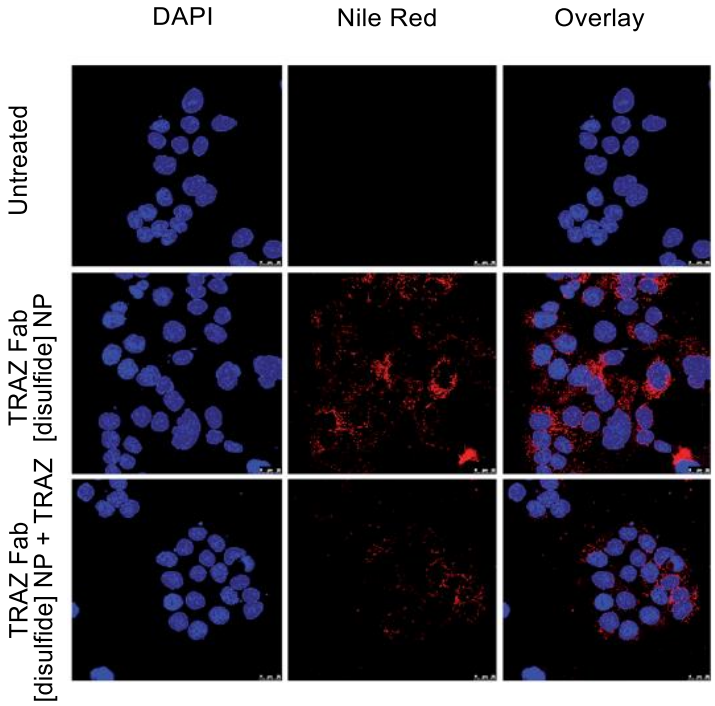

Figure 23. Validation of TRAZ Fab functionality in cell-based assays. Confocal microscopy images of HCC19954 cells treated with TRAZ Fab [disulfide] NP encapsulating nile red (400 μg polymer per mL) ± TRAZ Full Antibody. Scale bar = 25 μm. Dr Michelle Greene proceeded with this set of experiments.

As a final series of studies, the therapeutic effect of the TRAZ Fab conjugates *in vitro* was examined. The BT474 breast cancer cell line was preferred to conduct this study for two reasons: i) the cell line HCC1952, which was utilised for the confocal studies, showed limited sensitivity to TRAZ; and ii) TRAZ full antibody and its fragments are reported and well-known to reduce BT474 cell viability.[147]

The goal of this study was to understand whether TRAZ Fab nanoconjugates (both native TRAZ Fab NP and TRAZ Fab [disulfide] NP) could induce a similar or more pronounced reduction in viability of BT474 cells compared to the activity of the TRAZ Fab alone.

Whilst TRAZ Fab **28** alone led to a gradual reduction in cell viability over time, as anticipated, this effect was less pronounced for the native TRAZ Fab NP (*vide infra*, Figure 24). This could be explained by the fact that the TRAZ Fab NP structure limits the orientation of the antibody fragments onto their surface, hence reducing binding to the HER2 antigen.

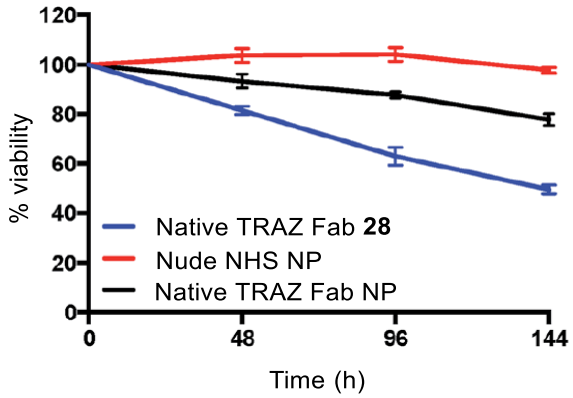

Figure 24. BT474 were treated with native TRAZ Fab NP (previously treated with 525.33 pmoles of Fab/mg of polymer) and respective controls (500 µg polymer per mL). The CellTiter-Glo assay was performed at 48, 96 and 144 h following treatment. Sample number: 3. Data expressed as mean ± SEM. Dr Michelle Greene proceeded with this set of experiments.

Interestingly, for TRAZ Fab [disulfide] NP the reduction in cell viability is much more comparable to the TRAZ Fab [disulfide] **29** (Figure 25), supporting the theory that the orientation provided by the site-specific conjugation approach is near-optimal (*i.e.* due to a free movement of native TRAZ Fab, it has the flexibility to orientate itself towards the epitope optimally whilst when a Fab is attached to a nanoparticle the orientation is imposed and more rigid).

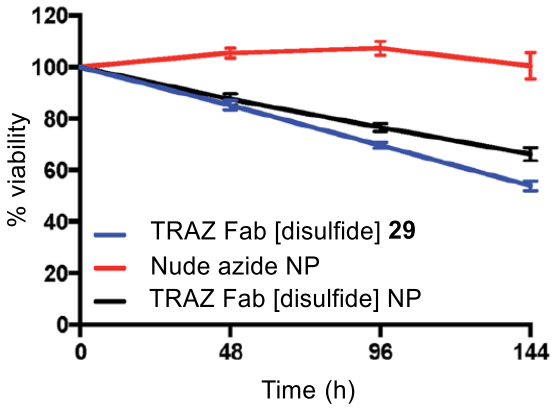

Figure 25. BT474 were treated with TRAZ Fab[disulfide] NP (previously treated with 525.33 pmoles of Fab/mg of polymer) and respective controls (500 µg polymer per mL). The CellTiter-Glo assay was performed at 48, 96 and 144 h following treatment. Sample number: 3. Data expressed as mean ± SEM. Dr Michelle Greene proceeded with this set of experiments.

It is also important to highlight that free TRAZ Fab [disulfide] **29** was also used as a control, providing similar results to native TRAZ Fab **28** (see Figures 24 and 25), confirming that the installation of a pyridazinedione linker does not adversely affect the functionality of TRAZ Fab.

In summary, it was concluded that the controlled orientation of TRAZ Fab on the nanoparticles leads to superior binding to HER2 antigen when compared with traditional NHS ester coupling chemistry *via* lysine residues – the latter demonstrated retention of Fab functionality in a cell-based assay due to the lack of orientation.

This work offers a significant contribution to nanoconjugate refinement in terms of design and efficiency, reinforcing the importance of controlled chemical ligation for the overall performance of nanoconjugates, and thus will be a basis for future works in the context of this thesis.

Chapter 3 Further exploration of CTX AFPDs binding to EGFR

In the previous chapter, it was demonstrated that the controlled orientation of TRAZ Fab fragments onto the surface of nanoparticles had a significant impact on HER2 antigen binding. Also, in cell-based assays, targeting of the nanoconjugate was improved through the site-selective modification method used. Thus, it was theorised that these findings could be extended to other receptor-ligand pairings, highlighting the versatility of this novel approach. In this chapter, it is proposed that Cetuximab Fab, previously used as a negative control for the antigen binding specificity of Trastuzumab to HER2, is used as a targeting agent to bind to EGFR and deliver a toxic payload into tumour cells.

Cetuximab is a mouse-human chimeric monoclonal antibody and has been attracting attention due to its ability to improve the outcome of metastatic colorectal, head and neck cancers treatments.[148] Cetuximab binds to the extracellular domain of the EGFR before the resulting complex is internalised into the cell and further degraded, resulting in down-regulation of EGFR expression.[149] However, the efficacy of adding Cetuximab to chemotherapy treatments is still limited (*e.g.* 57% of patients show a reduction in tumour size when Cetuximab is administrated in combination with FOLFIRI (chemotherapeutic regimen), compared to a 39% reduction when FOLFIRI is administrated alone). This is partly because the amount of chemotherapeutic cannot be increased in combination therapy, *i.e.* it is still dose-limited.[150] However, by encapsulating chemotherapeutic drugs into a nanoparticle that is functionalised with Cetuximab (or associated fragments) on its surface, it is envisioned that superior efficacy will be observed (*i.e.* the amount of toxic drug will no longer be so dose-limited as the nanoparticle will, in essence, prevent release of it in the blood prior to reaching the targeted tumour). Thus, it is key to equip Cetuximab antibody-nanoparticle conjugates with higher amounts of cytotoxic payloads than combination therapy allows in order to improve therapeutic potential. In view of this, the aim of this chapter involves combining the aforementioned Chapter 2 strategy to modify nanoparticle surfaces with antibody fragments with PEG-PLGA nanoparticles' ability

to entrap cytotoxic drugs. In this way, it could be possible to establish an advantage of antibody-nanoparticle conjugates over not only traditional chemotherapeutic approaches but also ADCs (where only a relatively small quantity of toxic payloads are tolerated on the antibody scaffold, e.g. *ca.* < 4 drug per antibody – higher loadings tend to lead to rapid clearance of the ADC from the blood).

3.1 Generating CTX Fab fragments – a new approach

Initially, a Cetuximab Fab fragment (CTX Fab) was chosen as a targeting ligand. Generation of CTX Fab was achieved by a one-step enzyme digestion using papain, following by a protein A resin antibody purification, to separate Fab and Fc-containing fragments (Scheme 16). This procedure not only provided CTX Fab in better yield when compared to the 2-step protocol employed for the same antibody in Chapter 2 (68% vs 54%) but was also demonstrated to be more efficient, since digestion times were shortened (5 h vs 21 h).

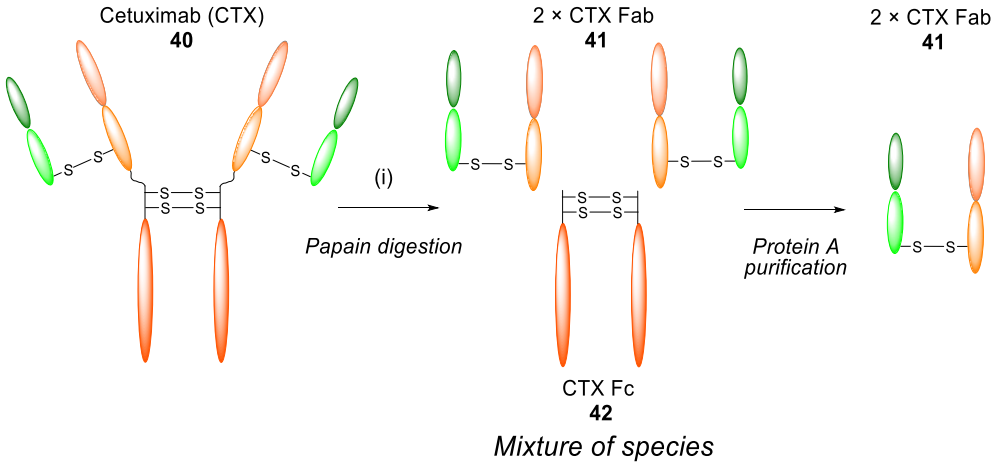

Scheme 16. Optimised digestion protocol applied to Cetuximab antibodies, to yield CTX Fab fragments.

Reagents and conditions: (i) Papain, digest buffer pH 6.8, 37 °C, 5 h.

3.2 Redesign of Strained Alkyne Pyridazinedione-based linkers (Mepstra PD) and conjugation to CTX Fab

Whilst formulating new approaches for new nanoconjugates, parallel work within the Chudasama group demonstrated new methodologies for generating Pyridazinedione linkers more efficiently.[151] These improvements led to the development of a new DiBr PD strained alkyne species, *i.e.* diBrMe**p**stra PD **46** (Scheme 17). diBrMepstra PD **46** differs from diBrMestra PD **35** in the addition of an extra methylene group between the amine and PD core as this gave superior yields in the synthesis. Intermediate NHS-ester species **45** is also isolatable, storable for many months, and participates in a more reliable NHS-mediated coupling strategy to commercially available BCN(endo)-PEG_2-NH_2 **13** compared to using other coupling reagents such as PyBOP. Synthesis of the strained alkyne functionalised pyridazinedione **46** proceeded from readily available starting materials in a facile manner over five steps (Scheme 17). Di-boc protection of hydrazine **31** and consequent Michael addition to *tert*-butyl acrylate yielded hydrazine **43**. Following this, deprotection and dehydration under acid conditions afforded acid PD **44**. Subsequent esterification of **44** with NHS afforded the amine-reactive PD **45**. In the final step, an addition-elimination reaction between commercially available BCN(endo)-PEG_2-NH_2 **13** and PD **45** yielded desired diBrMepstra linker **46.**

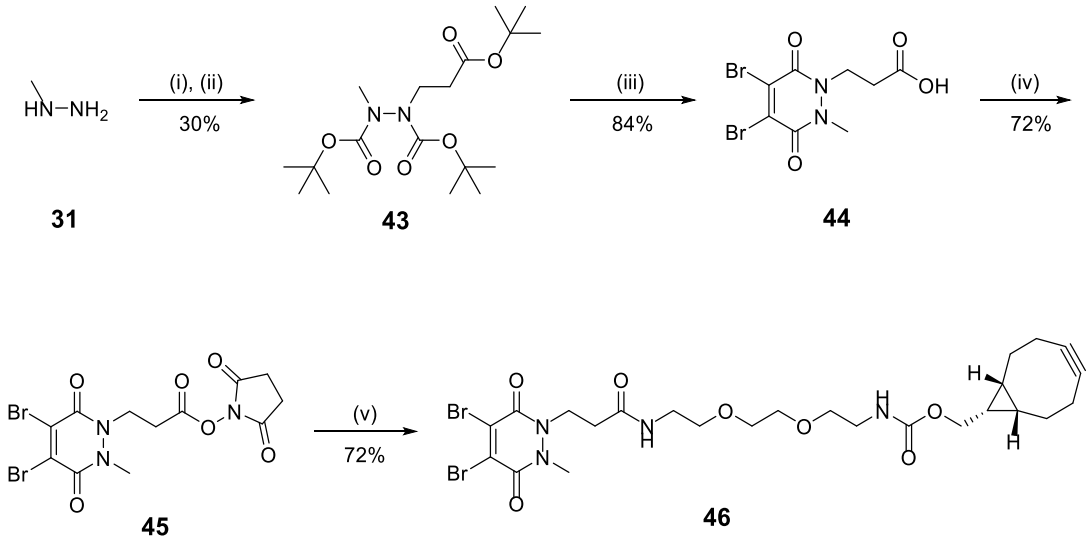

Scheme 17. Synthesis route of diBrMepstra PD **46**.

Reagents and Conditions: (i) Boc anhydride, *i*-PrOH, DCM, 21 °C, 16 h; (ii) *tert*-butyl acrylate, *i*-PrOH, 60 °C, 24 h; (iii) Dibromomaleic acid, AcOH, reflux, 5 h; (iv) DCC, NHS, THF, 21 °C, 16 h (v) BCN(endo)-PEG_2-NH_2 **13**, MeCN, 21 °C, 16 h.

Following the preparation of CTX Fab fragment **41** and diBrMepstra PD **46**, their conjugation was trialled using the methods previously described in Section 2.2.2. As expected, the reaction proceeded efficiently, and due to the employment of a newly-synthesised linker, the resulting bioconjugate is hereafter referred as CTX Fab Mepstra **47**. As before, the availability of the strained alkyne to participate in a 'click' reaction was demonstrated through a SPAAC reaction with Alexafluor®-488-N_3 **37** (see Scheme 18), yielding CTX Fab Mepstra Alexafluor **48**. Successful generation of conjugates **47** and **48** were confirmed by SDS-PAGE, UV/Vis and LC-MS (See experimental for Chapter 3, Fig(s) 66 to 71).

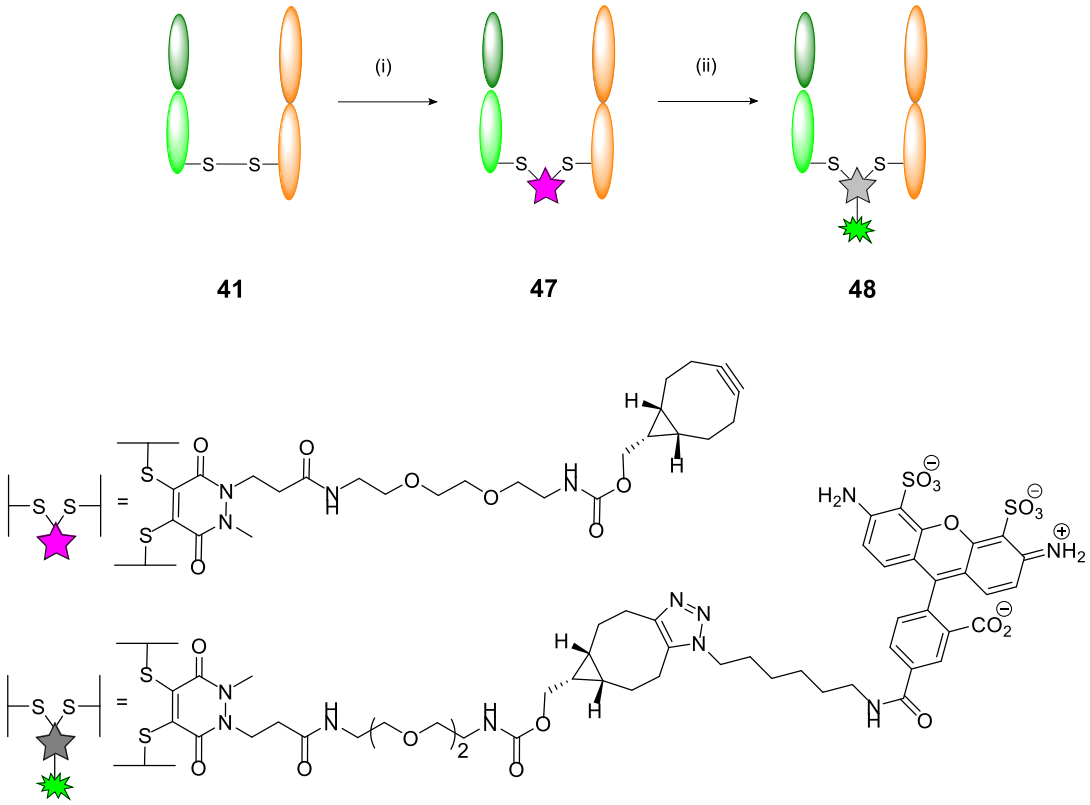

Scheme 18. Modification of TRAZ Fab with diBrMepstra PD **46** and 'click' with an Alexafluor®-488-N_3 **37**.

Reagents and conditions: (i) diBrMepstra PD **46**, TCEP.HCl, borate buffer pH 8.0 (5 mM EDTA), 21 °C, 15 h; (ii) Alexafluor®-488-N_3 **37**, phosphate buffer pH 7.4, 21 °C, 2 h.

3.3 Attachment of CTX AFPD conjugates to PEG-PLGA nanoparticles

The modified fragments were again sent to our collaborators in Queens University in Belfast for appraisal in the formation of nanoparticle conjugates thereof. Dr Michelle Greene proceeded with nanoparticle formulation and modification experiments. I shadowed and assisted Dr Michelle Greene in carrying out some of the following BCA and FLISA assays.

In accordance with Chapter 2, a 25%:75% polymer blend of PLGA 502H : PLGA-PEG-azide was used to formulate nanoparticles of approximately 200 nm in diameter, with a monodisperse size distribution. Subsequently, aforementioned nanoparticles

were incubated with modified CTX Fab Mepstra **47** for 2 h at 21 ºC. Several equimolar controls were prepared in the same conditions and conducted for the first set of experiments (Figure 26): (i) a native CTX Fab **41** conjugated to NHS-functionalised nanoparticles (**native CTX Fab NP**), (ii) a modified CTX Fab fragment **47** conjugated to azide-functionalised nanoparticles (**CTX Fab Mepstra NP**); (iii) and also the correspondent controls, both azide and NHS nanoparticles (**Nude azide NP** and **Nude NHS NP**).

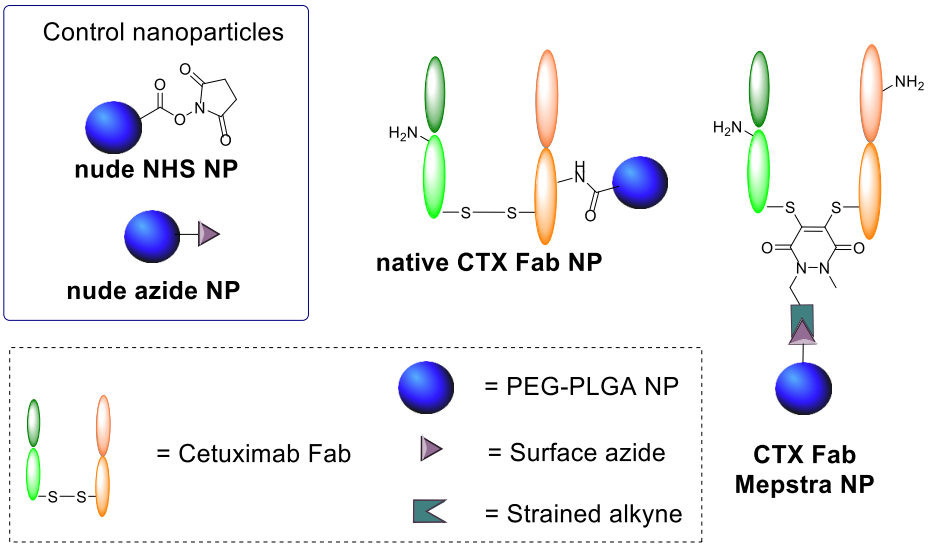

Figure 26. Representation of all nanoformulations tested: nude NHS-ester functionalised NP; nude azide functionalised NP; native CTX Fab NP; CTX Fab Mepstra NP.

Bicinchoninic protein assay (BCA)

As before, CTX Fab conjugation to the PEG-PLGA nanoparticles was tested to confirm the conjugation efficiency of strained alkyne over NHS-ester chemistry (see Section 2.5):

Nanoformulation	Polymer	Diameter (nm)	PDI	Zeta potential (mV)	Fab conjugated (µg/mg polymer)[a,b]	Conjugation efficiency (%)
1.Nude NHS NP	PLGA-PEG-NHS	207.5 ± 13.9	0.12 ± 0.07	2.87	-	-
2.Native CTX Fab NP	PLGA-PEG-NHS	215.0 ± 13.0	0.15 ± 0.06	-3.16	10.1 ± 2.7	20
3.Nude azide NP	PLGA-PEG-azide	204.7 ± 10.2	0.07 ± 0.03	-3.92	-	-
4.CTX Fab Mepstra NP	PLGA-PEG-azide	211.7 ± 5.6	0.08 ± 0.05	-0.63	16.1 ± 1.5	32

Table 4. Characterisation of all different nanoformulations. Number of samples: 3. Also, quantification of Fab content reveals marginal enhanced efficiency for CTX Fab Mepstra NP compared to Native CTX Fab NP. [a] Data expressed as mean ± SD. [b] Equimolar amounts of each Fab domain were initially added to the nanoparticle conjugation reaction. Dr Michelle Greene proceeded with this set of experiments.

These results demonstrated enhanced conjugation for CTX Fab Mepstra NP, visible by the conjugation efficiency value of 32% when compared to the value of native CTX Fab NP of 20% (Table 4). This enhancement in nanoconjugation, although marginal, could be attributed to the greater reaction profile of 'click' chemistry in such nanoconjugate formation conditions when compared to NHS-ester approaches, even though there are multiple lysine residues in each CTX Fab fragment available for reaction.

After confirming the initial efficiency of conjugation with the new linker diBrMepstra PD **46**, it was of critical importance to assess the CTX Fab nanoconjugates affinity to its correspondent antigen. CTX Fab fragments were previously attached to PEG-PLGA nanoparticles in the previous Chapter (see section 2.5), however the resulting nanoconstructs were used as negative controls for the antigen binding specificity of TRAZ nanoconstructs to HER2. CTX mAb and its fragments bind to the EGFR and this needed to be appraised.

FLISA

Analogous to what was previously performed for the TRAZ AFPD nanoparticle conjugates (see section 2.5), a FLISA assay was performed. The observed trend was in agreement with the previous studies with TRAZ AFPD nanoparticle conjugates, demonstrating CTX Fab Mepstra NP's superior binding to EGFR when compared to native CTX Fab NP and remaining controls (Figure 27). Likewise, this test reinforces the importance of the site-selective nature of pyridazinedione linkers in arranging the CTX Fab fragments in an oriented fashion, enhancing paratope accessibility, and demonstrates successful translation of the chemistry to a new antibody.

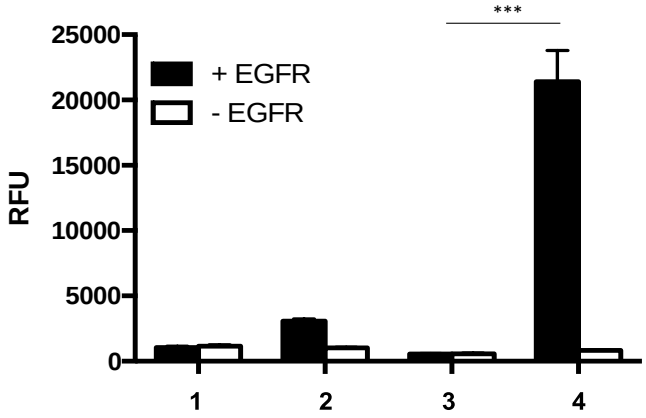

Figure 27. FLISA assessment of CTX Fab Mepstra NP and associated controls (polymer concentrations of 1 mg/mL). **1)** Nude NHS NP. **2)** Native CTX Fab NP. **3)** Nude azide NP. **4)** CTX Fab Mepstra NP. Number of samples: 3. Statistical significance was established by one-way ANOVA and Tukey's post-hoc test (***$p \leq 0.001$). I actively participated in doing this experiment.

Blocking and competition assays

Targeting specificity was further validated *via* other FLISA assessments, where EGFR coated wells are pre-incubated with an excess of CTX full antibody **40** with the purpose of impeding nanoparticle binding *via* Fab fragments, analogous to the experiments carried out in the previous TRAZ AFPD nanoparticles' work. Likewise, specificity was confirmed since there was a considerable reduction in antigen binding values when EGFR coated wells were pre-blocked with CTX full antibody **40** compared to the non-blocked coated wells (measurement 4, - CTX and + CTX, Figure 28).

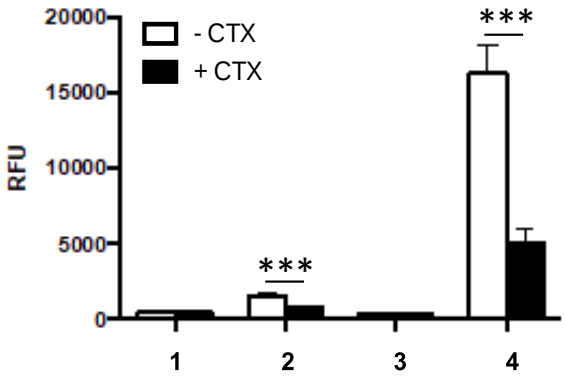

Figure 28. FLISA competition assay: EGFR binding activity of CTX Fab Mepstra NP and associated controls (polymer concentrations of 0.5 mg/mL): **1)** Nude NHS NP **2)** Native CTX Fab NP **3)** Nude azide NP **4)** CTX Fab Mepstra NP. Number of samples: 3. Statistical significance was established by one-way ANOVA and Tukey's post-hoc test (***$p \leq 0.001$). I actively participated in doing this experiment.

In yet another approach, CTX full antibody **40** and CTX Fab Mepstra NP were added simultaneously to EGFR-coated wells. In this case, nanoconjugate binding was progressively inhibited with each concentration increment of free competing CTX full antibody **40**, confirming target EGFR specificity (Figure 29).

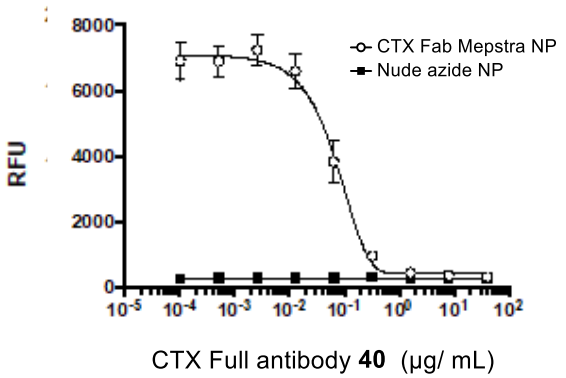

Figure 29. FLISA competition assay: EGFR binding activity of CTX Fab Mepstra NP when added incremental amounts of CTX Full antibody **40** (0.0001024 – 40 µg/mL, polymer concentrations of 0.5 mg/mL). Number of samples: 3. Dr Michelle Greene proceeded with this set of experiments.

SPR assays

As done previously in TRAZ AFPD conjugates work, it was next sought to complement antigen binding affinity FLISA results with SPR assays, in which nanoparticles are not loaded with a fluorescent dye. Fittingly with what was observed in the TRAZ Fab nanoparticle conjugates work, these studies demonstrated that binding of CTX Fab Mepstra NP was at least over 9-fold greater than that of native CTX Fab NP, at all polymer concentrations tested (Figure 30).

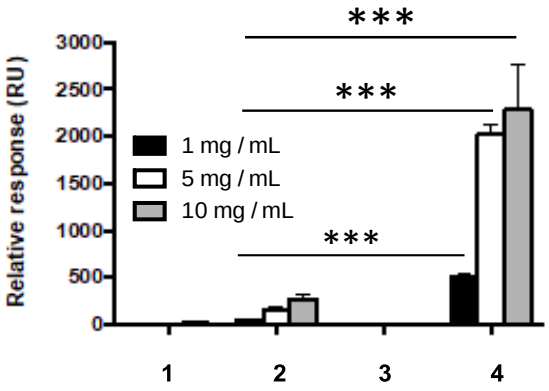

Figure 30. SPR Biacore® data for the EGFR binding activity of all formulations at different polymer concentrations: **1)** Nude NHS NP **2)** Native CTX Fab NP **3)** Nude azide NP **4)** CTX Fab Mepstra NP. Number of samples: 3. Statistical significance was established by one-way ANOVA and Tukey's post-hoc test (***$p \leq 0.001$). Dr Michelle Greene proceeded with this set of experiments.

Collectively, these results confirmed the translatability of the pyridazinedione-mediated conjugation method for enhanced receptor binding, when compared to random lysine modification strategies for the generation of antibody-nanoparticle conjugates.

3.4 Cell-binding studies on CTX AFPDs conjugated to PEG-PLGA nanoparticles

After demonstrating superior binding to EGFR of CTX Fab Mepstra NP over native CTX Fab NPs *via* multiple FLISA and SPR assays, the aforementioned nanoconjugates were then tested in a biological setting; Michelle Greene carried out the following cell-based assays.

The human pancreatic cancer cell line PANC-1 was chosen as a suitable model for these studies, due to high surface expression of EGFR.[152] These cells were initially chilled at 4 ºC to limit EGFR internalisation and maintained at this temperature throughout the incubation period with fluorescently labelled nanoparticles. Consistent with previous ELISA and SPR results, cellular binding of CTX Fab Mepstra NP was enhanced when compared to native CTX Fab NP (Figure 31a). To confirm that the observed binding was due to EGFR engagement, the cells were then incubated with non-fluorescent nanoformulations at 4 ºC prior to labelling of surface-expressed EGFR with an antibody tagged with fluorescein isothiocyanate (FITC). High basal staining of EGFR was detected on untreated cells as expected (**Figure 31b**, control 3) and a similar pattern was also perceptible following incubation with the nude control nanoparticles (**Figure 31b**, control 4 and 5). In contrast, EGFR staining was markedly reduced upon treatment with native CTX Fab NP and, to a more pronounced extent, by CTX Fab Mepstra NP (**Figure 31b**, control 7). These findings suggest that both CTX Fab nanoformulations engage EGFR on the surface of PANC-1 cells, thereby impeding binding of the fluorophore-tagged antibody to the receptor.

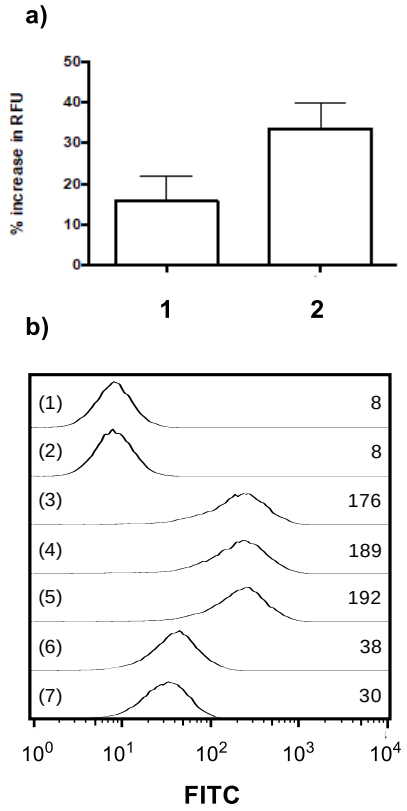

Cell treatment	Cell Stain
(1) Unstimulated	Unstained
(2) Unstimulated	Isotype- FITC
(3) Unstimulated	EGFR-FITC
(4) Nude NHS NP	EGFR-FITC
(5) Nude azide NP	EGFR-FITC
(6) Native CTX Fab NP	EGFR-FITC
(7) CTX Fab Mepstra NP	EGFR-FITC

Figure 31. a) Cellular binding of nanoconjugates **1)** native CTX Fab NP and **2)** CTX Fab Mepstra NP. Results **1)** and **2)** are presented as % increase in RFU versus the corresponding nude NHS NP and nude azide NP controls, respectively. PANC-1 cells were treated with fluorescent nanoformulations (800 µg polymer/mL) for 45 min at 4 ºC. Cells were then washed and analysed on a fluorescent microplate reader. **b)** Flow cytometry analysis: PANC-1 cells were treated with various nanoformulations (500 µg polymer/mL) for 1 h at 4 °C. Cells were then washed, stained with FITC-labelled EGFR or isotype control antibodies. Representative histograms are shown for each of the numbered treatments (1) – (7), with inset values denoting the geometric mean fluorescence intensity. Dr Michelle Greene proceeded with this set of experiments.

These studies were also replicated in two other EGFR-positive pancreatic cancer cell lines, MIA PaCa-2 and BxPC-3, both used extensively in pancreatic cancer research and therapy development.[153,154] As anticipated, EGFR binding to the surface of the cell trends were largely comparable to those observed in the PANC-1 model (Figure 32).

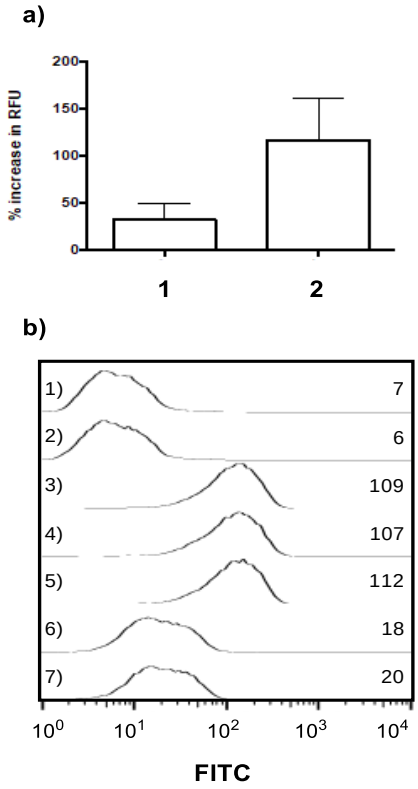

Cell treatment	Cell Stain
(1) Unstimulated	Unstained
(2) Unstimulated	Isotype- FITC
(3) Unstimulated	EGFR-FITC
(4) Nude NHS NP	EGFR-FITC
(5) Nude azide NP	EGFR-FITC
(6) Native CTX Fab NP	EGFR-FITC
(7) CTX Fab Mepstra NP	EGFR-FITC

Figure 32. a) MIA PaCa-2 cells were treated with fluorescent nanoformulations (600 µg polymer/mL) for 45 min at 4 ºC. Cells were then washed and analysed on a fluorescent microplate reader. Results for native CTX Fab NP and CTX Fab Mepstra NP are presented as % increase in RFU versus the corresponding nude NHS NP and nude azide NP controls, respectively. **b)** BxPC-3 cells were treated with various nanoformulations (500 µg polymer/mL) for 1 h at 4 ºC. Cells were then washed, stained with FITC-labelled EGFR or isotype control antibodies and analysed by flow cytometry. Representative histograms are shown for each of the numbered treatments (1) – (7), with inset values denoting the geometric mean fluorescence intensity. Dr Michelle Greene proceeded with this set of experiments.

Collectively, this *in vitro* dataset confirms that the superior EGFR binding activity of modified CTX Fab Mepstra NP translates to a cell-based setting.

3.5 Encapsulation of Camptothecin into CTX AFPD conjugated to PEG-PLGA nanoparticles

Following the successful development and validation of CTX Fab nanoparticles in cellular EGFR-binding assay, their utility as a targeted drug delivery platform was still to be explored. The topoisomerase I inhibitor camptothecin (CPT) was selected as a model drug for these studies, due to low solubility in aqueous media that facilitates entrapment within the hydrophobic core of PLGA nanoparticles. Moreover, the clinical relevance of this drug selection is supported by the recent approval of a nanoformulated CPT analogue (Onivyde®) for pancreatic cancer therapy.[155] CPT was added directly to the organic phase during nanoparticle synthesis prior to emulsification in an aqueous polyvinyl alcohol (PVA) solution. Similar drug loading was achieved within NHS- and azide-functionalised nanoparticles, equating to 4.9 ± 4.2 and 4.8 ± 3.8 μg CPT/mg polymer, respectively (Table 5). Furthermore, physicochemical characteristics including size and PDI were comparable the previous nanoformulations containing no drug cargo (Table 5).

Nanoformulation	Polymer	Diameter (nm)[a]	PDI[a]	Fab conjugated (μg/mg polymer)[a,b]	CPT entrapped (μg/mg polymer)[a]
Non-loaded					
Nude NHS NP	PLGA-PEG-NHS	207.5 ± 13.9	0.12 ± 0.07	-	-
Native CTX Fab NP	PLGA-PEG-NHS	215.0 ± 13.0	0.15 ± 0.06	10.1 ± 2.7	-
Nude azide NP	PLGA-PEG-azide	204.7 ± 10.2	0.07 ± 0.03	-	-
CTX Fab Mepstra NP	PLGA-PEG-azide	211.7 ± 5.6	0.08 ± 0.05	16.1 ± 1.5	-
Rhodamine 6G-loaded					
Nude NHS NP	PLGA-PEG-NHS	218.8 ± 20.8	0.13 ± 0.06	-	-
Native CTX Fab NP	PLGA-PEG-NHS	226.1 ± 23.7	0.15 ± 0.04	12.2 ± 5.3	-
Nude azide NP	PLGA-PEG-azide	215.1 ± 12.2	0.08 ± 0.04	-	-
CTX Fab Mepstra NP	PLGA-PEG-azide	218.8 ± 13.8	0.07 ± 0.04	16.0 ± 5.6	-
CPT-loaded					
Nude NHS CPT NP	PLGA-PEG-NHS	209.7 ± 10.8	0.14 ± 0.05	-	4.9 ± 4.2
Native CTX Fab CPT NP	PLGA-PEG-NHS	214.2 ± 12.5	0.14 ± 0.05	16.6 ± 1.5	4.9 ± 4.2
Nude azide CPT NP	PLGA-PEG-azide	209.0 ± 16.2	0.10 ± 0.04	-	4.8 ± 3.8
CTX Fab Mepstra CPT NP	PLGA-PEG-azide	215.7 ± 13.5	0.12 ± 0.03	14.2 ± 3.4	4.8 ± 3.8

Table 5. Characterisation of all nanoformulations. [a] Data expressed as mean ± SD. [b] Equimolar amounts of each Fab domain were initially added to the nanoparticle conjugation reaction. I actively participated in collecting these results.

Upon testing the *in vitro* cytotoxicity of the nanoparticles alongside equimolar concentrations of free CPT, a dose-dependent reduction in PANC-1 and MIA PaCa-2 cell viability was observed for all drug formats (Figure 33). Thus, these findings confirm that CPT may be readily formulated within NHS- and azide-capped polymeric nanoparticles without loss of activity.

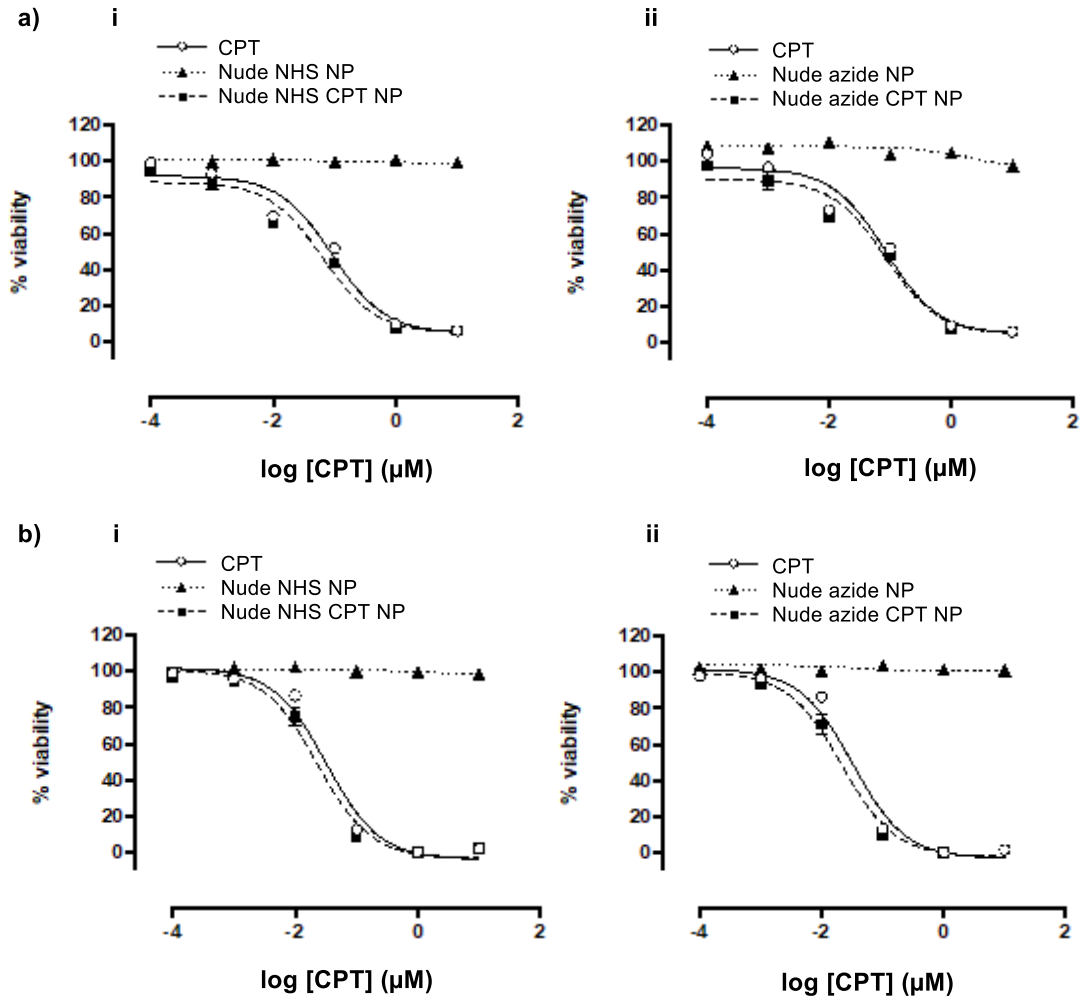

Figure 33. a) PANC-1 cells and **b)** MIA PaCa-2 cells were treated with **(i)** CPT, nude NHS NP and nude NHS CPT NP or **(ii)** CPT, nude azide NP and nude azide CPT NP. Both free and nanoencapsulated CPT were added to cells in equimolar concentrations ranging from 0.0001 μM to 10 μM. Control nanoformulations containing no CPT were added to cells at an equivalent polymer concentration as the corresponding drug-loaded nanoformulations. At 96 h following treatment, cell viability was assessed by the CellTiter-Glo assay. Dr Michelle Greene proceeded with this set of experiments.

3.6 Targeted delivery of CPT-loaded CTX AFPD conjugated to PEG-PLGA nanoparticles

In a final set of studies, it was examined whether functionalisation of CPT-loaded nanoparticles with CTX Fab could enable preferential targeting of the drug to EGFR-expressing cells. Site-selective and random lysine conjugation was performed *via* distinct chemistries as before, leading to the generation of nanoconjugates, this time with a similar loading of targeting moiety CTX Fab (CPT-loaded nanoconjugates, Table 5). This similarity exposes the random nature of lysine modification strategies for the generation of nanoconjugates and consequent unreliability (*i.e.* NHS-ester conjugation efficiency is typically lower when compared to 'click' chemistry, however, in this case it is marginally higher. This can be explained by the abundant number of lysine residues available to react, causing batch-to-batch variability, highlighting the importance of the PD-mediated site-selective approach for reproducibility). Other characteristics were not markedly affected following functionalisation, with only a minor increase in diameter compared to the corresponding non-targeted formulations (Table 5). Both PANC-1 and MIA PaCa-2 cells were then treated with these nanoparticles and associated controls at 4 ºC; under such conditions, binding to surface-expressed EGFR was possible, although internalisation of the receptor was restricted. Thereafter, the cells were washed and maintained at 37 ºC overnight to allow uptake of membrane-bound treatments, prior to re-plating for assessment of clonogenic ability. Colony formation was reduced to the greatest extent by native CTX Fab CPT NP and CTX Fab Mepstra CPT NP, suggesting that both nanoformulations could engage surface EGFR and thus withstand removal during washing (Figure 34).

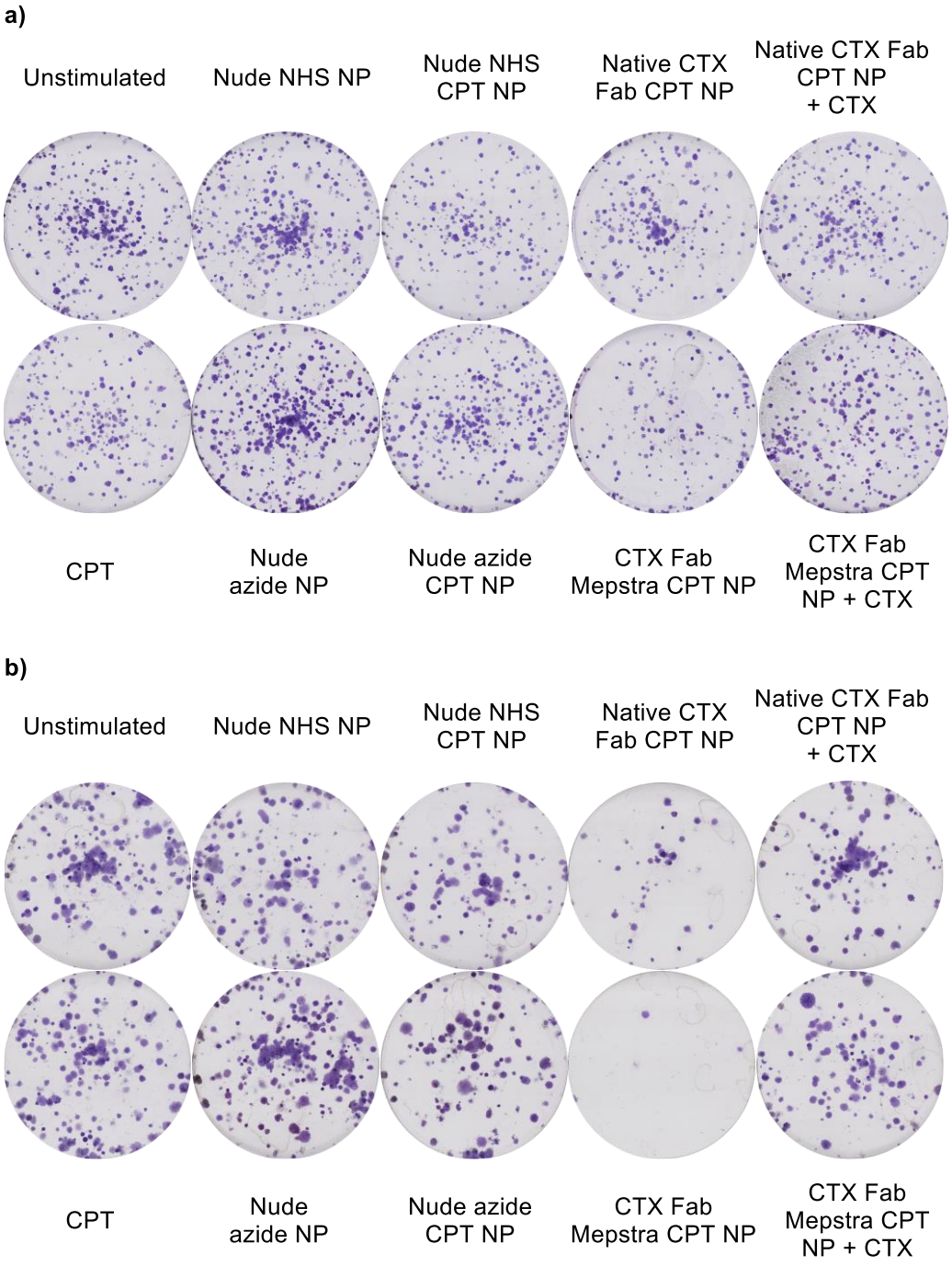

Figure 34. a) PANC-1 cells and **b)** MIA PaCa-2 cells were treated with 200 µg/mL free CTX full antibody **40** for 15 min at 4 °C where appropriate, followed by the addition of free CPT and various nanoformulations for a further 45 min at 4 °C. Both free and nanoencapsulated CPT were added to cells in equimolar concentrations ranging from 0.7 µM (PANC-1) to 1.4 µM (MIA PaCa-2). Control nanoformulations containing no CPT were added to cells at an equivalent polymer concentration as the corresponding drug-loaded nanoformulations. Following treatment, cells were washed and then maintained at 37 ºC to allow colony formation. As this work has

been done quite recently, there is still no quantitative data to demonstrate, but cells will be quantified individually for each treatment, therefore, only representative images are shown. Dr Michelle Greene proceeded with this set of experiments.

Upon transfer to 37 ºC, the nanoparticle-EGFR complexes were then endocytosed, leading to intracellular delivery of CPT and subsequent cytotoxic effects. Notably, these effects were more pronounced in the case of modified CTX Fab Mepstra CPT NP, providing credible prospects that site-specific functionalisation leads to superior EGFR binding. To corroborate that the observed reduction in colony formation was mediated *via* EGFR-targeted delivery of CPT, cells were pre-incubated with an excess of CTX full antibody **40** prior to treatment with the nanoformulations. This led to an evident partial restoration in clonogenic survival, demonstrating the EGFR targeting specificity of native CTX Fab CPT NP and modified CTX Fab CPT Mepstra NP (Figure 34).

Taken together, this data highlights the exceptional utility of CTX Fab Mepstra NP as a targeted drug delivery vehicle and underlines the importance of site-specific functionalisation approaches for optimal nanocarrier performance.

Chapter 4 Use of variable New Antigen Receptors (V_{NARs}) for targeting PEG-PLGA nanoparticles

Besides their versatility, mAbs and their fragments are highly specific proteins that make them well suited for the detection of pathogens and are therefore one of the most-used vehicles for antigen targeting. Nonetheless, there are other antigen receptors that are reported to be smaller (a single-domain conformation) but still highly efficient. In fact, some smaller-sized proteins possess several advantages for biotechnological applications, such as improved stability and higher solubility when compared to larger proteins.[156] These advantages have attracted a great deal of attention to a particular class of proteins; the naturally-occurring heavy-chain antibodies (HCAb) from camelids and sharks (Ig_{NARs}) (Figure 35). Both camelid and shark antibodies possess a variable single-domain chain of *ca.* 12-15 kDa, which is pre-disposed to bind novel or cryptic epitopes (V_{HH} in camelid antibodies and V_{NAR} in shark antibodies). Although V_{HH} fragments are finding numerous applications as targeting proteins for the treatment of diseases such as cancer,[157] this chapter will focus on V_{NARs} and their applications.

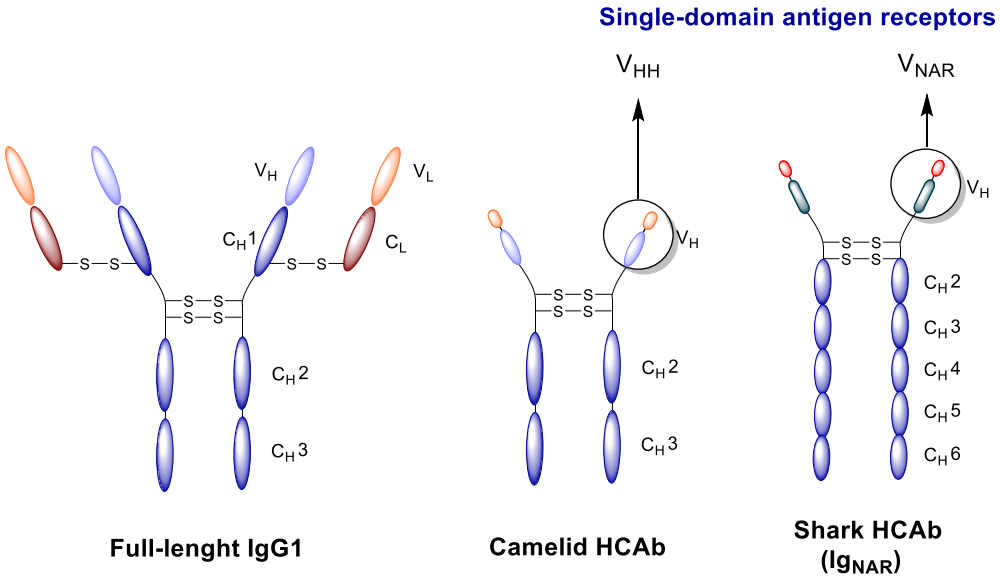

Figure 35. Comparison between canonical, full-length antibody structure with camelid and shark heavy-chain antibodies.

V_{NARs} comprise a variable segment (V), three diverse peptide segments prevenient from the heavy chain (D), one joining segment (J) and a constant segment (C), and their recombination occurs exclusively within one cluster (Figure 36).[158] V_{NARs} are amongst the antigen receptors that bind to Delta like canonical Notch ligand 4 (DLL4), a key regulator that activates Notch signaling pathways directly related with early embryonic vascular development in tumor angiogenesis.[159]

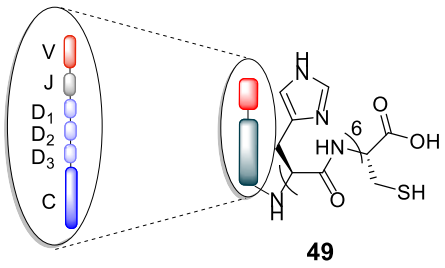

Figure 36. Structure of the first variant of a variable New Antigen Receptor (V_{NAR}) Clone E4. A His-tag (6 histidines) separates the single cysteine residue from the main V_{NAR} scaffold.

V_{NARs} are reported to tolerate extreme pHs (down to 1.5) and high temperature conditions, allowing a variety of chemistry strategies to be employed in drug attachment. Moreover, V_{NAR} simple molecular architecture presents a suitable and versatile platform for re-formatting and engineering (*e.g.* V_{NARs} have been engineered

to increase their solubility and refolding ability).[160,161] Porter *et al.* pioneered the discovery of these antibody-like proteins and also reported the ability to isolate V_{NAR} clones that are highly specific for antigen binding.[162] Further interest in these clones lead his team to the creation of Elasmogen, a biopharmaceutical company that has been building a library of monoclonal V_{NARs} that are amenable to genetic engineering and are currently being used to generate new therapeutic drugs.[163] However, their application within the nanotechnology field remains to be explored. Thus, the aim of this work was to use the V_{NARs} to graft them onto PEG-PLGA nanoparticles, generating nanoconjugates that target the inhibition of endothelial sprouting and proliferation, processes involved in tumour angiogenesis.[164] Having successfully shown the enhanced model for different antibody fragments decorating drug nanocarriers in previous chapters, it was believed that by applying a similar approach to these proteins, their potential could be maximised, *i.e.* antigen binding enhancement due to the high orientation and number of proteins on a nanoparticle's surface. Also, this approach would enable larger payload deliveries due to the ability of PEG-PLGA nanoparticles to encapsulate high drug loadings and, consequently, being capable of internalising and killing the cancer cells, as shown in Section 3.6. For the above stated reasons, Elasmogen provided one of their clones, the anti-DLL4 E4 V_{NAR} **49**, for it to be tested in an antibody-nanoparticle complex.

4.1 V_{NAR} bioconjugation

To enhance the reactivity of V_{NARs} to the surface of nanoparticles it was necessary to install a reactive handle onto the V_{NARs}' scaffold. Due to the success of the SPAAC reaction employed for the generation of the previously mentioned polymeric nanoconjugates (Chapter 2 and 3), the same approach was to be employed in this section – a strained alkyne bearing pyridazinedione conjugated to a protein that would be 'clicked' to azide PEG-PLGA nanoparticles. However, there are several structural differences between IgG fragments and V_{NARs} that needed to be considered. Most importantly, Trastuzumab and Cetuximab Fabs benefit from this approach because they incorporate a disulfide bridge whilst mutant V_{NAR} **49** contains only one solvent accessible single cysteine.

Because these V_{NAR} domains were specifically engineered to integrate a single cysteine residue in the distal site to the paratope, a monobromopyridazinedione strained alkyne (monoBrMestra PD **50**, Figure 37), specialised for single free cysteine modification, *i.e.* one addition-elimination event (reagent initially synthesised by Dr Daniel Richards), was utilised to assess V_{NAR} modification.

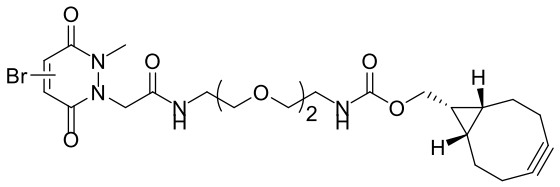

monoBrMestra PD **50**

Figure 37. Chemical structure of monoBrMestra PD **50**.

Bioconjugation was initially tested *via* SDS-PAGE, where, surprisingly, it was found that successful conversion could only occur under a reducing TCEP environment, since SDS-PAGE analysis demonstrated that mutant **49** was existing partially as the dimer due to spontaneous disulfide formation (Figure 38, lane 1, band at *ca.* 25 kDa confirms presence of dimer).

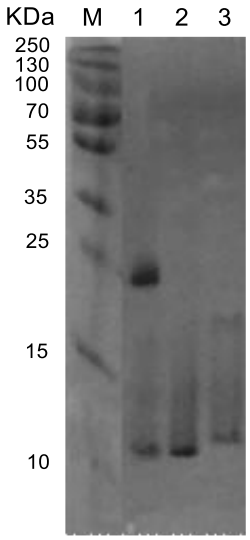

Figure 38. SDS-PAGE analysis of V_{NAR} conjugation; M) Molecular weight marker. 1) Native V_{NAR} E4 clone. 2) Reduced V_{NAR} E4 clone. 3) V_{NAR} E4 clone reacted with PD **50**.

Originally, the aim of this work was to show that it was possible to: i) achieve complete modification of the V_{NARs} with pyridazinediones; and ii) purify the resulting bioconjugate from the reducing agent and any excess monoBrMestra PD **50** with minimum protein loss - the small size of the protein could potentially cause difficulties in purification (*i.e.* antibody Fab fragments are almost five times bigger in size and protein purification procedures mostly rely on removing excess small molecules *via* ultrafiltration where there is a significant difference between the filter cut-off value and the size of the protein conjugate).

After reaction with monoBrMestra PD **50**, several attempts to purify the conjugates, for analysis and isolation, were attempted, such as size-exclusion chromatography, Zeba™ Spin desalting columns and several different Pierce™ Protein Concentrators (10 kDa, 5 kDa and 3 kDa). Although some of these methods afforded clean conjugates, they resulted in unpredictable and frequently poor yields (below 20% protein recovery). For instance, UV-Vis analysis after size-exclusion chromatography showed significant loss of material (Figure 39).

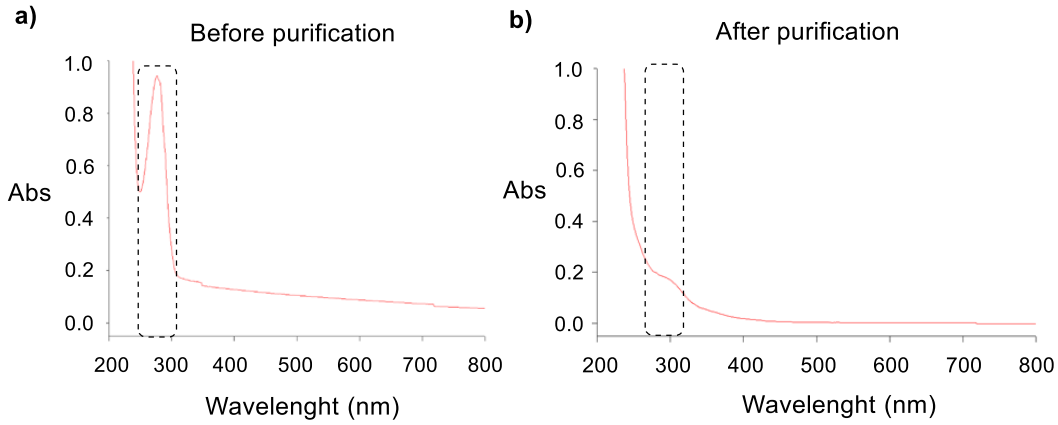

Figure 39. UV-Vis analysis after size-exclusion chromatography shows less than 20% recovery of modified V_{NAR}.

Fortunately, it was found that by lowering the concentration of DMSO in the sample by preparing a more concentrated sample of monoBrMestra PD **50** (80 µM compared to the standard 20 µM), it was possible to achieve recoveries of over 80% whilst removing excess small molecules *via* ultrafiltration.

After finding a way to isolate the conjugate, several optimisation parameters (varying reaction time and temperature, equivalents of TCEP and monoBrMestra PD **50**) were

tuned to obtain pure conjugate **51** (Figure 40). As a result, successful site-selective modification through pre-incubation of the V_{NAR} with TCEP (10 eq.), followed by addition of monoBrMestra PD **50** (20 eq.) was confirmed by LC-MS.

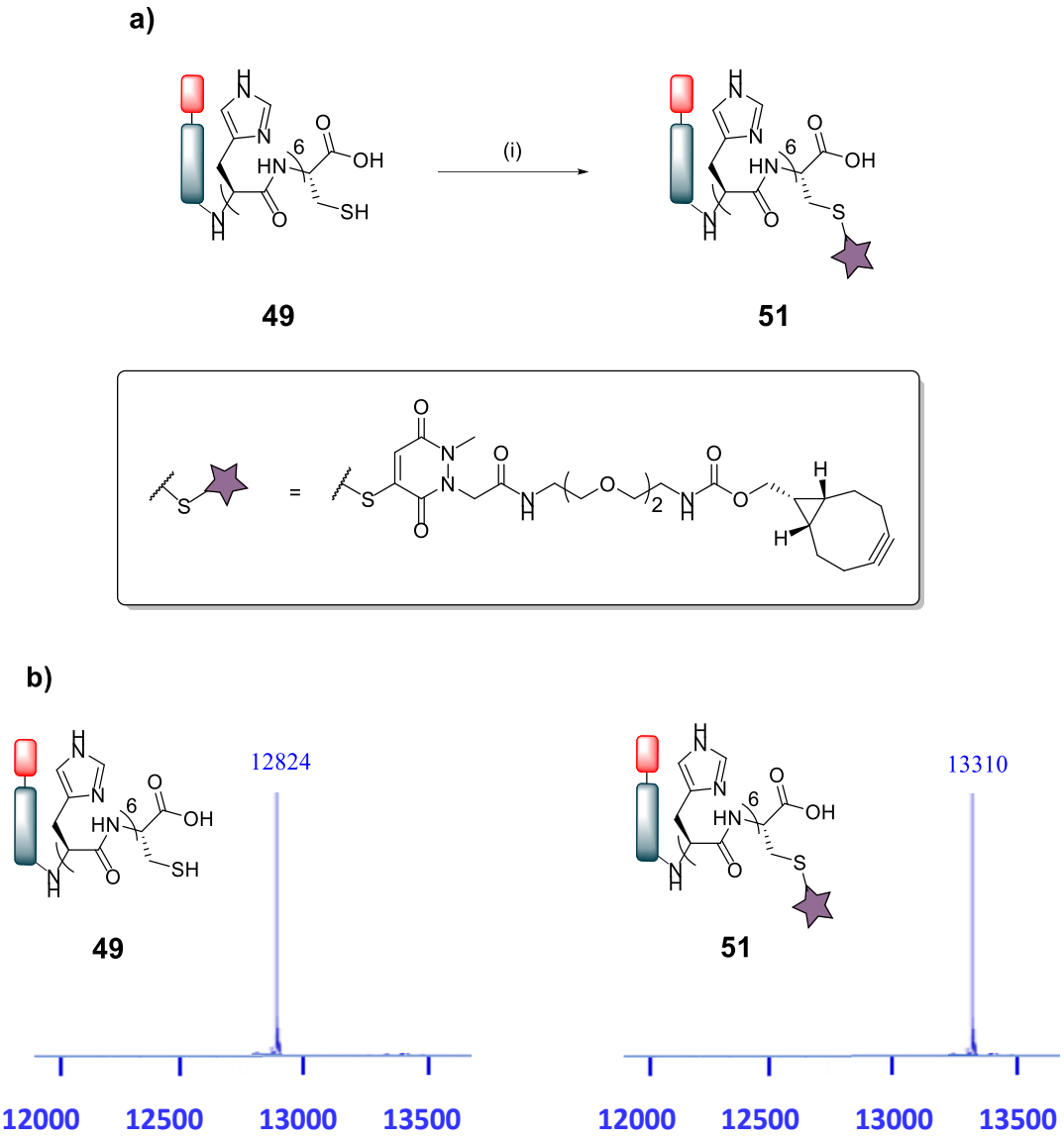

Figure 40. a) V_{NAR} modification with monoBrMestra PD **50**.
Reagents and conditions: (i) TCEP.HCl (10 eq.), monoBrMestra PD **50** (20 eq.), phosphate buffer pH 7.4, 21 °C, 16 h. Expected masses for **49**: 12824 and **51**: 13310. **b)** LC-MS data showing successful conversion to conjugate **51**. Spectra have been modified for clarity, see experimental Fig(s) 75 and 76 for full spectral data.

Unfortunately, after 15 days of appropriate storage at 4 °C of the V_{NAR} conjugate **51**, LC-MS indicated significant degradation of the sample; the expected mass peak kept

decreasing over time (Figure 41). To appraise if this effect was specific to PD modification, V_{NAR} **49** was modified with other cysteine modification reagents (*e.g.* maleimide and iodoacetamide) and the stability of these conjugates appraised. A similar degradation pattern was observed, confirming that it was not a specific issue with using a PD linker (see experimental, Fig(s) 78 and 79).

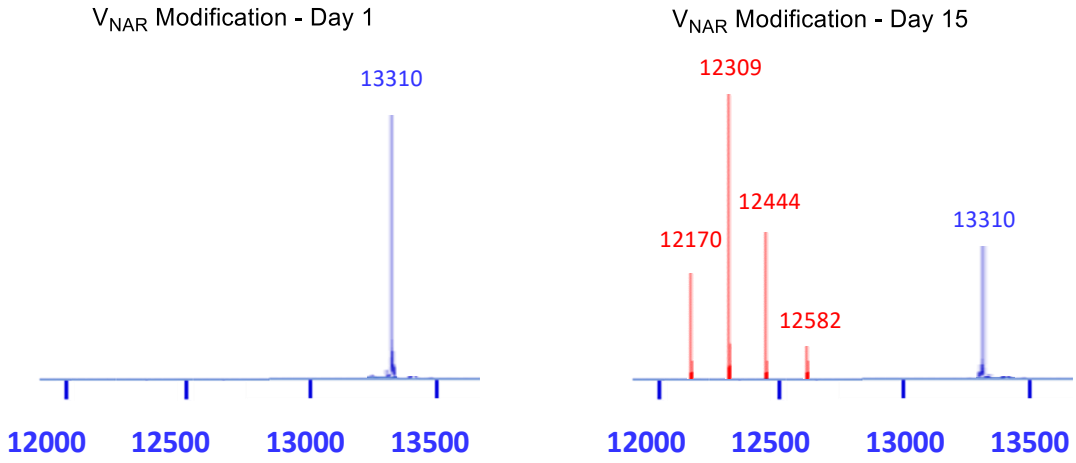

Figure 41. Degradation of the modified V_{NAR}, when repeating the monoBrMestra PD modification, 15 days later. LC-MS data showing degradation of conjugate **51**. Spectra have been modified for clarity, see experimental Fig(s) 76 and 77 for full spectral data.

Finally, to assure that this affect was not dependent on modification of the V_{NAR} itself, the unmodified clone was also analysed by LC-MS. Consistent with the modified mutants, the unmodified clone was also found to be degrading over time. Looking closely into the peak values, it was possible to observe that the six polyhistidines (polyHis-tag) present after the C-terminus were degrading one by one, breaking apart the terminal single-cysteine residue (Figure 42). It was, however, noted that no degradation past the histidine residues was observed.

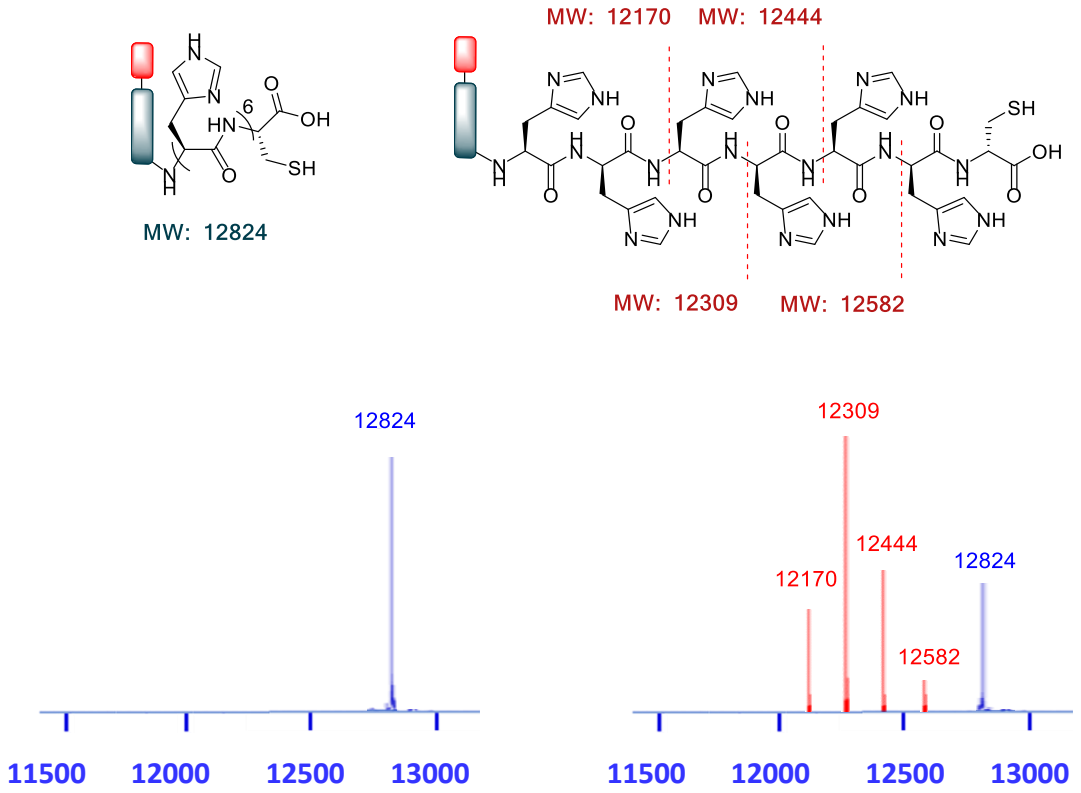

Figure 42. LC-MS data showing degradation of native V_{NAR} clone E4 after 15 days and representation of what is believed to be the degradation pattern. Spectra have been modified for clarity, see experimental Fig(s) 73 and 74 for full spectral data.

4.2 Redesign of V_{NARs}

It was then hypothesised that this cleavage was due to C-terminal cysteine residues being more prone to cleavage *via* decarboxylative routes.[165] It was proposed that by shifting the position of the cysteine residue from a region after the polyHis tag to a region before the polyHis tag, the stability of the V_{NARs} would be improved. Elasmogen agreed to provide these mutants after the ruling out of the possibility of any left-over enzymes causing the issue. Elasmogen generated a new internal cysteine E4 clone with the His tag at the terminus, referred to as native E4HisCTerminal **52**, and this new V_{NAR} was sent over to UCL for further bioconjugation studies (Scheme 19).

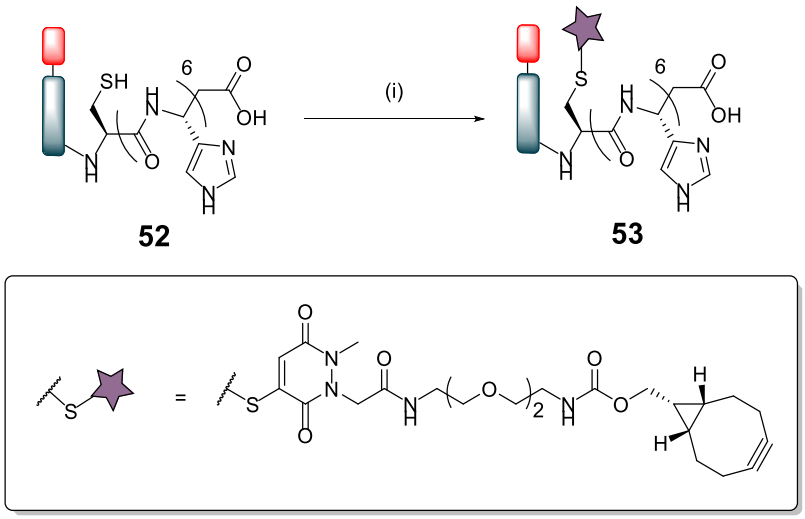

Scheme 19. Native E4HisCTerminal **52** modification with monoBrMestra PD **50**. PolyHis tag is now placed in the terminal position.

Reagents and conditions: (i) TCEP.HCl (10 eq.), monoBrMestra PD **50** (20 eq.), phosphate buffer pH 7.4, 21 °C, 16 h.

Somewhat surprisingly, degradation from the C-terminus was still observed in these new V_{NAR} samples. After a total of 30 days of storage, the native E4HisCTerminal **52** clone was analysed again and already had lost three of the six histidines from the poly His-tag complex. Furthermore, reaction with monoBrMestra PD **50** showed the degradation of four histidines. Fortunately, however, the newly shifted cysteine residue was no longer being cleaved due to its new position in the protein sequence. As such, even though not ideal, any installed functionality would remain on the protein scaffold (at least for a long enough period for subsequent studies) if appended to the newly positioned cysteine residue. Moreover, as the histidines are not required for protein function, their loss was not seen as significant for the purpose of DLL4 binding studies. Since the cysteine is no longer at the C-terminal, it is unreasonable that a decarboxylative cleavage is responsible, and more likely that there is some other route to cleavage; perhaps *via* some contaminant protease that is not detectable with current levels of analysis.

4.3 Synthesis of Monobromo PD-based linkers

Due to the short-life nature of strained alkyne bearing molecules, there is the need to synthesise these reagents regularly. Being aware of the new facile, high yielding

synthesis procedures for diBrMepstra PD **46**, it was decided that the same method would be employed to make a new version of the single-cysteine modification reagent. Thus, a new version of the monobromopyridazinedione was synthesised (Scheme 20), according to previously established methods for the synthesis of diBrMepstra **46** (see Section 3.2).[151] This molecule, monoBrMepstra PD **56**, would supersede the use of aforementioned monoBrMestra PD **50** for the above stated reasons.

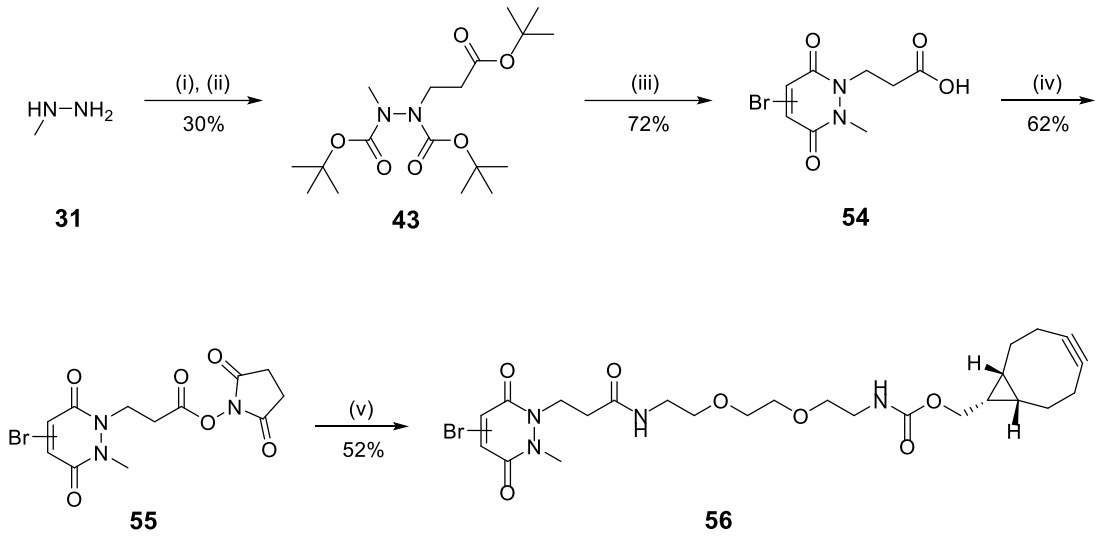

Scheme 20. Synthesis route of monoBrMepstra PD **56**.

Reagents and Conditions: (i) Boc anhydride, *i*-PrOH, DCM, 21 °C, 16 h; (ii) *tert*-Butyl acrylate, *i*-PrOH, 60 °C, 24 h; (iii) Bromomaleic acid, AcOH, reflux, 5 h; (iv) DCC, NHS, THF, 21 °C, 16 h (v) BCN(endo)-PEG_2-NH_2 **13**, MeCN, 21 °C, 16 h.

Having generated new monoBrMepstra PD **56**, it was conjugated to the redesigned native E4HisCTerminal **52** (Scheme 21). This reaction proceeded smoothly, with successful modification and isolation of E4HisCTerminal Mepstra **57** being accomplished. To demonstrate the availably of the strained alkyne E4HisCTerminal Mepstra **57** to participate in a 'click' reaction, **57** was successfully reacted with Alexafluor®-488-N_3 **37**, generating fluorescent E4HisCTerminal Mepstra Alexafluor **58** (Scheme 21); Successful conjugation of **57** and **58** was appraised by SDS-PAGE and LC-MS (See experimental, Fig(s) 80 to 86).

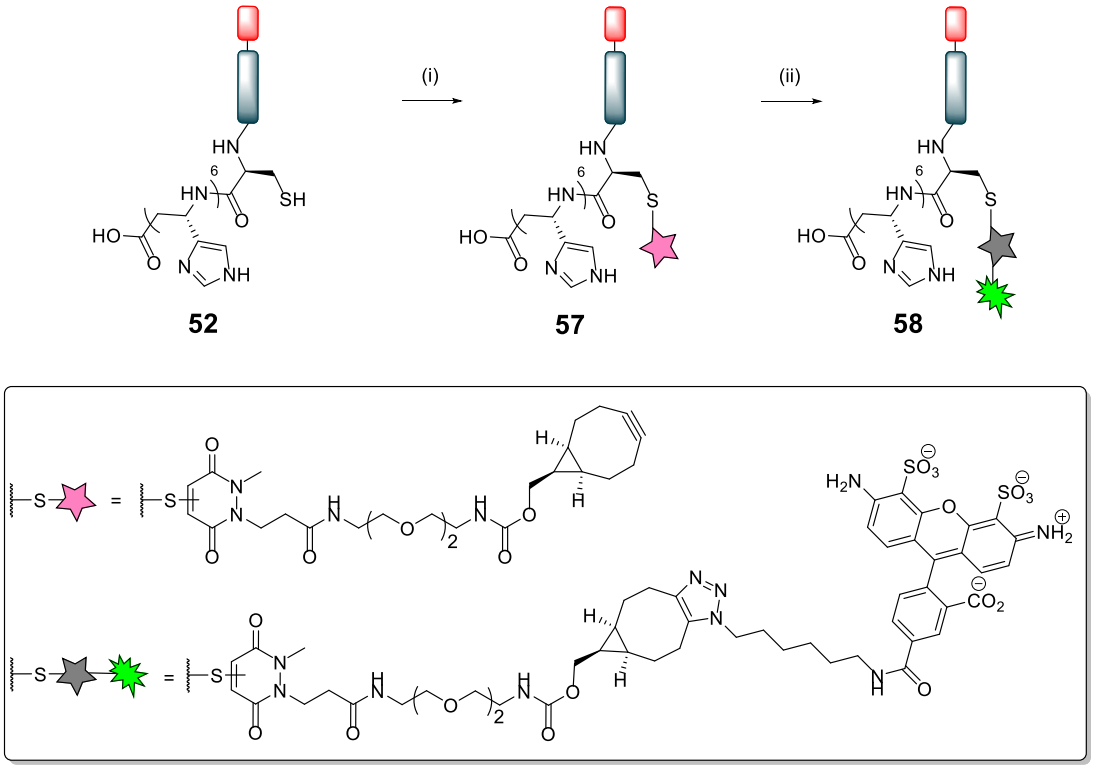

Scheme 21. Native E4HisCTerminal **52** modification with monoBrMepstra PD **56** and subsequent 'click' test reaction with Alexafluor®-488-N_3.
Reagents and conditions: (i) TCEP.HCl (10 eq.), monoBrMepstra PD **56** (20 eq.), phosphate buffer pH 7.4, 21 °C, 16 h. (ii) Alexafluor®-488-N_3 **37**, phosphate buffer pH 7.4, 21 °C, 5 h.

4.4 Attachment of V_{NAR} conjugates to PEG-PLGA Nanoparticles

Although Trastuzumab and Cetuximab Fab fragments were previously attached to PEG-PLGA nanoparticles in previous Chapters (see Chapter 2 and 3), there are several structural differences between IgG fragments and V_{NARs} (*i.e.* V_{NAR} mutant contains only one solvent accessible single cysteine whilst Trastuzumab and Cetuximab Fabs incorporate a disulfide bridge). Therefore, it was critical to understand if a V_{NAR} containing a single cysteine on a near terminal site would also provide similar orientation benefits to what was seen for IgG1 fragments (modified TRAZ and CTX fragments).

As previously, the newly-formed conjugate E4HisCTerminal Mepstra **57** was sent to our collaborators in Belfast, where Michelle Greene proceeded with the generation of Rhodamine-6G loaded nanoconjugates and respective controls: (i) native E4HisCTerminal **52** conjugated to NHS-functionalised nanoparticles (**E4HisCTerminal NP**), (ii) E4HisCTerminal Mepstra **57** conjugated to azide-functionalised nanoparticles (**E4HisCTerminal Mepstra NP**); (iii) and also the correspondent controls, both azide and NHS nanoparticles (**Nude azide NP** and **Nude NHS NP**) (Figure 43). Once again, I was involved in doing some of the repeats and had significant input in analysing and compiling the results.

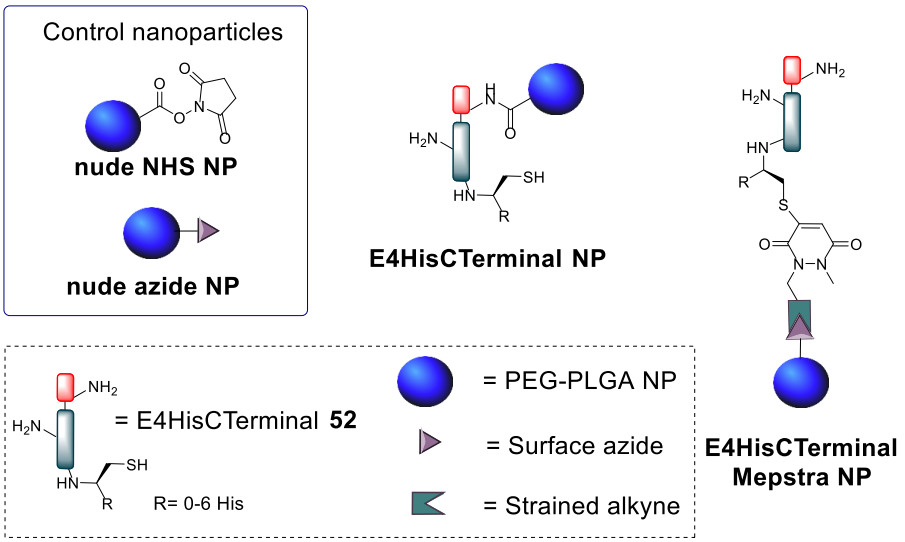

Figure 43. Representation of all nanoformulations tested: nude NHS NP; nude azide NP; E4HisCTerminal NP and E4HisCTerminal Mepstra NP.

To confirm that V_{NAR} E4 still retained its antigen binding affinity after chemical manipulation and nanoconjugation to the Rhodamine-6G loaded NPs, all the aforementioned nanoformulations were incubated with recombinant human DLL4 immobilised on microtiter plates. Dose-dependent binding of E4HisCTerminal Mepstra NP to DLL4 was observed, with each increment in NP concentration leading to a stepwise enhancement in fluorescence (Figure 44). Despite similar concentration-dependent binding of E4HisCTerminal NP to DLL4, fluorescence readouts were significantly lower than those observed for E4HisCTerminal Mepstra NP. The controls showed the binding of non-targeted control NPs (nude azide and NHS NPs) to be negligible. Collectively, these findings demonstrate that our novel chemistry may be exploited for the site-specific 'click' installation of DLL4-targeted V_{NARs} bearing a

free cysteinyl residue on the corona of polymeric NP, yielding nanoconjugates with superior binding ability to DLL4 than those formulated using conventional methods.

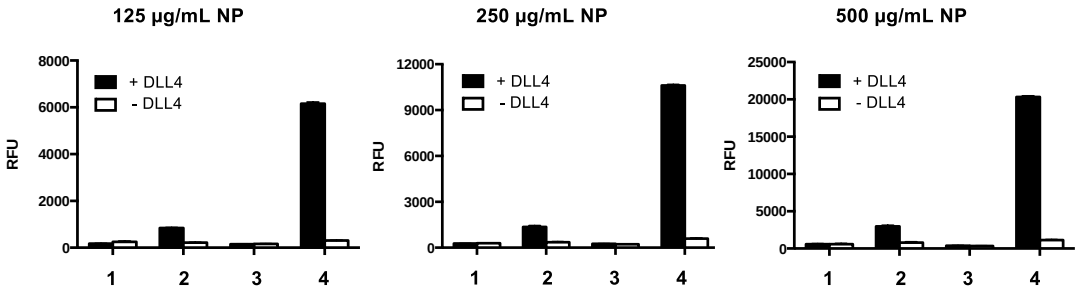

Figure 44. Binding of all nanoformulations to DLL4. Number of samples 3. **1)** Nude NHS NP. **2)** E4HisCTerminal NP. **3)** Nude azide NP. **4)** E4HisCTerminal Mepstra NP.

Site-selective cysteine modified E4HisCTerminal Mepstra NP to DLL4 is greatly enhanced compared to random lysine modified E4HisCTerminal NP. Binding of all the nanoformulations (125, 250 and 500 µg polymer/mL) to DLL4 was analysed by FLISA. Data expressed as mean ± SEM. I actively participated in doing these experiments.

Following this, verification was sought that the observed enhancement in fluorescence in the above binding assays was attributed to specific interactions between the targeted nanoformulations and the immobilised DLL4 antigen. Although the previous studies offered preliminary confirmation in this respect through inclusion of control wells that were not coated with DLL4 (where only background fluorescence was detected), further corroboration to these findings using a variety of assay formats was sought.

Initially, E4 paratopes on the surface of the NP were saturated with an excess of free DLL4 prior to incubation in microtiter plate wells coated with the same antigen. Binding of E4HisCTerminal Mepstra NP and E4HisCTerminal NP was inhibited following pre-incubation with DLL4, as evidenced by significantly lower fluorescence readouts for these samples (Figure 45a). As an alternative approach, both E4HisCTerminal Mepstra NP and an anti-DLL4 monoclonal antibody were added simultaneously to DLL4-immobilised wells. In these studies, NP binding was progressively impeded with increasing concentrations of competing anti-DLL4 (Figure 45b). Taken together, these distinct experimental setups provide robust confirmation that the ability of the NP formulations to bind to DLL4 was dependent

upon the surface conjugation of the V_{NAR} proteins.

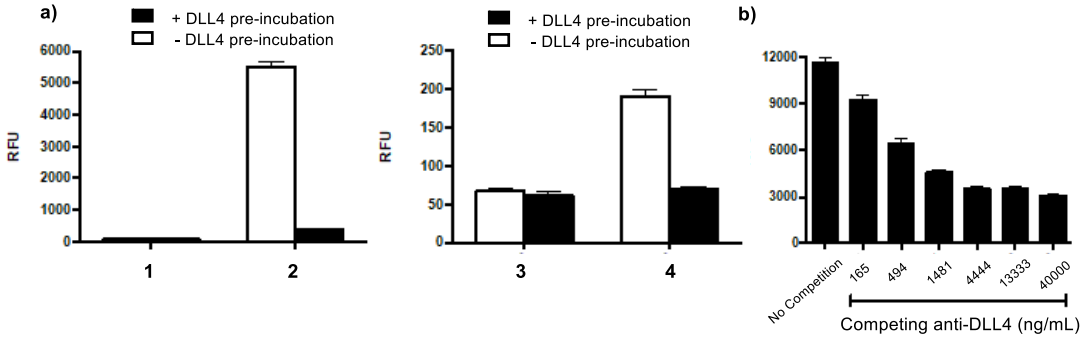

Figure 45. Binding of E4 nanoformulations is DLL4-specific. Number of samples: 3. **a)** Binding of fluorescently labelled **1)** Nude azide NP. **2)** E4HisCTerminal Mepstra NP. **3)** Nude NHS NP. **4)** E4HisCTerminal NP. All nanoformulations were at 50 µg polymer/mL concentration and binding to DLL4 was analysed by ELISA ± pre-incubation with anti-DLL4 monoclonal antibody (10 µg/mL). **b)** Binding of fluorescently labelled E4HisCTerminal Mepstra NP (250 µg polymer/mL) to DLL4 was analysed by ELISA ± competition with anti-DLL4 monoclonal antibody (165-40000 ng/mL). Data expressed as mean ± SEM. I actively participated in doing these experiments.

It was next investigated whether the superior binding of site-selective cysteine E4HisCTerminal Mepstra NP was contingent upon both surface display of azide and cysteine modification of the V_{NAR}. Various nanoformulations were synthesised by incubating E4HisCTerminal Mepstra **57** with a NP comprised solely of PLGA-502H, or a blend of PLGA-502H and either PLGA-PEG-NHS or PLGA-PEG-azide. Binding of these NPs to immobilised DLL4 was minimal, with the exception of those formulated *via* 'click' coupling of E4HisCTerminal Mepstra **57** to complementary azide-terminated NP (Figure 46). Furthermore, native E4HisCTerminal **52** was also incubated with the above polymeric NP formulation; all three formulations showed only marginal levels of DLL4 binding (Figure 46). These findings clearly indicate that the enhanced DLL4 binding activity of E4HisCTerminal Mepstra NP is not simply mediated *via* non-specific surface adsorption of the V_{NAR} clone. Rather it shows that the presence of the surface-exposed azide and the cysteine modified V_{NAR} are critical determinants of nanoconjugate performance, thus, confirming the site-selectivity and importance of our covalent conjugation approach.

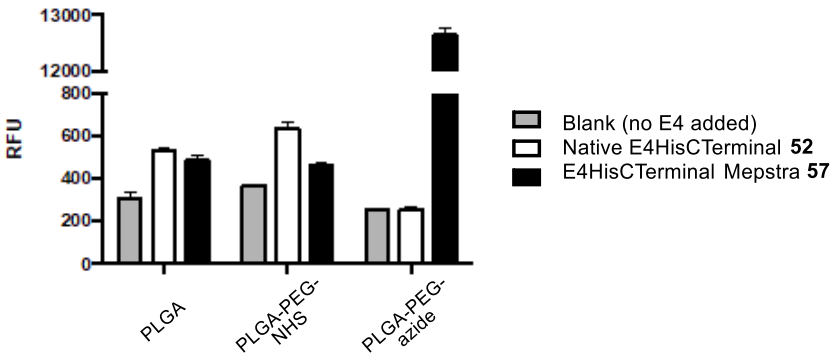

Figure 46. Enhanced DLL4 binding by E4HisCTerminal Mepstra NP is dependent upon site-specific 'click' coupling. Number of samples: 3. E4HisCTerminal Mepstra **57** and non-conjugated native E4HisCTerminal **52** were incubated with fluorescently labelled NP composed of PLGA-502H, a 75:25 blend of PLGA-502H:PLGA-PEG-NHS and a 75:25 blend of PLGA-502H:PLGA-PEG-azide. Binding of these nanoformulations and corresponding blank NP controls (500 µg polymer/mL) to DLL4 was analysed by ELISA. Number of samples: 3. Data expressed as mean ± SEM. I shadowed Dr Michelle Greene in doing this experiment.

The final set of studies examined the influence of several formulation parameters on the DLL4 binding activity of E4HisCTerminal Mepstra NP. Firstly, the effect of varying the amount of azide functionality on the surface of the NP was investigated. A 95:5, 85:15, 75:25 or 65:35 blend of PLGA-502H:PLGA-PEG-azide was used to generate a series of NP batches with graduated levels of azide moieties presented for conjugation. Following incubation with DLL4-coated wells, fluorescence measurements revealed that each gain in azide content led to a corresponding enhancement in NP binding. Surprisingly, it was found that a 65:35 ratio was superior to the 75:25 previously shown to be optimal for TRAZ fragment nanoparticles (Figure 47a). This effect could be attributed to the smaller size of V_{NAR} proteins, which, in theory, would allow a higher protein packing on nanoparticles surface, reinforcing the idea that smaller proteins/antibody fragments could provide a better antigen-binding profile of PEG-PLGA nanoparticle-V_{NAR} conjugate. Thereafter, it was also explored the impact of different loadings of E4HisCTerminal Mepstra **57** on the surface of the NP. This was achieved by varying the input amount of **57** to the NP conjugation reactions from 0.25 to 4 nanomoles per milligram of polymer, leading to the generation of nanoconjugates with incremental improvements in DLL4 binding activity (Figure 47b). Interestingly, fluorescence levels plateaued upon adding

>2 nanomoles of E4HisCTerminal Mepstra **57**, suggestive of DLL4 epitope saturation. In summary, these data showcase the exceptional versatility and highly controllable nature of our NP functionalisation technology, demonstrating how DLL4 binding may be tuned to the desired specification through facile manipulation of various NP formulation components.

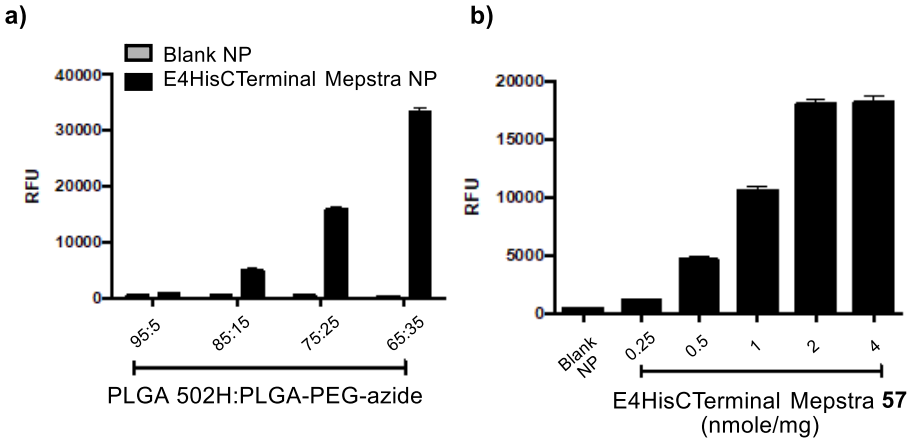

Figure 47. DLL4 binding activity of E4HisCTerminal Mepstra NP is highly controllable. Number of samples: 3. **a)** E4HisCTerminal Mepstra **57** was incubated with fluorescently labelled NP composed of a 95:5, 85:15, 75:25 or 65:35 blend of PLGA-502H:PLGA-PEG-azide. Binding of these nanoformulations and corresponding blank NP control (500 µg polymer/mL) to DLL4 was analysed by ELISA. **b)** Various amounts of E4HisCTerminal Mepstra **57** were incubated with fluorescently labelled NP composed of a 75:25 blend of PLGA-502H:PLGA-PEG-azide. Binding of these nanoformulations and the corresponding blank NP control (500 µg polymer/mL) to DLL4 was analysed by ELISA. Input amounts of E4HisCTerminal Mepstra **57** are annotated as nanomoles of V_{NAR} per milligram of polymer. Data expressed as mean ± SEM. Dr Michelle Greene proceeded with this set of experiments.

This chapter showcases a new modular method for attaching V_{NAR} proteins onto the surfaces of a PEG-PLGA polymeric nanoparticle *via* 'click' chemistry. A novel heterobifuncitional PD linker was designed and used to enable site selective cysteine conjugation of a V_{NAR} clone to form a bioconjugate that was attached to an azide decorated nanoparticle using SPAAC conjugation. This nanoparticle-V_{NAR} construct, with orientated protein presentation on the nanoparticle surface, showed favorable properties in terms of binding when compared to traditional nanoparticle-protein conjugation chemistries.

These results were encouraging, as initially it was thought of the possibility that the orientation provided by disulfide re-bridging approach in previous experiments (*e.g.* with CTX and TRAZ Fab) could be less impactful with the new single-cysteine modification approach. Fortunately, the results demonstrate the same orientation benefits as the cysteine is distal from the receptor binding site.

This work resulted in the generation of a nanoparticle-V_{NAR} conjugate for the first time. Furthermore, the importance of controlled chemical ligation for the overall performance of nanoconjugates was confirmed.[166] Thus, this work is seen as a contribution to the study of active targeted nanoconjugates and how their extensive refinement can lead to an impact on overall efficiency.

Conclusions and Future Work

Outlook

Throughout this thesis, the use of pyridazinediones as novel surface-bound linkers for the installation of targeting antibodies onto azide-terminated nanoparticles was reported. Several different fragments of antibodies and small proteins were tested as targeting moieties, generating ANCs with previously unmet degrees of control, and thus greatly enhancing antigen-binding capabilities. Additionally, the collaboration with Queen's University of Belfast was considered of major importance, as their expertise in developing PEG-PLGA nanoparticles with exquisite properties (*e.g.* ability to functionalise with functional groups such as azides or NHS-esters, ability to encapsulate drugs, etc.) facilitated the appraisal of success of such ANCs. In this way, it was possible to demonstrate that the more controlled chemistry offered by the pyridazinedione linker allows a more oriented arrangement of the antibody onto the surface of the nanoparticle, and thus provides a significant improvement in antigen binding capability. This enhancement in avidity of pyridazinedione-mediated nanoconjugation methods also demonstrated enhanced efficacy in drug delivery and consequent cell killing when compared to competitor nanoconjugates (e.g. non-targeted nanoparticles, nanoconjugates where random lysine residues are modified), suggesting antigen-mediated NP internalisation into the cells.

In conclusion, a unique technology has been developed that enables the construction of drug-loaded 'active-targeted' ANCs. Given the success of the enhanced conjugation techniques presented for antigen-binding and cell-based assays, it is envisioned their future academic and commercial applications in the field.

Future work

Amine-reactive pyridazinediones project

Previously, it was reported that carbodiimide chemistries are still one of the preferred approaches to covalently attach antibodies/antibody fragments to nanoconstructs, as they activate carboxylic groups present on the surface of nanoparticles. As shown throughout this thesis, this approach is considered sub-optimal, but it is still commonly utilised due to its simplicity and the commercial availability of carboxylate functionalised nanomaterials and polymers. Also, amine-functionalised nanoparticles are amongst the most frequently used for the generation of active-targeted nanoconjugates. Thus, it was projected a way in which these positive factors could be combined with our technology to fabricate ANCs with a high degree of control in a facile fashion. Rather than utilise the carboxylate functions to couple directly to the targeting antibody, it was envisioned to synthesise NHS-ester functionalised pyridazinedione linkers (Scheme 22a) to mediate the link between ligand and particle; thus, disulfide selectivity could be introduced to commercial materials using simple chemistry. Hence, it is presented an alternative approach based on carbodiimide chemistries, where both site-selectivity and orientation of the antibody/antibody fragment onto the nanoparticles are preserved (Scheme 22b). Additionally, amine terminations are stable at physiological conditions, providing a more reliable platform for further modifications.

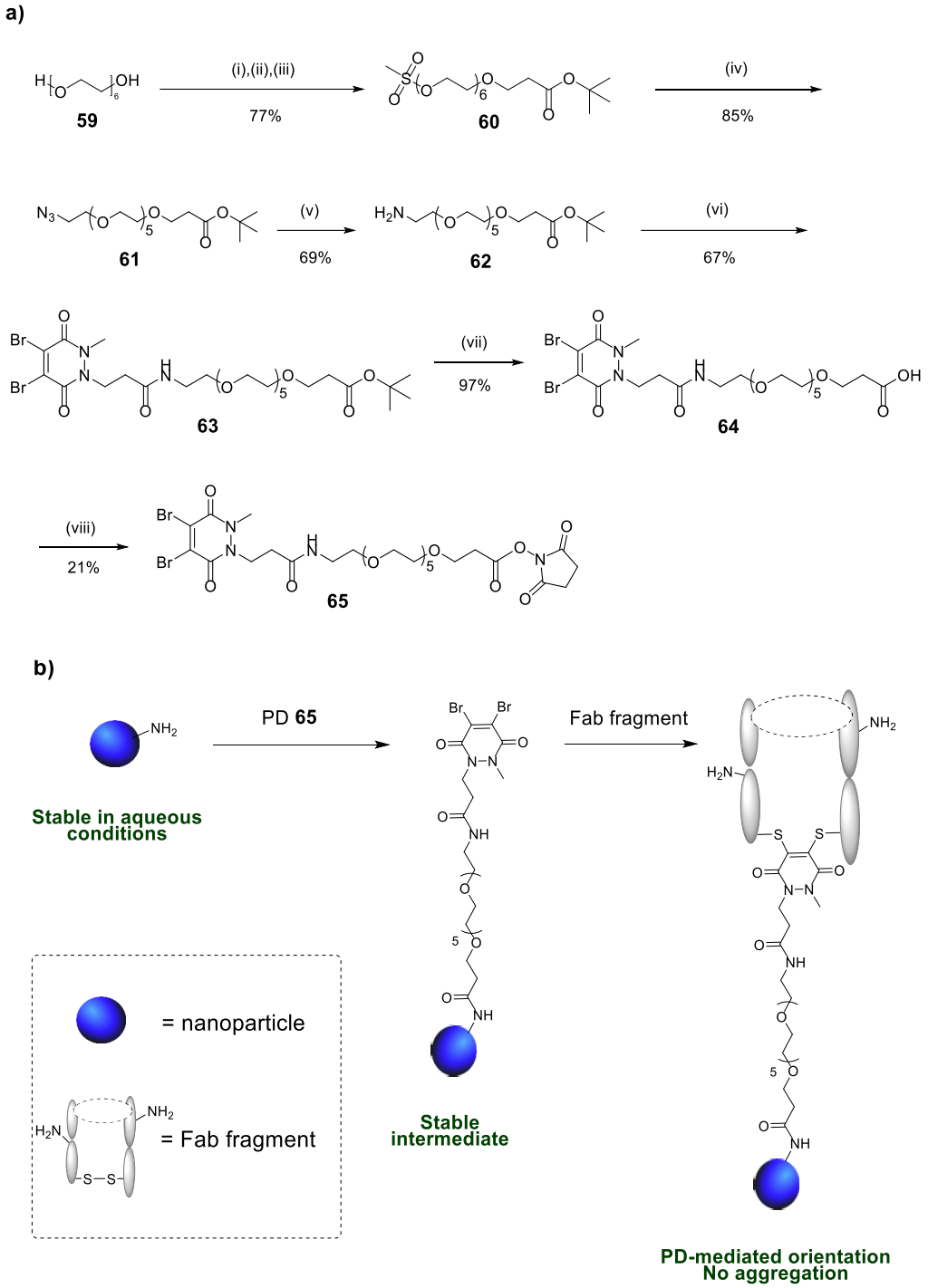

Scheme 22. a) Synthesis of amine-reactive PD **65**.

Reagents and conditions: (i) NaH (60%), *tert*-butyl acrylate, THF, 21 ºC. (ii) AcOH, 21 ºC, 2 h. (iii) Methanesulfonyl chloride, NEt_3, DCM, 21 ºC, 24 h. (iv) NaN_3, DMF, 21 ºC, 72 h. (v) Triphenylphosphine, THF, H_2O, 21 ºC, 16 h. (vi) PD **45**, MeCN, 21 ºC, 16 h. (vii) TFA, DCM, 21 ºC, 2 h. (viii) *N,N'*-dicyclohexylcarbodiimide, *N*-hydrosuccinimide, 21 ºC, 16 h.

b) Representation of envisioned approach for the use of carbodiimide chemistry for

the formation of nanoconjugates in a site-selective manner, highlighting main advantages.

The aforementioned strategy would also allow the nanoparticle-PD conjugate to be fully characterised, stored and shipped to collaborators in high quantities, providing a useful platform for those who lack the tools and expertise for protein modification and/or nanoparticle functionalisation (*i.e*. by having this stable NP-PD intermediate, only one step is needed to graft antibodies/antibody fragments in an oriented, site-selective manner, generating highly-controlled ANCs with optimal antigen binding).

Application of tetrazine PD linkers for the generation of nanoconjugates

As nanoparticle research is thriving, multiple research groups are more and more interested in equipping nanoparticles with reactive handles so they can be further functionalised with drugs, fluorophores or targeting entities. For this purpose, and as described in Chapter 1, 'click' chemistry reagents have brought large benefits to the bioconjugation field as they deliver reliable, rapid and simple reactions, even a wide range of conditions. Although strained alkyne/azide reactions were employed during this thesis, tetrazine/trans-cyclooctene (TCO) 'click' is also attracting attention in the field of biorthogonal labelling and crosslinking. Moreover, this method is reported to excel at very low concentrations, making it a suitable candidate for application in biological systems, due to the extremely rapid reaction kinetics.[167] Although there are two main types of tetrazines that are commonly utilised, 6-methyl-substituted supersedes the use of 6-hydrogen-substituted tetrazines due to its higher stability in aqueous media and superior tolerance to harsh reaction conditions (even though not offering the same reaction kinetics as the latter) making it a suitable reagent for functionalisation of proteins/nanoparticles. Thus, it was envisioned to synthesise a 6-methyl tetrazine precursor for further application within the nanoconjugate field as response to a growing interest in this 'clickable' reagent (Scheme 23).

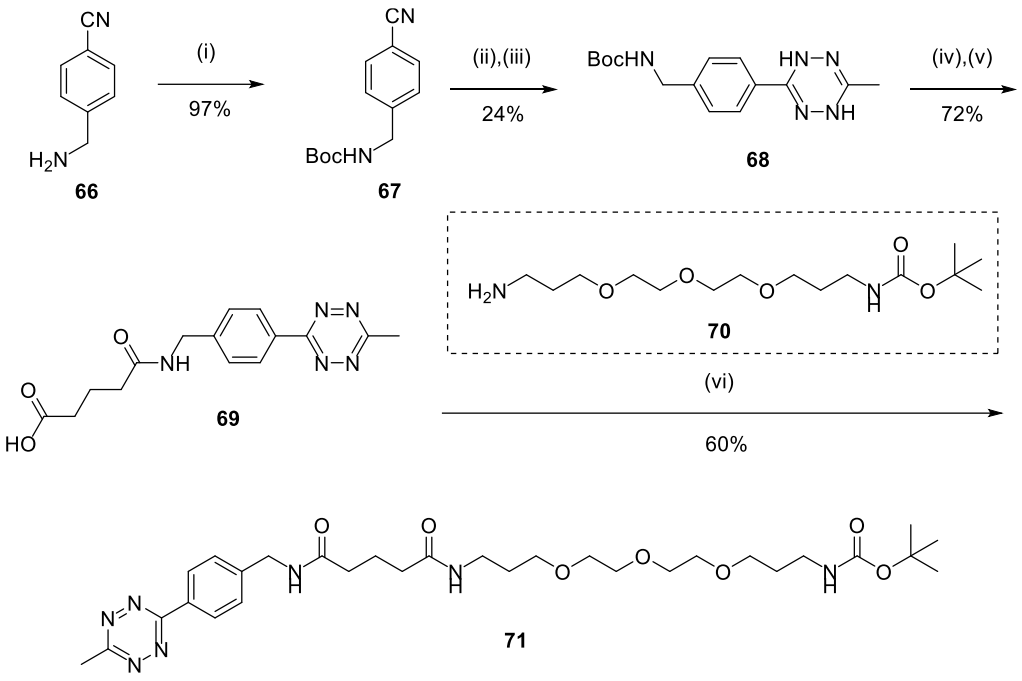

Scheme 23. Synthesis of tetrazine precursor **71**.

Reagents and conditions: (i) Di-*tert*-butyl decarbonate, NaOH, H_2O, 21 ºC, 16 h. (ii) $Zn(OTf)_2$, 1,4-dioxane, MeCN, 65 ºC, 72h. (iii) $NaNO_2$, AcOH, DCM, 21 ºC, 15 min. (iv) TFA, DCM, 21 ºC, 2 h. (v) Glutaric anhydride, THF, 55 ºC, 16 h. (vi) Amine **70**, NEt_3, HATU, DCM, 21 ºC, 16 h.

Tetrazine precursor **71** can be used to equip a pyridazinedione handle in a facile manner by undergoing a boc de-protection reaction, followed by coupling to any of the NHS-ester PDs previously synthesised (Figure 48). In fact, work has been initiated in this regard as has been included as an appendix experimental in this thesis to ensure transfer of knowledge to future members of the Chudasasma research group.

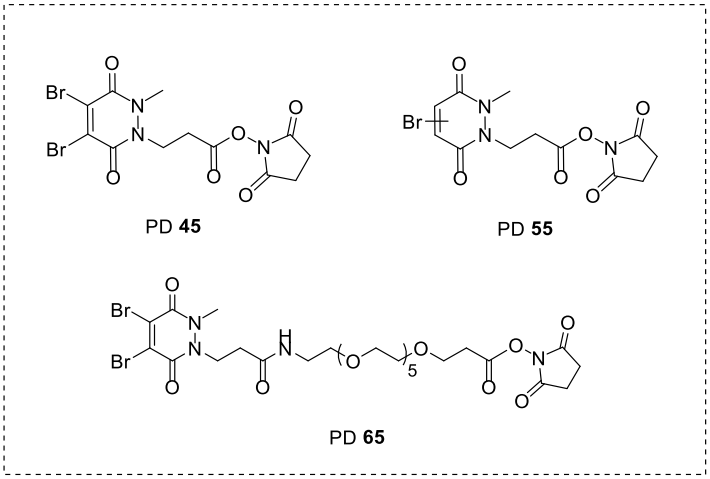

Figure 48. Library of NHS-ester pyridazinediones.

Hence, when pyridazinedione linkers are synthesised, it will be possible to compare the tetrazine/TCO against strained alkyne/azide efficiency, particularly for the application in assays where high sensitivity is needed (*e.g.* lateral flow assays).

CTX Fab NP

As it was envisaged for my PhD, several nanoconjugates were developed and their improved avidity demonstrated. Additionally, one of the main goals of this project was testing CTX Fab NPs in a model of pancreatic cancer, which was successfully achieved, with excellent results. The following steps would be testing CTX Fab nanoconjugates in an *in vivo* setting.

General Experimental

Chemicals

All reagents were purchased from Aldrich, Alfa Aesar or Lumiprobe and were used as received without purification, unless stated.

Chromatography

All small molecule reactions were monitored by thin-layer chromatography (TLC) on pre-coated SIL G/UV254 silica gel plates (254 μm) purchased from VWR. TLC plates were initially examined under short wave UV light and then developed using aqueous potassium permanganate or ninhydrin stains, when appropriate. Flash column chromatography was carried out with pre-loaded GraceResolv™ flash cartridges on a Biotage® Isolera Spektra One flash chromatography system.

Spectroscopy

^{1}H and ^{13}C NMR spectra were recorded at ambient temperature on a Bruker Avance 300 instrument operating at a frequency of 300 MHz for ^{1}H and 75 MHz for ^{13}C, a Bruker Avance 500 instrument operating at a frequency of 500 MHz for ^{1}H and 125 MHz for ^{13}C, and a Bruker Avance 600 instrument operating at a frequency of 600 MHz for ^{1}H and 150 MHz for ^{13}C in $CDCl_3$, CD_3OD or DMSO-d_6 (as indicated below). The chemical shifts (δ) for ^{1}H and ^{13}C are quoted relative to residual signals of the solvent on the ppm scale. ^{1}H NMR peaks are reported as singlet (s), doublet (d), triplet (t), quartet (q), pentet (p), m (multiplet) and br (broad). Coupling constants (*J* values) are reported in Hertz (Hz) and are H-H coupling constants unless otherwise stated. Where rotamer peaks are presented, analysis was conducted by integration of all rotamer peaks. Chemical shifts of only the major rotamer peaks are reported. Infrared spectra were obtained on a Perkin Ekmer Spectrum 100 FTIR spectrometer operating in ATR mode. UV-vis spectroscopy was used to determine antibody fragment concentrations using a nanodrop ND-1000 spectrophotometer and a Varian Cary 100 Bio UV-Visible spectrophotometer, operating at room temperature. Sample buffer was used as blank for baseline correction. UV-vis spectroscopy was also used to determine PAR (Pyridazinedione to Antibody Ratio) and FAR (Fluorophore to

Antibody Ratio). Calculation of molecule over antibody ratio, *r*, follows the formula below, as previously described:[32]

$$r = \frac{A_\lambda / \varepsilon_\lambda}{(A_{280} - \sum_\lambda CF_\lambda \times A_\lambda)/\varepsilon_{280}}$$

SDS-PAGE gels

Non-reducing glycine-SDS-PAGE at 12% and 15% acrylamide gels were performed following standard lab procedures. A 6% stacking gel was used and a broad-range MW marker (10–250 kDa, Prestained Pageruler Plus Protein Standards, Bio-Rad) was co-run to estimate protein weights. Samples (15 µL at ~12 µM construct) were mixed with loading buffer (3 µL, composition for 6 × SDS: 1 g SDS, 3 mL glycerol, 6 mL 0.5 M Tris buffer pH 6.8, 2 mg bromophenol blue in 10 mL) and heated at 75 °C for 1 min. The gels were run at 30 mA for 50 min in 1 × SDS running buffer. The gels were stained with Coomassie blue dye.

Protein LC-MS

Antibodies, antibody fragments and their respective conjugates were prepared for analysis by repeated diafiltration into distilled water to achieve approximate concentrations of 4-5 µM (1.0 mg×ml^{-1}) and submitted to the UCL Chemistry Mass Spectrometry Facility at the Chemistry Department, UCL for analysis on the Agilent 6510 QTOF LC-MS system (Agilent, UK). 10 µL of each sample was injected onto a PLRP-S, 1000A, 8 µM, 150 mM × 2.1 mM column, which was maintained at 60 °C. The separation was achieved using mobile phase A (95% water, 5% MeCN, 0.1% formic acid) and B (5% water, 95% MeCN, 0.1% formic acid) using a gradient elution. The column effluent was continuously electrosprayed into the capillary ESI source of the Agilent 6510 QTOF mass spectrometer and ESI mass spectra were acquired in positive electrospray ionisation (ESI) mode using the m/z range 1,000−8,000 in profile mode. The raw data was converted to zero charge mass spectra using a maximum entropy deconvolution algorithm, over the appropriate regions as identified *via* the LC trace, with the software, MassHunter (version B.07.00). All full antibody samples were deglycosylated with PNGase F enzyme treatment prior to LC-MS analysis, a well-established method in literature.[168]

LC-MS for V_{NAR} proteins and correspondent conjugates was performed on protein samples using a Thermo Scientific uPLC connected to MSQ Plus Single Quad Detector (SQD). Column: Hypersil Gold C4, 1.9 μm, 2.1 × 50 mm. Wavelength: 254 nm. Mobile Phase: 99:1 Water (0.1% formic acid): MeCN (0.1% formic acid) to 1:9 Water (0.1% formic acid): MeCN (0.1% formic acid) gradient over 4.5 min. Flow Rate: 0.3 mL/min. MS Mode: ES+. Scan Range: m/z = 500–2000. Scan time: 1.5 s. Data obtained in continuum mode. The electrospray source of the MS was operated with a capillary voltage of 3.5 kV and a cone voltage of 50 V. Nitrogen was used as the nebulizer and desolvation gas at a total flow of 600 L/h. Ion series were generated by integration of the total ion chromatogram (TIC) over the 2.0–5.0 min range. Total mass spectra for protein samples were reconstructed from the ion series using the pre-installed ProMass software using default settings for large proteins in m/z range 500–1500.

Miscellaneous

All reactions involving moisture sensitive techniques were performed under an atmosphere of dry argon *via* standard vacuum line techniques and glassware was flame dried and allowed to cool under reduced pressure. Reactions performed at 0 °C were cooled with an ice and water bath. Concentration *in vacuo* refers to distillation on a Büchi rotary evaporator, and where appropriate, under high vacuum. Where described below, Petrol refers to petroleum ether (b.p. 40-60 °C). Melting points were measured with gallenkamp apparatus and are uncorrected.

Experimental for Chapter 2

Synthesis of compounds

tert-Butyl 1-methylhydrazine-1-carboxylate[169] **32**

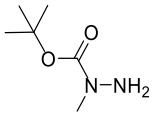

32

To a stirring solution of *N*-methylhydrazine **31** (1.73 g, 37.5 mmol) in DCM (100 mL) at 0 °C was added dropwise di-*tert*-butyl dicarbonate (8.12 g, 37.5 mmol, pre-dissolved in DCM (40 mL)) over 40 min. The mixture was allowed to warm to room temperature (21 °C) and stirred for a further 3 h. After this time, the reaction mixture was concentrated *in vacuo* to yield *tert*-butyl-1-methylhydrazine-1-carboxylate **32** (5.15 g, 35.3 mmol, 94%) as a yellow liquid without further purification. ^{1}H NMR ($CDCl_3$, 600 MHz) δ 4.01 (br s, 2H), 3.02 (s, 3H), 1.44 (s, 9H); ^{13}C NMR ($CDCl_3$, 150 MHz) δ 157.2 (C), 80.4 (C), 38.3 (CH_3), 28.6 (CH_3); IR (thin film) 3330, 2977, 2932, 1668 cm^{-1}.

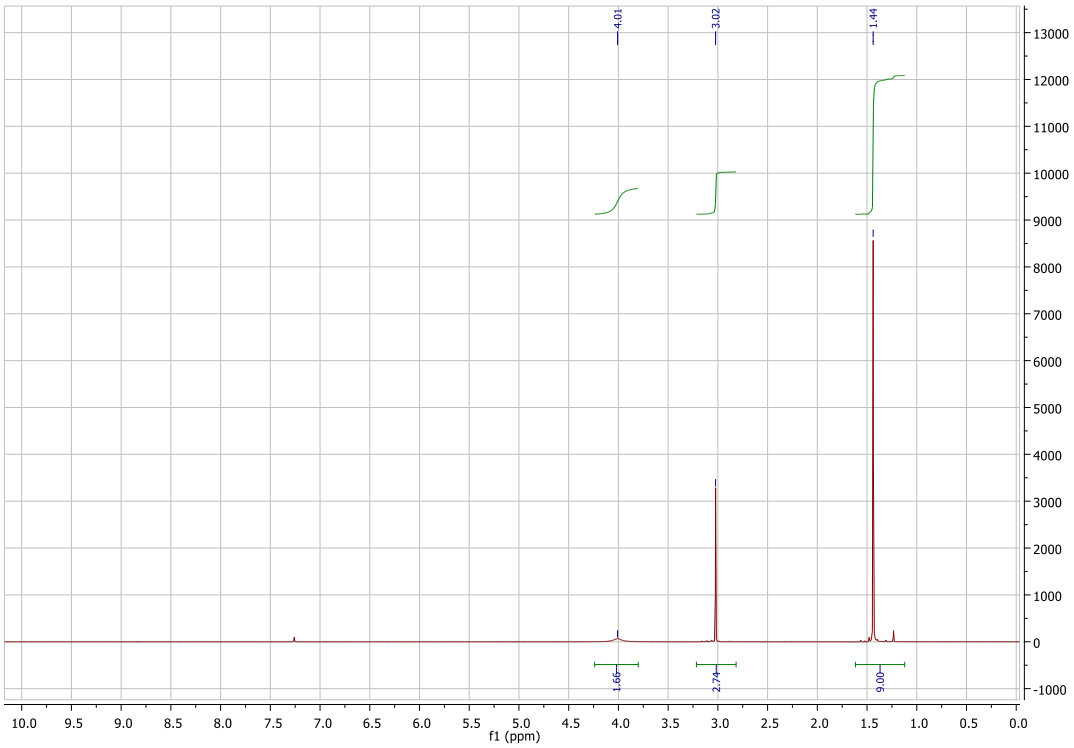
4.01
3.02
1.44
1.66
2.74
9.00
f1 (ppm)

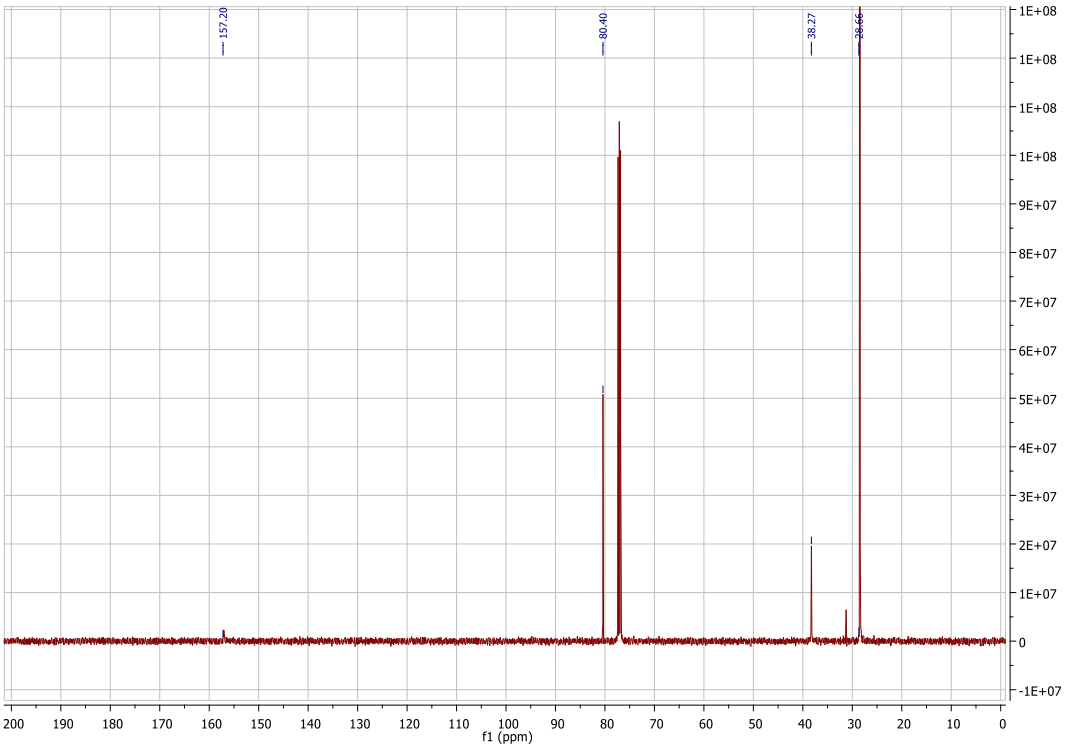
157.20
80.40
38.27
28.66
f1 (ppm)

((*tert*-Butoxycarbonyl)(methyl)amino)glycine[169] **33**

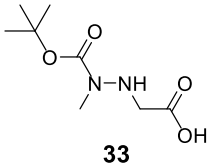

33

tert-Butyl 1-methylhydrazine-1-carboxylate **32** (585 mg, 4.00 mmol) and glyoxylic acid (296 mg, 4.00 mmol) were dissolved in *i*-PrOH (10 mL) and the reaction mixture stirred at 21 °C for 5.5 h. 10% Pd/C (80 mg) was subsequently added and the flask placed under vacuum to remove all air. The flask was filled with an atmosphere of H_2 *via* a balloon and the suspension stirred for 24 h. After this time, the solution was filtered through Celite® 545 and the filtrate concentrated *in vacuo* to yield a crude oil. Trituration with DCM afforded ((*tert*-butoxycarbonyl)(methyl)amino)glycine **33** (170 mg, 0.800 mmol, 20%) as a yellow foam. Data matched the literature[170]. ^{1}H NMR (DMSO-d_6, 400 MHz) δ 3.46 (s, 2H), 2.93 (s, 3H), 1.40 (s, 9H); ^{13}C NMR (DMSO-d_6, 100 MHz) δ 171.9 (C), 152.0 (C), 81.9 (C), 50.9 (CH_2), 27.7 (CH_3), 28.0 (CH_3); IR (thin film) 3299, 3025, 2977, 2931, 1733, 1668 (br) cm^{-1}.

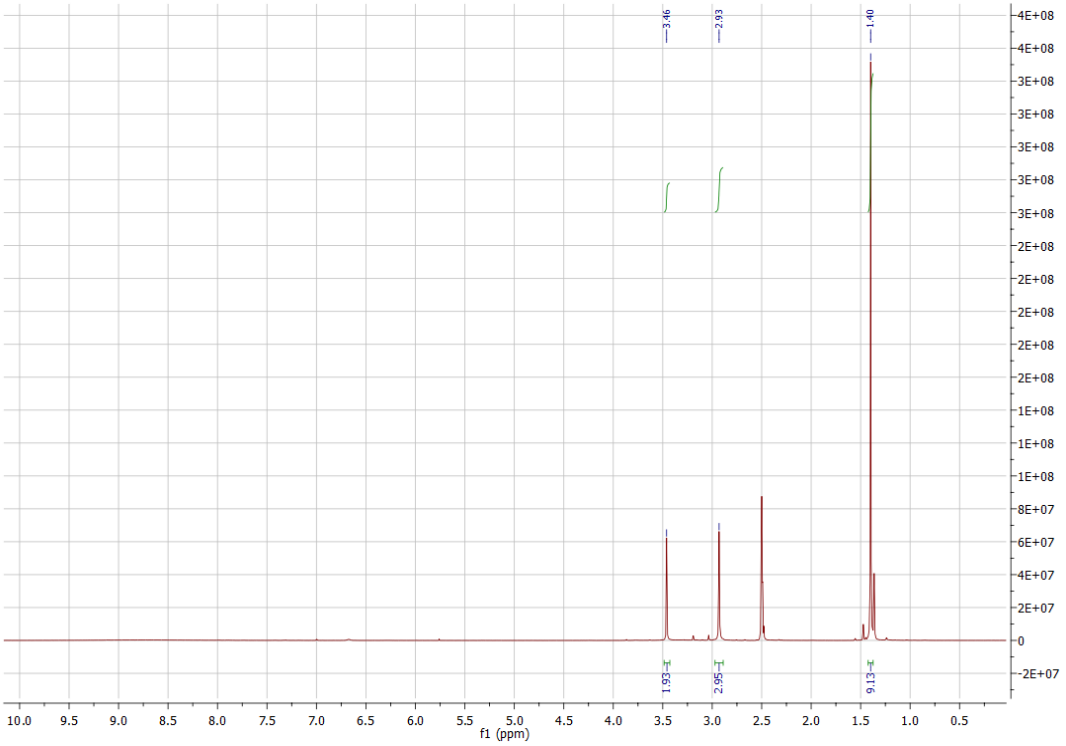
3.46
2.93
1.40
1.93
2.95
9.13
f1 (ppm)

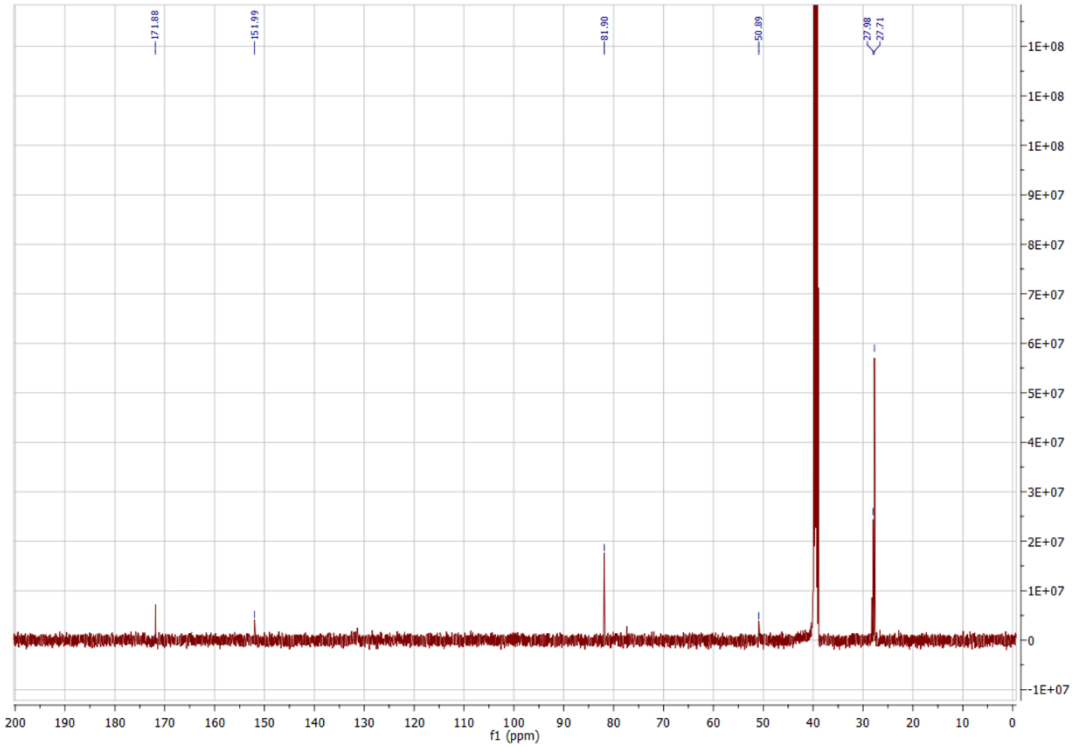
171.88
151.99
81.90
50.89
27.98
27.71
f1 (ppm)

2-(4,5-Dibromo-2-methyl-3,6-dihydropyridazin-1(2*H*)-yl)acetic acid[169] **34**

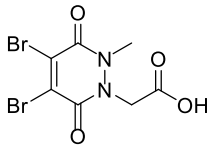

34

To a solution of ((*tert*-butoxycarbonyl)(methyl)amino)glycine **33** (150 mg, 0.73 mmol) in AcOH (10 mL) was added dibromomaleic acid (546 mg, 2.00 mmol). The reaction mixture was refluxed for 24 h. After this time, all solvent was removed *in vacuo* with toluene co-evaporation (3 × 20 mL). The crude material was then dissolved in EtOAc (25 mL), washed with water (3 × 15 mL), and dried ($MgSO_4$). The organic layer was concentrated *in vacuo* and purification by flash column chromatography (10% MeOH/DCM with 1% AcOH) yielded 2-(4,5-dibromo-2-methyl-3,6-dioxo-3,6-dihydropyridazin-1(2*H*)-yl)acetic acid **34** (107 mg, 0.310 mmol, 43%) as a brown solid: m.p. 135–140 °C; ^{1}H NMR (600 MHz, MeOD) δ 4.96 (s, 2H), 3.62 (s, 3H); ^{13}C NMR (150 MHz, MeOD) δ 170.2 (C), 154.8 (C), 154.0 (C), 137.4 (C), 135.7 (C), 49.5 (CH_2), 35.0 (CH_3); IR (solid) 3023, 2969, 1731, 1662, 1631 cm^{-1}.

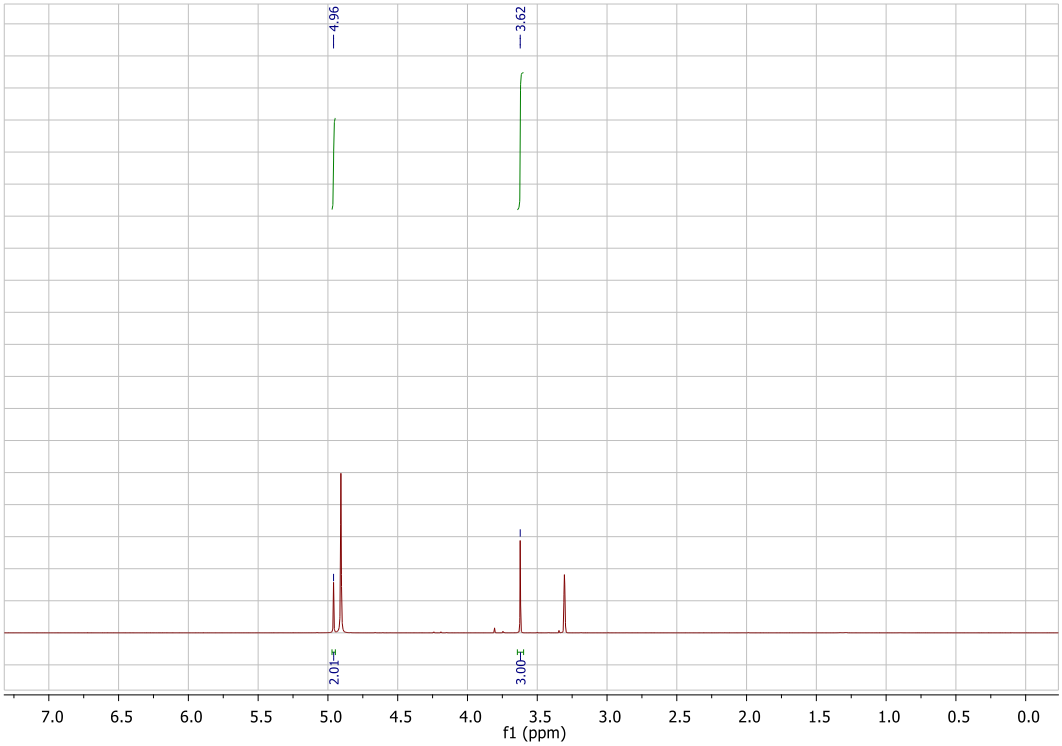
4.96
3.62
2.01
3.00
7.0
6.5
6.0
5.5
5.0
4.5
4.0
3.5
3.0
2.5
2.0
1.5
1.0
0.5
0.0
f1 (ppm)

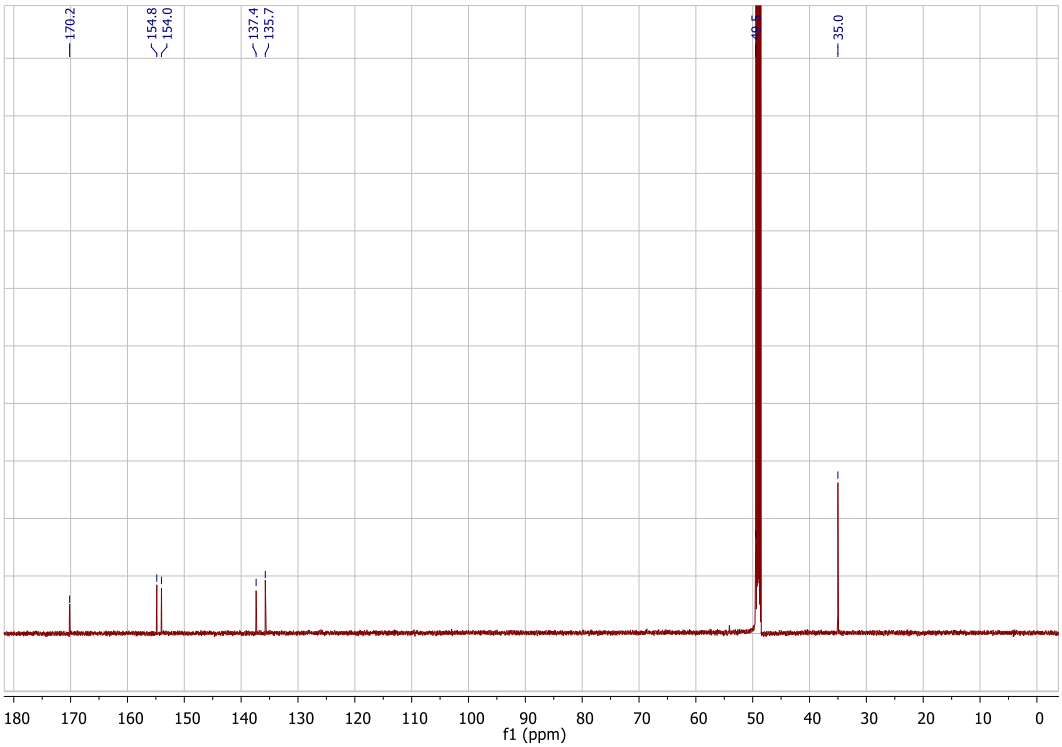
170.2
154.8
154.0
137.4
135.7
35.0
180
170
160
150
140
130
120
110
100
90
80
70
60
50
40
30
20
10
0
f1 (ppm)

((1*R*,8*S*,9*S*)-Bicyclo[6.1.0]non-4-yn-9-yl)methyl(2-(2-(2-(2-(4,5-dibromo-2-methyl-3,6-dioxo-3,6-dihydropyridazin-1(2*H*)-yl)acetamido)ethoxy)ethoxy)ethyl)carbamate[169] **35**

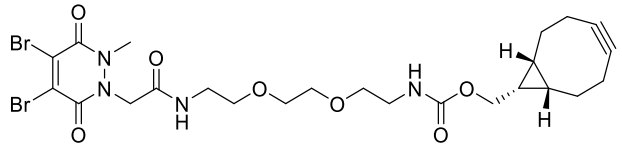

35

To a solution of 2-(4,5-dibromo-2-methyl-3,6-dihydropyridazin-1(2*H*)-yl)acetic acid **34** (30 mg, 0.087 mmol), PyBOP (50 mg, 0.10 mmol), and DIPEA (12 mg, 0.10 mmol) in DCM (2.5 mL) was added *N*-[(1*R*,8*S*,9*S*)-bicyclo[6.1.0]non-4-yn-9-ylmethyloxycarbonyl]-1,8-diamino-3,6-dioxaoctane **13** (28 mg, 0.087 mmol). The resulting solution was then stirred at 21 °C for 16 h. After this time, the reaction mixture was diluted with H_2O (10 mL), extracted with EtOAc (3 × 10 mL), the combined organic layers dried ($MgSO_4$) and concentrated *in vacuo*. The crude residue was purified by flash column chromatography (neat EtOAc) to afford ((1*R*,8*S*,9*S*)-bicyclo[6.1.0]non-4-yn-9-yl)methyl(2-(2-(2-(2-(4,5-dibromo-2-methyl-3,6-dioxo-3,6-dihydropyridazin-1(2*H*)-yl)acetamido)ethoxy)ethoxy)ethyl) carbamate **35** (7 mg, 0.011 mmol, 13%) as a yellow oil: ^{1}H NMR (600 MHz, $CDCl_3$, mixture of rotamers) δ 8.34 (br s, 0.5H), 7.00 (br. s, 0.5H), 5.96 (br. s, 0.5H), 5.29 (br. s, 0.5H), 4.85–4.73 (m, 2H), 4.12 (d, *J* = 8.2 Hz, 2H), 3.76–3.50 (m, 11H), 3.50–3.43 (m, 2H), 3.40–3.30 (m, 2H), 2.31–2.17 (m, 6H), 1.61–1.51 (m, 2H), 1.41–1.24 (m, 1H), 1.01–0.85 (m, 2H); ^{13}C NMR (150 MHz, $CDCl_3$) (major rotamer) δ 165.6 (C), 157.8 (C), 153.4 (C), 152.5 (C), 137.0 (C), 134.8 (C), 98.9 (C), 77.4 (CH_2), 77.2 (CH_2), 77.0 (CH_2), 70.8 (CH_2), 70.6 (CH_2), 70.5 (CH_2), 70.3 (CH_2), 70.2 (CH_2), 70.0 (CH_2), 69.6 (CH_2), 69.4 (CH_2), 63.0 (CH_2), 50.9 (CH_2), 50.3 (CH_2), 40.9 (CH_2), 39.7 (CH_2), 35.0 (CH_3), 29.1 (CH), 21.5 (CH_2), 20.2 (CH), 17.8 (CH_2); IR (thin film) 3338, 2925, 1685, 1662, 1633 cm $^{-1}$.

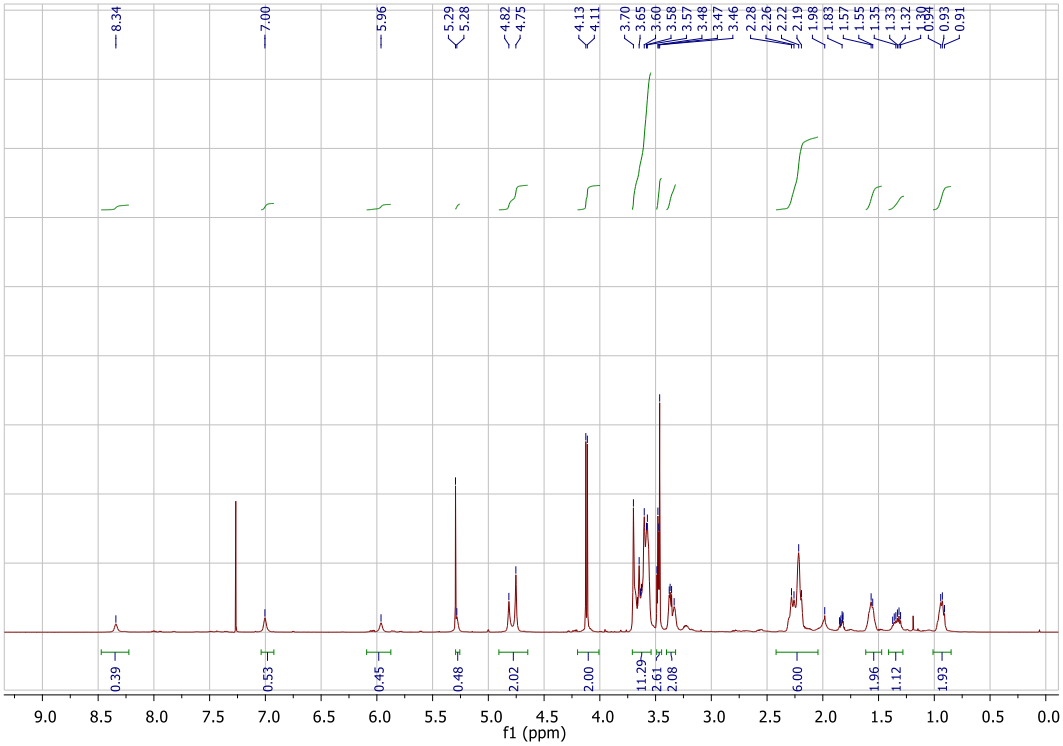
8.34
7.00
5.96
5.29
5.28
4.82
4.75
4.13
4.11
3.70
3.65
3.60
3.58
3.57
3.48
3.47
3.46
2.28
2.26
2.22
2.19
1.98
1.83
1.57
1.55
1.35
1.33
1.32
1.30
0.94
0.93
0.91
0.39
0.53
0.45
0.48
2.02
2.00
11.29
2.61
2.08
6.00
1.96
1.12
1.93
f1 (ppm)

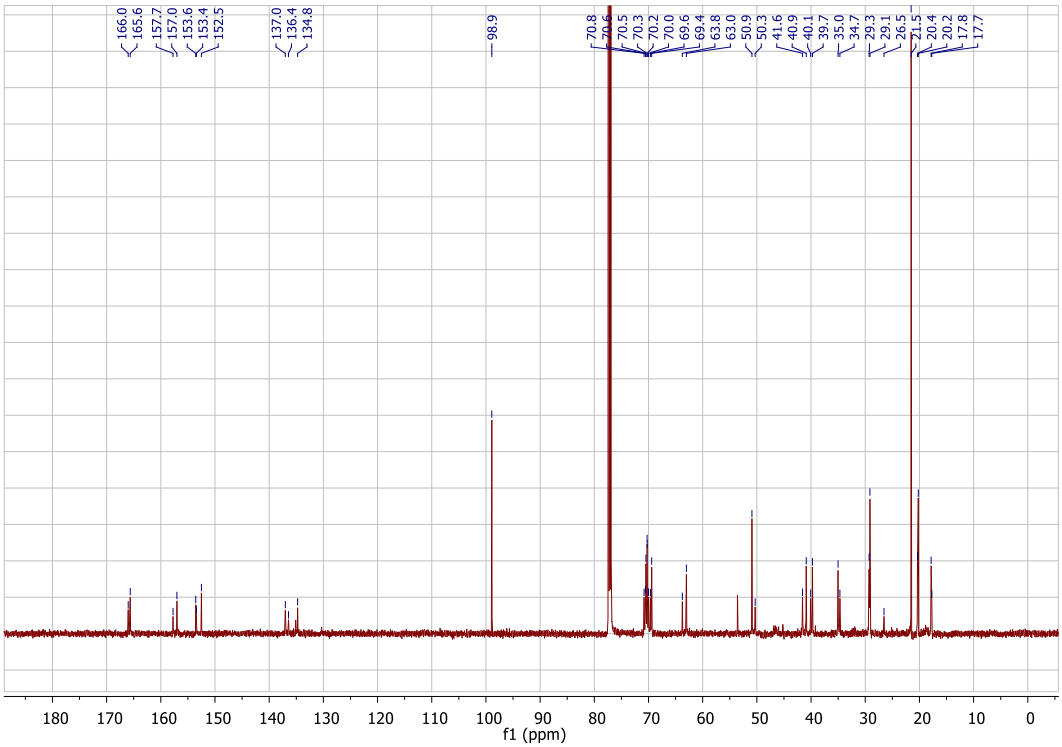
166.0
165.6
157.7
157.0
153.6
153.4
152.5
137.0
136.4
134.8
98.9
70.8
70.6
70.5
70.3
70.2
70.0
69.6
69.4
63.8
63.0
50.9
50.3
41.6
40.9
40.1
39.7
35.0
34.7
29.3
29.1
26.5
21.5
20.4
20.2
17.8
17.7
f1 (ppm)

Chemical biology

Untreated Trastuzumab Control (TRAZ) **27**

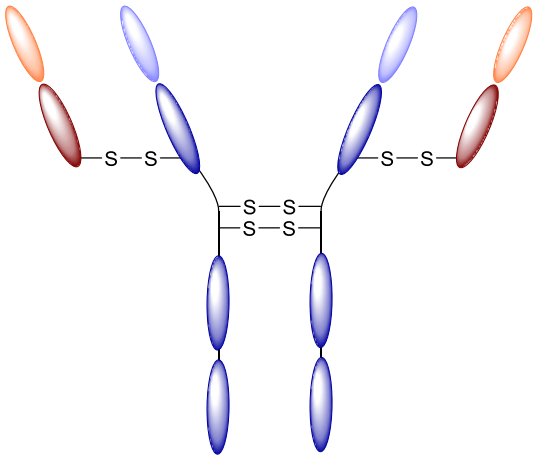

27

Expected mass: 145,532 Da Observed mass: 145,171 Da.

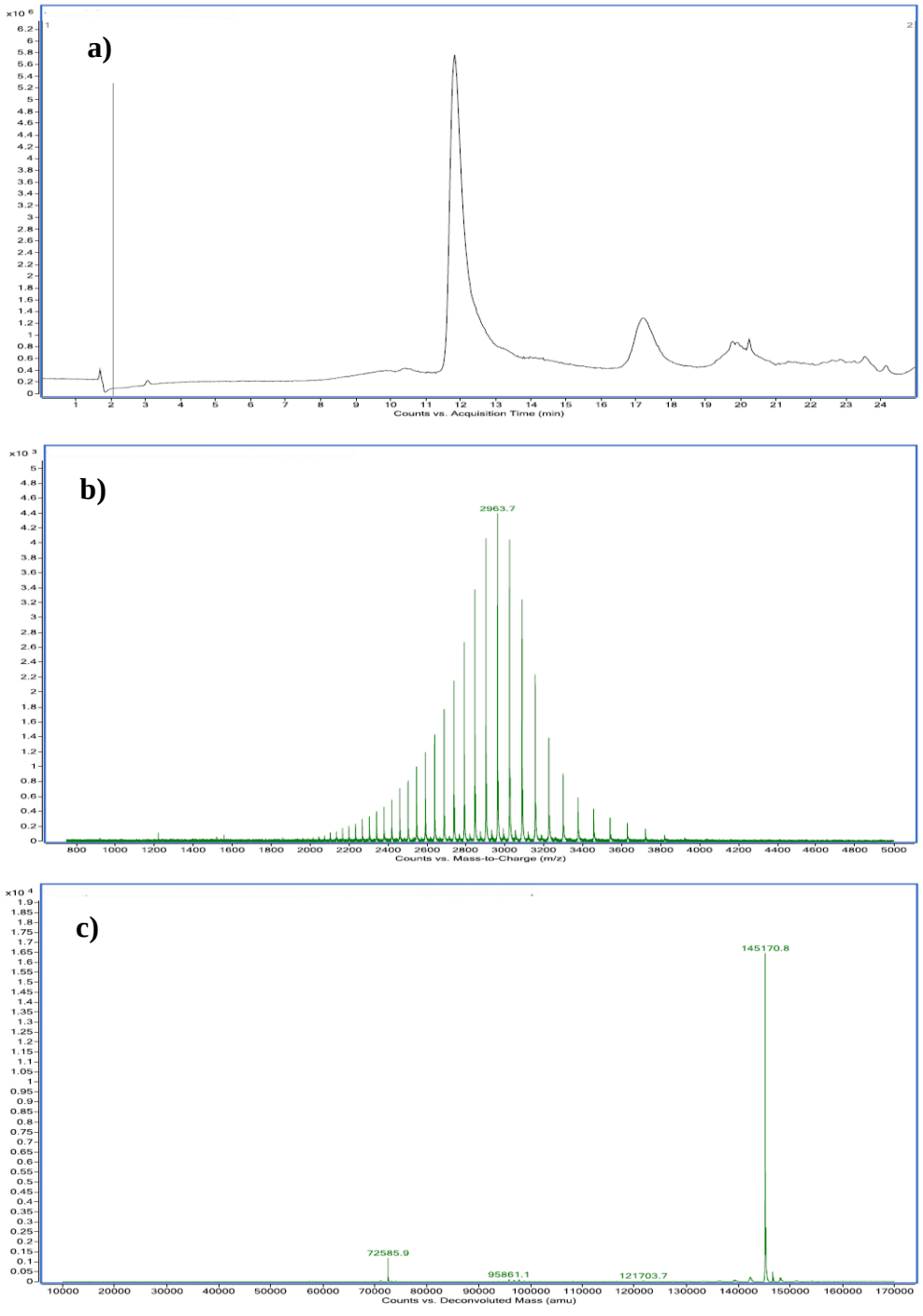

Figure 49. (a) TIC, **(b)** non-deconvoluted LC-MS trace and **(c)** deconvoluted MS data for TRAZ **27**.

Digestion protocols[169]

Trastuzumab F(ab')$_2$

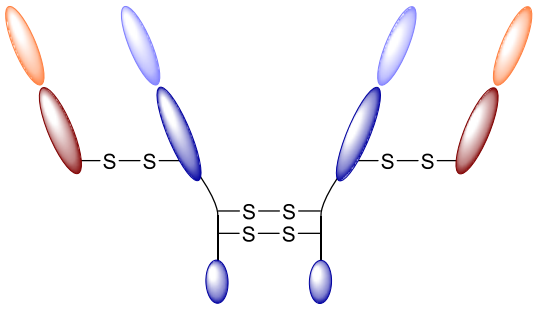

Immobilized pepsin (0.6 mL) was washed with acetate buffer (4 × 0.3 mL, 20 mM sodium acetate trihydrate, pH 3.1). Trastuzumab **27** (19.5 mg, 3 mL, 6.55 mg·mL^{-1} in acetate buffer) was added and the mixture incubated for 5 h under constant agitation (1100 rpm) at 37 °C. The digest solution was separated from the resin beads, which were washed with digest buffer (50 mM phosphate, 150 mM NaCl, 1 mM EDTA, pH = 6.8) (3 × 0.4 mL). The washings were combined with the digest and the entire mixture buffer swapped into BBS (25 mM sodium borate, 1 mM disodium ethyl-enediaminetetraacetic acid (EDTA), pH = 8.0). Concentration was estimated using UV/Vis (ε_{280} = 140,000 cm^{-1}·M^{-1}). Trastuzumab F(ab')$_2$ (12 mg, 93% yield) was confirmed using SDS-PAGE and LC-MS. Expected mass: 97,125 Da. Observed mass 97,289 Da.

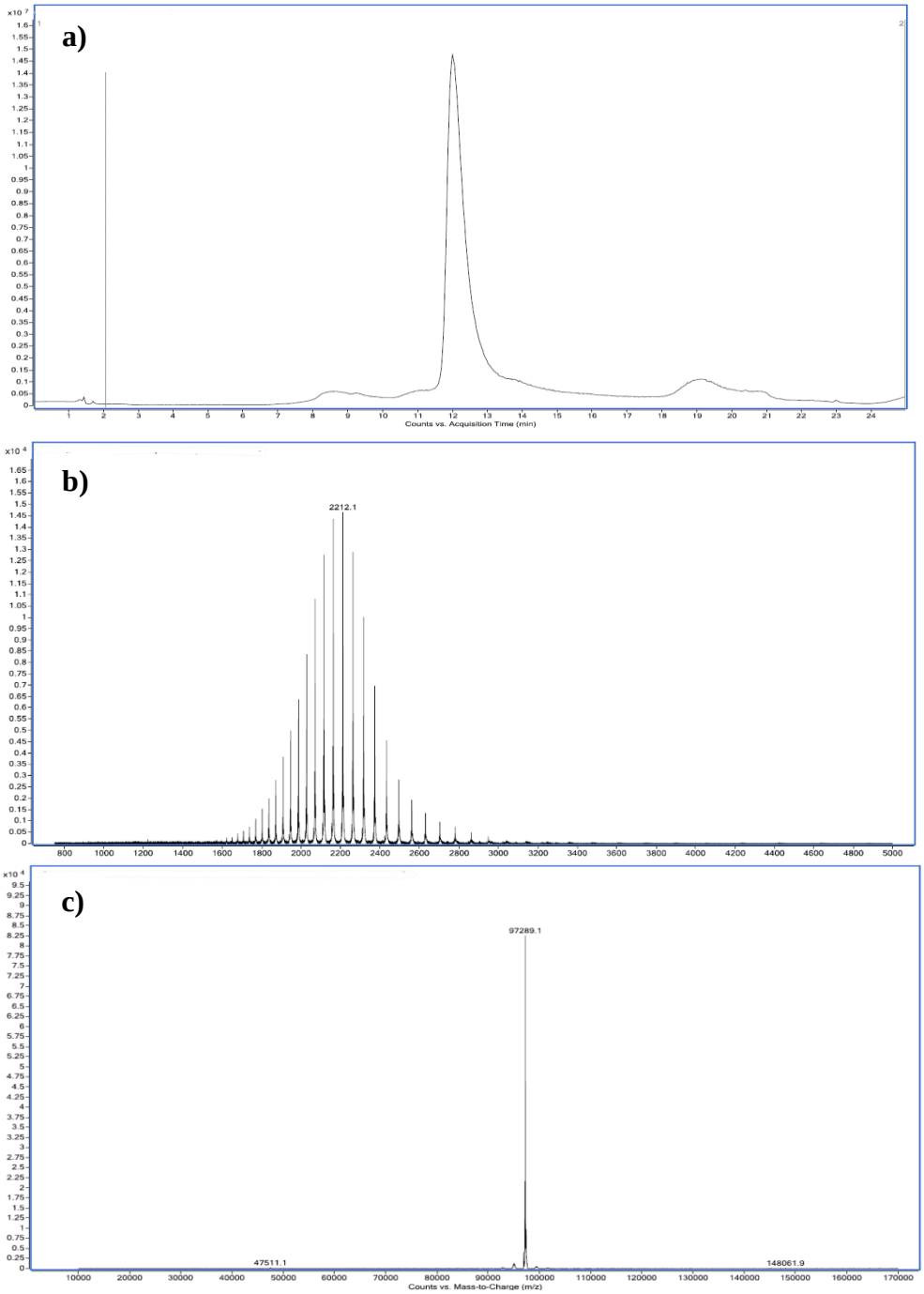

Figure 50. (a) TIC, **(b)** non-deconvoluted LC-MS trace and **(c)** deconvoluted MS data for F(ab')$_2$ fragment of Trastuzumab.

Native TRAZ Fab **28**

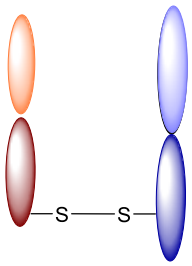

28

Immobilised papain (2 mL, 0.25 mg·mL^{-1}) was incubated in buffer (10 mM DTT in digest buffer) at 37 °C with constant agitation (1100 rpm) for 1 h. The papain resin was subsequently filtered and washed with digest buffer 4 times, and trastuzumab F(ab')$_2$ (8 mg, 2 mL, 46 µM in digest buffer) was added to the beads. The mixture was incubated at 37 °C with constant agitation (1100 rpm) for 16 h, before being separated from the digest *via* spin filtration and washed with BBS (3 × 0.4 mL, 25 mM sodium borate, 25 mM NaCl, 0.5 mM EDTA). The digest and the washes were combined and buffer swapped for BBS using spin filtration columns (10,000 MWCO), and the volume was adjusted to 0.5 mL. Yield of Fab was determined by UV/Vis spectroscopy (ε_{280} = 68,590 M^{-1}·cm^{-1}). Native TRAZ Fab **28** (7.2 mg, 90% yield) was confirmed using SDS-PAGE and LC-MS. Expected mass: 47,629 Da. Observed mass: 47,637 Da.

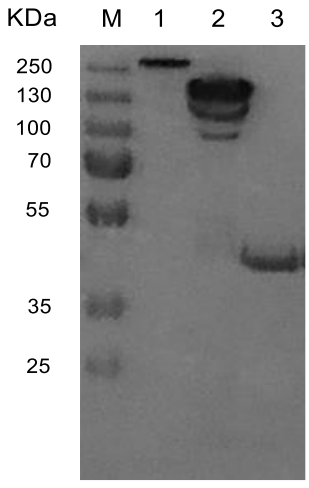

Figure 51. SDS-PAGE gel for Trastuzumab digestion**: M)** Molecular weight marker. **1)** Native TRAZ **27**. **2)** Trastuzumab F(ab')$_2$. **3)** Native TRAZ Fab **28**.

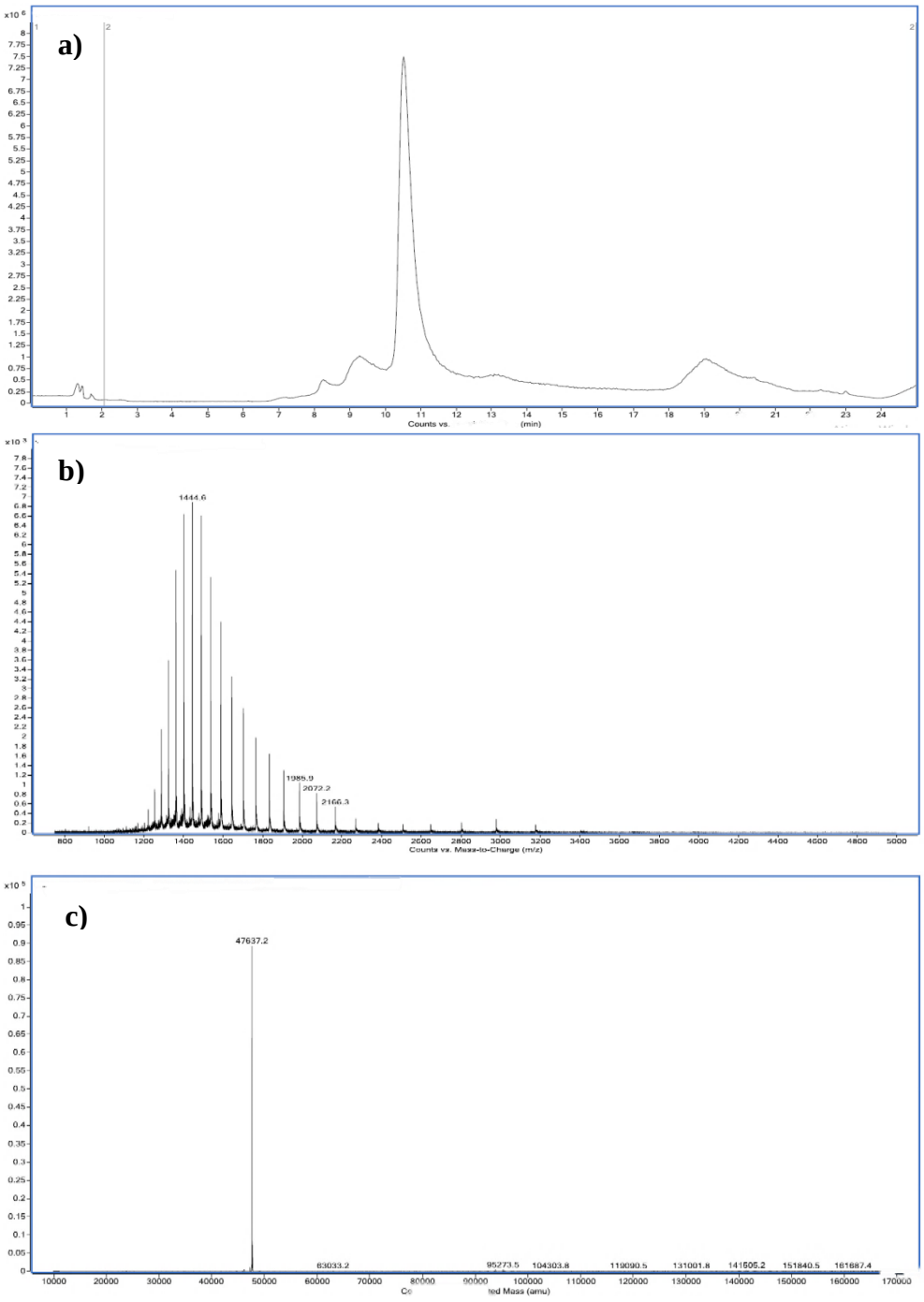

Figure 52. (a) TIC, **(b)** non-deconvoluted LC-MS trace and **(c)** deconvoluted MS data for Fab fragment of Trastuzumab.

Bioconjugation protocols[169]

TRAZ Fab [disulfide] **29**

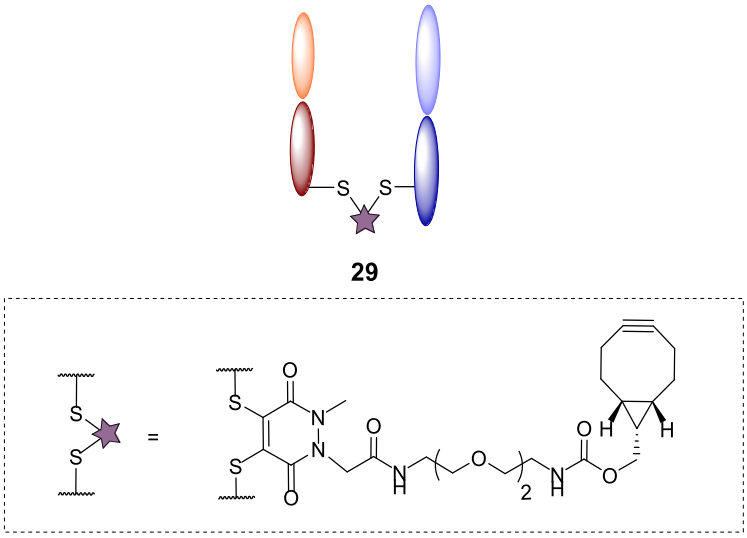

29

To a solution of native TRAZ Fab **28** (50 µL, 20 µM, 1 eq.) in BBS (25 mm sodium borate, 25 mm NaCl, 1 mm EDTA, pH 8.0 + 3% DMSO) was added diBrMestra PD **35** (0.5 µL, 20 mM in DMSO, 10 eq.), followed by TCEP (0.25 µL, 20 mM in BBS pH = 8, 5 eq.) and the reaction mixture incubated at 21 °C for 2 h. The excess reagents were then removed by repeated diafiltration into fresh buffer using VivaSpin sample concentrators (GE Healthcare, 10,000 MWCO). Following this, analysis by SDS-PAGE, LC-MS and UV-Vis revealed >95% conversion to TRAZ Fab [disulfide] **29**. Expected mass: 48,125 Da. Observed mass: 48,126 Da.

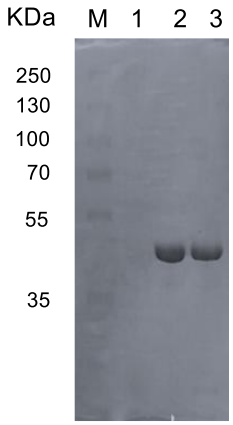

Figure 53. SDS-PAGE gel for Trastuzumab Fab fragment modification**: M)** Molecular weight marker. **1)** Empty. **2)** Native TRAZ Fab **28**. **3)** *In situ* reduction of **28** and reaction with pyridazinedione **35** at 21 °C (10 eq.).

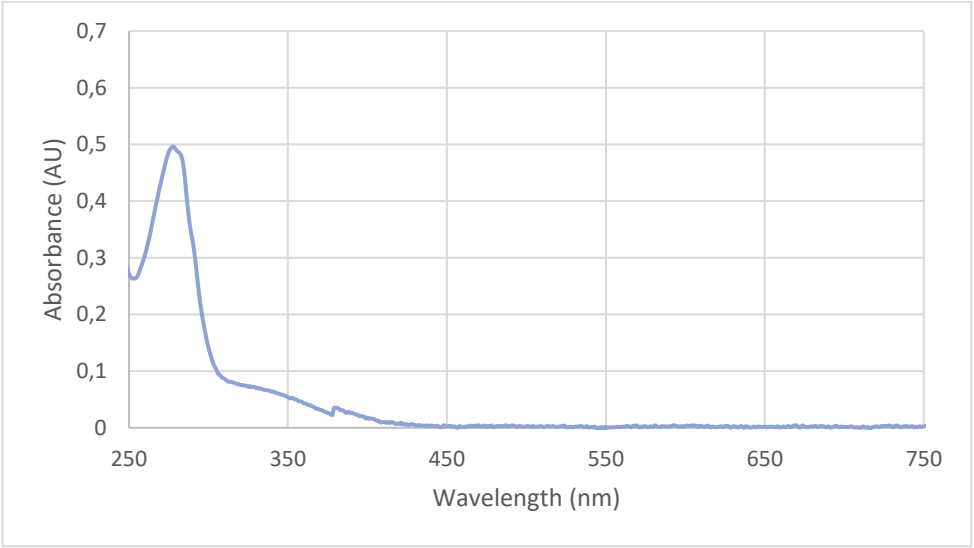

Figure 54. UV-Vis data for TRAZ Fab [disulfide] **29**, Pyridazinedione-to-Antibody Ratio (PAR) ≈ 0.9.

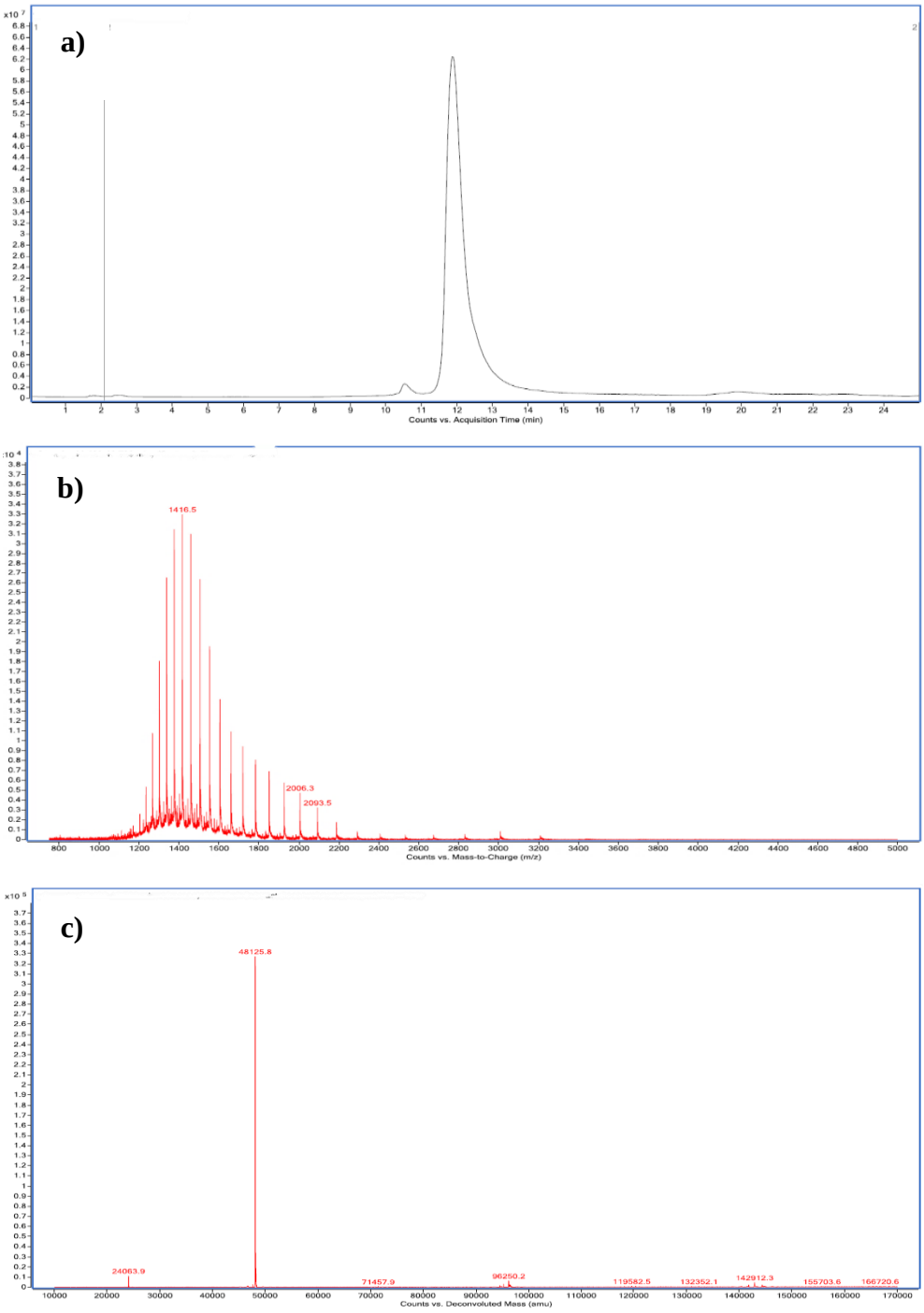

Figure 55. (a) TIC, **(b)** non-deconvoluted LC-MS trace and **(c)** deconvoluted MS data for TRAZ Fab [disulfide] **29**.

TRAZ Fab [disulfide] Alexafluor **36**

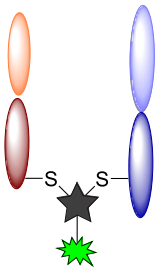

36

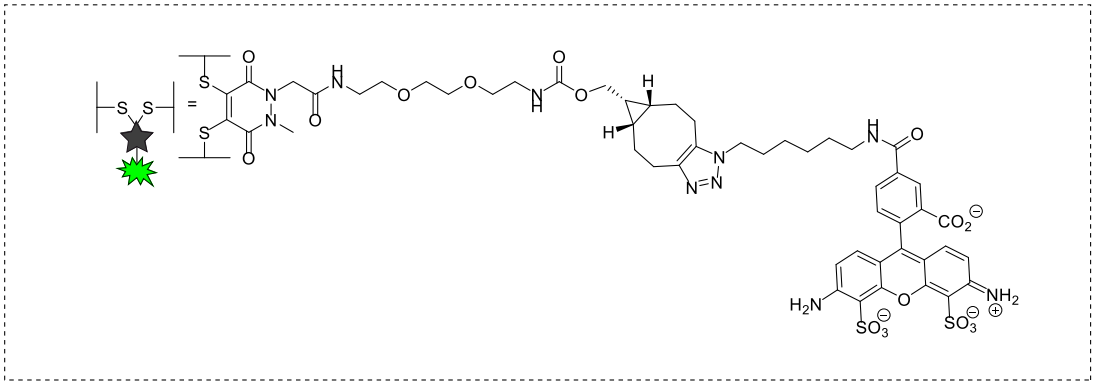

To a solution of TRAZ Fab [disulfide] **29** (50 µL, 20 µM, 1 eq.) in BBS (+3% DMSO) was added Alexafluor®-488-N_3 **37** (0.2 µL, 20 mM in DMSO, 4 eq.) and the reaction mixture incubated at 21 °C for 2 h. The excess reagents were then removed by repeated diafiltration into fresh buffer using VivaSpin sample concentrators (GE Healthcare, 5,000 MWCO). Successful conjugation of labelled protein **36** was confirmed by SDS-PAGE, LC-MS and UV-Vis analysis. Expected mass: 48,781 Da. Observed mass: 48,784 Da.

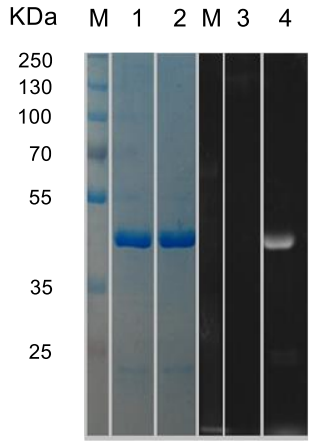

Figure 56. SDS-PAGE gel for TRAZ Fab [disulfide] Alexafluor **36**: **M)** Molecular weight marker. **1)** TRAZ Fab [disulfide] **29** stained gel. **2)** TRAZ Fab [disulfide] Alexafluor **36** stained gel. **3)** TRAZ Fab [disulfide] **29** under UV lamp **4)** TRAZ Fab [disulfide] Alexafluor **36** under UV lamp.

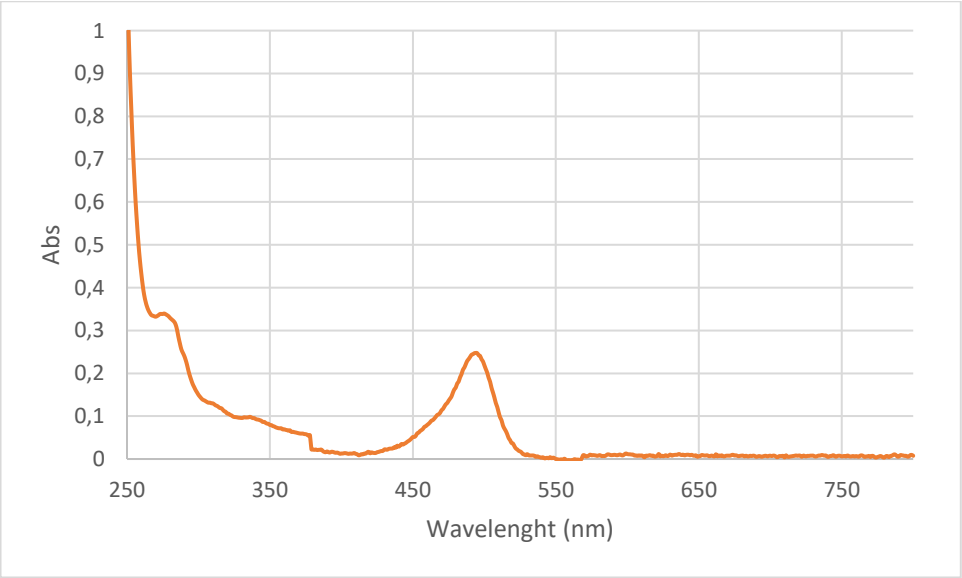

Figure 57. UV-Vis data for TRAZ Fab [disulfide] Alexafluor **36**. Fluorophore-to-Antibody Ratio (FAR) ≈ 0.8.

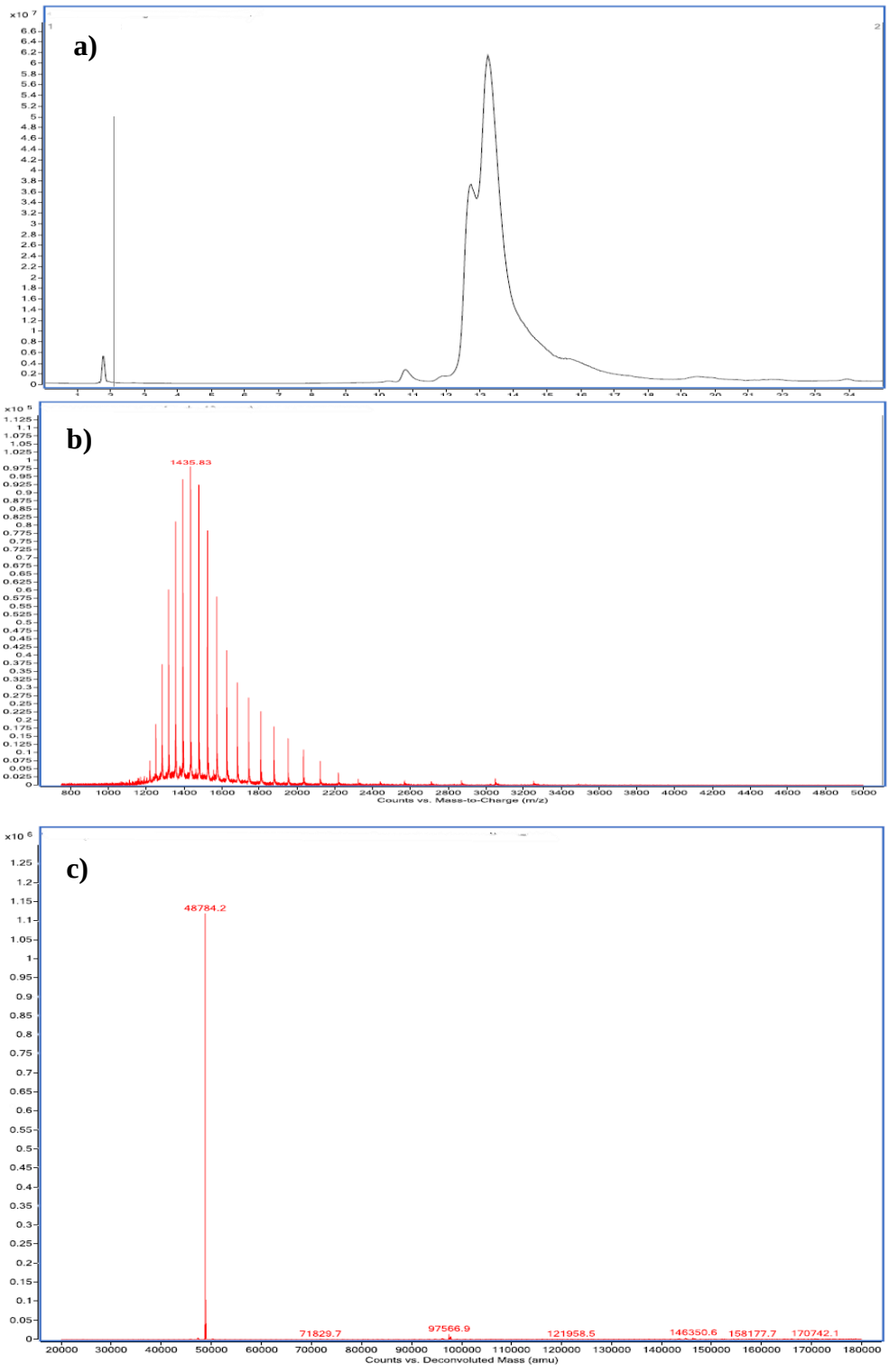

Figure 58. (a) TIC, **(b)** non-deconvoluted LC-MS trace and **(c)** deconvoluted MS data for TRAZ Fab [disulfide] Alexafluor **36**.

TRAZ Fab [lys] **38**

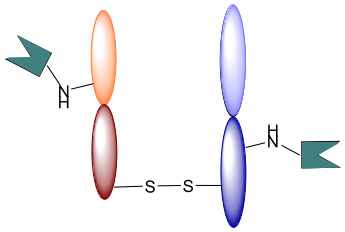

38

Compound **39** (10 µL, 60 mM in DMSO, 40 equiv.) was added to a solution of TRAZ Fab **28** (250 µL, 60 µM in BBS pH = 8) and incubated at 37 °C for 4 hours. Excess reagents were removed by repeated diafiltration into PBS (pH = 7.4) using VivaSpin sample concentrators (GE Healthcare, 10,000 MWCO). A small sample (40 µL at 20 µM) was reacted with Alexafluor488®-azide (2 µL, 50 equiv., 20 mM in DMSO) at room temperature for 16 hours to check for the presence of a strained alkyne. Excess reagents were removed by repeated diafiltration into PBS (pH = 7.4) using VivaSpin sample concentrators (GE Healthcare, 10,000 MWCO). The samples were analysed by SDS-PAGE, and UV-vis spectroscopy was used to determine a loading of 1 : 4.8 (TRAZ Fab : strained alkyne). An extinction coefficient of 71000 M^{-1} cm^{-1} was used for Alexafluor488®. A correction factor of 0.11 x A_{494} was used to correct at A_{280} for Alexafluor488®.

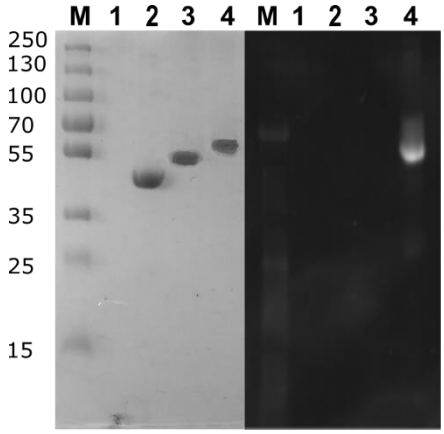

Figure 59. SDS-PAGE gel. M) Molecular weight marker in KDa: 1) Empty; 2) TRAZ Fab **28**; 3) TRAZ Fab [lys] **39** 4) TRAZ F(ab) [lys]-Alexafluor488®.

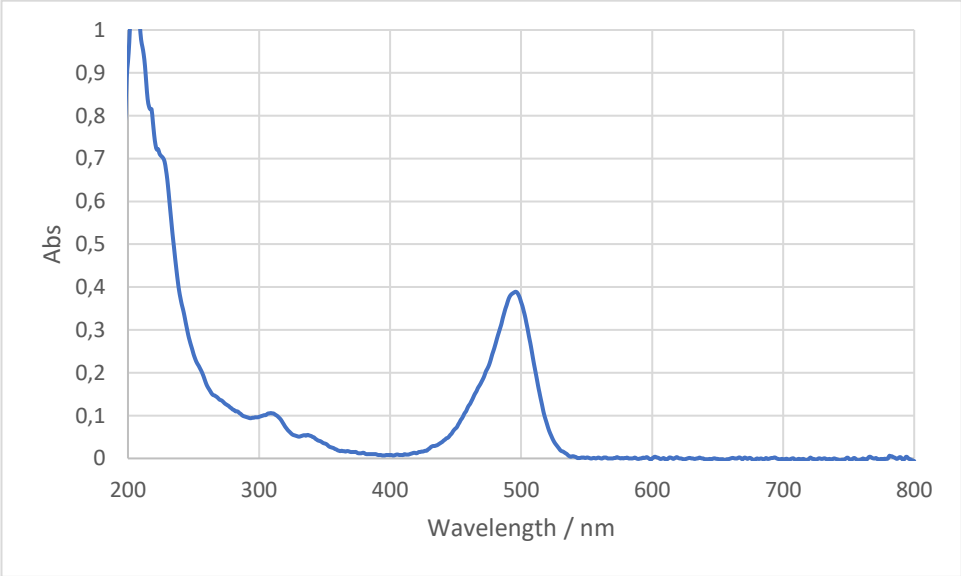

Figure 60. UV-Vis data for TRAZ F(ab) [lys]-Alexafluor488®, loading of 1 : 4.8 (TRAZ Fab : strained alkyne).

Native CTX Fab **41**

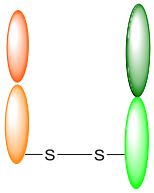

Immobilized pepsin (0.15 mL) was washed with acetate buffer (20 mM sodium acetate trihydrate, pH 3.1) four times and Cetuximab **40** (1 mg, 0.5 mL, 13.8 µM, in acetate buffer) was added. The mixture was incubated for 5 h at 37 °C whilst shaking (1100 rpm). The resin was separated from the digest using a filter column, and washed with digest buffer (50 mM phosphate, 150 mM NaCl, 1 mM EDTA, pH = 6.8) three times. The digest was combined with the washes and the combined mixture buffer swapped into digest buffer (25 mM sodium borate, 25 mM NaCl, pH 8.0) via diafiltration (4 × 15 mL, GE Healthcare, 10,000 MWCO). This yielded Cetuximab F(ab')$_2$ (0.5 mL, 13.7 µM, 97% yield). Concentration was determined photometrically using ε_{280} = 140000 $M^{-1} \cdot cm^{-1}$. Immobilized papain (0.5 mL, 0.25 $mg \cdot mL^{-1}$) was activated with 10 mM DTT in digest buffer whilst shaking (1100 rpm) for 1 h at 37 °C. The resin was washed with digest buffer (without DTT) four times and Cetuximab F(ab')$_2$ was added (0.5 mL, 13.7 µM). The mixture was incubated for 20 h at 37 °C whilst shaking (1100 rpm). Then the resin was separated from the digest using a filter column, and washed with BBS (25 mM sodium borate, 25 mM NaCl, 0.5 mM EDTA, pH 8.0) three times. The digest was combined with the washes and the buffer was exchanged completely for BBS using diafiltration columns (4 × 15 mL, GE Healthcare, 10000 MWCO) to remove impurities. This yielded native CTX Fab **41** (373 µg, 54% yield) as confirmed by SDS-PAGE. Concentration was determined photometrically using ε_{280} = 70000 $M^{-1} \cdot cm^{-1}$.

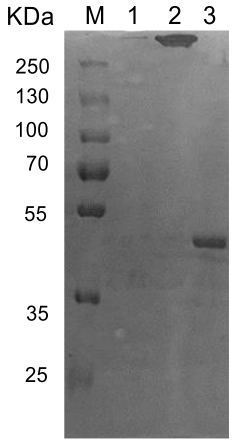

Figure 61. SDS-PAGE gel after digestion of Cetuximab antibody. **M)** Molecular weight marker. **1)** Empty. **2)** Cetuximab native antibody **40**. **3)** Native CTX Fab **41**.

CTX Fab [disulfide]

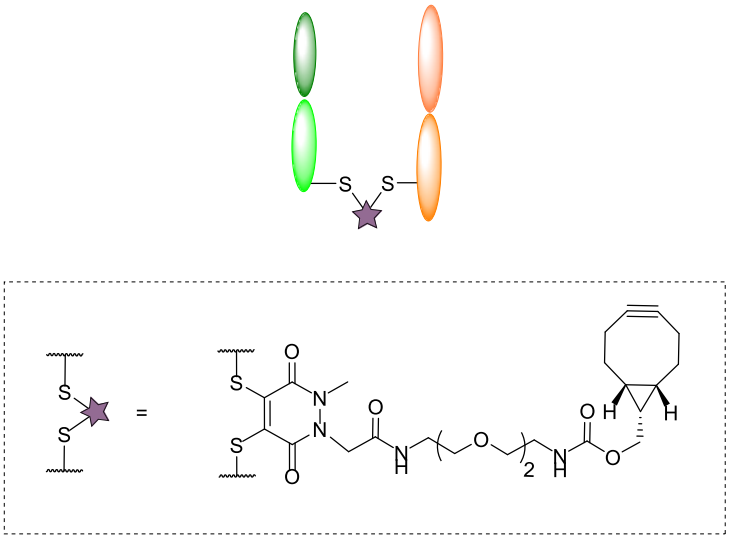

To a solution of CTX Fab **41** (50 µL, 20 µM, 1 eq.) in BBS (25 mm sodium borate, 25 mm NaCl, 1 mm EDTA, pH 8.0 + 3% DMSO) was added diBrMestra **35** (0.5 µL, 20 mM in DMSO, 10 eq.), followed by TCEP (0.25 µL, 20 mM in BBS pH = 8, 5 eq.) and the reaction mixture incubated at 21 °C for 2 h. The excess reagents were then removed by repeated diafiltration into fresh buffer using VivaSpin sample concentrators (GE Healthcare, 10,000 MWCO). Following this, analysis by SDS-PAGE and UV-Vis revealed > 95% conversion to CTX Fab [disulfide].

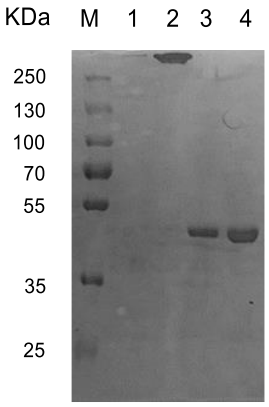

Figure 62. SDS-PAGE gel for Cetuximab Fab fragment modification. **M)** Molecular weight marker. **1)** Empty. **2)** Native Cetuximab Antibody. **3)** Native CTX Fab. **4)** *In situ* reduction of CTX Fab and reaction with pyridazinedione **35** at 21 °C (10 eq.).

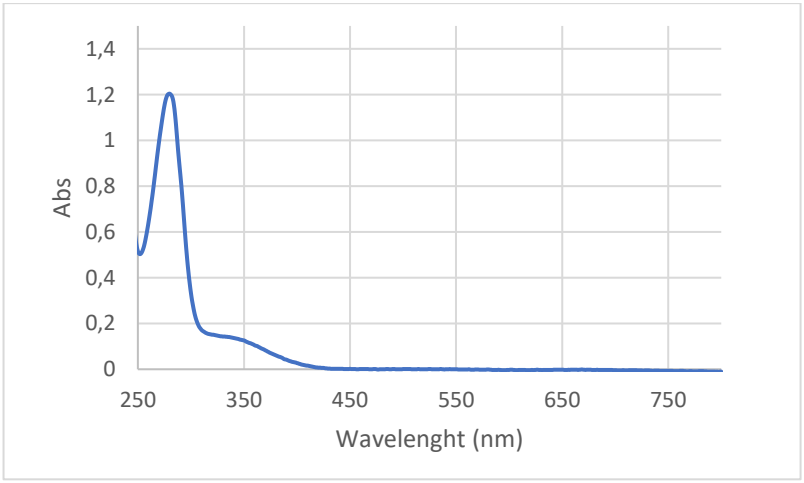

Figure 63. UV-Vis data for CTX Fab [disulfide], Pyridazinedione-to-antibody ratio (PAR) ≈ 0.95.

CTX Fab [disulfide] Alexafluor

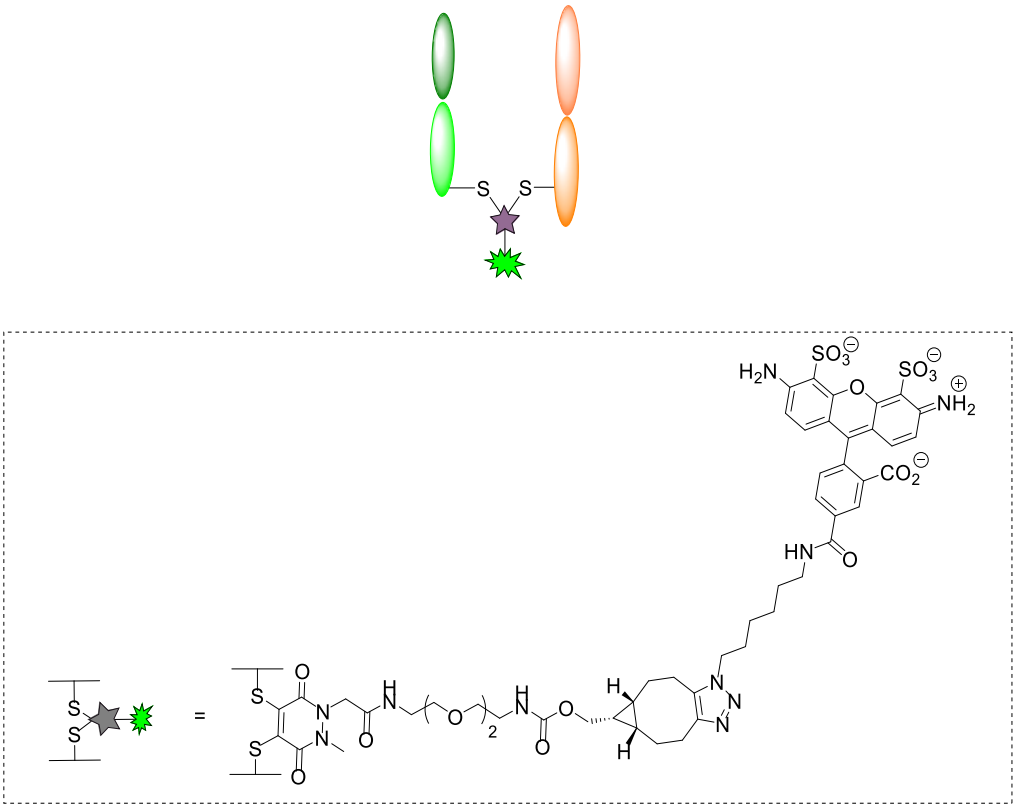

To a solution of CTX Fab [disulfide] (50 µL, 20 µM, 1 eq.) in BBS (+3% DMSO) was added Alexafluor®-488-N_3 **37** (0.2 µL, 20 mM in DMSO, 4 eq.) and the reaction mixture incubated at 21 °C for 2 h. The excess reagents were then removed by repeated diafiltration into fresh buffer using VivaSpin sample concentrators (GE Healthcare, 5,000 MWCO). Successful conjugation of fluorophore was confirmed by SDS-PAGE analysis.

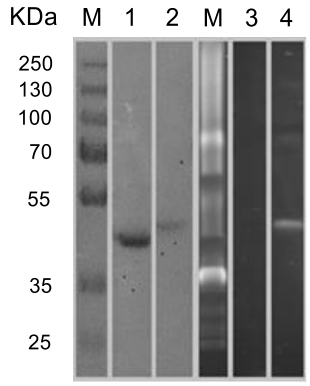

Figure 64. SDS-PAGE gel for Cetuximab Fab click**: M)** Molecular weight marker. **1)** CTX Fab [disulfide] control stained gel. **2)** CTX Fab [disulfide] reacted with Alexafluor®-488-N_3 **37** stained gel. **3)** CTX Fab [disulfide] control, under UV lamp. **4)** CTX Fab [disulfide] reacted with Alexafluor®-488-N_3 **37,** under UV lamp.

PEG-PLGA nanoparticle stability

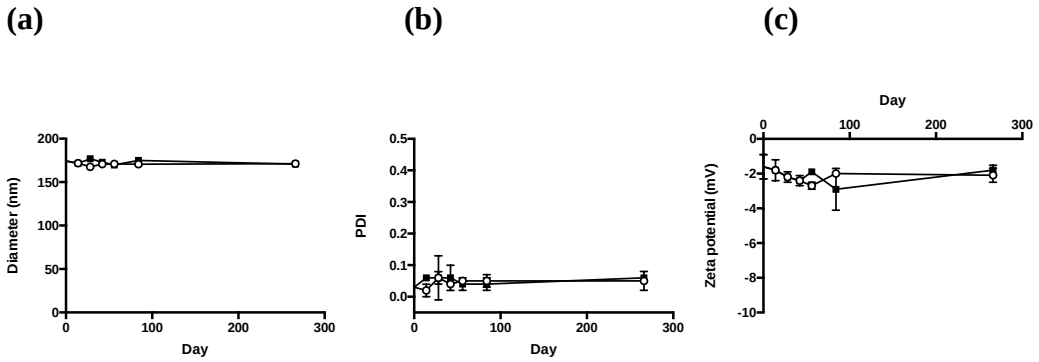

Figure 65. Stability assessment of nude azide NP. Aliquots of nude azide NP were stored at + 4^{o}C or - 20^{o}C. Nanoparticle **(a)** diameter, **(b)** PDI and **(c)** zeta potential were measured at various timepoints post-formulation, ranging from 14 to 266 days. Data expressed as mean ± SD.

Nanoparticle formulation

Polymer blends consisting of 5 mg PLGA-PEG-NHS (Akina AI064; MW ~ 17000:3000 Da) plus 15 mg PLGA RG502H (Evonik Industries), or 5 mg PLGA-PEG-azide (Akina Ai085; MW ~ 15000:5000 Da) plus 15 mg PLGA RG502H, were initially dissolved in 1 mL of dichloromethane (DCM). Nanoparticles were fluorescently labelled where required *via* addition of 100 uL of 2 mg/mL rhodamine 6G or 70 uL of 2 mg/mL nile red, both dissolved in DCM, to the organic phase. The organic phase was then injected into 7 mL of 2.5% w/v polyvinyl alcohol in 50 mM 2-(*N*-morpholino) ethanesulfonic acid (MES) hydrate buffer at pH 5, whilst stirring on ice. The emulsion was sonicated in pulse mode for 90 s on ice at an amplitude of 50% using a Model 120 sonic dismembrator (Fisher Scientific) and left stirring overnight to allow organic solvent evaporation. Nanoparticles were centrifuged at 17000 *x g* for 20 min at 4 °C and resuspended in 50 mM MES hydrate buffer at pH 5 *via* sonication. Following a further two centrifugation-resuspension cycles, nanoparticles were adjusted to 1 mg polymer/mL in 50 mM MES hydrate buffer at pH 5 prior to further manipulation.

Nanoparticle functionalisation

Equimolar amounts of native or modified Fab were added to NHS- or azide-functionalised nanoparticles resuspended at 1 mg polymer/mL in 50 mM MES hydrate buffer at pH 5, respectively (1050 pmol of Fab per mg polymer, unless otherwise indicated). After stirring at low speed for 2 h, nanoparticles were centrifuged at 12000 *x g* for 20 min at 4 °C and resuspended in PBS *via* sonication. This centrifugation-resuspension cycle was repeated to ensure removal of unbound Fab and nanoparticles were adjusted to the required concentration in PBS or water prior to downstream studies.

Nanoparticle characterisation

Nanoparticle size, zeta potential and polydispersity index (PDI) were analysed using a Zetasizer Nano ZS (Malvern Instruments). All measurements were performed following resuspension of nanoparticles at 1 mg polymer/mL in PBS. The bicinchoninic (BCA) protein assay (Thermo Fisher Scientific) was used to quantify

Fab attachment to nanoparticles, in accordance with the manufacturer's instructions. Fab content was determined by reference to standard curves, which were prepared by spiking known amounts of native or modified Fab into nude NHS NP or nude azide NP suspensions, respectively. Fab conjugation efficiency was calculated as follows:

$$Fab\ conjugation\ (\%) = \frac{\text{amount of Fab on NPs surface}}{\text{amount of Fab initially added to NPs}} * 100$$

In preparation for environmental scanning electron microscope (ESEM) studies, nanoparticles were resuspended at 5 mg polymer/mL in water and 4 μL droplets were dried overnight on double-sided copper tape fixed to aluminium stubs. Nanoparticles were then sputter-coated with gold and imaged using a Quanta 250 FEG ESEM (FEI) at 30,000x magnification.

Surface plasmon resonance (SPR)

SPR studies were performed on a Biacore Q instrument in HBS-EP running buffer (GE Healthcare) at 25°C. Recombinant human HER2 or EGFR Fc chimera protein (Sino Biological) was immobilised on a CM5 sensor chip (GE Healthcare), comprised of a surface matrix of carboxymethylated dextran that facilitated ligand coupling *via* carbodiimide chemistry. During immobilisation, carboxyl groups on the sensor chip surface were initially activated by injection of 0.4 M EDC and 0.1 M NHS. Ligand was then injected at 20 μg/mL in 10 mM sodium acetate buffer at pH 4.5, followed by quenching of residual NHS esters with 1 M ethanolamine hydrochloride at pH 8.5. All of the above solutions were injected for a total contact time of 7 min each at a flow rate of 10 μL/min, with typical immobilisation levels of approximately 12,000 resonance units (RU) per flow channel. Nanoparticles were resuspended at 10 mg polymer/mL in HBS-EP running buffer and injected over immobilised ligand for 15 s at a flow rate of 20 μL/min. HER2- and EGFR-coated chip surfaces were regenerated between samples with 50 mM or 25 mM sodium hydroxide, respectively, for 15 s at a flow rate of 20 μL/min. For SPR data presented in tabular or bar chart format, binding responses were calculated relative to baseline, by measuring the change in RU between two report points at 10 s before and 30 s following each injection. Representative sensorgrams show binding responses in absolute RU.

Fluorescence linked immunosorbent assay (FLISA)

High-binding black 96-well microplates (Greiner Bio-One) were coated with 0.5 μg/mL HER2 Fc chimera protein (Sino Biological) in PBS (100 μL per well) and incubated at 4 °C overnight. Excess protein was discarded and the wells were washed (3x) by immersion in 0.1% v/v Tween 20 in PBS (PBST). Non-specific binding sites were blocked with 1% w/v bovine serum albumin (BSA) in PBS (blocking buffer; 150 μL per well) for 1 h at 21 ºC, after which washing was repeated as before. Fluorescent rhodamine 6G-loaded nanoparticles ± TRAZ full antibody in blocking buffer (100 μL per well; concentrations stated in figure legends) were then added for 2 h at 21 ºC. Alternatively, microplates were pre-incubated with 20 μg/mL TRAZ full antibody in blocking buffer (100 μL per well) for 2 h at 21 ºC, followed by washing (3x) and nanoparticle addition for a further 2 h. Finally, wells were washed (8x), bound nanoparticles were dissolved in a 1:1 volume ratio of ACN:DMSO (50 μL per well) and fluorescence was measured at 530_{ex} / 590_{em} using a Synergy HT plate reader (BioTek).

Confocal microscopy

HCC1954 breast cancer cells were seeded at 30,000 per well on an eight-well glass culture slide (BD Falcon) and allowed to adhere overnight. Cells were stimulated with 400 μg polymer/mL nile red-loaded nanoparticles ± 200 μg/mL TRAZ full antibody for 18 h, washed in PBS (3×) and fixed with 4% w/v paraformaldehyde in PBS for 20 min. Following further washes in PBS (3×), cells were permeabilised with 0.5% v/v Triton X-100 in PBS for 5 min. Cells were then washed in PBS (3×) and coverslips were positioned following application of Vectashield antifade mounting medium with DAPI (Vector Laboratories). Slides were viewed on a SP5 confocal microscope (Leica Microsystems) equipped with LAS AF software. Images were captured with a x63 lens zoomed ×1-4, 1024 × 1024 frame and 100 Hz scanning speed.

CellTiter-Glo assay

BT474 breast cancer cells were seeded at 4000 per well on a white 96-well plate and allowed to adhere overnight. Cells were stimulated with 500 μg polymer/mL nude NHS NP, nude azide NP, native TRAZ Fab NP and modified TRAZ Fab NP

[disulfide]. Stimulations also included native TRAZ Fab and modified TRAZ Fab [disulfide] in free format, which were added at equimolar concentrations to the corresponding nanoformulations. The CellTiter-Glo luminescent cell viability assay (Promega) was performed immediately before and at 48, 96 and 144 h following stimulation, in accordance with the manufacturer's instructions. Luminescence values before stimulation were used as a baseline, from which the relative % change in cell number was calculated at subsequent timepoints.

Experimental for Chapter 3

Synthesis of compounds

Di-*tert*-butyl 1-methylhydrazine-1,2-dicarboxylate[151]

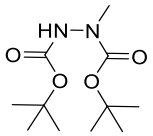

To a stirring solution of *N*-methylhydrazine **31** (157 mg, 3.42 mmol) in *i*-PrOH (4.3 mL) was added dropwise di-*tert*-butyl dicarbonate (1.6 g, 7.5 mmol, pre-dissolved in DCM (3.4 mL)) over 20 min. The mixture was then stirred for 16 h at 21 °C. After this time, solvent was removed *in vacuo* and purification by flash column chromatography (20% Et_2O/petrol) yielded di-*tert*-butyl 1-methylhydrazine-1,2-dicarboxylate (407 mg, 2.05 mmol, 60%) as a white solid: m.p. 58–62 °C (*lit m.p.* 54–56 °C). ^{1}H NMR (600 MHz, $CDCl_3$, rotamers) δ 6.55-6.10 (br s, 1H), 3.11 (s, 3H), 1.47 (s, 18H); ^{13}C NMR (150 MHz, $CDCl_3$, rotamers) δ 171.2 (C), 155.9 (C), 81.3 (C), 60.4 (CH_3), 28.3 (CH_3); IR (solid) 3316, 2978, 2932, 1701 cm^{-1}.

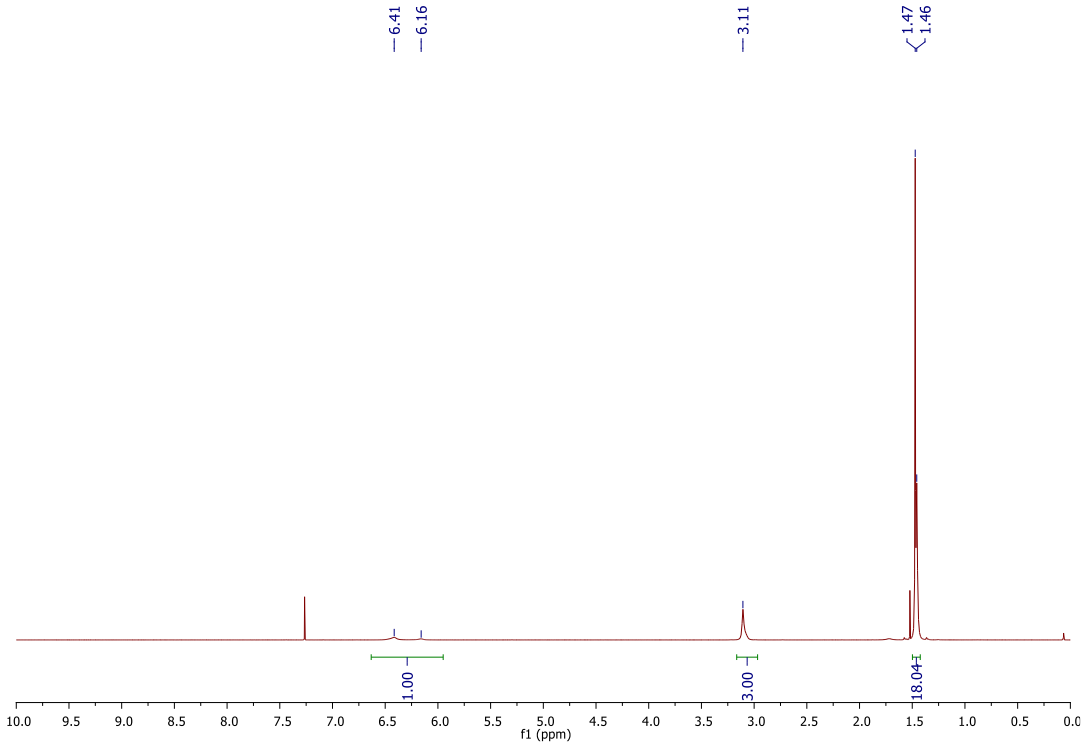
6.41
6.16
3.11
1.47
1.46
1.00
3.00
18.04
f1 (ppm)

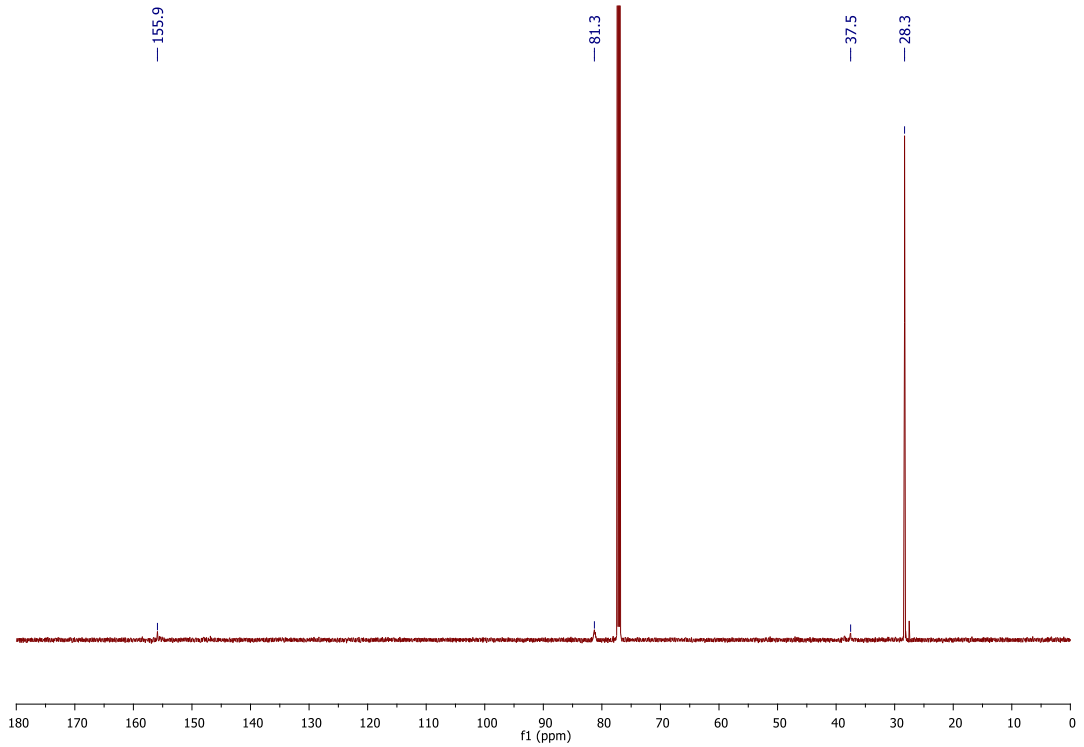
155.9
81.3
37.5
28.3
f1 (ppm)

Di-*tert*-butyl 1-(3-(tert-butoxy)-3-oxopropyl)-2-methylhydrazine-1,2-dicarboxylate[151] **43**

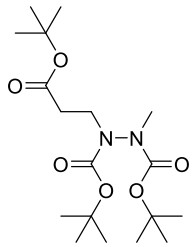

43

To a solution of di-*tert*-butyl 1-methylhydrazine-1,2-dicarboxylate (3.00 g, 12.2 mmol) in *t*-BuOH (5 mL), was added 10% NaOH (0.5 mL) and the reaction mixture stirred at 21 °C for 10 min. After this, *tert*-butyl acrylate (5.31 mL, 36.6 mmol) was added to the solution and the reaction mixture was heated at 60 °C for 24 h. Following this, the solvent was removed *in vacuo* and the crude residue was dissolved in EtOAc (150 mL) and washed with water (3 × 50 mL). The organic layer was then dried ($MgSO_4$) and concentrated *in vacuo*. Purification of the residue by flash column chromatography (0% to 20% EtOAc/petrol) afforded di-*tert*-butyl-1-(3-(*tert*-butoxy)-3-oxopropyl)-2-methylhydrazine-1,2-dicarboxylate **43** (2.24 g, 5.98 mmol, 49%) as a clear oil. ^{1}H NMR (600 MHz, $CDCl_3$, rotamers) δ 3.85–3.52 (m, 2H), 3.06–2.99 (m, 3H), 2.51 (t, J = 7.2 Hz, 2H), 1.48–1.43 (m, 27H). ^{13}C NMR (150 MHz, $CDCl_3$, rotamers) δ 171.0 (C), 155.4 (C), 154.4 (C), 81.0 (C), 44.6 (CH_3), 36.6 (CH_2), 34.1 (CH_2), 28.3 (CH_3). IR (thin film) 2976, 2933, 1709 cm^{-1}. LRMS (ESI) 375 (100, $[M+H]^+$), 319 (30, $[M-C_4H_9+2H]^+$. HRMS (ESI) calcd for $C_{18}H_{35}N_2O_6$ $[M+H]^+$ 376.2524; observed 376.2516.

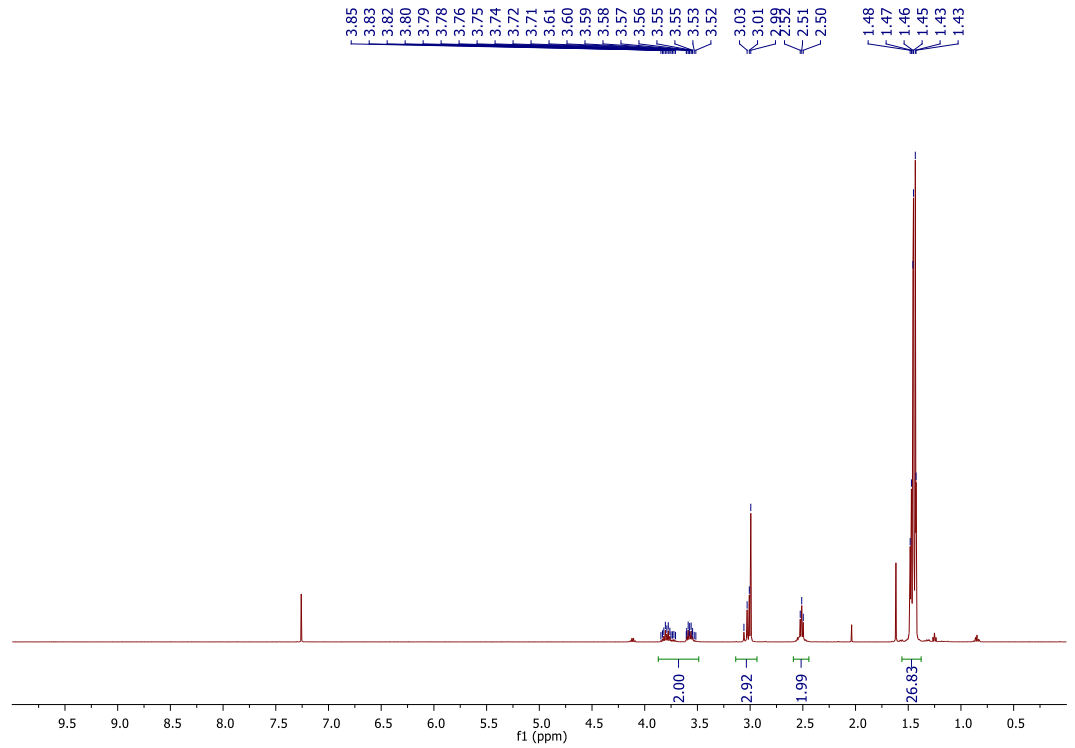
3.85
3.83
3.82
3.80
3.79
3.78
3.76
3.75
3.74
3.72
3.71
3.61
3.60
3.59
3.58
3.57
3.56
3.55
3.55
3.53
3.52
3.03
3.01
2.99
2.52
2.51
2.50
1.48
1.47
1.46
1.45
1.43
1.43
2.00
2.92
1.99
26.83
f1 (ppm)

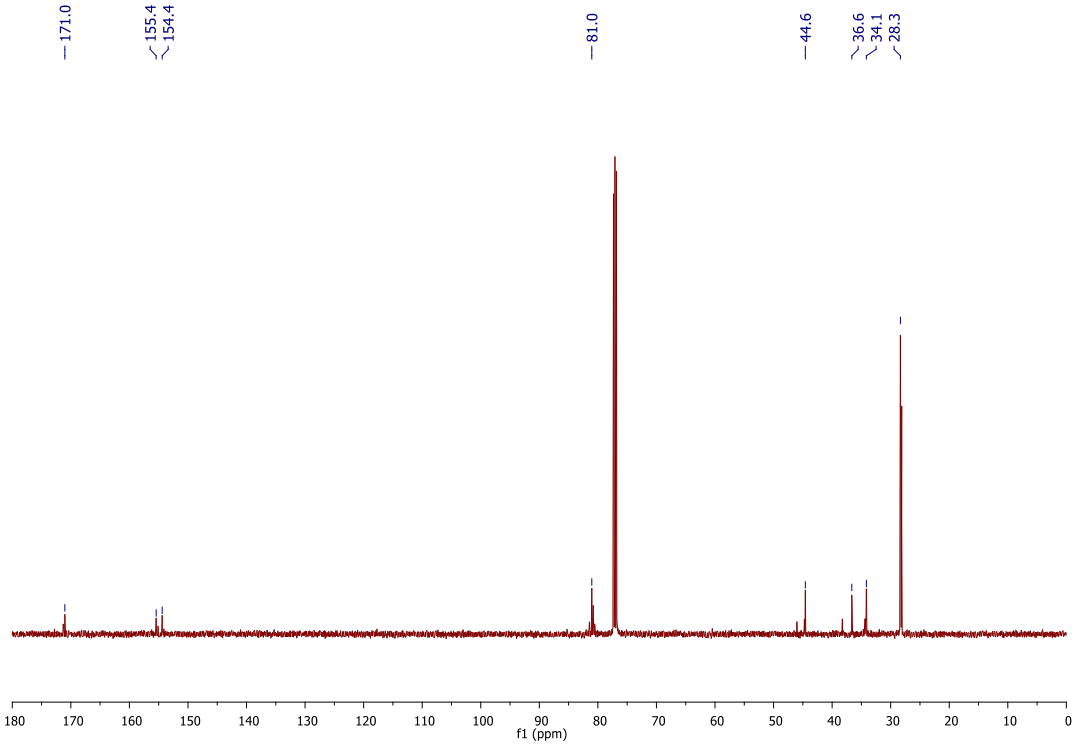
171.0
155.4
154.4
81.0
44.6
36.6
34.1
28.3
f1 (ppm)

3-(4,5-Dibromo-2-methyl-3,6-dioxo-3,6-dihydropyridazin-1(2*H*)-yl) propanoic acid[151] **44**

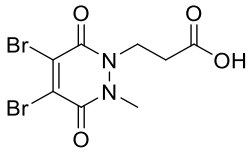

44

Dibromomaleic acid (4.93 g, 17.9 mmol) was dissolved in AcOH (25 mL) and heated under reflux for 30 min. To this solution, was added di-*tert*-butyl-1-(3-(*tert*-butoxy)-3-oxopropyl)-2-methylhydrazine-1,2-dicarboxylate **43** (5.60 g, 14.9 mmol) and the reaction heated under reflux for a further 4 h. After this time, the reaction mixture was concentrated *in vacuo* with toluene co-evaporation (3 × 30 mL, as an azeotrope) and the crude residue purified by flash column chromatography (50% to 100% EtOAc/petrol (1% AcOH)) to afford 3-(4,5-dibromo-2-methyl-3,6-dioxo-3,6-dihydropyridazin-1(2*H*)-yl) propanoic acid **44** (3.41 g, 9.57 mmol, 64%) as a yellow solid. m.p. 140–144 °C ^{1}H NMR (600 MHz, DMSO-d_6) δ 4.28 (t, *J* = 7.3 Hz, 2H), 3.56 (s, 3H), 2.63 (t, *J* = 7.3 Hz, 2H). ^{13}C NMR (150 MHz, DMSO-d_6) δ 171.9 (C), 152.7 (C), 152.4 (C), 135.3 (C), 135.0 (C), 43.1 (CH_3), 34.7 (CH_2), 31.7 (CH_2). IR (solid) 3044, 1725, 1606, 1570 cm^{-1} LRMS (ESI). 359 (50, $[M^{81}Br^{81}Br+H]^+$) 357 (100, $[M^{79}Br^{81}Br+H]^+$), 355 (50, $[M^{79}Br^{79}Br+H]^+$). HRMS (ESI) calcd for $C_8H_9Br_2N_2O_4$ $[M^{79}Br^{81}Br+H]^+$ 358.8883; observed 358.8882.

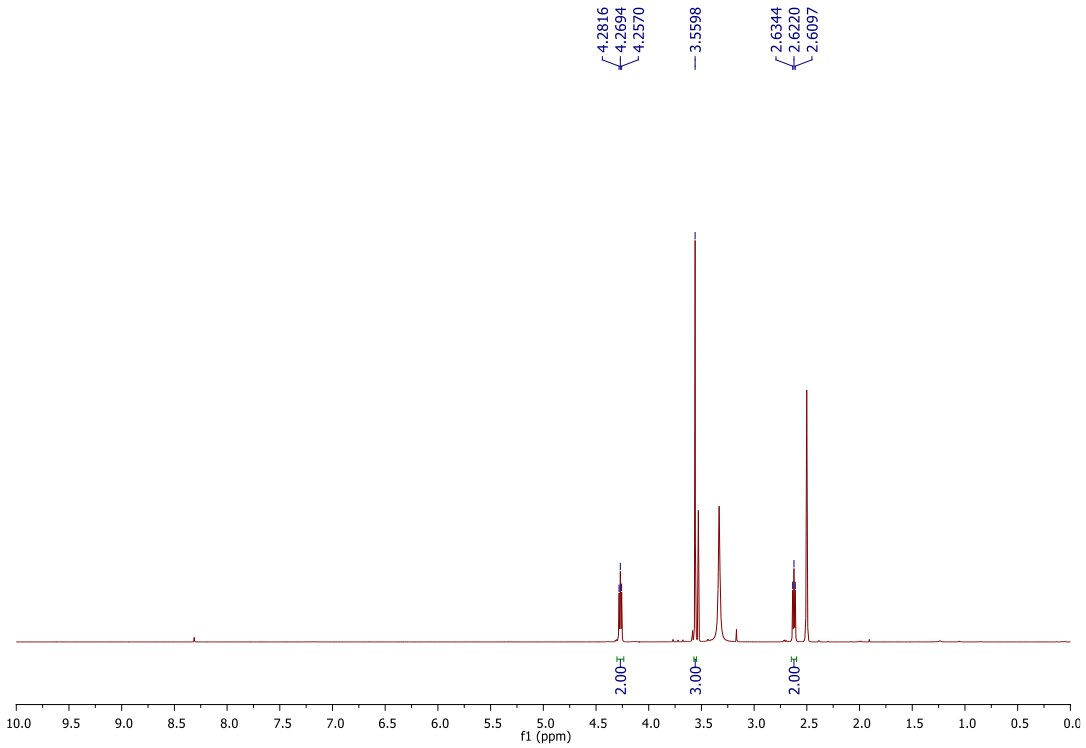
4.2816
4.2694
4.2570
3.5598
2.6344
2.6220
2.6097
2.00
3.00
2.00
f1 (ppm)

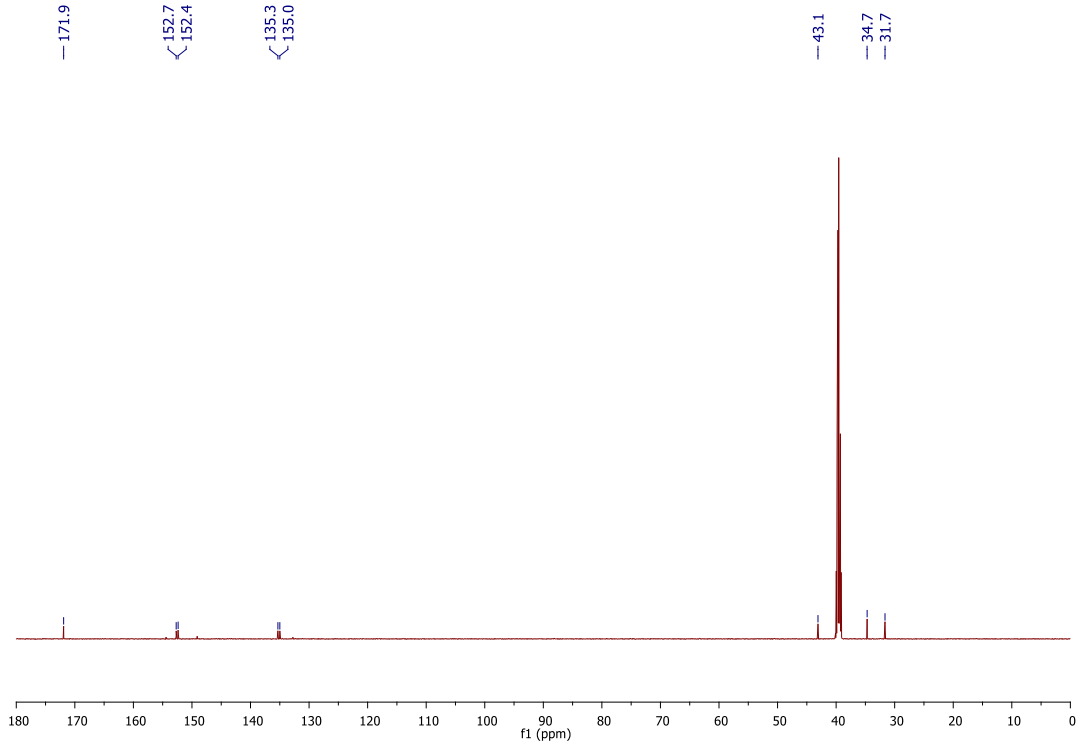
171.9
152.7
152.4
135.3
135.0
43.1
34.7
31.7
f1 (ppm)

2,5-Dioxopyrrolidin-1-yl 3-(4,5-dibromo-2-methyl-3,6-dioxo-3,6-dihydropyridazin-1(2*H*)-yl) propanoate[151] **45**

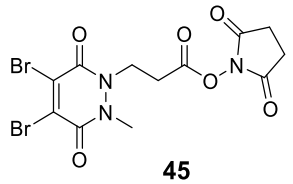

45

To a solution of 3-(4,5-dibromo-2-methyl-3,6-dioxo-3,6-dihydropyridazin-1(2*H*)-yl) propanoic acid **44** (750 mg, 2.13 mmol) in THF (10 mL), cooled to 0 °C, N,N'-dicyclohexylcarbodiimide (480 mg, 2.34 mmol) was added. The homogeneous solution was then stirred at 0 °C for 30 min. After this time, *N*-hydroxysuccinimide (89 mg, 0.78 mmol) was added and the reaction stirred at 21 °C for a further 16 h. The newly formed heterogenous mixture was then filtered and the filtrate concentrated *in vacuo*. Purification of the crude residue by flash column chromatography (20% to neat EtOAc/petrol) afforded 2,5-dioxopyrrolidin-1-yl 3-(4,5-dibromo-2-methyl-3,6-dioxo-3,6-dihydropyridazin-1(2*H*)-yl) propanoate **45** (511 mg, 1.13 mmol, 53%) as a white solid. m.p. 100–104 °C. ^{1}H NMR (600 MHz, $CDCl_3$) δ 4.48 (t, J = 6.9 Hz, 2H), 3.68 (s, 3H), 3.11 (t, J = 6.9 Hz, 2H), 2.85 (s, 4H). ^{13}C NMR (150 MHz, $CDCl_3$) δ 168.7 (C), 166.0 (C), 153.3 (C), 153.1 (C), 136.9 (C), 135.3 (C), 43.0 (CH_2), 35.3 (CH_3), 29.1 (CH_2), 25.7 (CH_2). IR (solid) 2992, 1814, 1782, 1735, 1634, 1576 cm^{-1}.

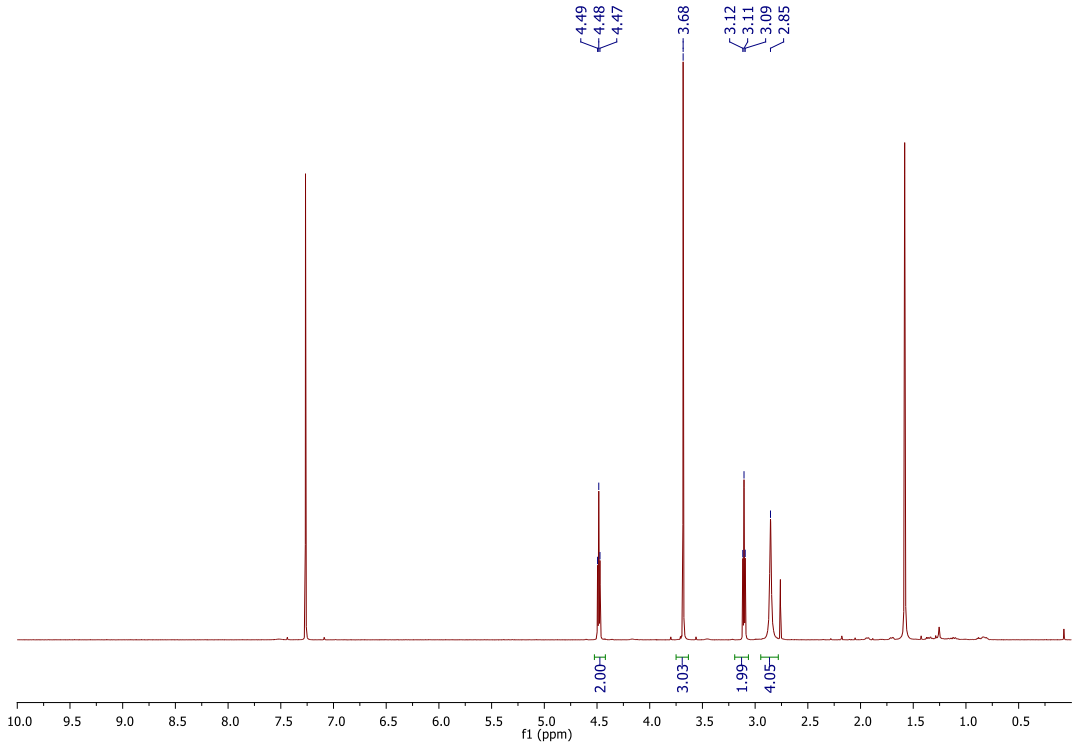
4.49
4.48
4.47
3.68
3.12
3.11
3.09
2.85
2.00
3.03
1.99
4.05
f1 (ppm)

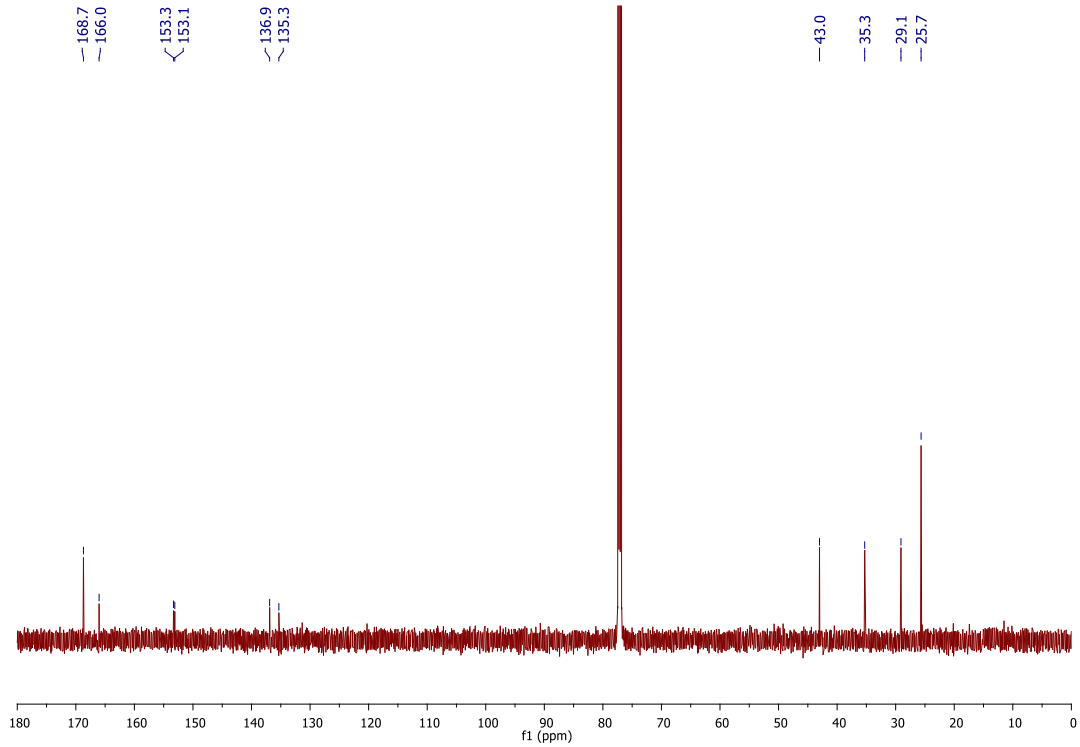
168.7
166.0
153.3
153.1
136.9
135.3
43.0
35.3
29.1
25.7
f1 (ppm)

((1*R*,8*S*,9*S*)-Bicyclo[6.1.0]non-4-yn-9-yl)methyl (2-(2-(2-(3-(4,5-dibromo-2-methyl-3,6-dioxo-3,6-dihydropyridazin-1(2*H*)-yl)propanamido)ethoxy)ethoxy)ethyl) carbamate[151] **46**

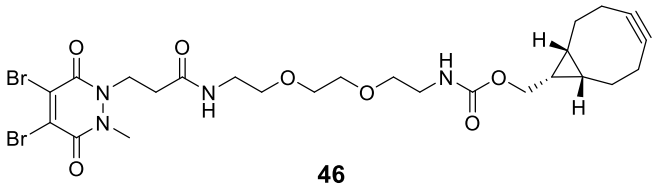

46

To a solution of 2,5-dioxopyrrolidin-1-yl 3-(2-bromo-2-methyl-3,6-dioxo-3,6-dihydropyridazin-1(2*H*)yl) propanoate **45** (132 mg, 0.200 mmol, pre-dissolved in MeCN (10 mL)), was added *N*-[(1*R*,8*S*,9*S*)-bicyclo[6.1.0]non-4-yn-9-ylmethyloxycarbonyl]-1,8-diamino-3,6-dioxaoctane **13** (71 mg, 0.220 mmol) and the reaction mixture was stirred at 21 °C for 16 h. After this time, the reaction mixture was concentrated *in vacuo* and the crude residue dissolved in $CHCl_3$ (10 mL) and washed with water (2 × 5 mL) and saturated aq. K_2CO_3 (10 mL). The organic layer was then dried ($MgSO_4$) and concentrated *in vacuo*. Purification of the crude residue by flash column chromatography (0% to 10% MeOH/EtOAc) afforded ((1*R*,8*S*,9*S*)-Bicyclo[6.1.0]non-4-yn-9-yl)methyl (2-(2-(2-(3-(4,5-dibromo-2-methyl-3,6-dioxo-3,6-dihydropyridazin-1(2*H*)-yl)propanamido)ethoxy)ethoxy)ethyl) carbamate **46** (105 mg, 0.160 mmol, 72%) as a yellow oil: ^{1}H NMR (600 MHz, $CDCl_3$, rotamers) δ 7.84 (s, 0.5H), 6.34 (s, 0.5H), 5.82 (s, 0.5H), 5.29 (s, 0.5H), 4.44 (t, *J* = 6.6 Hz, 2H), 4.14–4.12 (m, 2H), 3.73–3.71 (m, 3H), 3.60–3.38 (m, 12H), 2.62 (t, *J* = 6.6 Hz, 2H), 2.29-2.22 (m, 6H), 1.61–1.57 (m, 2H), 1.39–1.24 (m, 1H), 0.96–0.94 (m, 2H); ^{13}C NMR (150 MHz, $CDCl_3$, rotamers) δ 169.1 (C), 156.9 (C), 153.1 (C), 153.0 (C), 136.4 (C), 135.5 (C), 98.9 (C), 70.4 (CH_2), 70.3 (CH_2), 69.7 (CH_2), 63.0 (CH_2), 44.6 (CH_2), 40.8 (CH_2), 39.5 (CH_2), 35.1 (CH_3), 34.1 (CH_2), 29.3 (CH_2), 29.2 (CH_2), 21.6 (CH_2), 20.2 (CH_2), 17.9 (CH), 14.3 (CH); IR (thin film) 3329, 2920, 2858, 1708, 1630, 1572, 1534 cm^{-1}; LRMS (ESI), 687 (50, $[M^{81}Br^{81}Br+Na]^+$) 685 (100, $[M^{79}Br^{81}Br+Na]^+$), 683 (50, $[M^{79}Br^{79}Br+Na]^+$), 663 (60, $[M^{79}Br^{81}Br+H]^+$); HRMS (ESI) calcd for $C_{25}H_{35}Br_2N_4O_7$ $[M^{79}Br^{81}Br+H]^+$ 663.0847; observed 663.0846.

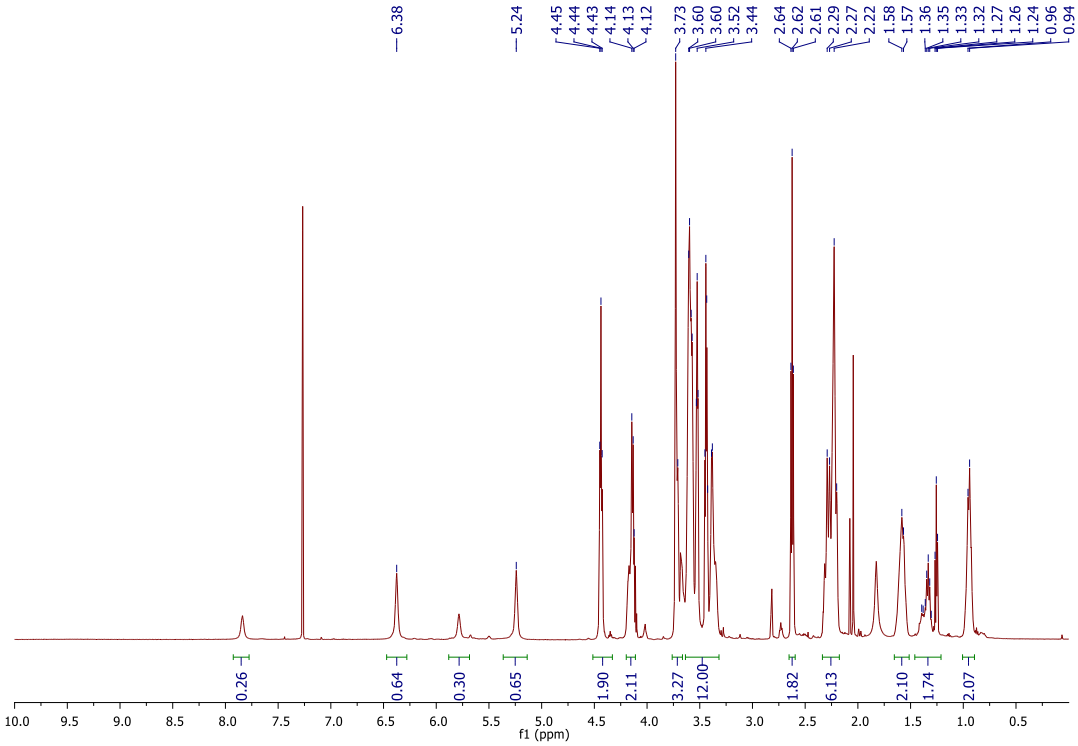
6.38
5.24
4.45
4.44
4.43
4.14
4.13
4.12
3.73
3.60
3.60
3.52
3.44
2.64
2.62
2.61
2.29
2.27
2.22
1.58
1.57
1.36
1.35
1.33
1.32
1.27
1.26
1.24
0.96
0.94
0.26
0.64
0.30
0.65
1.90
2.11
3.27
12.00
1.82
6.13
2.10
1.74
2.07
f1 (ppm)

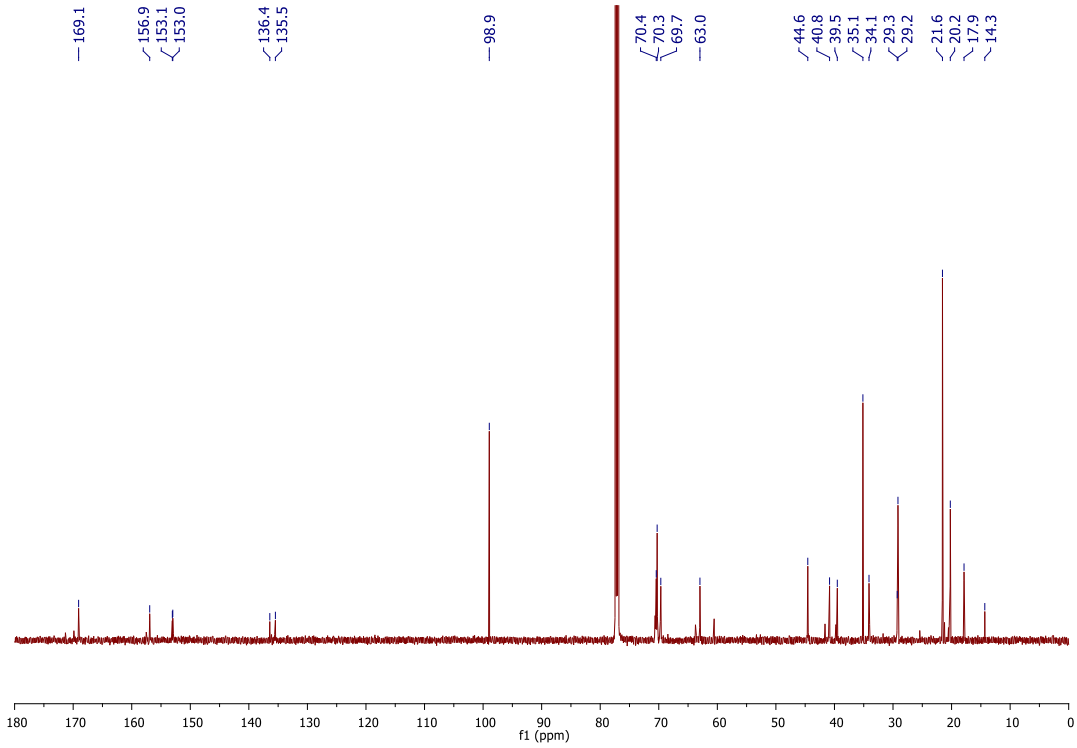
169.1
156.9
153.1
153.0
136.4
135.5
98.9
70.4
70.3
69.7
63.0
44.6
40.8
39.5
35.1
34.1
29.3
29.2
21.6
20.2
17.9
14.3
f1 (ppm)

Chemical biology

Native CTX Fab **41** (Alternative digestion protocol)

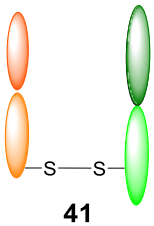

41

Cetuximab **40** (10 mg, 10 mg/mL) was digested with 1 mL of immobilized papain beads (Cetuximab/papain ratio 40:1) in a digest buffer (20 mM sodium phosphate monobasic, 10 mM EDTA, and 80 mM cysteine·HCl, pH = 7) for 4 h at 37 °C. Subsequently, the reaction mixture was centrifuged at 10,000 rpm for 1 min to remove the immobilized papain. The reaction mixture containing Cetuximab Fab **41** was subsequently purified by passing through a Protein A column. The concentration and purity of Cetuximab Fab was evaluated by UV/Vis spectroscopy (ε_{280} = 68,590 $M^{-1}\cdot cm^{-1}$) and SDS-PAGE (see characterisation for CTX Fab Mepstra **47**). The molecular weight of CTX Fab **41** was determined by LC-MS. Observed mass: 49788 Da. Glycosylation results in heterogeneous populations of CTX Fab **41**, visible by LC-MS.

Protein A purification

Crude sample was applied to a NAb protein A column (Thermo Scientific) and incubated at 20 °C with end-over-end mixing for 10 min. The Fab fraction, CTX Fab, was eluted three times with Pierce™ Protein A Binding Buffer, the column washed three times with Pierce™ Protein A binding buffer. The Fc fraction, CTX Fc, was eluted four times with Pierce™ IgG elution buffer, which was neutralised with Tris buffer (1 M, pH 8.5, 10% of eluted volume). The Fab fraction was combined with the washes and both Fab and Fc solutions were buffer exchanged into BBS (37 mM, pH 8.0, 2mM EDTA).

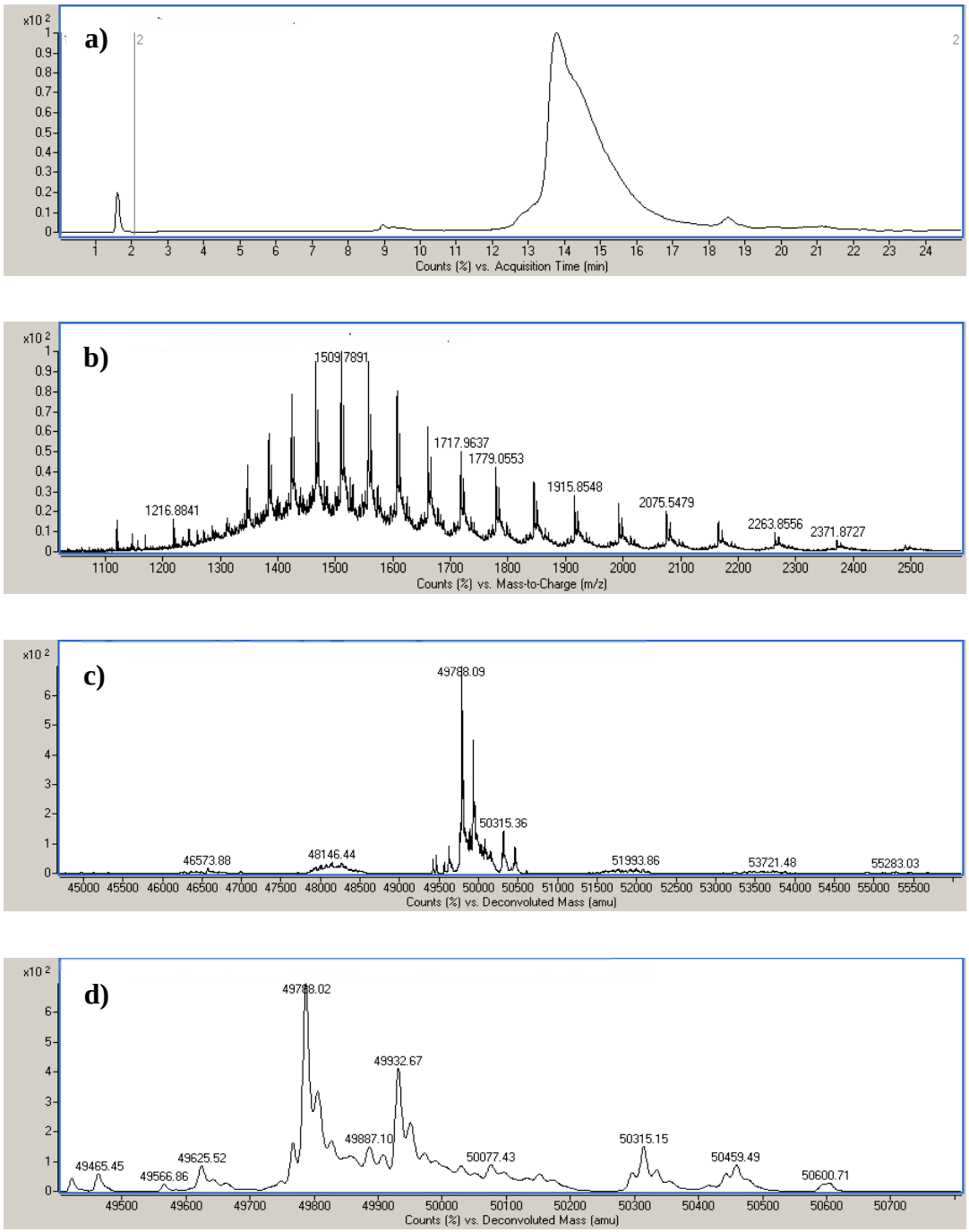

Figure 66. (a) TIC, **(b)** non-deconvoluted LC-MS trace, **(c)** deconvoluted MS data for CTX Fab **41**, **(d)** zoom in of deconvoluted MS data for CTX Fab **41** after Protein A purification, highlighting the N-Glycan residues present in the Fab fragment (M+145 Da, M+528 Da, M+671 Da).

CTX Fab Mepstra **47**

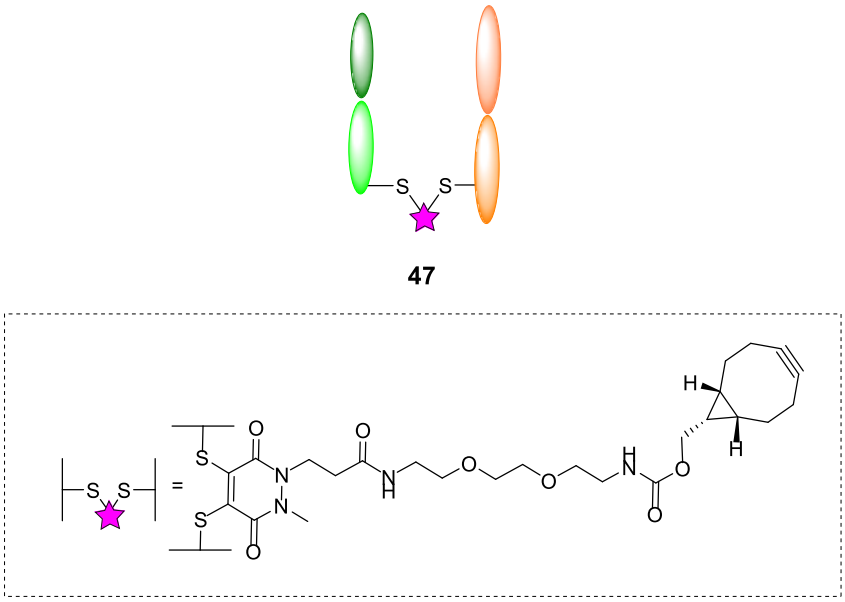

47

To a solution of Cetuximab Fab **41** (50 µL, 20 µM, 1 eq.) in BBS (25 mm sodium borate, 25 mm NaCl, 1 mm EDTA, pH 8.0 + 3% DMSO) was added PD **46** (1 µL, 20 mM in DMSO, 20 eq.), followed by TCEP (1 µL, 20 mM in BBS pH = 8, 20 eq.) and the reaction mixture incubated at 21 °C for 16 h. The excess reagents were then removed by repeated diafiltration into fresh buffer using VivaSpin sample concentrators (GE Healthcare, 10,000 MWCO). Following this, analysis by SDS-PAGE, LC-MS and UV-Vis revealed > 95% conversion to CTX Fab Mepstra **47**. Expected mass: 50,290 Da. Observed mass: 50,288 Da. Glycosylation results in heterogeneous populations of CTX Fab Mepstra **47**.

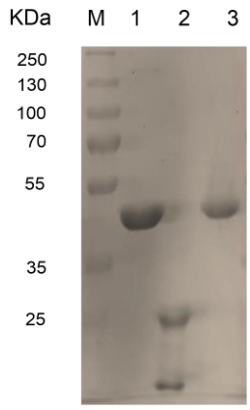

Figure 67. SDS-PAGE gel for successful formation of CTX Fab Mepstra **47: M)** Molecular weight marker. **1)** CTX Fab **41**. **2)** CTX Fab reduced control (20 eq. TCEP). **3)** CTX Fab Mepstra **47.**

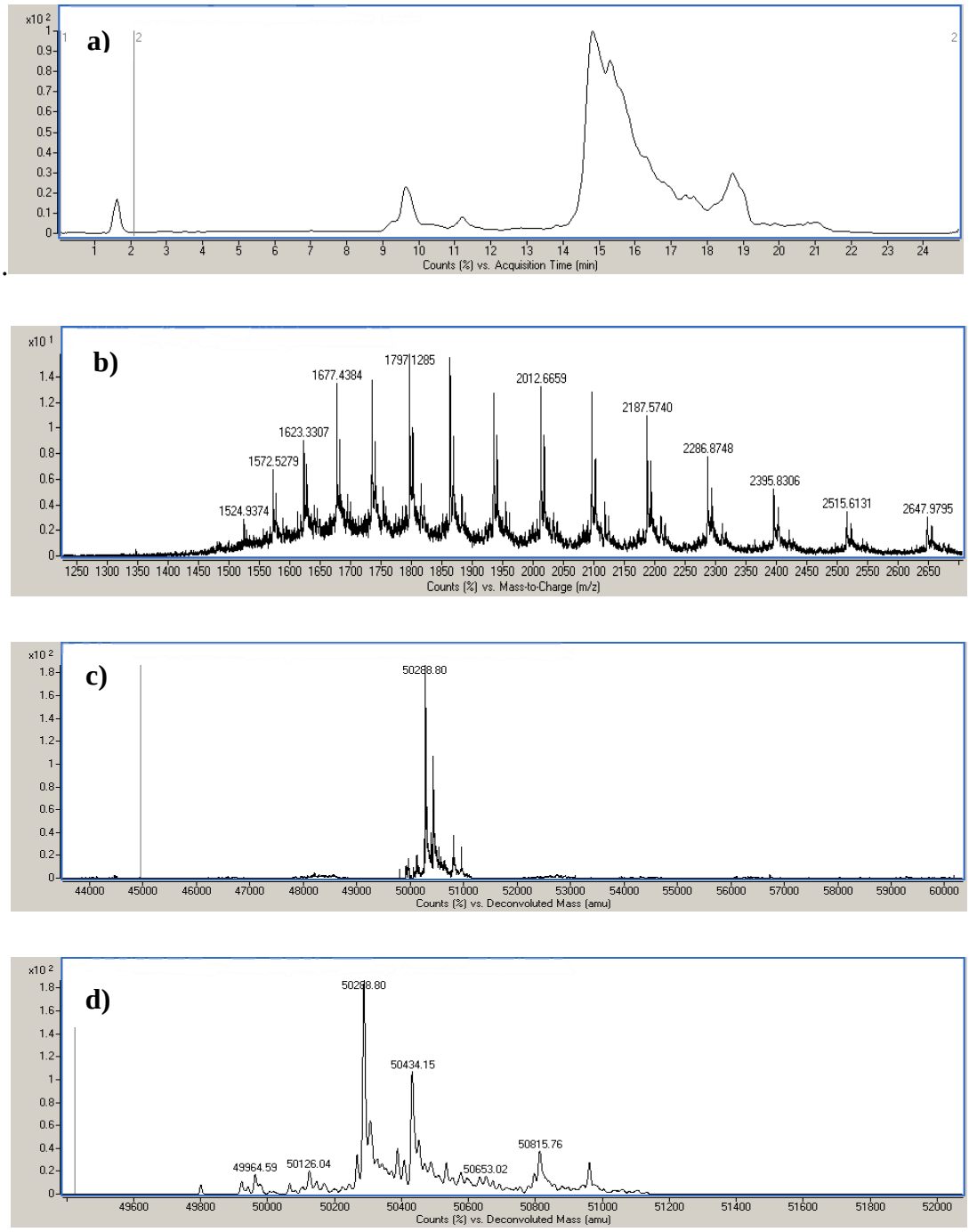

Figure 68. (a) TIC, **(b)** non-deconvoluted LC-MS trace, **(c)** deconvoluted MS data for CTX Fab Mepstra **47** and **(d)** zoom in of deconvoluted MS data for CTX Fab Mepstra **47**, confirming the presence of N-Glycan residues in the modified Fab fragment (M+145 Da, M+528 Da, M+671 Da).

CTX Fab Mepstra Alexafluor **48**

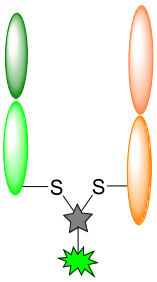

48

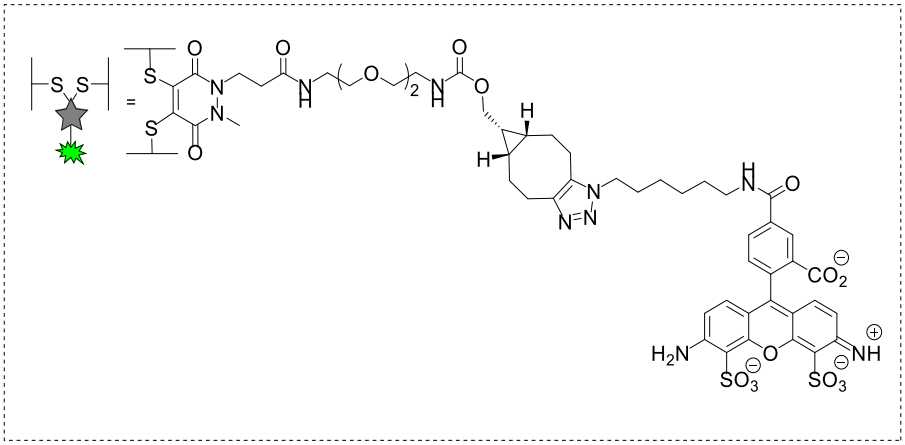

To a solution of CTX Fab Mepstra **47** (50 µL, 20 µM, 1 eq.) in PBS (pH = 7.4) was added Alexafluor®-488-N_3 **37** (0.2 µL, 20 mM in DMSO, 4 eq.) and the reaction mixture incubated at 21 °C for 2 h. The excess reagents were then removed by repeated diafiltration into fresh buffer using VivaSpin sample concentrators (GE Healthcare, 5,000 MWCO). Successful conjugation was confirmed by SDS-PAGE, UV-Vis analysis and LC-MS. Expected mass: 50,946 Da. Observed mass: 50,946 Da. Glycosylation results in heterogeneous populations of CTX Fab Mepstra Alexafluor **48**.

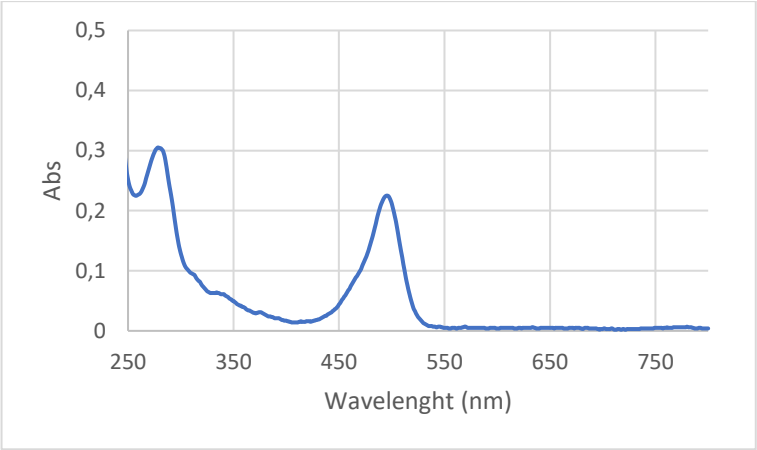

Figure 69. UV-Vis data for CTX Fab Mepstra Alexafluor **48**, FAR ≈ 0.8.

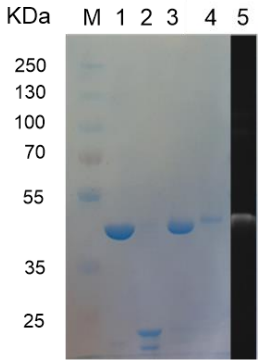

Figure 70. SDS-PAGE gel for successful formation of CTX Fab Mepstra Alexafluor **48: M)** Molecular weight marker. **1)** CTX Fab **41**. **2)** CTX Fab reduced control (20 eq. TCEP). **3)** CTX Fab Mepstra **47**. **4)** CTX Fab Mepstra Alexafluor **48**, under UV/Vis light.

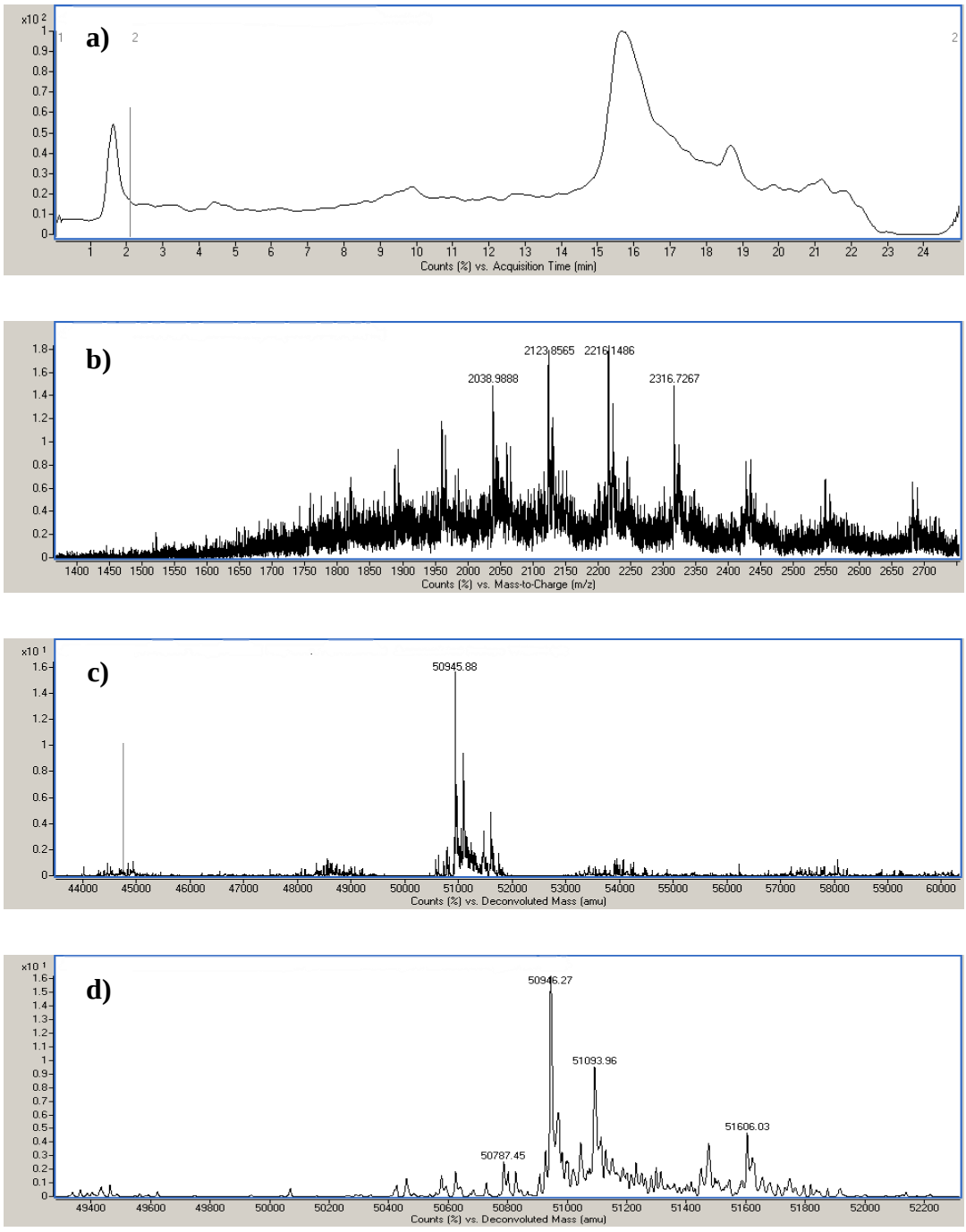

Figure 71. (a) TIC, **(b)** non-deconvoluted LC-MS trace, **(c)** deconvoluted MS data for CTX Fab Mepstra Alexafluor **48** and **(d)** zoom in of deconvoluted MS data for CTX Fab Mepstra Alexafluor **48**, confirming the presence of N-Glycan residues in CTX Fab Mepstra Alexafluor **48** (M+145 Da, M+528 Da, M+671 Da).

Protein Nanoparticle formulations

Nanoparticles were synthesised in 20 mg batches consisting of either **(1)** PLGA 502H, **(2)** a 3 : 1 blend of PLGA 502H : PLGA-PEG-NHS or **(3)** a 3 : 1 blend of PLGA 502H : PLGA-PEG-azide. All were prepared in accordance with Chapter 2. Where required, camptothecin was dissolved at 5 mg/mL in DMSO and 40 µL was added to the organic phase during nanoparticle synthesis.

Flow cytometry

PANC-1 and BxPC-3 cells were suspended at 1.6×10^5/mL in culture media and seeded on 6-well plates (2.5 mL/well). Following overnight adherence, cells were washed in PBS (2.5 mL/well) and incubated in EDTA solution (0.1% w/v in PBS; 0.5 mL/well) for 10 min at 37 ℃. Detached cells from each well were transferred into 1.5 mL microtubes, centrifuged at 200 × g for 5 min and suspended in culture media (1 mL/tube). After repeating this centrifugation-resuspension wash step, cells were incubated in culture media (1 mL/tube) containing 0.5 mg/mL nanoparticles for 1 hr at 4 ℃ under gentle agitation. Cells were then centrifuged at 200 × g for 5 min and incubated in FACS buffer (5% v/v FBS in PBS; 0.2 mL/tube) containing 5 µg/mL FITC-labelled anti-human EGFR or FITC-labelled anti-mouse IgG2a isotype control antibodies (both Santa Cruz Biotechnology) for 45 min at 4 ℃. Following the addition of FACS buffer (1 mL/tube), cells were centrifuged at 200 × g for 5 min and this wash cycle was then repeated. Cells were suspended in FACS buffer (0.5 mL/tube) prior to measurement of FITC fluorescence on a FACSCalibur flow cytometer (Becton Dickinson). FlowJo software was used to analyse a minimum of 30000 events per sample.

Clonogenic assay

MIA PaCa-2 and PANC-1 cells were seeded at 250000 per well on 6-well plates. Following overnight adherence, cells were chilled in cold media at 4 ℃ for 10 min and maintained under these conditions during subsequent treatments. Initially, cells were treated with PBS or 500 µg/mL free CTX full antibody for 15 min, followed by

the addition of 250 ng/mL (PANC-1) or 500 ng/mL (MIA PaCa-2) free CPT, or drug equivalents in nanoencapsulated format, for a further 45 min. Cells were then washed in PBS (5×) and incubated in fresh media at 37 ℃. On the following day, cells were detached from culture plasticware, seeded at 250 (MIA PaCa-2) or 500 (PANC-1) per well on 6-well plates and incubated at 37^{O}C for several days to allow colony formation. At study endpoint, cells were stained in crystal violet solution (0.4% w/v) for 10 min. Representative images are shown.

Binding of nanoparticles to EGFR-expressing cells

MIA PaCa-2 and PANC-1 cells were seeded at 10000 per well on black 96-well plates. Following overnight adherence, cells were chilled in cold media at 4 ℃ for 20 min and maintained under these conditions during subsequent treatment with rhodamine 6G-loaded nanoformulations at 600 µg polymer/mL (MIA PaCa-2) or 800 µg polymer/mL (PANC-1) for a further 30 min. Cells were then washed in PBS (3×) and lysed by adding 50 µL of Triton X-100 in 0.2 M NaOH to each well. Fluorescence was measured at 516_{ex} / 557_{em} nm using a Cytation 5 instrument (BioTek).

Experimental for Chapter 4

Synthesis of compounds

3-(Bromo-2-methyl-3,6-dioxo-3,6-dihydropyridazin-1(2*H*)-yl)propanoic acid **54**

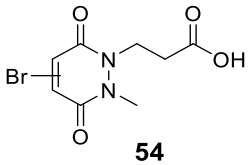

54

To a solution of di-*tert*-butyl-1-(3-(*tert*-butoxy)-3-oxopropyl)-2-methylhydrazine-1,2-dicarboxylate **43** (1.50 g, 4.01 mmol) in AcOH (20 mL) was added bromomaleic anhydride (0.41 mL, 4.41 mmol) and the reaction heated under reflux for 4 h. After this time, the reaction mixture was concentrated *in vacuo* with toluene co-evaporation (3 × 30 mL, as an azeotrope). The crude residue was then purified by flash column chromatography (0% to 10% MeOH/EtOAc (1% AcOH)) to afford an inseparable mixture of regioisomers 3-(4-bromo-2-methyl-3,6-dioxo-3,6-dihydropyridazin-1(2*H*)-yl)propanoic acid and 3-(5-bromo-2-methyl-3,6-dioxo-3,6-dihydropyridazin-1(2*H*)-yl)propanoic acid **54** (804 mg, 2.90 mmol, 72%) as a white solid. m.p. 142–145 °C. ^{1}H NMR (600 MHz, DMSO, regioisomers (2:1)) δ 7.59 (s, 1H), 7.58 (s, 1H), 4.28 (t, *J* = 7.4 Hz, 2H), 4.21 (t, *J* = 7.4 Hz, 2H), 3.58 (s, 3H), 3.50 (s, 3H), 2.62–2.57 (m, 4H). ^{13}C NMR (150 MHz, DMSO, regioisomers (1:1)) δ 172.0 (C), 171.9 (C), 155.4 (C), 155.1 (C), 153.5 (C), 153.2 (C), 135.8 (CH), 135.5 (CH), 132.8 (C), 132.3 (C) 42.7 (CH_2), 41.5 (CH_2), 34.2 (CH_3), 32.9 (CH_3), 31.8 (CH_2). IR (solid) 3058, 1722, 1619 cm^{-1}. LRMS (ESI) 277 (100, $[M^{79}Br+H]^+$), 279 (95, $[M^{81}Br+H]^+$), HRMS (ESI) calcd for $C_8H_{10}BrN_2O_4$ $[M^{79}Br+H]^+$ 276.9818; observed 276.9820.

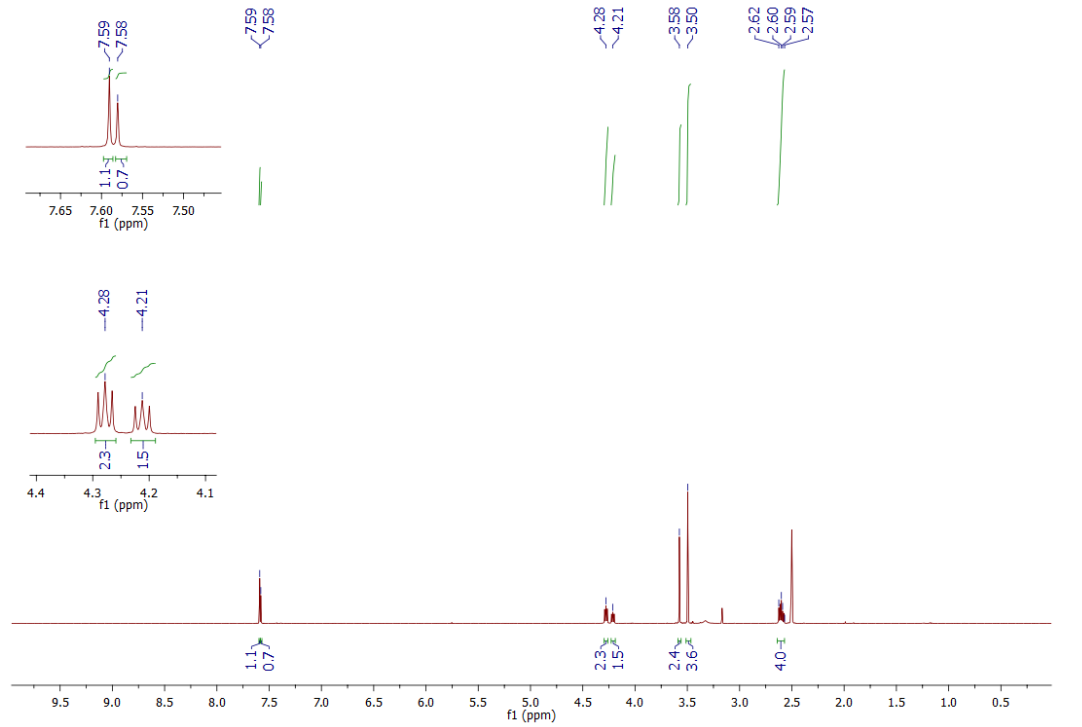
7.59
7.58
4.28
4.21
3.58
3.50
2.62
2.60
2.59
2.57
1.1
0.7
2.3
1.5
2.4
3.6
4.0
f1 (ppm)

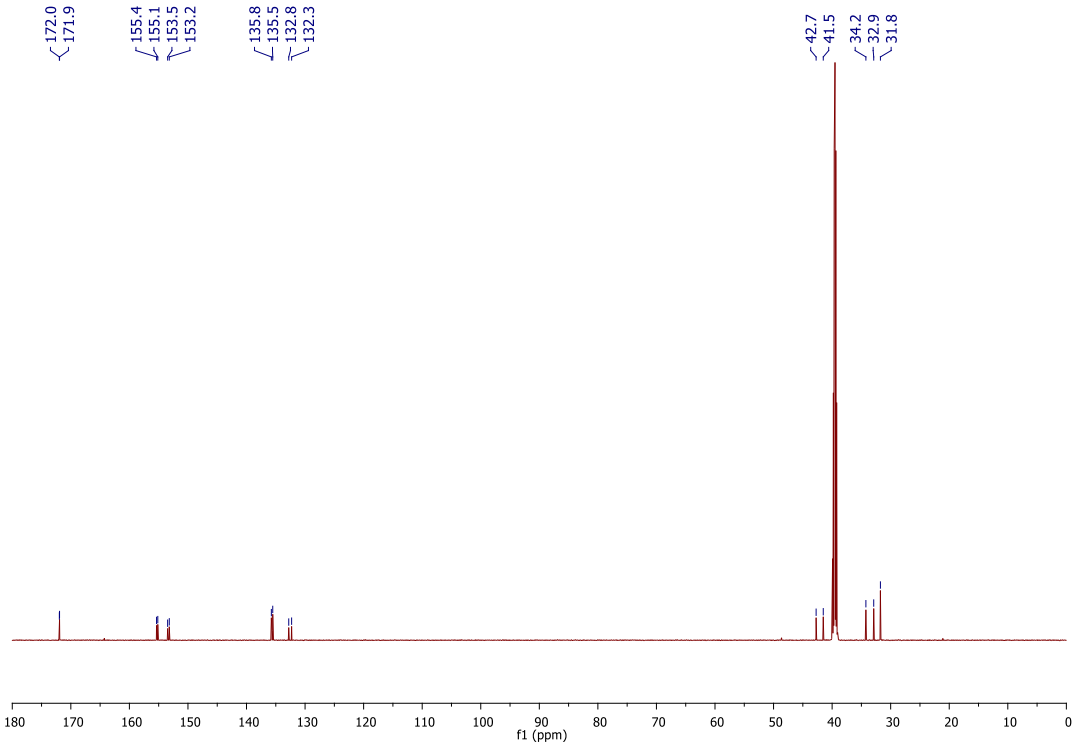
172.0
171.9
155.4
155.1
153.5
153.2
135.8
135.5
132.8
132.3
42.7
41.5
34.2
32.9
31.8
f1 (ppm)

2,5-Dioxopyrrolidin-1-yl 3-(4-bromo-2-methyl-3,6-dioxo-3,6-dihydropyridazin-1(2*H*)-yl)propanoate **55**

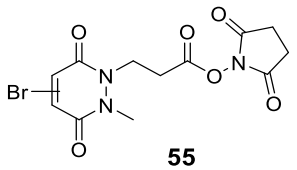

55

To a solution of 3-(bromo-2-methyl-3,6-dioxo-3,6-dihydropyridazin-1(2*H*)-yl) propanoic acid **54** (1.20 g, 4.33 mmol), in THF (10 mL), cooled to 0 °C, *N,N'*-dicyclohexylcarbodiimide (1.0 g, 4.85 mmol) was added. The homogeneous solution was then stirred at 0 °C for 30 min. After this time, *N*-hydroxysuccinimide (535 mg, 4.67 mmol) was added and the reaction was stirred at 21 °C for a further 16 h. The newly formed heterogenous mixture was then filtered and the filtrate concentrated *in vacuo*. Purification of the crude residue by flash column chromatography (50% to 100% EtOAc/petrol) afforded an inseparable mixture of regioisomers 2,5-dioxopyrrolidin-1-yl 3-(4-bromo-2-methyl-3,6-dioxo-3,6-dihydropyridazin-1(2*H*)-yl)propanoate and 2,5-dioxopyrrolidin-1-yl 3-(5-bromo-2-methyl-3,6-dioxo-3,6-dihydropyridazin-1(2*H*)-yl)propanoate **55** (1.0 g, 2.69 mmol, 62%) as a white powder. m.p. 140-145 °C. ^{1}H NMR (500 MHz, DMSO-d_6, regioisomers (2:1)) δ 7.34 (s, 1H), 7.31 (s, 1H), 4.42 (t, *J* = 7.2 Hz, 2H), 4.36 (t, *J* = 7.2 Hz, 2H), 3.62 (s, 3H), 3.55 (s, 3H), 3.06–3.01 (m, 4H), 2.79 (s, 8H). ^{13}C NMR (125 MHz, DMSO, regioisomers (1:1)) δ 170.0 (C), 166.7 (C), 155.4 (C), 155.2 (C), 153.5 (C), 153.3 (C), 135.9 (CH), 135.4 (CH), 133.0 (C), 132.1 (C), 41.7 (CH_2), 40.6 (CH_2), 34.3 (CH_3), 33.0 (CH_3), 28.5 (CH_2), 25.4 (CH_2). IR (solid) 2944, 1808, 1778, 1731, 1632, 1596 cm^{-1}. LRMS (ESI) 374 (100, $[M^{79}Br+H]^+$), 376 (95, $[M^{81}Br+H]^+$), HRMS (ESI) calcd for $C_{12}H_{12}BrN_3O_6$ $[M^{79}Br+H]^+$ 373.9988; observed 373.9979.

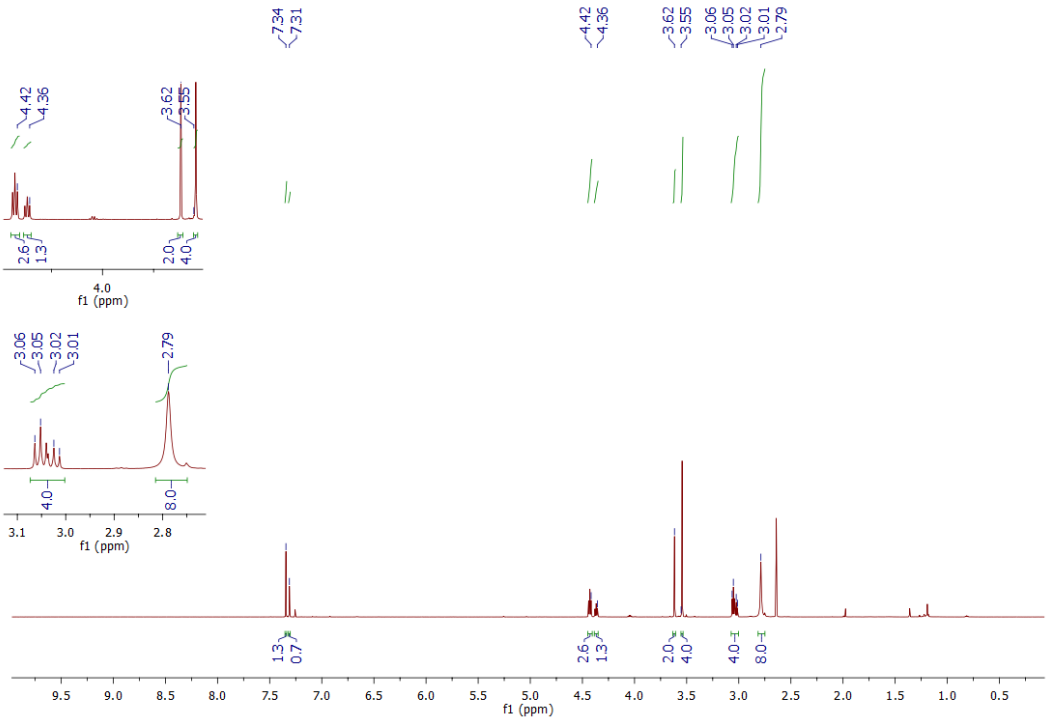
7.34
7.31
4.42
4.36
3.62
3.55
3.06
3.05
3.02
3.01
2.79
f1 (ppm)

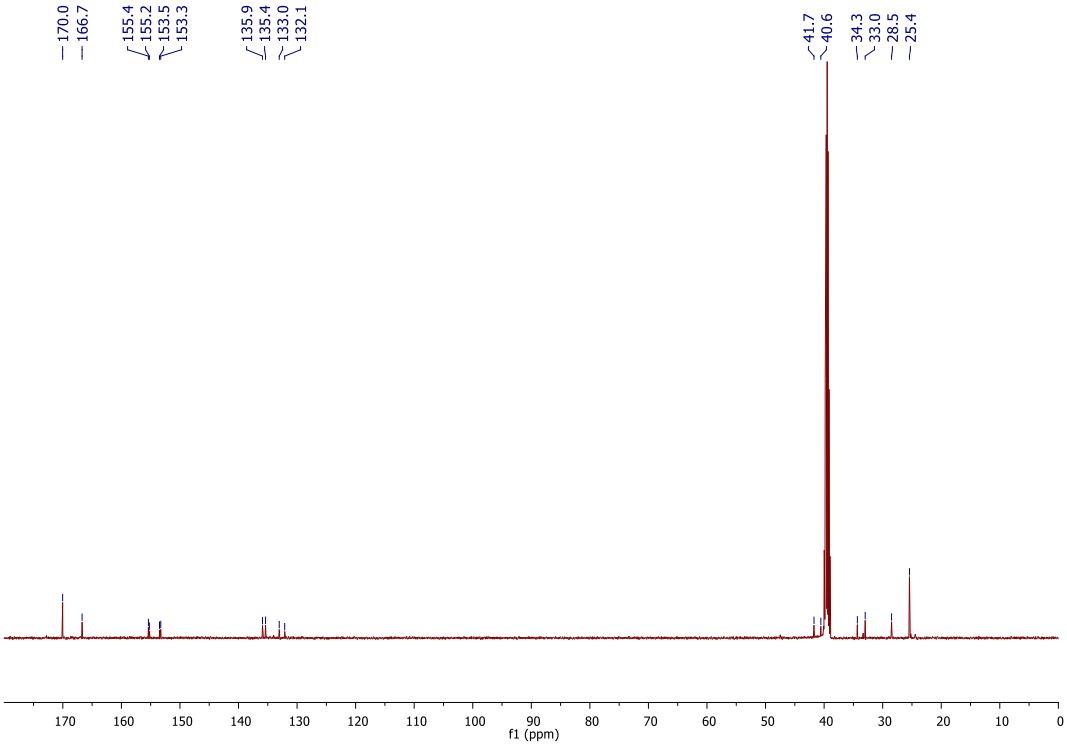
170.0
166.7
155.4
155.2
153.5
153.3
135.9
135.4
133.0
132.1
41.7
40.6
34.3
33.0
28.5
25.4
f1 (ppm)

((1*R*,8*S*,9*s*)-Bicyclo[6.1.0]non-4-yn-9-yl)methyl (2-(2-(2-(3-(4,5-dibromo-2-methyl-3,6-dioxo-3,6-dihydropyridazin-1(2*H*)-yl)propanamido)ethoxy)ethoxy)ethyl) carbamate **56**

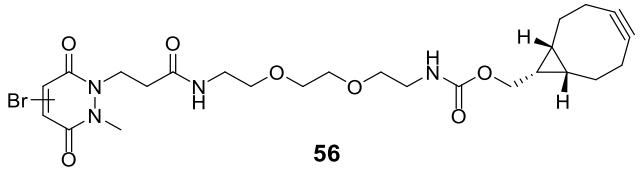

56

To a solution of 2,5-dioxopyrrolidin-1-yl 3-(bromo-2-methyl-3,6-dioxo-3,6-dihydropyridazin-1(2*H*)yl) propanoate **55** (50 mg, 0.110 mmol, pre-dissolved in MeCN (10 mL)), was added *N*-[(1*R*,8*S*,9*S*)-bicyclo[6.1.0]non-4-yn-9-ylmethyloxycarbonyl]-1,8-diamino-3,6-dioxaoctane **13** (31 mg, 0.122 mmol) and the reaction mixture was stirred at 21 °C for 16 h. to afford an inseparable mixture of regioisomers ((1*R*,8*S*,9*S*)-Bicyclo[6.1.0]non-4-yn-9-yl)methyl (2-(2-(2-(3-(bromo-2-methyl-3,6-dioxo-3,6-dihydropyridazin-1(2*H*)-yl)propanamido)ethoxy)ethoxy)ethyl) carbamate **56** (42 mg, 0.07 mmol, 52%) as a yellow oil: ^{1}H NMR (600 MHz, $CDCl_3$, regioisomers (1:1)) δ 7.86 (s, 0.5H), 7.80 (s, 0.5H), 7.38-7.36 (m, 2H), 6.42-6.39 (m,1H), 5.81-5.78 (m, 1H), 5.33 (s, 0.5H), 5.27 (m, 0.5H), 4.44 (t, *J* = 7.0 Hz, 2H), 4.37 (t, *J* = 7.0 Hz, 2H), 4.18-4.15 (m, 4H), 3.73-3.67 (m, 3H), 3.66-3.36 (m, 27H), 2.63-2.61 (m, 4H), 2.32-2.21 (m, 12H), 1.65-1.52 (m, 4H), 1.42-1.31 (m, 2H), 0.96-0.93 (m, 4H). ^{13}C NMR (150 MHz, $CDCl_3$, regioisomers (1:1)) δ 171.5 (C),168.9 (C), 156.9 (C), 155.9 (C), 139.4 (C), 136.1 (C), 135.7 (C), 98.9 (C), 70.7 (CH_2), 70.3 (CH_2), 69.7 (CH_2), 62.3 (CH_2), 60.6 (CH_2), 44.2 (CH_2), 43.4 (CH_2), 40.8 (CH_2), 39.5 (CH_2), 34.7 (CH_3), 34.0 (CH_2), 33.4 (CH_2), 33.1 (CH_2), 29.2 (CH_2), 21.6 (CH_2), 21.0 (CH_2), 20.2 (CH_2), 17.9 (CH), 14.3 (CH). IR (thin film) 3331, 2989, 2857, 1715, 1645, 1572, 1534 cm^{-1}. LRMS (ESI) 583 (95, $[M^{79}Br+H]^+$), 585 (100, $[M^{81}Br+H]^+$), HRMS (ESI) calcd for $C_{25}H_{35}BrN_4O_7$ $[M^{79}Br+H]^+$ 583.1714; observed 583.1763.

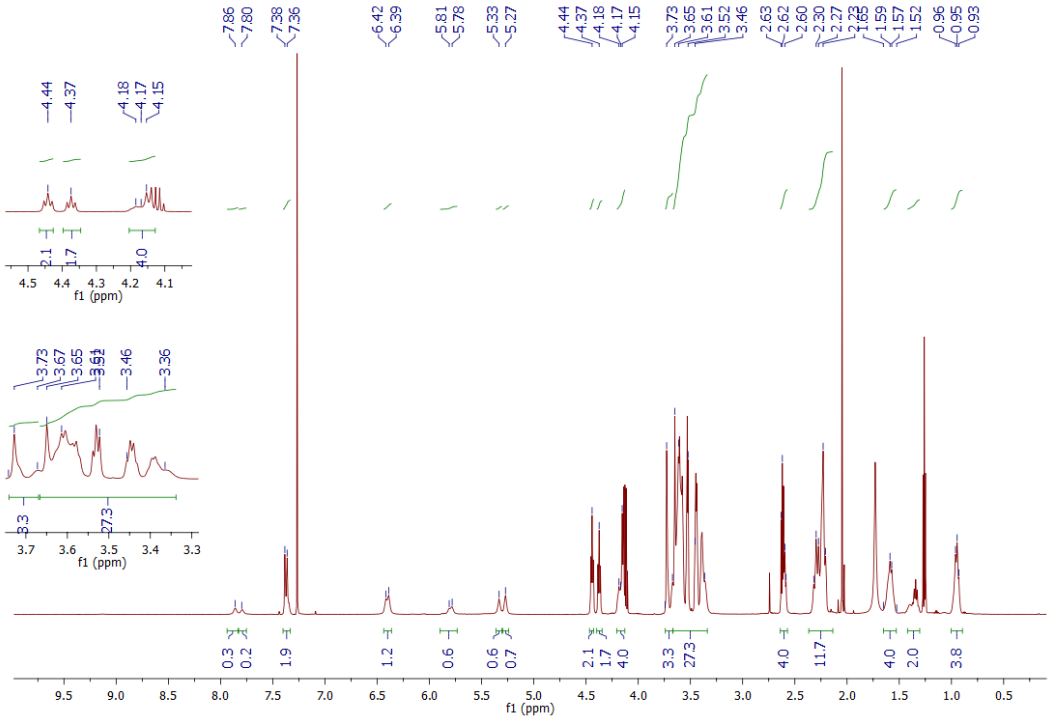

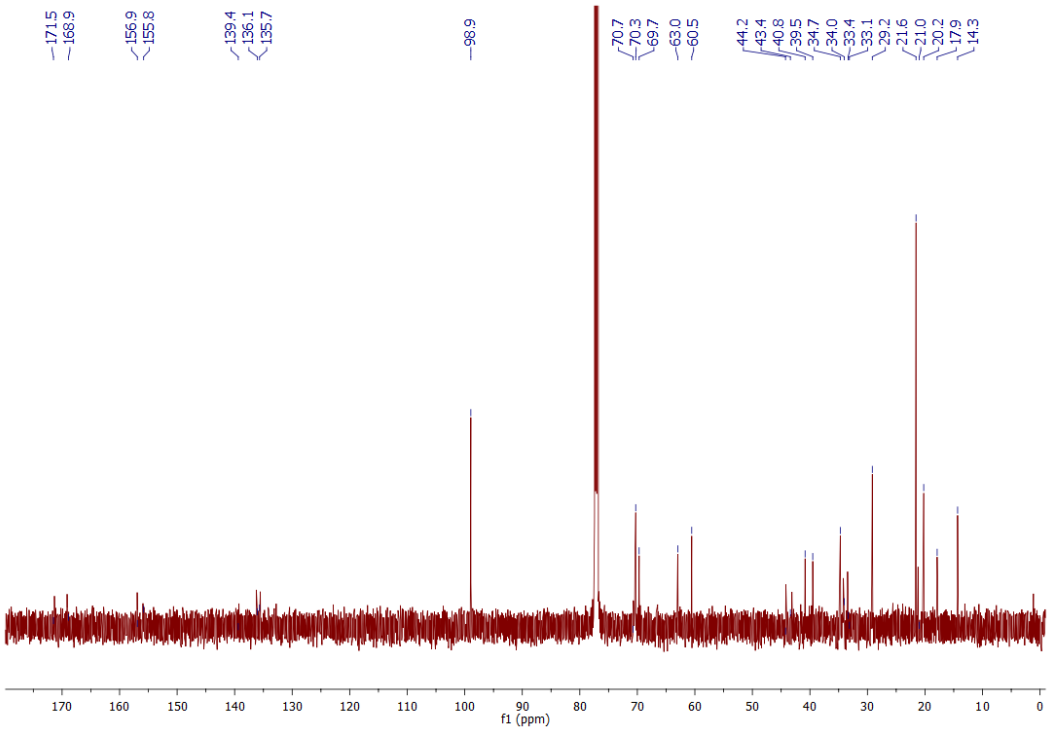

Chemical biology

V_{NAR} Clone E4 ACA version design and synthesis

The Alanine Cysteine Alanine (ACA) insertion in the C-terminal region of V_{NAR} E4 clone was designed in silico using DNASTAR® software. Flanking the V_{NAR} gene sequence *Nco*I and *EcoR*I restriction endonuclease sites as well as a poly-histidine (6×histidine) tag were incorporated to facilitate cloning into a prokaryotic expression and IMAC protein purification and immunodetection respectively (Figure 72). The in-house designed gene (Figure 72) was synthesised by PCR amplification of the V_{NAR} E4 DNA template using oligonucleotides #249_Forward and #256_Reverse using 2×Phusion High-Fidelity PCR Master Mix (New England Biolabs).

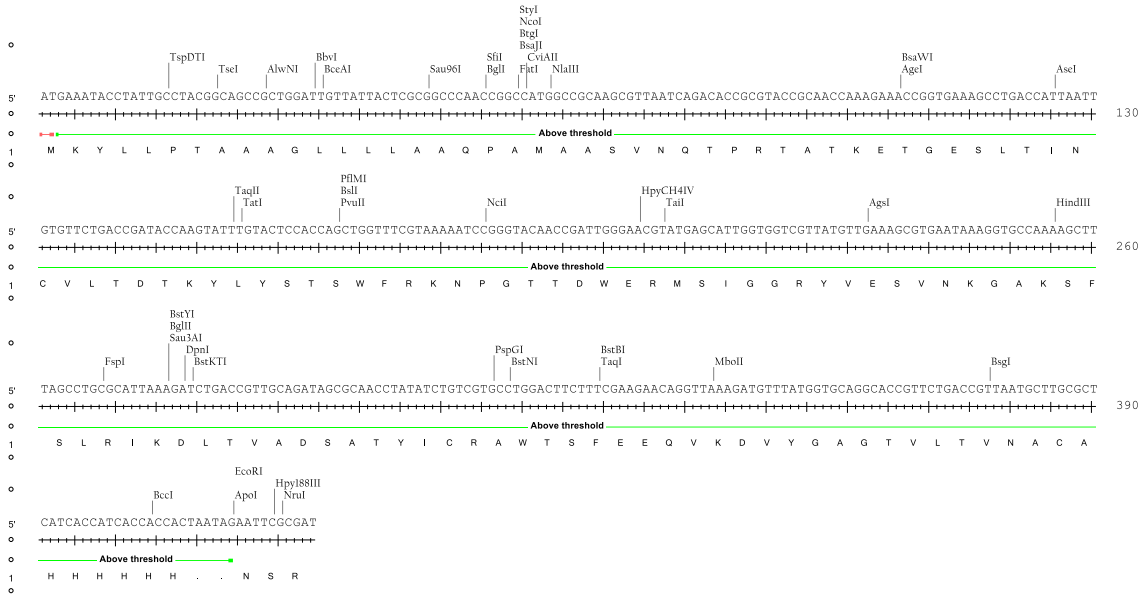

Figure 72. A detailed in-silico sequence of clone E4 highlighting the pelB leader sequence, restriction sites, ACA insertion, and poly histidine tag.

Anti-DLL4 E4 V_{NAR} **49**

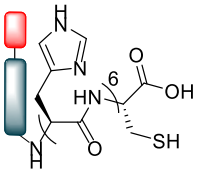

49

The Anti-DLL4 E4 V_{NAR} **49** was diluted to 33.5 µM, 100 µL, in PBS pH = 7.4 and then reduced at 21 ºC for 5 h with TCEP (2 µL, 16.75 mM, 10 eq. in PBS pH = 7.4). Molecular weight of **49** confirmed by LC-MS. Expected mass: 12824. Observed mass: 12824 Da.

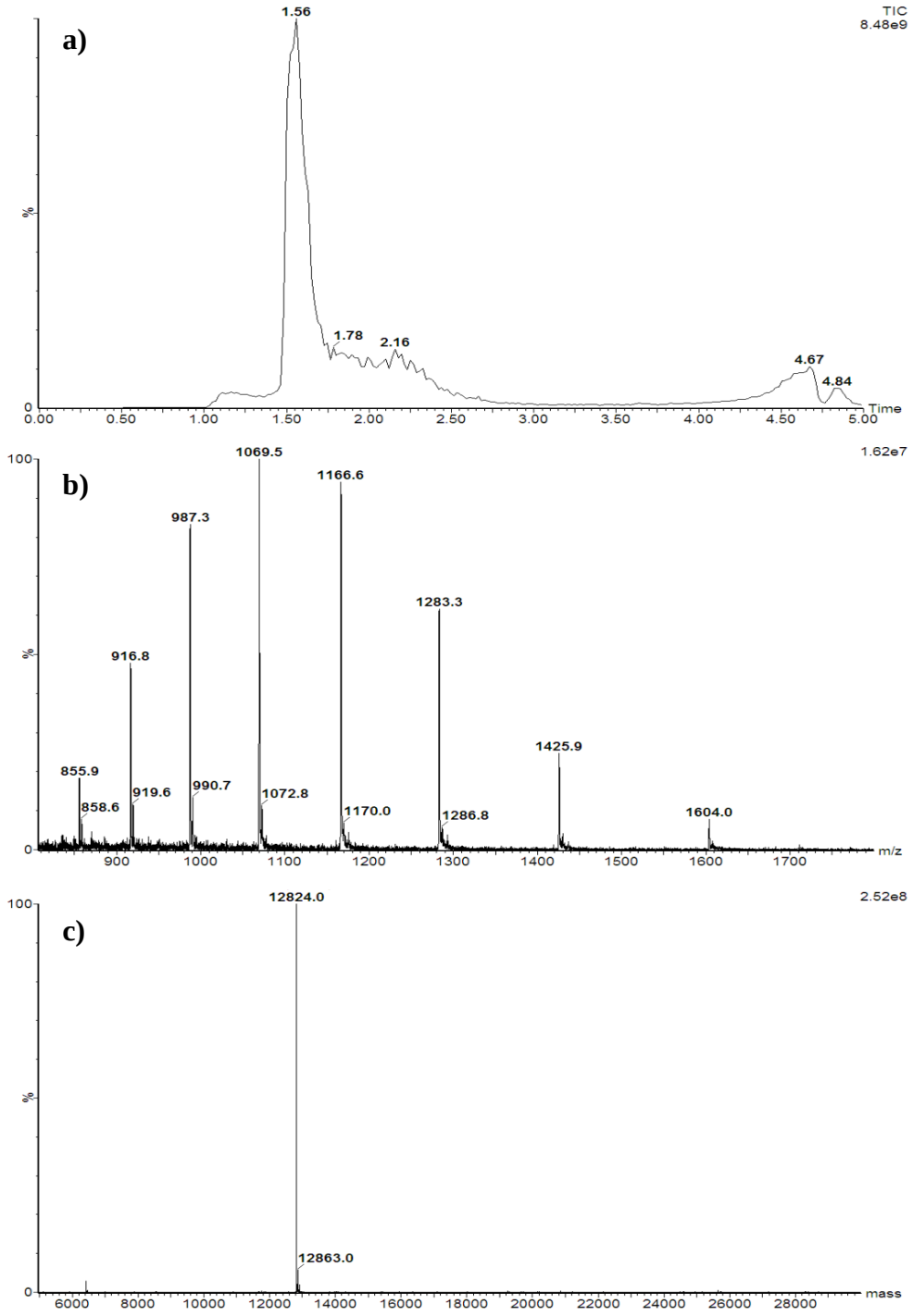

Figure 73. (a) TIC, **(b)** non-deconvoluted LC-MS trace, **(c)** deconvoluted MS data for reduced Anti-DLL4 E4 V_{NAR} **49**.

Anti-DLL4 E4 V_{NAR} **49** after 15 days

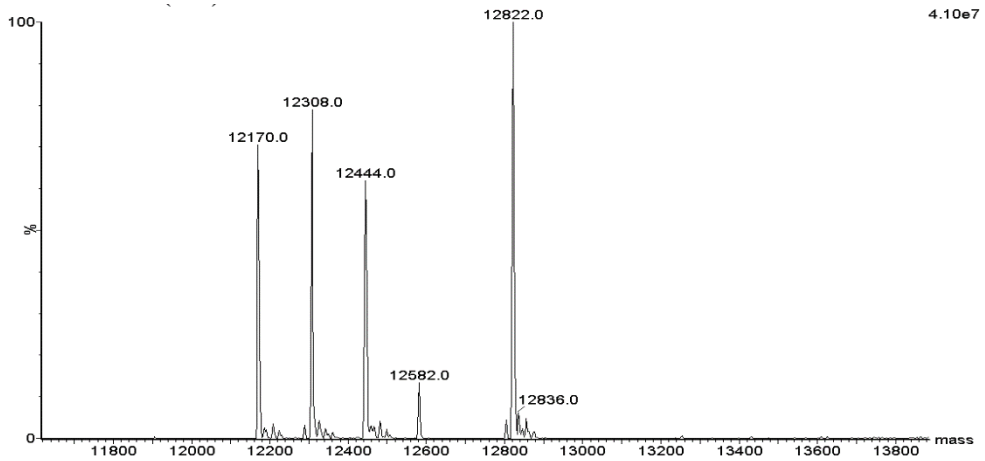

Figure 74. Deconvoluted MS data for reduced Anti-DLL4 E4 V_{NAR} **49**, after 15 days storage.

Anti DLL4-Clone E4 Mestra **51**

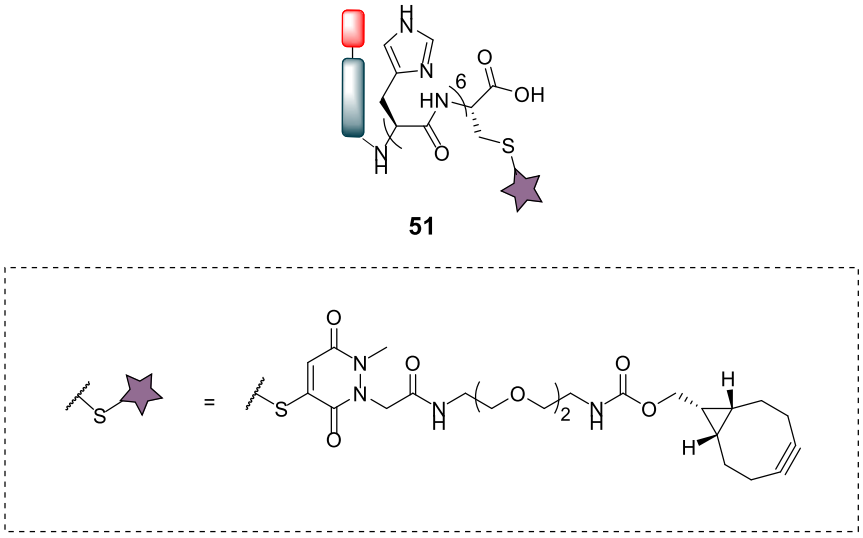

51

Anti-DLL4 E4 V_{NAR} **49** was diluted to 33.5 µM, 100 µL, in PBS pH = 7.4) and then reduced at 21 ºC for 5 h with TCEP (2 µL, 16.75 mM, 10 eq. in PBS pH = 7.4). After this time, PD **50** (0.85 µL, 80 mM, 20 eq. in DMSO) was added and reaction incubated at 21 °C for 16 h. The excess reagents were then removed by repeated diafiltration into fresh buffer using VivaSpin sample concentrators (GE Healthcare, 3,000 MWCO). Successful conjugation was confirmed by LC-MS and SDS-PAGE. Expected mass: 13310 Da. Observed mass: 13310 Da.

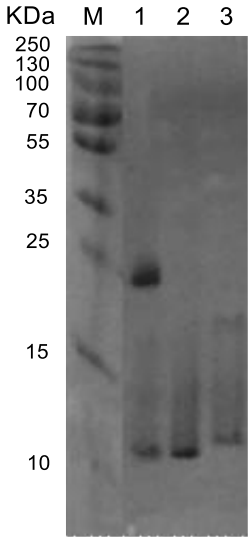

Figure 75. SDS-PAGE analysis: **M)** Molecular weight marker. **1)** Anti DLL4-Clone E4 (partial dimer formation). **2)** Reduced Anti DLL4-Clone E4. **3)** Anti DLL4-Clone E4 Mestra **51**.

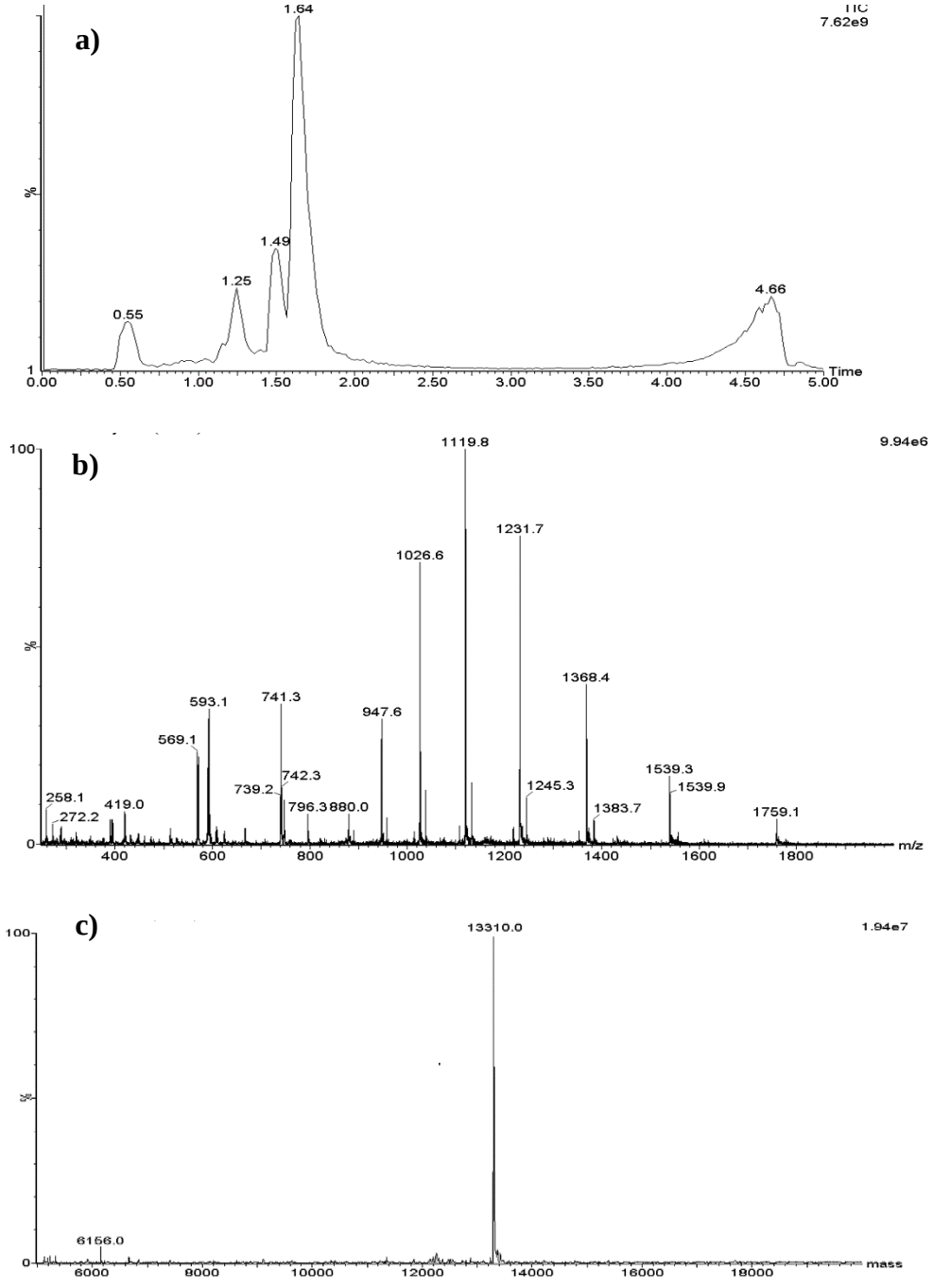

Figure 76. (a) TIC, **(b)** non-deconvoluted LC-MS trace, **(c)** deconvoluted MS data for Anti DLL4-Clone E4 Mestra **51**.

Anti DLL4-Clone E4 Mestra **51** after 15 days

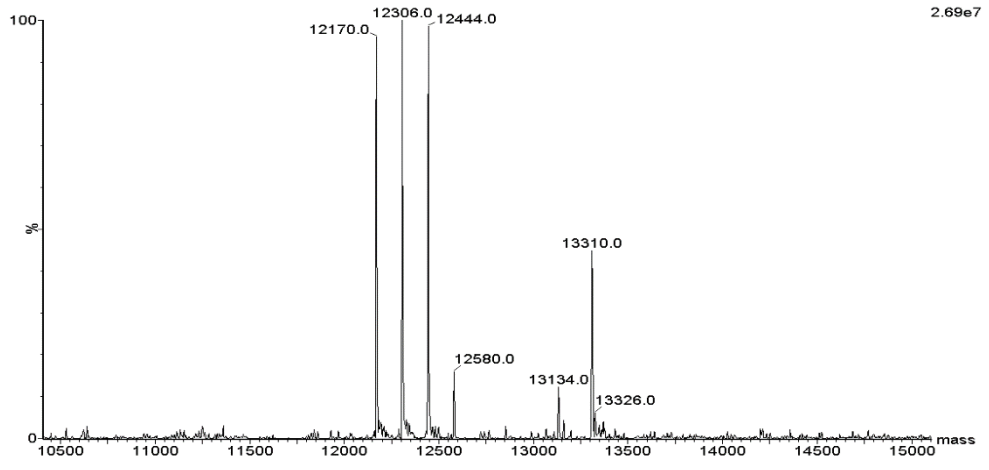

Figure 77. Deconvoluted MS data for Anti DLL4-Clone E4 Mestra **51**, after V_{NAR} storage for 15 days shows 4 main degradation peaks (12170, 12306, 12444 and 12582) which represent the falling off of the 4 Histidines + single cysteine residue.

Anti DLL4-Clone E4 maleimide after 15 days

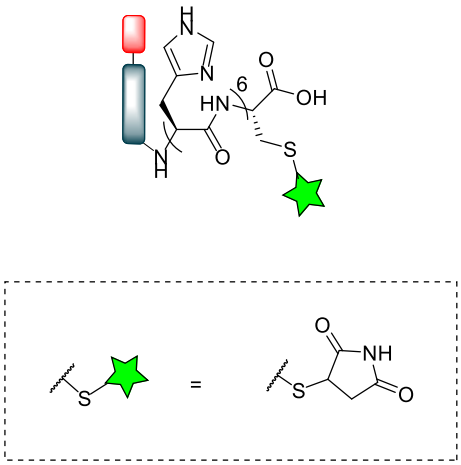

The Anti-DLL4 E4 V_{NAR} **49** was diluted to 33.5 µM, 100 µL, in PBS pH = 7.4) and then reduced at 21 ºC for 5 h with TCEP (2 µL, 16.75 mM, 10 eq. in PBS pH = 7.4). After this time, maleimide (0.85 µL, 80 mM, 20 eq. in DMSO) was added, and reaction incubated at 21 °C for 16 h. The excess reagents were then removed by repeated diafiltration into fresh buffer using VivaSpin sample concentrators (GE Healthcare, 3,000 MWCO). Data analysed by LC-MS. Expected mass: 12920 Da. Observed mass (modification peak): 12918 Da.

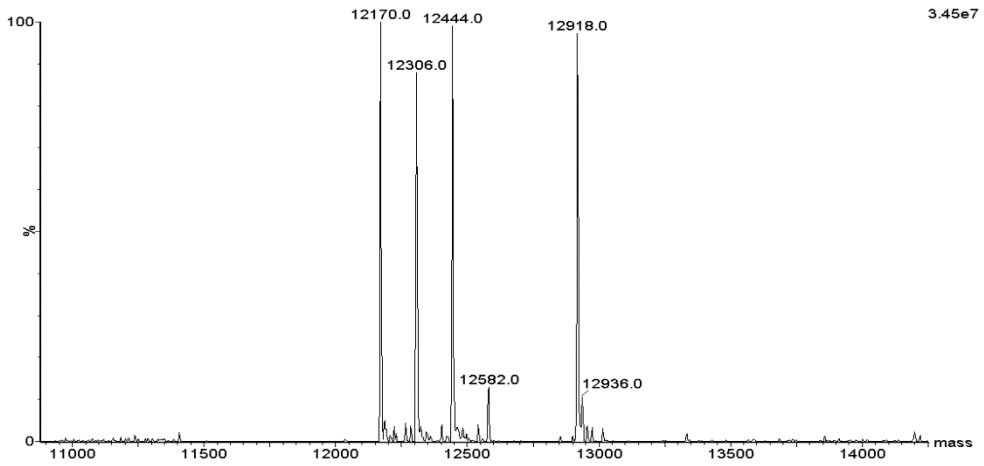

Figure 78. Deconvoluted MS data for Anti DLL4-Clone E4 maleimide, after V_{NAR} storage for 15 days, showing the same degradation peaks as the native clone (12170, 12306, 12444 and 12582), confirming the cleavage of the terminal single cysteine residue.

Anti DLL4-Clone E4 acetamide after 15 days

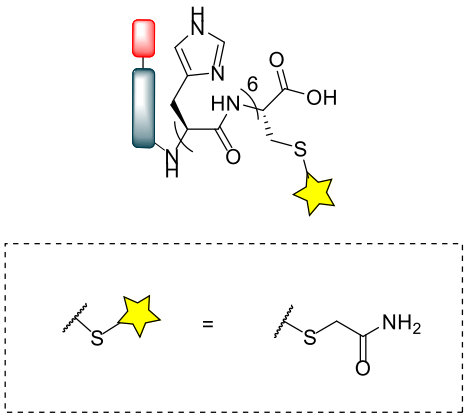

The Anti-DLL4 E4 V_{NAR} **49** was diluted to 33.5 µM, 100 µL, in PBS pH = 7.4) and then reduced at 21 ºC for 5 h with TCEP (2 µL, 16.75 mM, 10 eq. in PBS pH = 7.4). After this time, iodoacetamide (0.85 µL, 80 mM, 20 eq. in DMSO) was added, and reaction incubated at 21 °C for 16 h. The excess reagents were then removed by repeated diafiltration into fresh buffer using VivaSpin sample concentrators (GE Healthcare, 3,000 MWCO). Data analysed by LC-MS. Expected mass: 12880 Da. Observed mass (modification peak): 12878 Da.

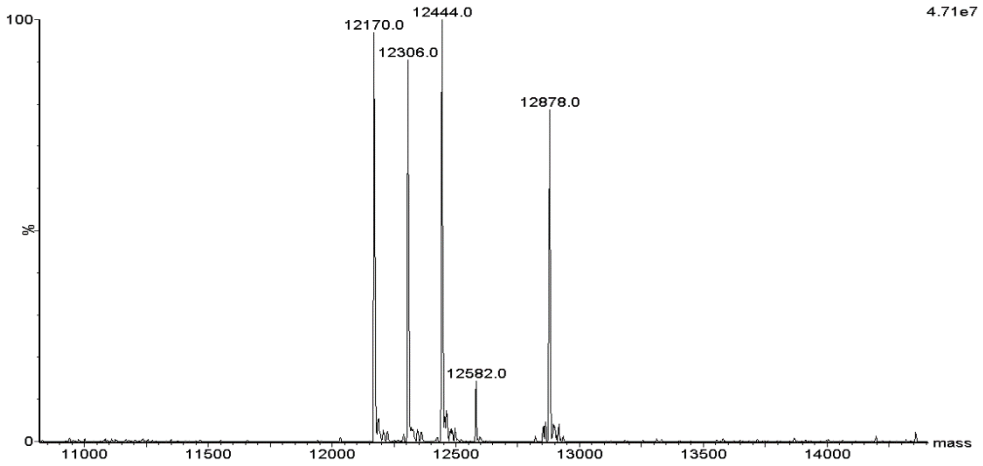

Figure 79. Deconvoluted MS data for Anti DLL4-Clone E4 acetamide, after V_{NAR} storage for 15 days, showing the same degradation peaks as the native clone (12170, 12306, 12444 and 12582), confirming the cleavage of the terminal single cysteine residue.

Native E4HisCTerminal **52**

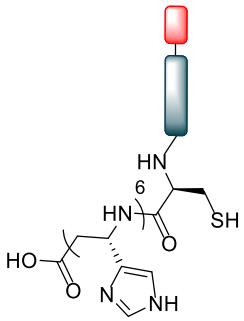

52

The E4HisCTerminal shark antibody **52** was diluted to 33.5 µM, 100 µL, in PBS pH = 7.4 and then reduced at 21 ºC for 5 h with TCEP (2 µL, 16.75 mM, 10 eq. in PBS pH = 7.4). Mass was assessed by LC-MS. Observed mass: 12754 Da.

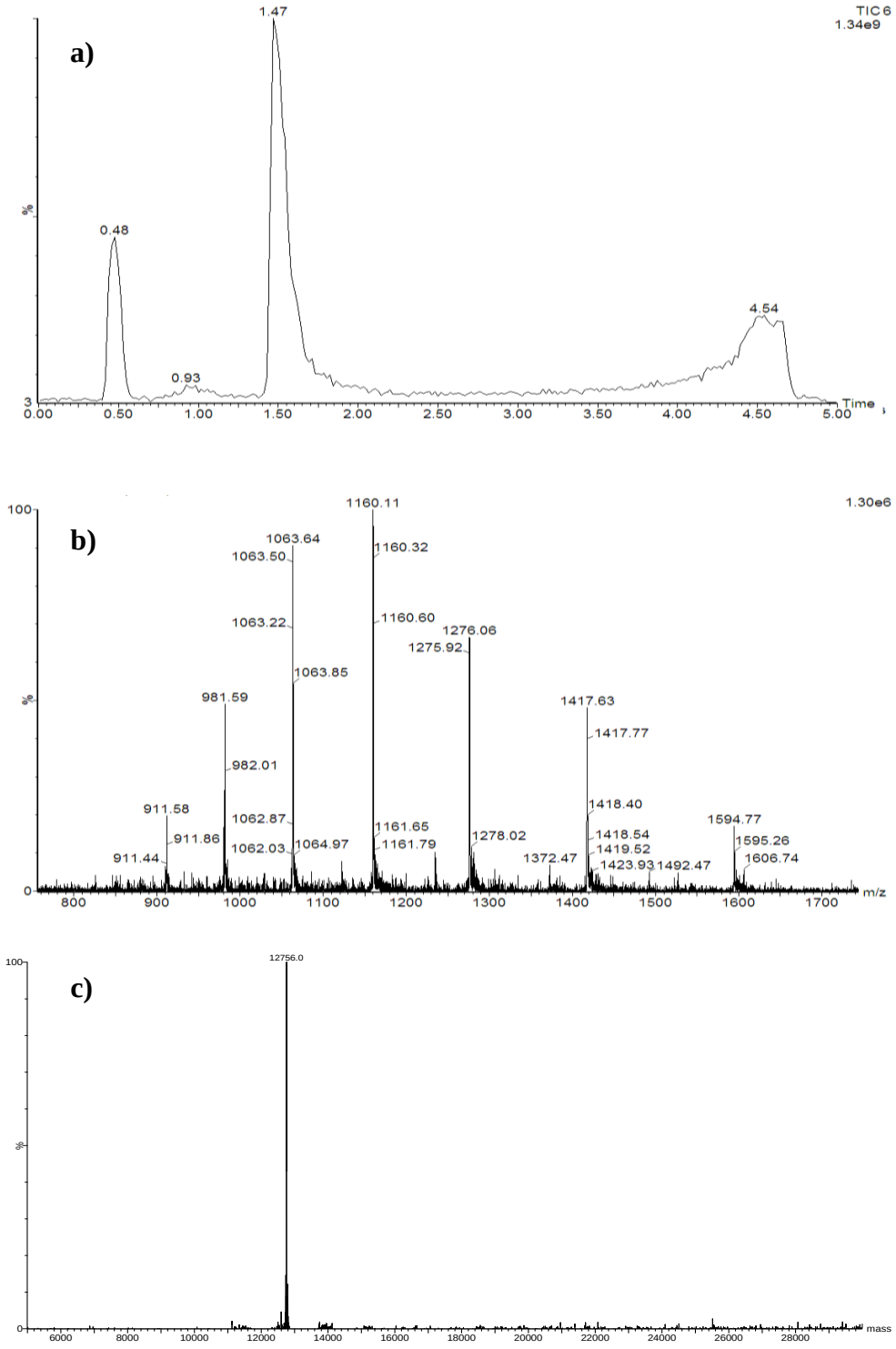

Figure 80. (a) TIC, **(b)** non-deconvoluted LC-MS trace, **(c)** deconvoluted MS data for native E4HisCTerminal **52**.

Native E4HisCTerminal **52** after 30 days

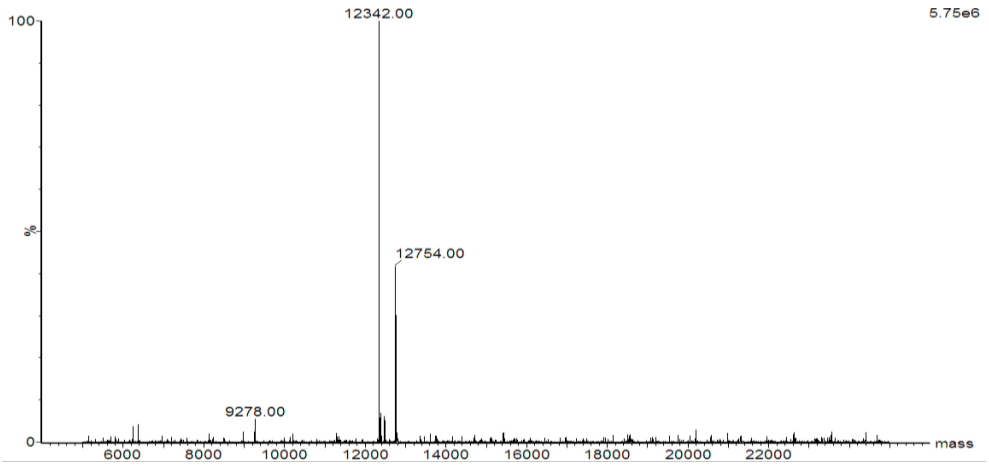

Figure 81. Deconvoluted MS data for E4HisCTerminal **52**, after 30 days storage. Degradation observed (peak 12342) corresponds to the falling off of of 3 Histidine residues.

E4HisCTerminal Mestra **53**

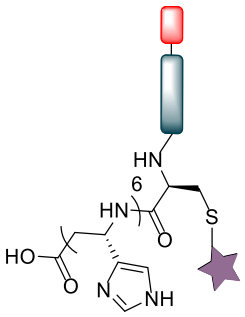

53

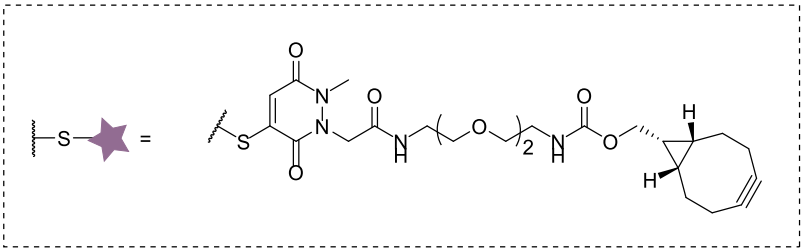

The E4HisCTerminal shark antibody **52** was diluted to 33.5 µM, 100 µL, in PBS pH = 7.4) and then reduced at 21 ºC for 5 h with TCEP (2 µL, 16.75 mM, 10 eq. in PBS pH = 7.4). After this time, monoBrMestra **50** (0.85 µL, 80 mM, 20 eq. in DMSO) was added, and reaction incubated at 21 °C for 16 h. The excess reagents were then removed by repeated diafiltration into fresh buffer using VivaSpin sample concentrators (GE Healthcare, 3,000 MWCO). Successful conjugation was confirmed by LC-MS. Expected mass: 13,242 Da. Observed mass: 13,242 Da.

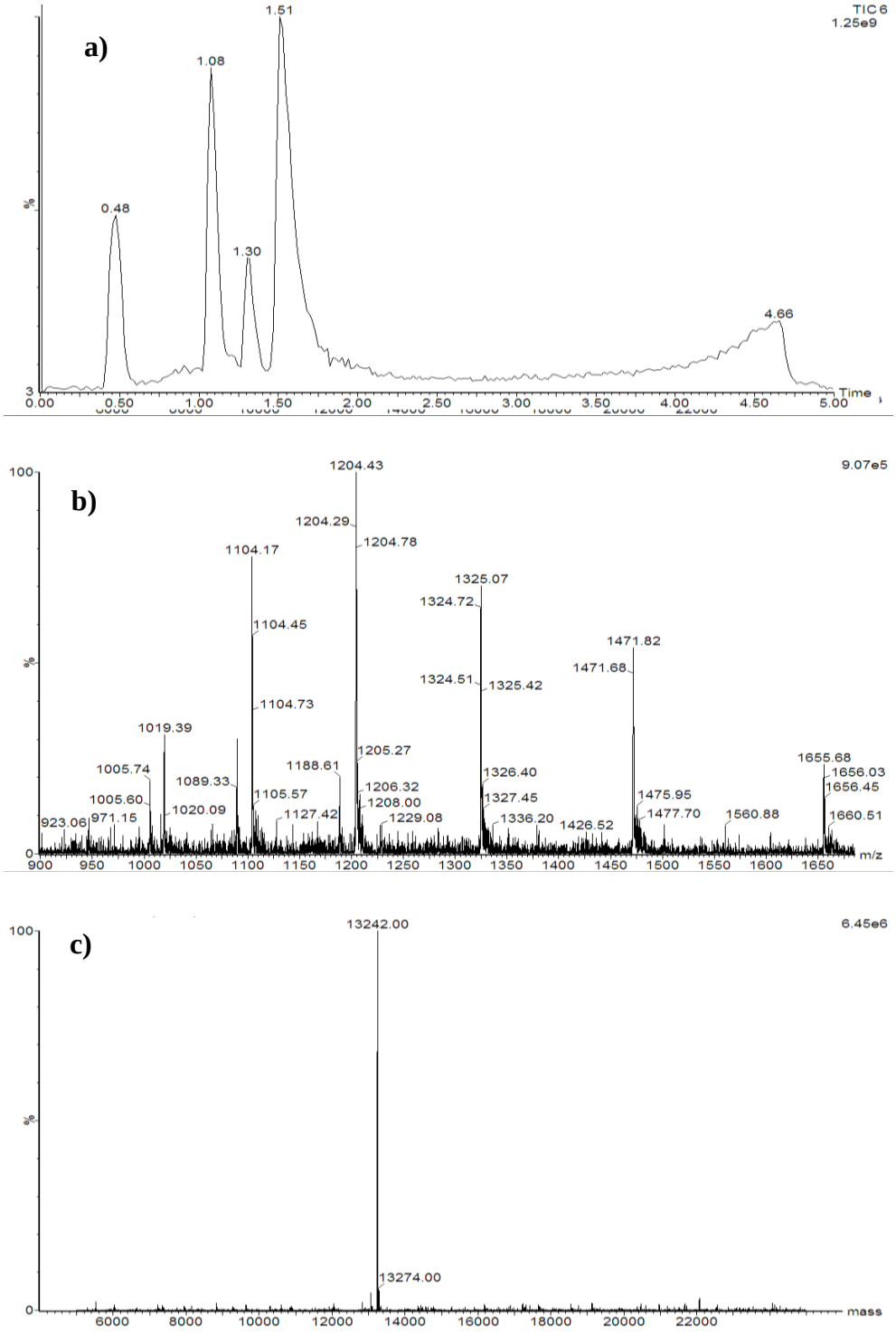

Figure 82. (a) TIC, **(b)** non-deconvoluted LC-MS trace, **(c)** deconvoluted MS data for E4HisCTerminal Mestra **53**.

E4HisCTerminal Mestra **53** after 30 days storage

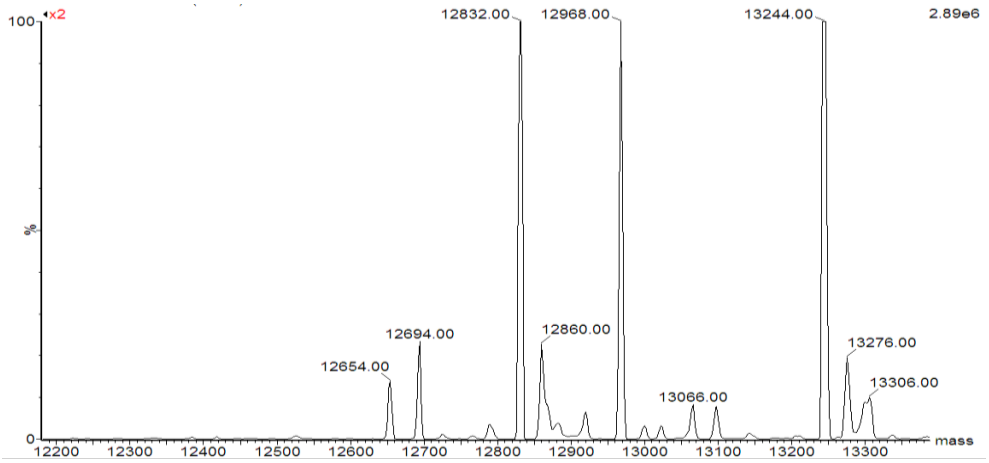

Figure 83. Deconvoluted MS data for E4HisCTerminal Mestra **53**, after 30 days storage. Degradation observed: peak 12694 corresponds to the falling off of 4 Histidine residues, peak 12832 corresponds to the falling off of 3 Histidine residues and peak 12968 corresponds to the falling off of two Histidine residues.

E4HisCTerminal Mepstra **57**

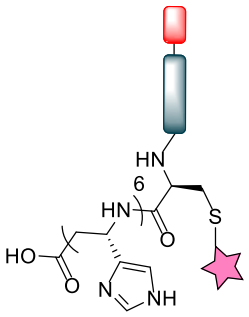

57

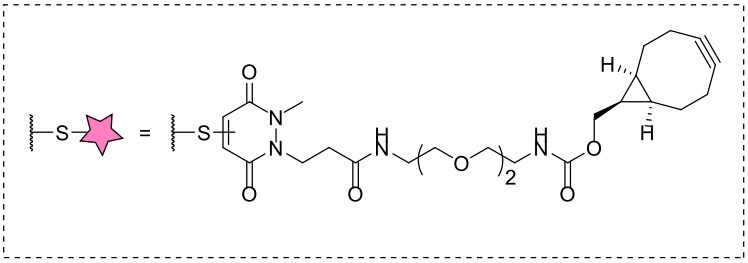

The E4HisCTerminal shark antibody **52** was diluted to 33.5 µM, 100 µL, in PBS, pH = 7.4 and then reduced at 21 ºC for 5 h with TCEP (2 µL, 16.75 mM, 10 eq. in PBS pH = 7.4). After this time, the clone was reacted with monoBrMepstra **56** (0.85 µL, 80 mM, 20 eq. in DMSO), and incubated at 21 °C for 16 h. The excess reagents were then removed by repeated diafiltration into fresh buffer using VivaSpin sample concentrators (GE Healthcare, 3,000 MWCO). Successful conjugation was confirmed by LC-MS. Expected mass: 13,256 Da. Observed mass: 13,274 Da.

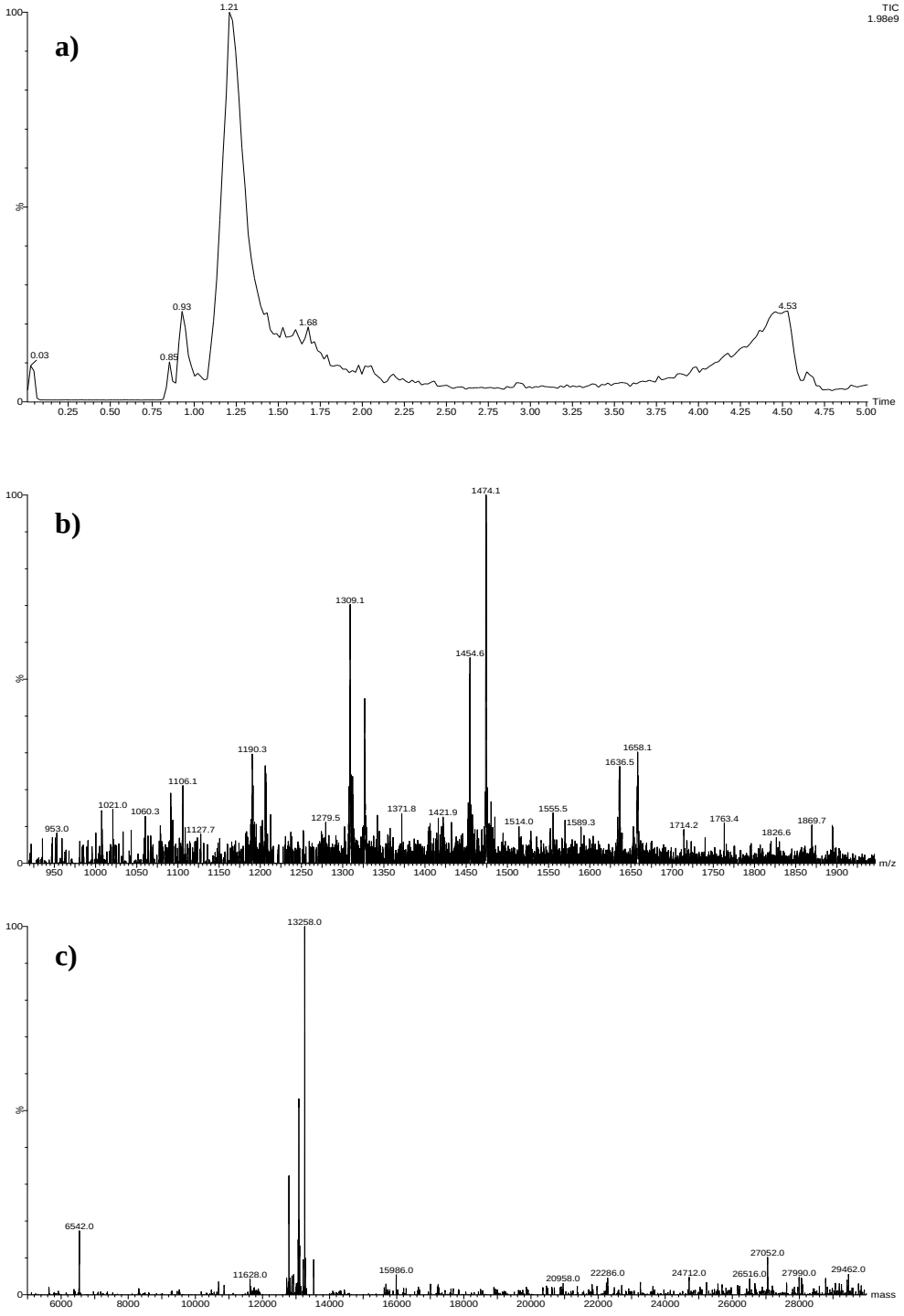

Figure 84. (a) TIC, **(b)** non-deconvoluted LC-MS trace, **(c)** deconvoluted MS data for E4HisCTerminal Mepstra **57**.

E4HisCTerminal Mepstra Alexafluor **58**

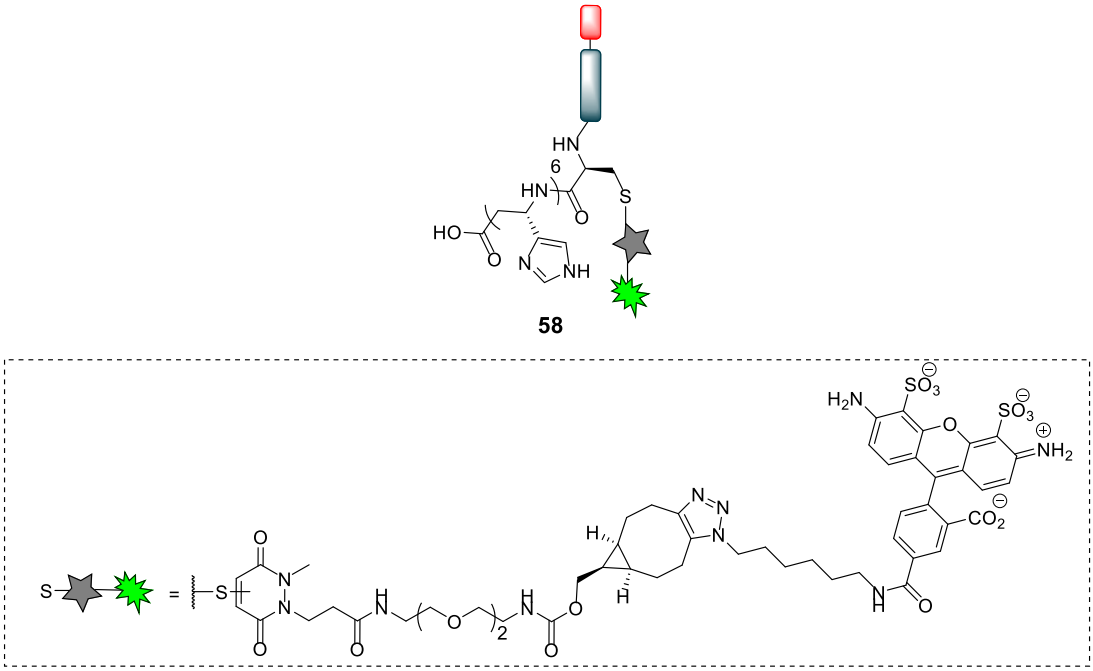

To a solution of E4HisCTerminal Mepstra **57** (50 µL, 33.5 µM) in PBS (pH= 7.4) was added Alexafluor®-488-N_3 (0.85 µL, 20 mM in DMSO, 10 eq.) and the reaction mixture incubated at 21 °C for 2 h. The excess reagents were then removed by repeated diafiltration into fresh buffer using VivaSpin sample concentrators (GE Healthcare, 5,000 MWCO). Successful conjugation was confirmed by SDS-PAGE and LC-MS. Expected mass: 13,916 Da. Observed mass: 13,918 Da.

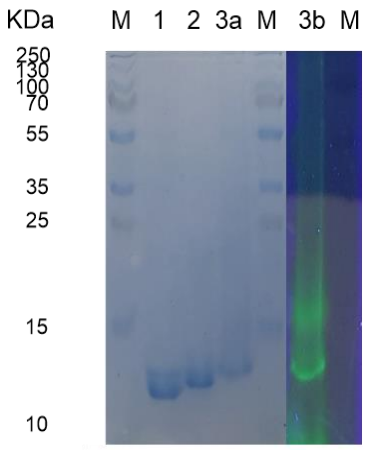

Figure 85. SDS-PAGE for E4HisCTerminal conjugates. M) Molecular weight marker; **1a)** Stained E4HisCTerminal **6**; **2a)** Stained E4HisCTerminal Mepstra **57**; **3a)** Stained E4HisCTerminal Mepstra Alexafluor **58**; **3b)** E4HisCTerminal Mepstra Alexafluor **58** under UV light.

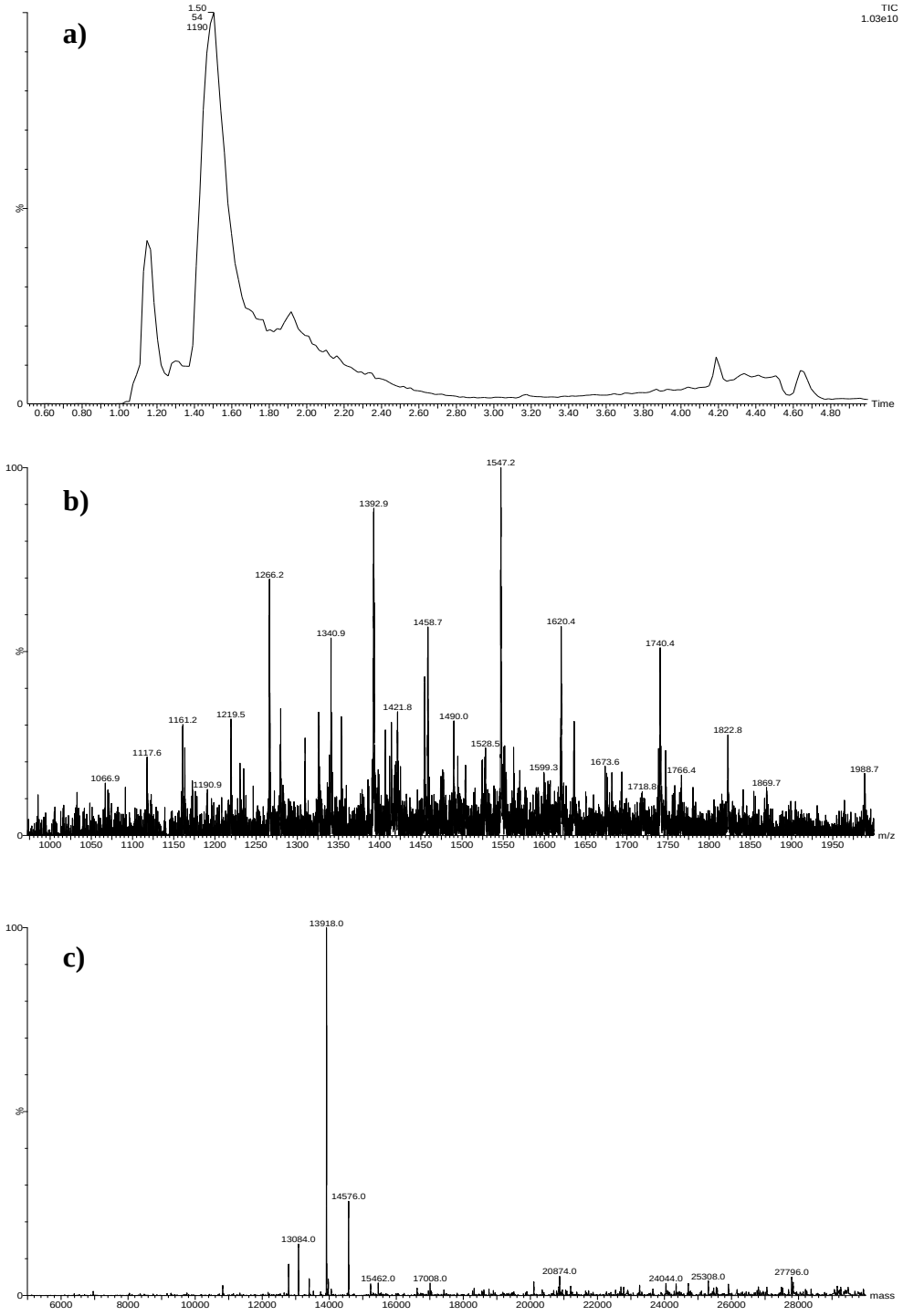

Figure 86. (a) TIC, **(b)** non-deconvoluted LC-MS trace, **(c)** deconvoluted MS data for E4HisCTerminal Mepstra Alexafluor **58**.

Experimental for ongoing/future work

Amine-reactive pyridazinedione synthesis

tert-Butyl 1-((methylsulfonyl)oxy)-3,6,9,12,15,18-hexaoxahenicosan-21-oate[171] **60**

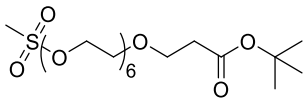

60

To a solution of hexaethylenoglycol **59** (6.50 g, 23.0 mmol) in THF (9 mL) was added a 60% Suspension of NaH in mineral oil (13 mg, 0.27 mmol) and the mixture was stirred at 21 °C for 10 min. After this time, was added *tert*-butyl acrylate (1 mL, 6.90 mmol). The mixture was then stirred at 21 °C for a further 48 h. Following this, to the solution was added AcOH (0.1 mL) and the reaction mixture concentrated *in vacuo*. The crude residue was dissolved in water (100 mL), the solution extracted with EtOAc (4 × 100 mL) and the combined organic extracts dried ($MgSO_4$) and concentrated *in vacuo* to afford crude *tert*-butyl 1-hydroxy-3,6,9,12,15,18-hexaoxahenicosan-21-oate (2.20 g, 5.36 mmol). The crude residue was dissolved in DCM (15 mL) and Et_3N (2.0 mL, 14.28 mmol) and methanesulfonyl chloride (1.0 mL, 12.9 mmol) was added. The resulting mixture was stirred for 24 h at 21 °C. After this time, the reaction mixture was diluted with DCM (50 mL), washed with sat. $NaHCO_3$ (2 × 50 mL) and concentrated *in vacuo* to provide *tert*-Butyl 1-((methylsulfonyl)oxy)-3,6,9,12,15,18-hexaoxahenicosan-21-oate **60** as a clear oil (2.57 g, 5.26 mmol, 77%). ^{1}H NMR (600 MHz, MeOD) δ 4.37-4.35 (m, 2H), 3.75 (t, J = 6.1 Hz, 2H) 3.65-3.59 (m, 22H), 3.11 (s, 3H), 2.47 (t, J = 6.2 Hz, 2H), 1.45 (s, 9H). ^{13}C NMR (150 MHz, MeOD) δ 172.9 (C), 81.5 (C), 71.6 (CH_2 × 10), 70.9 (CH_2), 69.9 (CH_2), 68.0 (CH_2), 37.6 (CH_3), 37.2 (CH_2), 28.4 (CH_3). IR (thin film) 2931, 1726 cm^{-1}.

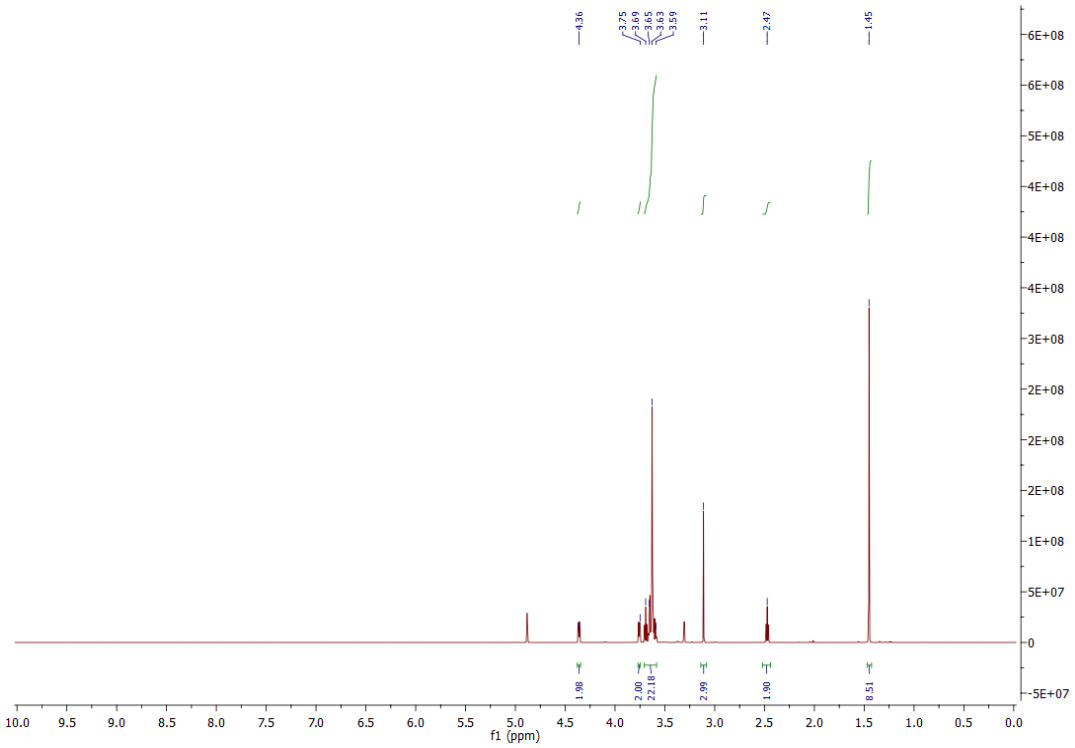
4.36
3.75
3.69
3.65
3.63
3.59
3.11
2.47
1.45
1.98
2.00
22.18
2.99
1.90
8.51
f1 (ppm)

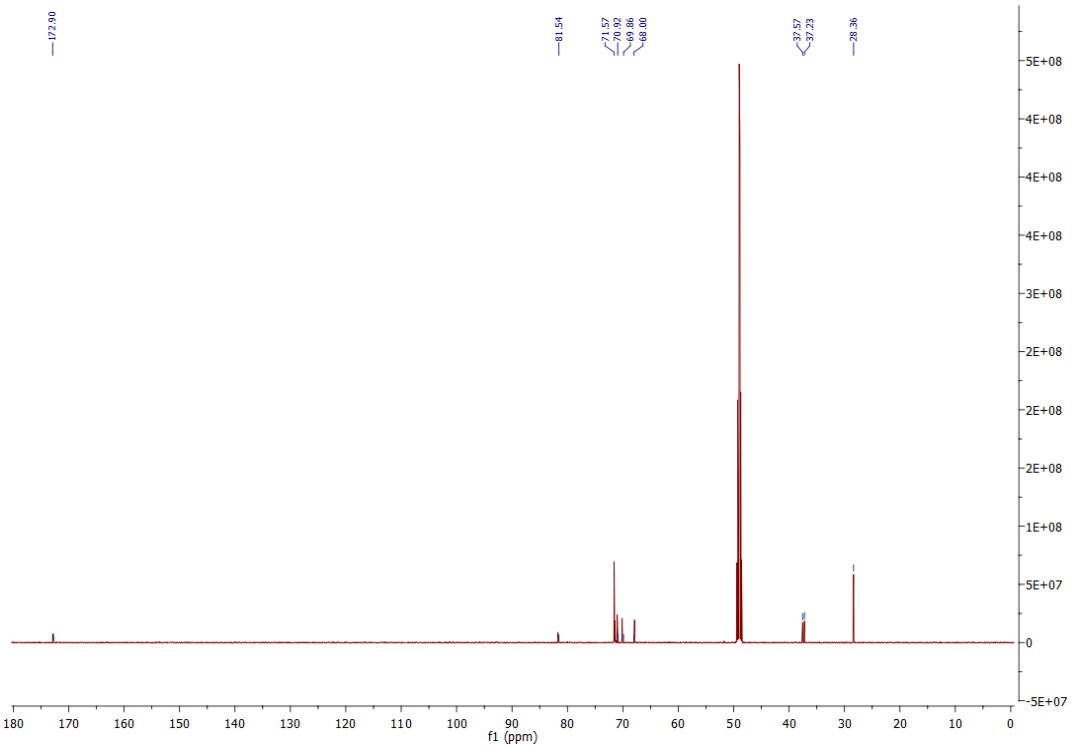
172.90
81.54
71.57
70.92
69.86
68.00
37.57
37.23
28.36
f1 (ppm)

tert-Butyl 1-azido-3,6,9,12,15,18-hexaoxahenicosan-21-oate[171] **61**

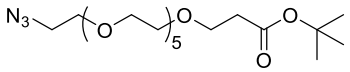

61

To a solution of *tert*-butyl 1-((methylsulfonyl)oxy)-3,6,9,12,15,18-hexaoxahenicosan-21-oate **60** (2.57 g, 5.26 mmol) in DMF (5 mL) was added NaN_3 (1.89 g, 29.1 mmol). The reaction mixture was stirred for 72 h at 21 °C. After this time, the mixture was diluted with EtOAc (100 mL), washed with water (3 × 50 mL), dried ($MgSO_4$), and concentrated *in vacuo*. Purification of the crude residue by flash column chromatography (5% EtOAc/MeOH) afforded *tert*-butyl 1-azido-3,6,9,12,15,18-hexaoxahenicosan-21-oate **61** (1.95 g, 4.47 mmol, 85%) as a pale yellow oil. ^{1}H NMR (600 MHz, MeOD) δ 3.67–3.58 (m, 24H), 3.37 (t, *J* = 4.9 Hz, 2H), 2.47 (t, *J* = 6.5 Hz, 2H), 1.45 (s, 9H). ^{13}C NMR (150 MHz, MeOD): δ 172.8 (C), 81.7 (C), 71.6 (CH_2), 71.5 (CH_2 × 9), 71.2 (CH_2), 67.9 (CH_2), 51.8 (CH_2), 37.2 (CH_2), 28.4 (CH_3). IR (thin film) 2867, 2100, 1726 cm^{-1}.

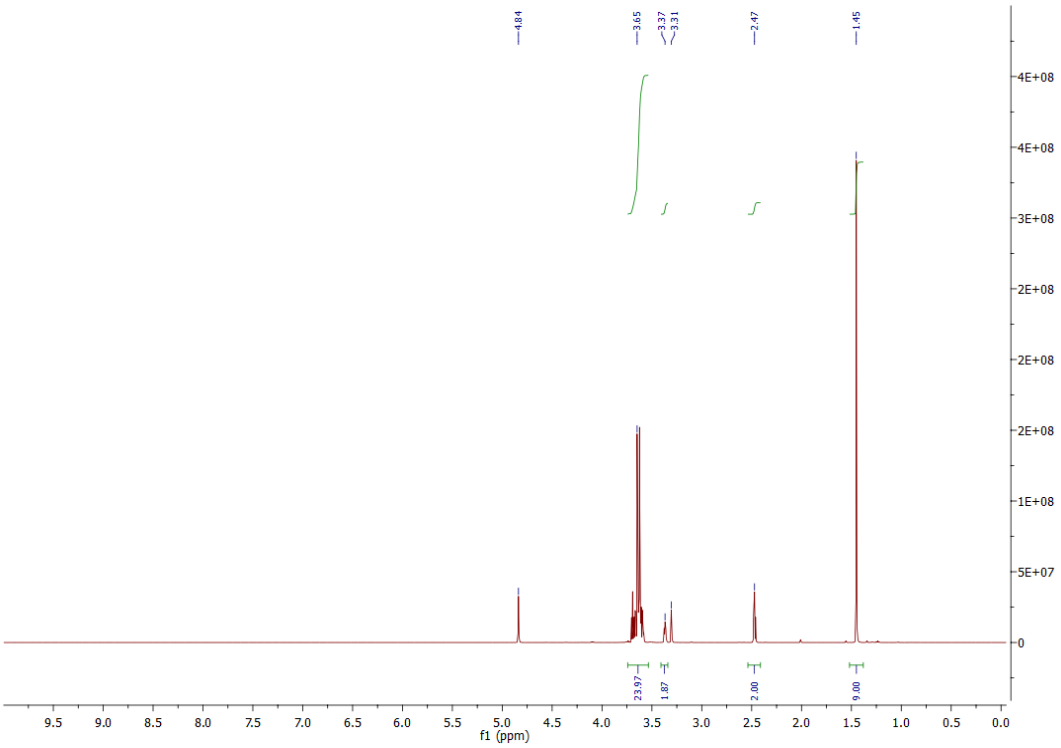
4.84
3.65
3.37
3.31
2.47
1.45
23.97
1.87
2.00
9.00
f1 (ppm)

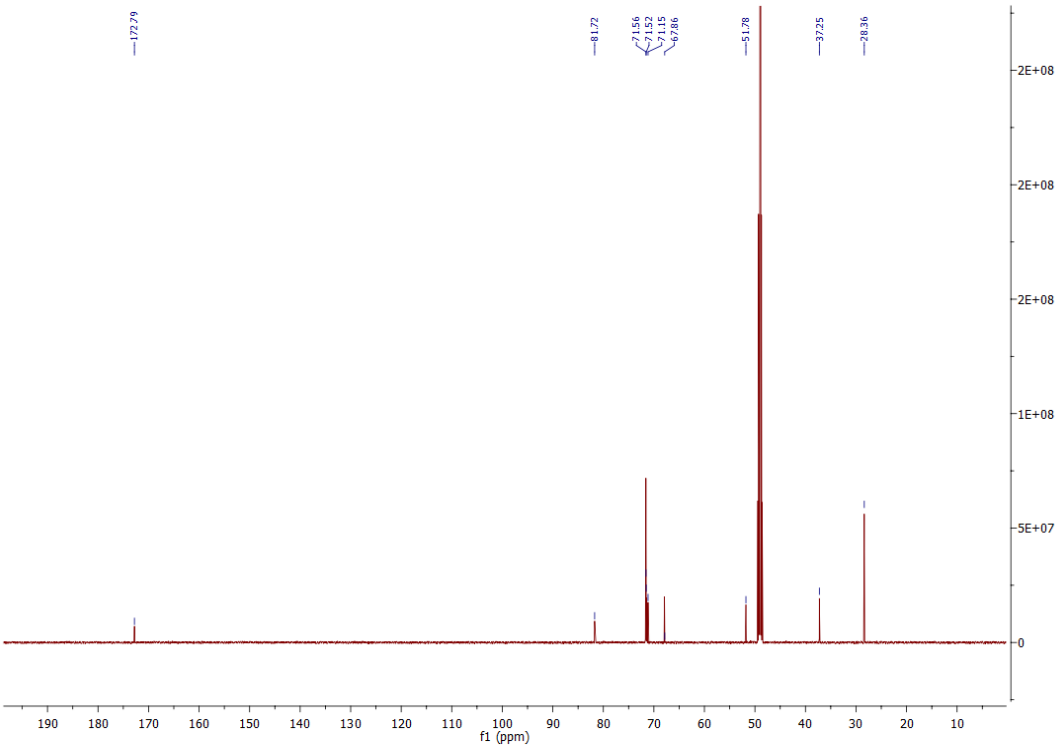
172.79
81.72
71.56
71.52
71.15
67.86
51.78
37.25
28.36
f1 (ppm)

tert-Butyl 1-amino-3,6,9,12,15,18-hexaoxahenicosan-21-oate[171] **62**

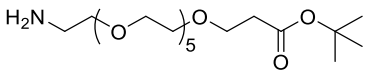

62

To a solution of *tert*-Butyl 1-azido-3,6,9,12,15,18-hexaoxahenicosan-21-oate **61** (33 mg, 0.78 mmol) in THF (7 mL) and H_2O (0.2 mL) was added triphenylphosphine (227 mg, 0.871 mmol). The reaction mixture was stirred for 16 h at 21 °C. After this time, the residue was concentrated *in vacuo*. Following this, the solid residue was dissolved in water (10 mL) and washed with toluene (3 × 10 mL, 0 °C). The aqueous layer was then concentrated *in vacuo* to afford *tert*-butyl 1-amino-3,6,9,12,15,18-hexaoxahenicosan-21-oate **62** (220 mg, 0.542 mmol, 69%) as a pale oil, without needing further purification. ^{1}H NMR (600 MHz, $CDCl_3$) δ 3.70 (t, J = 6.6 Hz, 2H), 3.64–3.61 (m, 20H), 3.51 (t, J = 5.2 Hz, 2H), 2.86 (t, J = 6.6 Hz, 2H), 2.50 (t, J = 6.6 Hz, 2H), 1.44 (s, 9H). ^{13}C NMR (150 MHz, $CDCl_3$): δ 170.9 (C), 80.8 (C), 73.4 (CH_2), 70.8 (CH_2 × 8), 70.7 (CH_2), 70.4 (CH_2), 66.9 (CH_2), 41.9 (CH_2), 36.4 (CH_2), 28.1 (CH_3). IR (thin film) 3338, 2868, 1726 cm^{-1}.

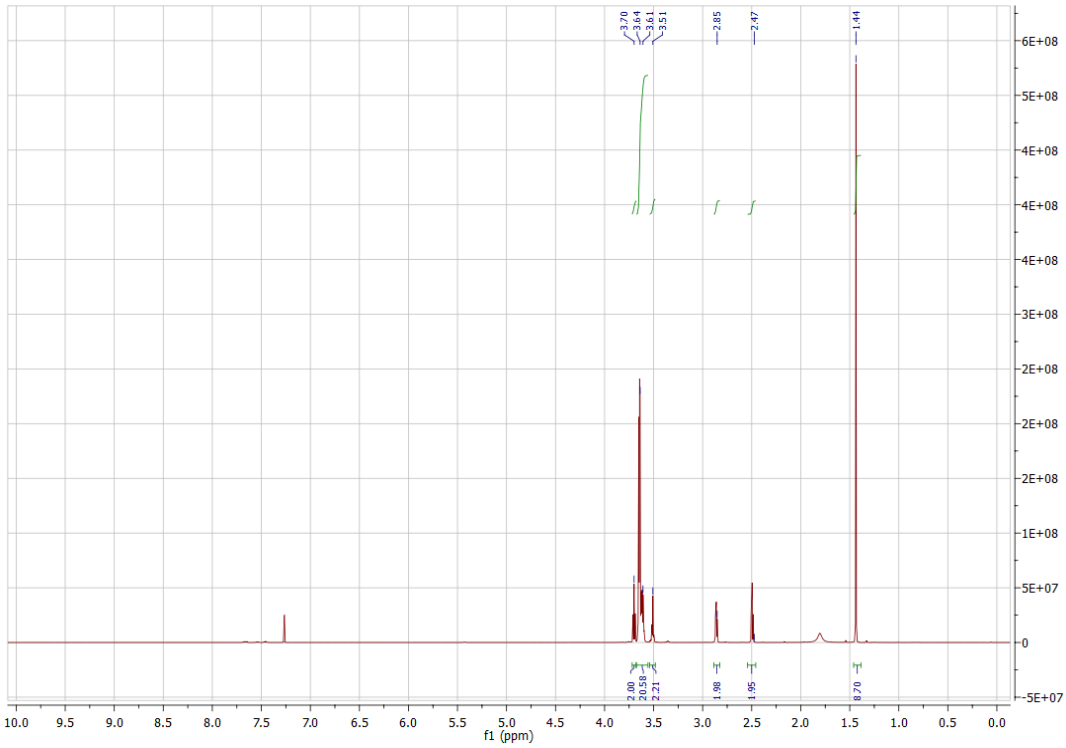
3.70
3.64
3.61
3.51
2.85
2.47
1.44
2.00
20.58
2.21
1.98
1.95
8.70
f1 (ppm)

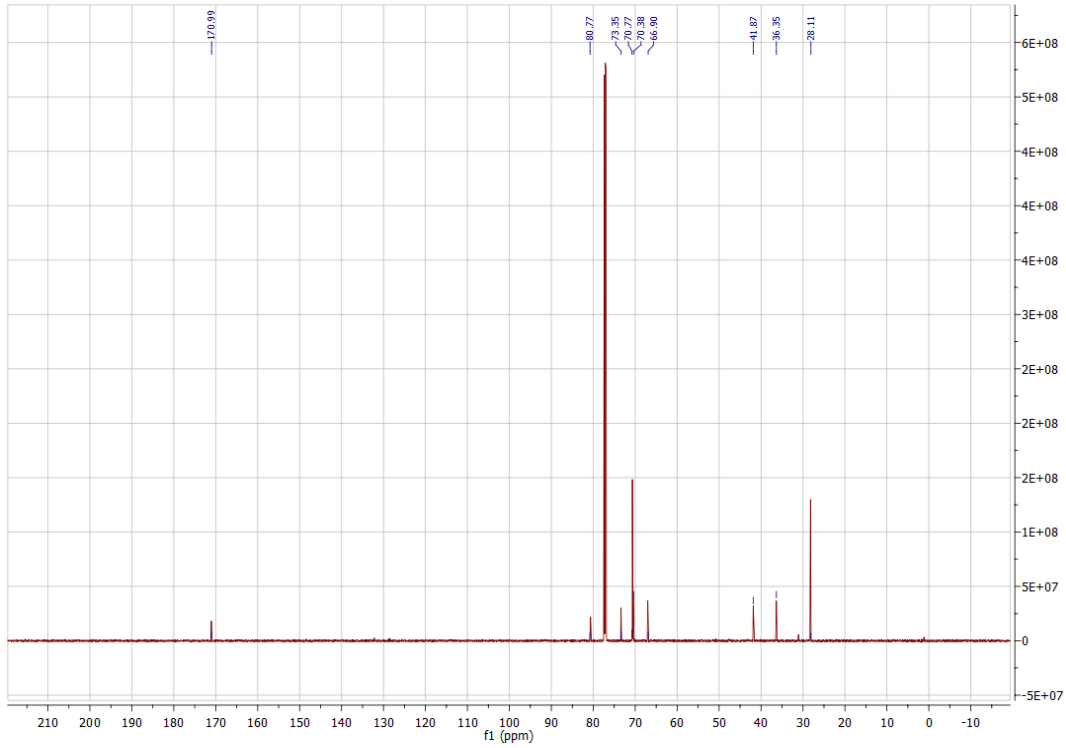
170.99
80.77
73.35
70.77
70.38
66.90
41.87
36.35
28.11
f1 (ppm)

tert-Butyl 1-(4,5-dibromo-2-methyl-3,6-dioxo-3,6-dihydropyridazin-1(2*H*)-yl)-3-oxo-7,10,13,16,19,22-hexaoxa-4-azapentacosan-25-oate **63**

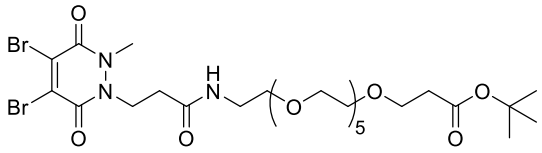

63

To a solution of 2,5-dioxopyrrolidin-1-yl 3-(5-bromo-2-methyl-3,6-dioxo-3,6-dihydropyridazin-1(2*H*)-yl)propanoate **45** (602 mg, 1.33 mmol) in MeCN (15 mL), was added *tert*-butyl 1-amino-3,6,9,12,15,18-hexaoxahenicosan-21-oate **62** (453 mg, 1.12 mmol) and the reaction mixture was stirred for 16 h at 21 °C. After this time, the solvent was removed *in vacuo* and purification of the crude residue by flash chromatography (0% to 15% MeOH/EtOAc) afforded *tert*-butyl 1-(4,5-dibromo-2-methyl-3,6-dioxo-3,6-dihydropyridazin-1(2*H*)-yl)-3-oxo-7,10,13,16,19,22-hexaoxa-4-azapentacosan-25-oate **63** (560 mg, 0.75 mmol, 67%) as a clear oil. ^{1}H NMR (600 MHz, $CDCl_3$) δ 6.99 (s, 1H), 4.44 (t, *J* = 7.0 Hz, 2H), 3.73-3.60 (m, 25H), 3.53 (t, *J* = 5.0 Hz, 2H), 3.42 (t, *J* = 5.0 Hz, 2H), 2.62 (t, *J* = 7.0 Hz, 2H), 2.50 (t, *J* = 6.6 Hz, 2H), 1.44 (s, 9H). ^{13}C NMR (150 MHz, $CDCl_3$, rotamers) δ 171.9 (C), 171.1 (C), 170.0 (C), 199.5 (C), 169.5 (C), 153.1 (C), 152.6 (C), 136.0 (C), 135.4 (C), 80.8 (C), 70.6 (CH_2 ×12), 70.4 (CH_2), 66.9 (CH_2), 44.7 (CH_2), 39.3 (CH_2), 36.4 (CH_2), 35.2 (CH_2), 33.9 (CH_3), 28.2 (CH_3). IR (thin film) 3336, 2868, 1779, 1726, 1636 cm^{-1}. LRMS (ESI) 765 (60, [M^{79}Br^{81}Br+H]$^{+}$; HRMS (ESI) calcd for $C_{27}H_{45}Br_2N_3O_{11}$ [M^{79}Br^{81}Br+H]$^{+}$ 748.1476; observed 748.1477.

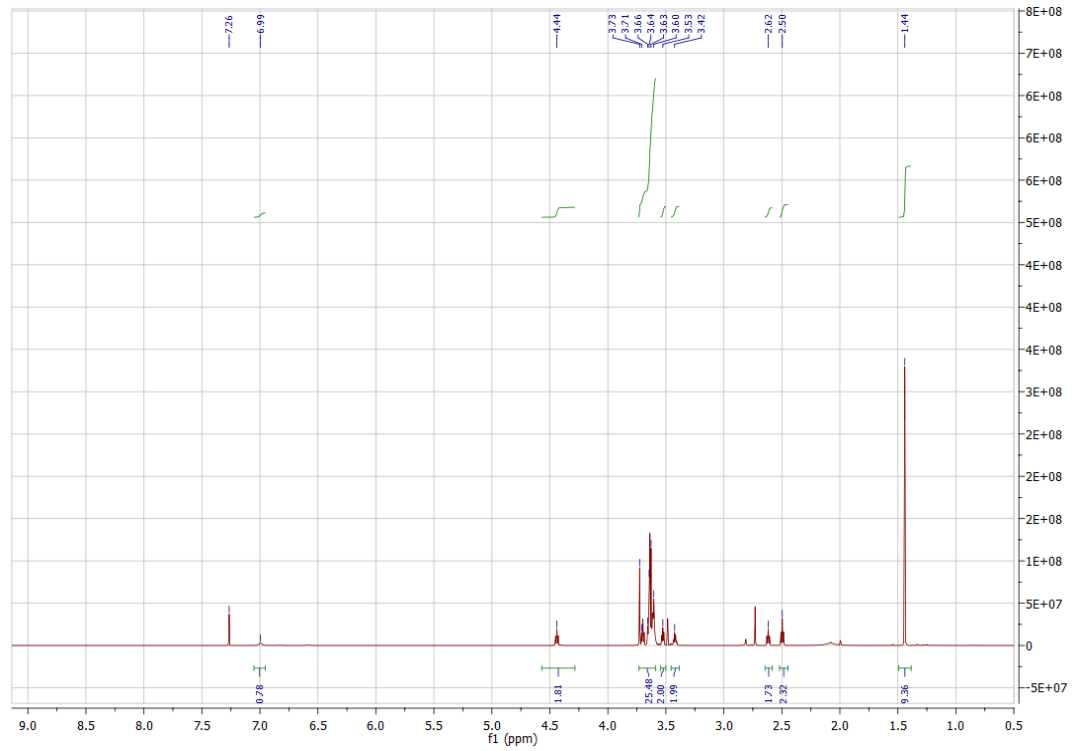
7.26
6.99
4.44
3.73
3.71
3.66
3.64
3.63
3.60
3.53
3.42
2.62
2.50
1.44
0.78
1.81
25.48
2.00
1.99
1.73
2.32
9.36
f1 (ppm)

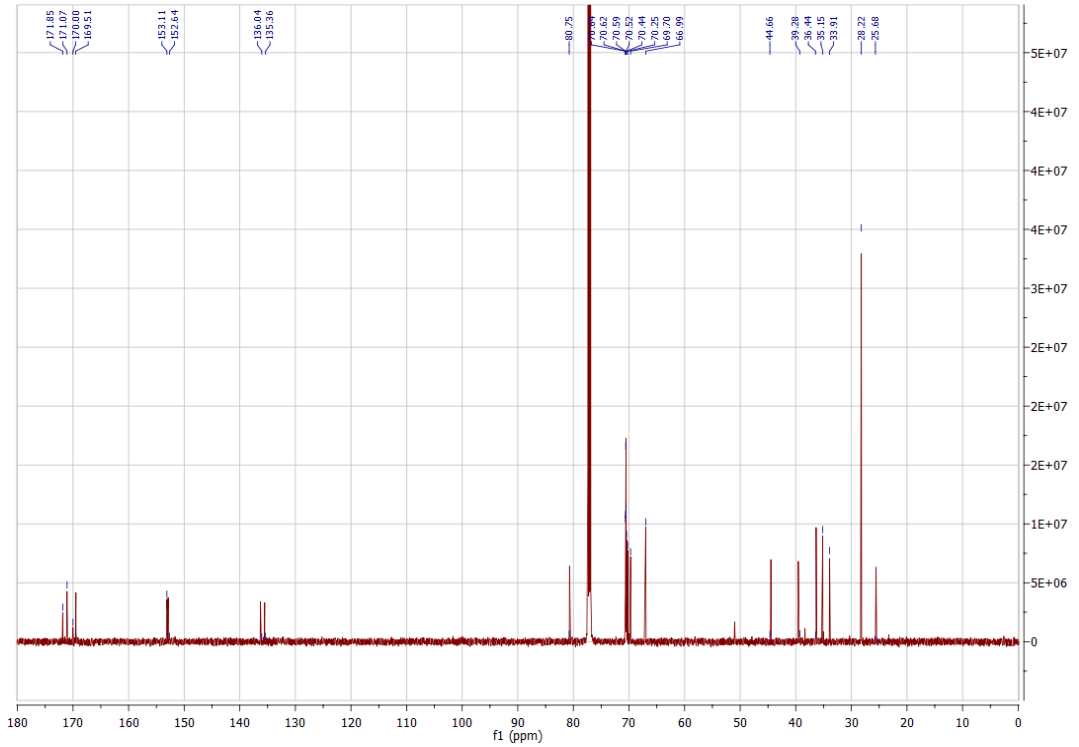
171.85
171.07
170.00
169.51
153.11
152.64
136.04
135.36
80.75
70.64
70.62
70.59
70.52
70.44
70.25
69.70
66.99
44.66
39.28
36.44
35.15
33.91
28.22
25.68
f1 (ppm)

1-(4,5-Dibromo-2-methyl-3,6-dioxo-3,6-dihydropyridazin-1(2*H*)-yl)-3-oxo-7,10,13,16,19,22-hexaoxa-4-azapentacosan-25-oic acid **64**

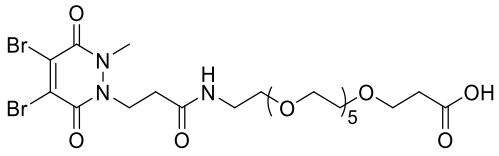

64

To a solution of *tert*-butyl 1-(4,5-dibromo-2-methyl-3,6-dioxo-3,6-dihydropyridazin-1(2*H*)-yl)-3-oxo-7,10,13,16,19,22-hexaoxa-4-azapentacosan-25-oate **63** (530 mg, 0.71 mmol) in DCM (6 mL), was added TFA (2 mL) and reaction stirred for 2h. After this time, solvent and excess TFA were removed *in vacuo* to afford 1-(4,5-dibromo-2-methyl-3,6-dioxo-3,6-dihydropyridazin-1(2*H*)-yl)-3-oxo-7,10,13,16,19,22-hexaoxa-4-azapentacosan-25-oic acid **64** (480 mg, 0.69 mmol, 97%) as a clear oil. ^{1}H NMR (600 MHz, $CDCl_3$) δ 7.37 (s, 1H), 4.45 (t, *J* = 7.0 Hz, 2H), 3.75 (t, *J* = 5.9 Hz, 2H), 3.72 (s, 3H), 3.66-3.61 (m, 20H), 3.57-3.55 (m, 2H), 3.43-3.40 (m, 2H), 2.65 (t, *J* = 7.0 Hz, 2H), 2.58-2.56 (m, 2H). ^{13}C NMR (150 MHz, $CDCl_3$, rotamers) δ 174.1 (C), 172.2 (C), 170.1 (C), 153.1 (C), 152.9 (C),136.3 (C), 135.5 (C), 70.6 (CH_2 × 10), 70.5 (CH_2), 70.3 (CH_2), 70.1 (CH_2), 69.7 (CH_2), 66.8 (CH_2), 50.9 (CH_2), 44.5 (CH_2), 39.6 (CH_2), 35.2 (CH_2), 35.1 (CH_2), 33.8 (CH_3), 25.6 (CH_2). IR (thin film) 3308, 2871, 1779, 1714, 1630 cm^{-1}. LRMS (ESI) 690 (60, $[M^{79}Br^{81}Br+H]^+$; HRMS (ESI) calcd for $C_{23}H_{37}Br_2N_3O_{11}$ $[M^{79}Br^{81}Br+H]^+$ 690.0717; observed 690.0716.

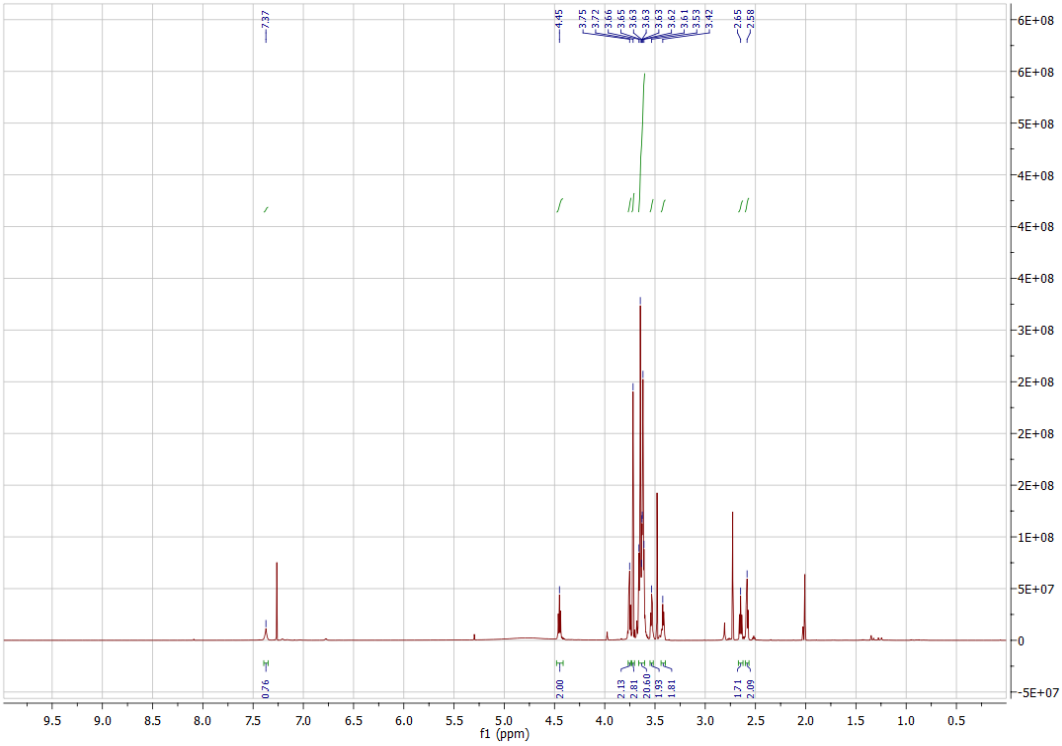
7.37
4.45
3.75
3.72
3.66
3.65
3.63
3.63
3.63
3.62
3.61
3.53
3.42
2.65
2.58
0.76
2.00
2.13
2.81
20.60
1.93
1.81
1.71
2.09
f1 (ppm)

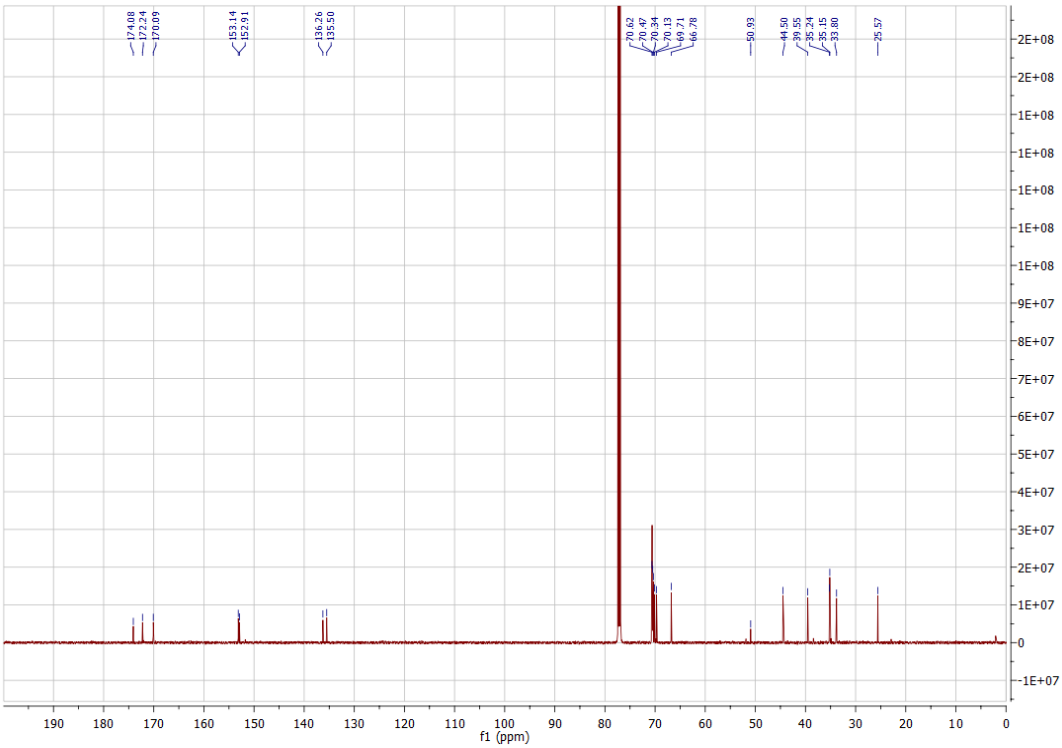
174.08
172.24
170.09
153.14
152.91
136.26
135.50
70.62
70.47
70.34
70.13
69.71
66.78
50.93
44.50
39.55
35.24
35.15
33.80
25.57
f1 (ppm)

2,5-dioxopyrrolidin-1-yl 1-(4,5-dibromo-2-methyl-3,6-dioxo-3,6-dihydropyridazin-1(2H)-yl)-3-oxo-7,10,13,16,19,22-hexaoxa-4-azapentacosan-25-oate **65**

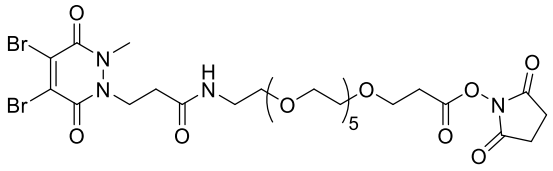

To a solution of 1-(4,5-dibromo-2-methyl-3,6-dioxo-3,6-dihydropyridazin-1(2*H*)-yl)-3-oxo-7,10,13,16,19,22-hexaoxa-4-azapentacosan-25-oic acid **64** (60 mg, 0.076 mmol) in THF (1 mL) at 0 °C, *N*,*N*'-dicyclohexylcarbodiimide (19 mg, 0.091 mmol) was added and the reaction was stirred for 30 min. After this time, *N*-hydrosuccinimide (11 mg, 0.091 mmol) was added and mixture was stirred for 16 h, at 21 °C. After this time, solvent was removed *in vacuo* and purification of the crude residue by flash chromatography (0% to 20% MeOH/EtOAc) afforded 2,5-dioxopyrrolidin-1-yl 1-(4,5-dibromo-2-methyl-3,6-dioxo-3,6-dihydropyridazin-1(2H)-yl)-3-oxo-7,10,13,16,19,22-hexaoxa-4-azapentacosan-25-oate **65** (13 mg, 0.016 mmol, 21%) as a yellow oil. ^{1}H NMR (600 MHz, $CDCl_3$, mixture of rotamers) δ 6.96-6.94 (m, 1H), 4.44-4.42 (m, 2H), 3.83 (t, *J* = 6.4 Hz, 2H), 3.71-3.60 (m, 25H), 3.53-3.51 (m, 2H), 3.42-3.40 (m, 2H), 2.90-2.88 (m, 2H), 2.83 (br s, 4H), 2.72-2.70 (m, 2H). ^{13}C NMR (125 MHz, $CDCl_3$, rotamers) δ 169.4 (C), 169.1 (C), 166.9 (C), 153.2 (C), 152.9 (C), 136.2 (C), 135.5 (C), 70.9 (CH_2), 70.6 (CH_2 × 10), 69.7 (CH_2), 65.9 (CH_2), 44.5 (CH_2), 39.5 (CH_2), 35.1 (CH_2), 33.9 (CH_2), 32.3 (CH_3), 25.7 (CH_2).

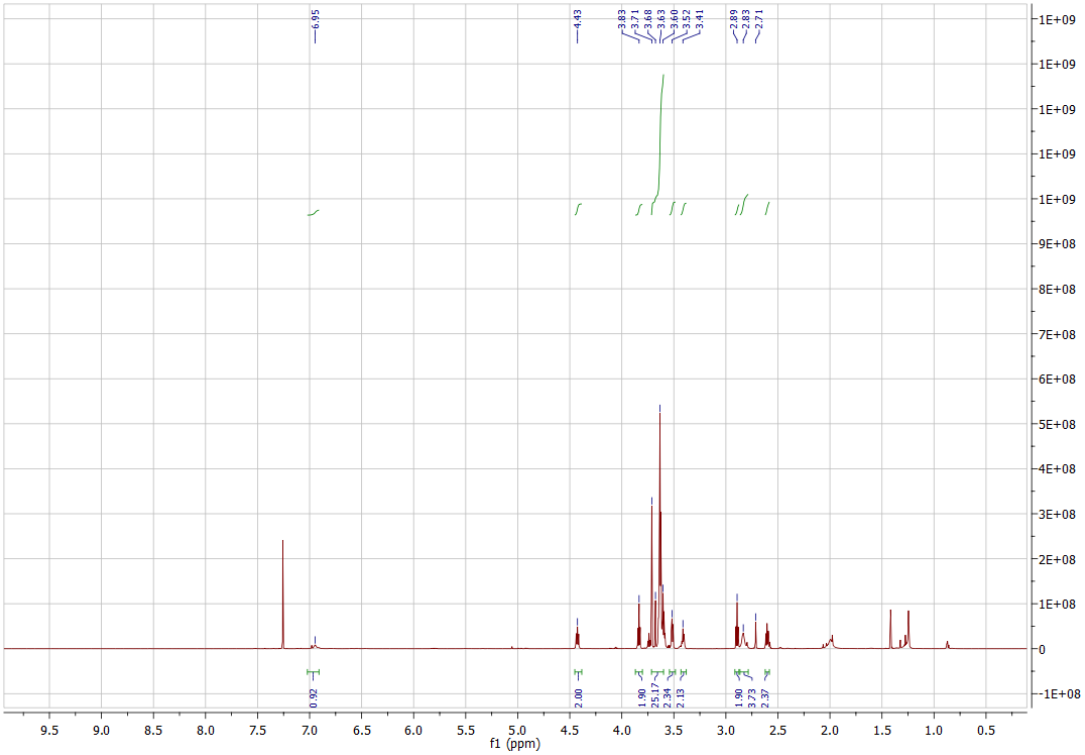
6.95
4.43
3.83
3.71
3.68
3.63
3.60
3.52
3.41
2.89
2.83
2.71
0.92
2.00
1.90
25.17
2.34
2.13
1.90
3.73
2.37
f1 (ppm)

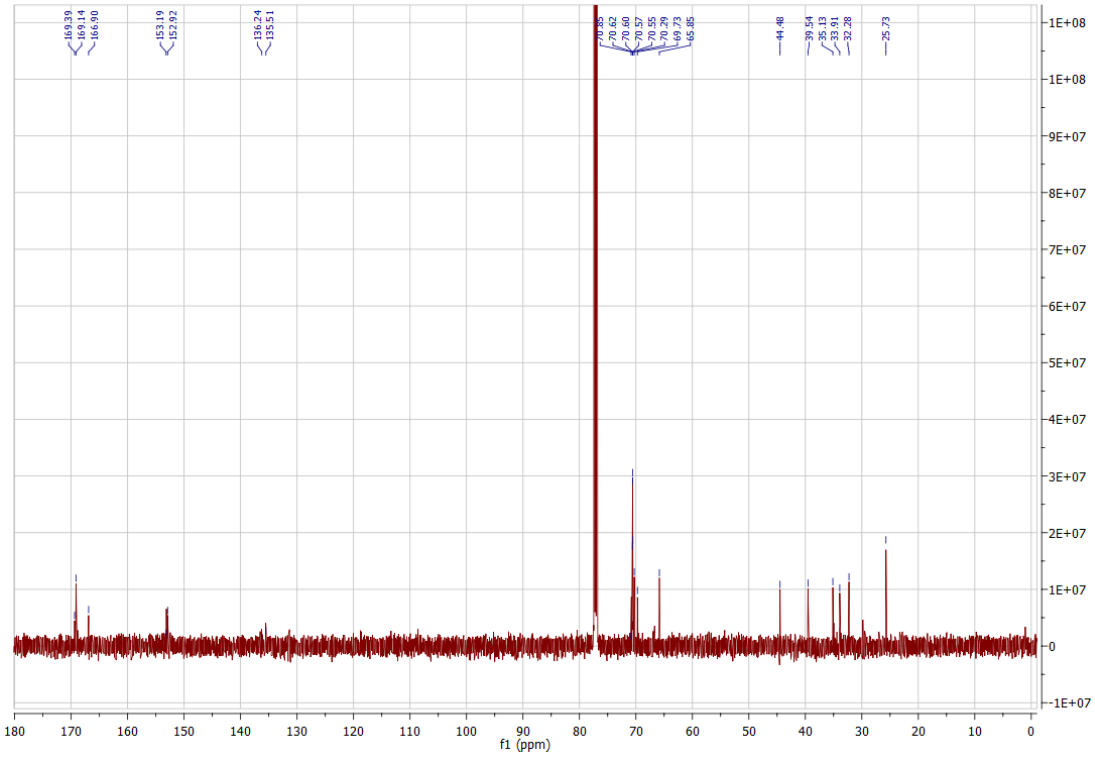
169.39
169.14
166.90
153.19
152.92
136.24
135.51
70.85
70.62
70.60
70.57
70.55
70.29
69.73
65.85
44.48
39.54
35.13
33.91
32.28
25.73
f1 (ppm)

Tetrazine pyridazinedione synthesis

tert-Butyl (4-cyanobenzyl)carbamate[172] **67**

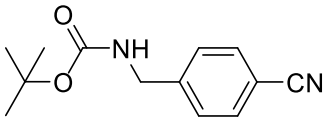

67

To a stirring solution of di-*tert*-butyl dicarbonate (7.1 g, 32.6 mmol), NaOH (3.6 g, 89.1 mmol) in H_2O (30 mL) at 21 ºC, 4-(aminomethyl)benzonitrile **66** (5.0 g; 29.7 mmol) was added. The mixture was stirred for 16 h, after which time a white precipitate had formed. The mixture was filtered, washed with H_2O (100 mL), and the resulting solid dried under vacuum to yield *tert*-butyl (4-cyanobenzyl)carbamate **67** as a white solid (6.71 g, 28.8 mmol, 97%). ^{1}H NMR (600 MHz, $CDCl_3$) δ 7.62 (d, *J* = 8.3, 2H), 7.38 (d, *J* = 8.3, 2H), 4.95 (br s, 1H), 4.36 (d, *J* = 5.9 Hz, 2H), 1.46 (s, 9H); ^{13}C NMR (150 MHz, $CDCl_3$) δ 144.7 (C), 132.5 (CH), 127.9 (CH), 118.8 (C), 111.1 (C), 80.1 (C), 44.3 (CH_2), 28.4 (CH_3); IR (solid) 3350, 2974, 2927, 2226, 1692 cm^{-1}.

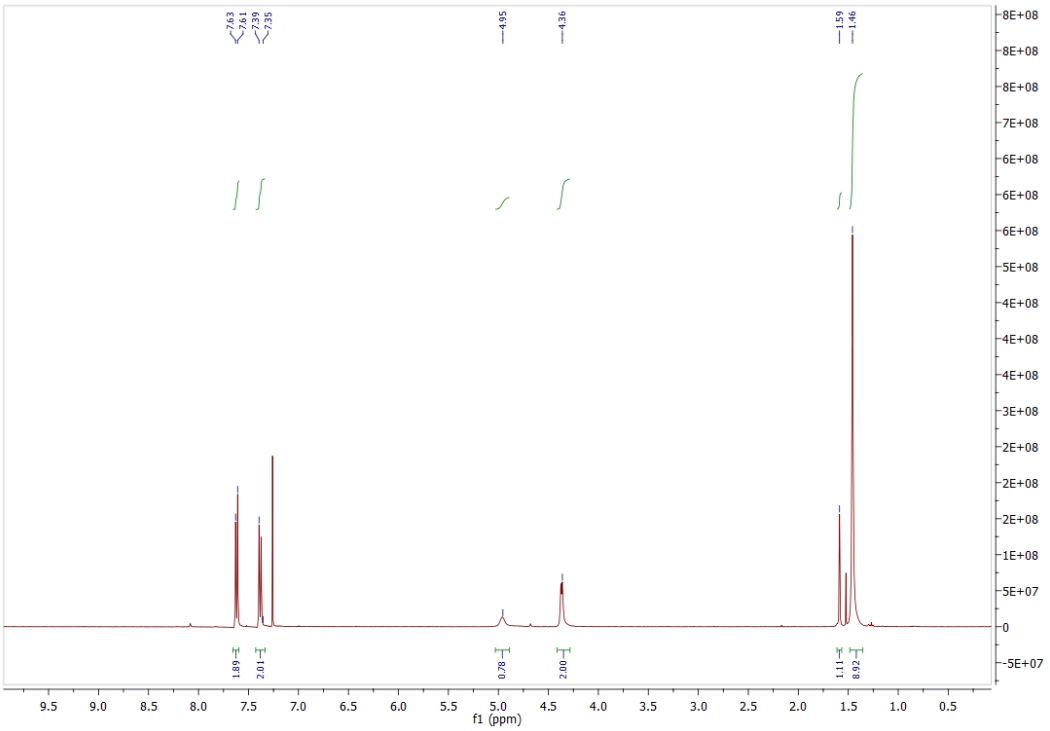
7.63
7.61
7.39
7.35
4.95
4.36
1.59
1.46
1.89
2.01
0.78
2.00
1.11
8.92
f1 (ppm)

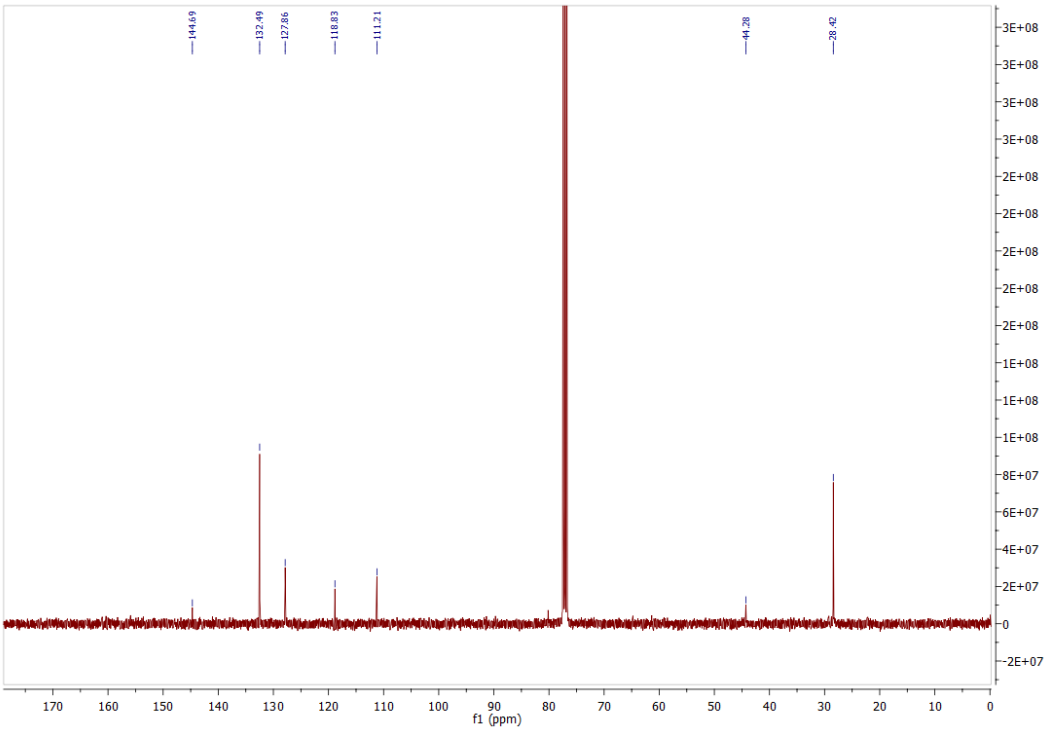
144.69
132.49
127.86
118.83
111.21
44.28
28.42
f1 (ppm)

tert-Butyl (4-(6-methyl-1,2,4,5-tetrazin-3-yl)benzyl)carbamate[172] **68**

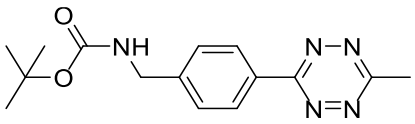

68

Hydrazine hydrate (80% w/w, 39.5 mL, 64.6 mmol) was added to a stirring suspension of *tert*-butyl carbamate **67** (3.0 g, 12.9 mmol), acetonitrile (6.72 mL, 12.9 mmol), and $Zn(OTf)_2$ (2.34 g, 6.46 mmol) in 1,4-dioxane (6 mL) at 21 ºC. The reaction was heated to 65 °C and stirred for 72 h. The reaction was cooled to 21 ºC and diluted with EtOAc (50 mL). The reaction was washed with 1 M HCl (50 mL) and the aqueous phase extracted with EtOAc (2 × 30 mL). The organic phase was dried ($MgSO_4$), filtered and evaporated under reduced pressure. The resulting crude residue was dissolved in a mixture of DCM and acetic acid (1:1, 200 mL), and $NaNO_2$ (17.8 g, 258 mmol) was added slowly over a period of 15 minutes, during which time the reaction turned bright red. The reaction was diluted with DCM (200 mL). The reaction mixture was washed with sodium bicarbonate (sat., aq., 200 mL) and the aqueous phase extracted with DCM (2 × 100 mL). The organic phase was dried ($MgSO_4$), filtered and the solvent removed *in vacuo*. The resulting residue was purified by silica gel chromatography (20% EtOAc/petrol) to yield *tert*-butyl (4-(6-methyl-1,2,4,5-tetrazin-3-yl)benzyl)carbamate **68** as a pink solid (920 mg, 3.05 mmol, 24%). ^{1}H NMR (600 MHz, $CDCl_3$) δ 8.53 (d, J = 8.4 Hz, 2H), 7.49 (d, J = 8.3 Hz, 2H), 5.00 (br s, 1H), 4.43 (s, 2H), 3.08 (s, 3H), 1.47 (s, 9H); ^{13}C NMR (150 MHz, $CDCl_3$) δ 167.3 (C), 164.0 (C), 144.1 (C), 130.9 (CH), 128.3 (CH), 128.1 (C), 80.1 (C), 28.4 (CH_3), 21.2 (CH_3); IR (solid) 3339, 2974, 2928, 1696, 1516 cm^{-1}.

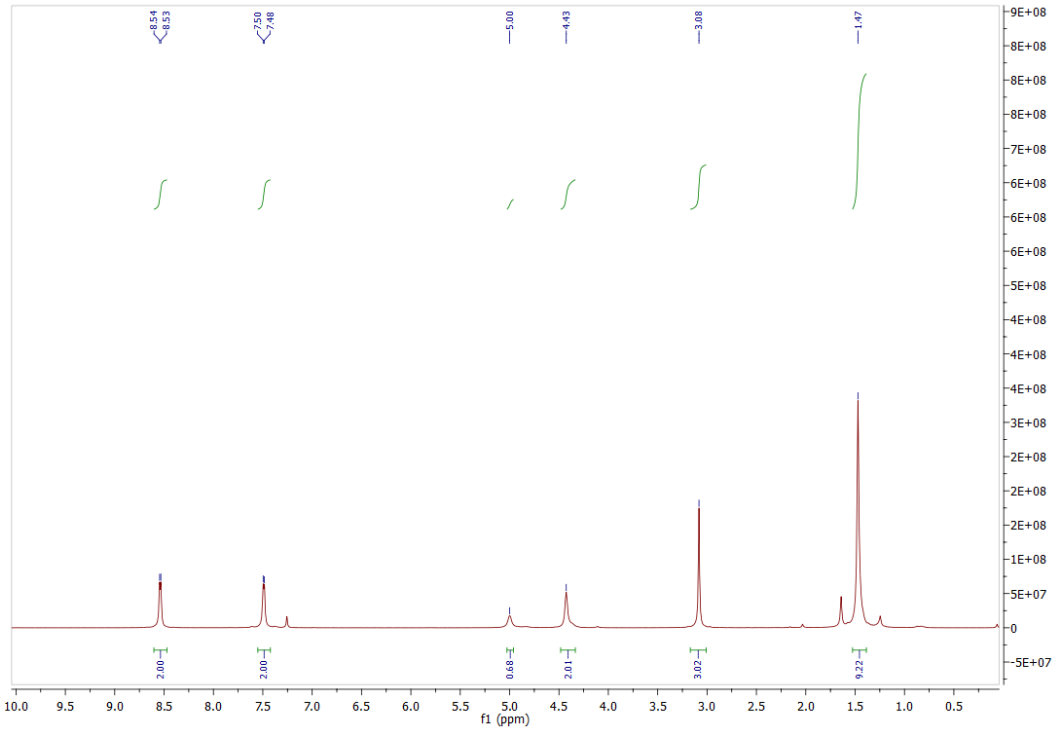
8.54
8.53
7.50
7.48
5.00
4.43
3.08
1.47
2.00
2.00
0.68
2.01
3.02
9.22
f1 (ppm)

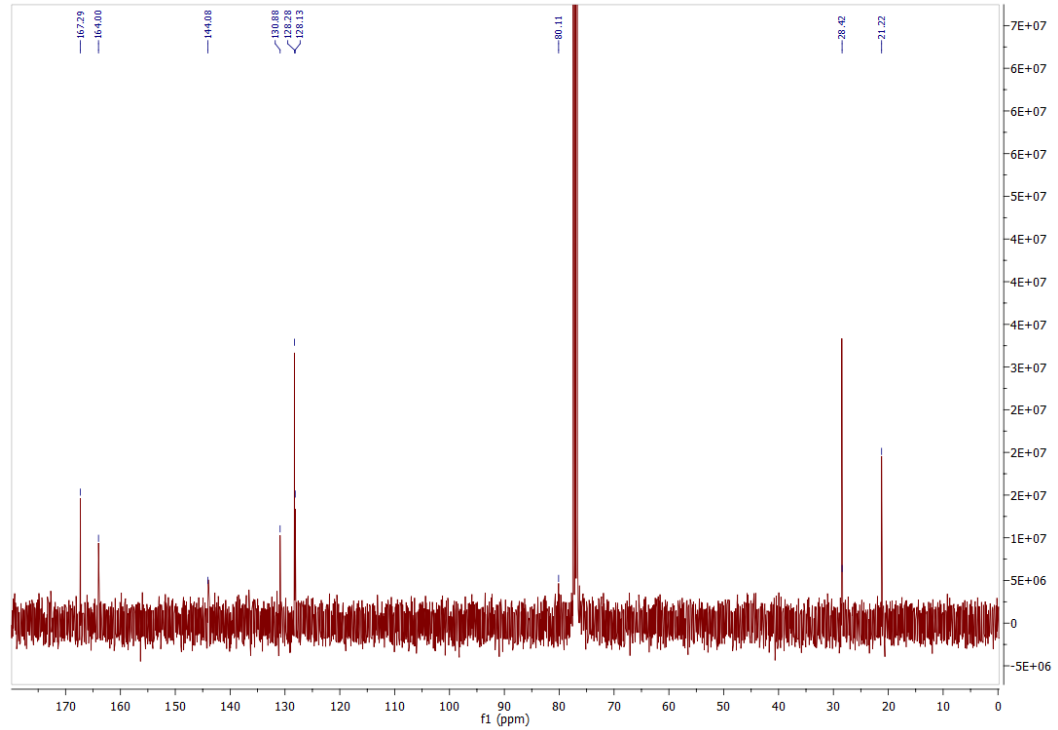
167.29
164.00
144.08
130.88
129.28
128.13
80.11
28.42
21.22
f1 (ppm)

5-((4-(6-Methyl-1,2,4,5-tetrazin-3-yl)benzyl)amino)-5-oxopentanoic acid **69**

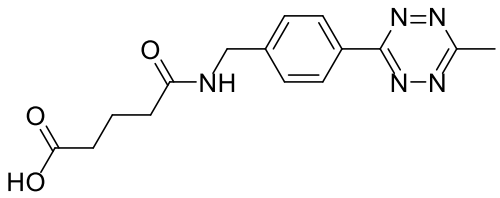

69

tert-Butyl (4-(6-methyl-1,2,4,5-tetrazin-3-yl)benzyl)carbamate **68** (800 mg, 2.65 mmol) in a mixture of TFA and DCM (1:4, 20 mL) was stirred at 21 ºC for 2 h. The solvent was removed *in vacuo* and the mixture re-dissolved in THF (50 mL). To this solution was added glutaric anhydride (605 mg, 5.31 mmol) and the mixture stirred at 55 °C for 16 h. The solvent was removed *in vacuo* and the mixture re-dissolved in saturated aqueous K_2CO_3 solution (100 mL). The mixture was then acidified with 15% HCl solution until the mixture stopped producing CO_2 (g) on acid addition. The mixture was then extracted with EtOAc (3 × 50 mL) and the combined organic phases washed with H_2O (4 × 30 mL), brine (30 mL), dried ($MgSO_4$). Any precipitate formed during extraction was re-dissolved in saturated aqueous K_2CO_3 solution (30 mL) and the work-up was repeated on this solution and the dried organic phases were combined, filtered and the solvent removed *in vacuo*, to yield 5-((4-(6-methyl-1,2,4,5-tetrazin-3-yl)benzyl)amino)-5-oxopentanoic acid **69** as a purple powder (603 mg, 1.92 mmol, 72%) without further purification. ^{1}H NMR (600 MHz, DMSO-d_6) δ 8.42 (d, *J* = 8.4, 2H), 7.52 (d, *J* = 8.5 Hz, 2H), 4.39 (d, *J* = 6.0 Hz, 2H), 2.99 (s, 3H), 2.23 (q, *J* = 7.4 Hz, 4H), 1.77 (m, 2 H); ^{13}C NMR (150 MHz, DMSO-d_6) δ 174.2 (C), 171.9 (C), 167.1 (C), 163.2 (C), 144.5 (C), 130.4 (CH), 128.1 (CH), 127.5 (C), 41.9 (CH_2), 34.4 (CH_2), 33.1 (CH_2), 20.8 (CH_3), 20.7 (CH_2); IR (solid) 3271, 3025, 2973, 2923, 2880, 1694, 1630, 1523 cm^{-1}.

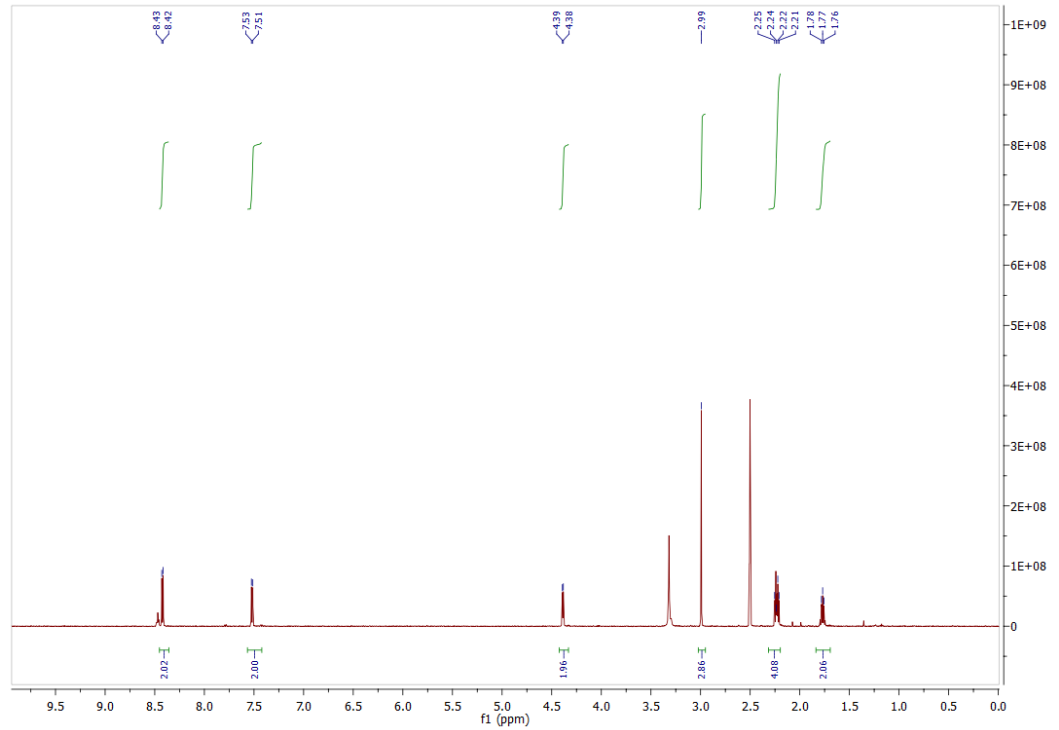
8.43
8.42
7.53
7.51
4.39
4.38
2.99
2.25
2.24
2.22
2.21
1.78
1.77
1.76
2.02
2.00
1.96
2.86
4.08
2.06
f1 (ppm)

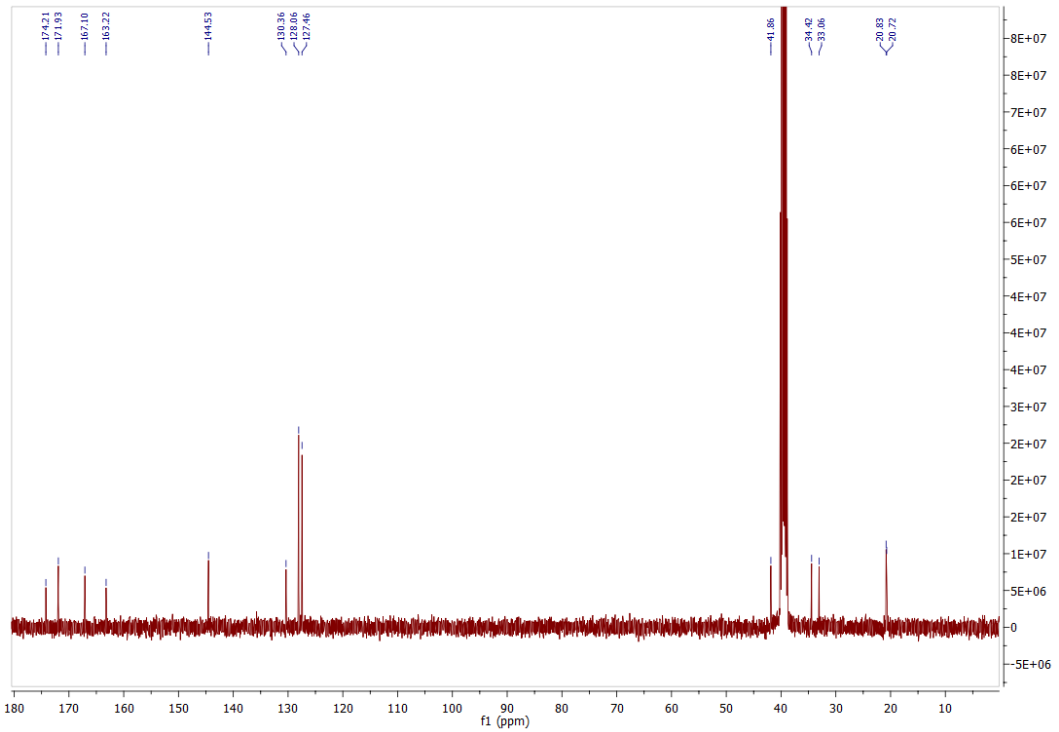
174.21
171.93
167.10
163.22
144.53
130.36
128.06
127.46
41.86
34.42
33.06
20.83
20.72
f1 (ppm)

tert-Butyl (3-(2-(2-(3-aminopropoxy)ethoxy)ethoxy)propyl)carbamate[173] **70**

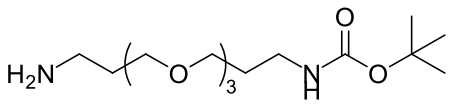

70

To a solution of 3,3'-((oxybis(ethane-2,1-diyl))bis(oxy))bis(propan-1-amine) (8.10 g, 37.1 mmol) in 1,4-dioxane (60 mL) was added dropwise di-*tert*-butyl dicarbonate (1.00 g, 4.60 mmol, pre-dissolved in 1,4-dioxane (25 mL)) over 2 h, ensuring that the temperature did not exceed 21°C. After this time, the reaction mixture was stirred at 21 °C for a further 30 min. Following this, the reaction mixture was concentrated *in vacuo*, the crude residue dissolved in water (50 mL), and the organic layer extracted with EtOAc (5 × 30 mL). The organic layers were combined, dried ($MgSO_4$) and concentrated *in vacuo* to yield *tert*-butyl (3-(2-(2-(3-aminopropoxy)ethoxy)ethoxy)propyl)carbamate **70** (880 mg, 27.2 mmol, 60%) as a colourless oil. ^{1}H NMR (600 MHz, $CDCl_3$) δ 5.10 (br s, 1H), 3.63-3.54 (m,12H), 3.22-3.21 (m, 2H), 2.83 (t, J = 6.7 Hz, 2H), 1.76-1.73 (m, 4H), 1.42 (s, 9H); ^{13}C NMR (150 MHz, $CDCl_3$) δ 156.3 (C), 79.0 (C), 70.7 (CH_2), 70.7 (CH_2), 70.3 (CH_2), 70.3 (CH_2), 69.7 (CH_2), 69.6 (CH_2), 39.8 (CH_2), 38.6 (CH_2), 32.8 (CH_2), 29.8 (CH_2), 28.6 (CH_3); IR (thin film) 3360, 2928, 2865, 1696, 1521, 1102 cm^{-1}.

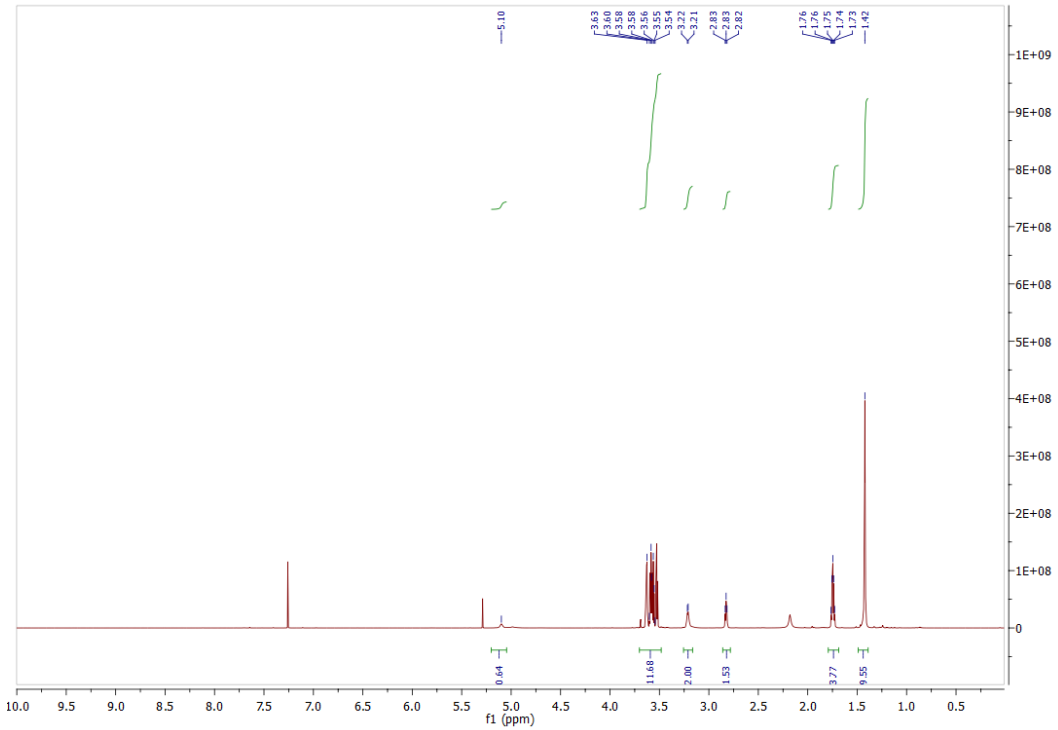
5.10
3.63
3.60
3.58
3.56
3.55
3.54
3.22
3.21
2.83
2.83
2.82
1.76
1.76
1.75
1.74
1.73
1.42
0.64
11.68
2.00
1.53
3.77
9.55
f1 (ppm)

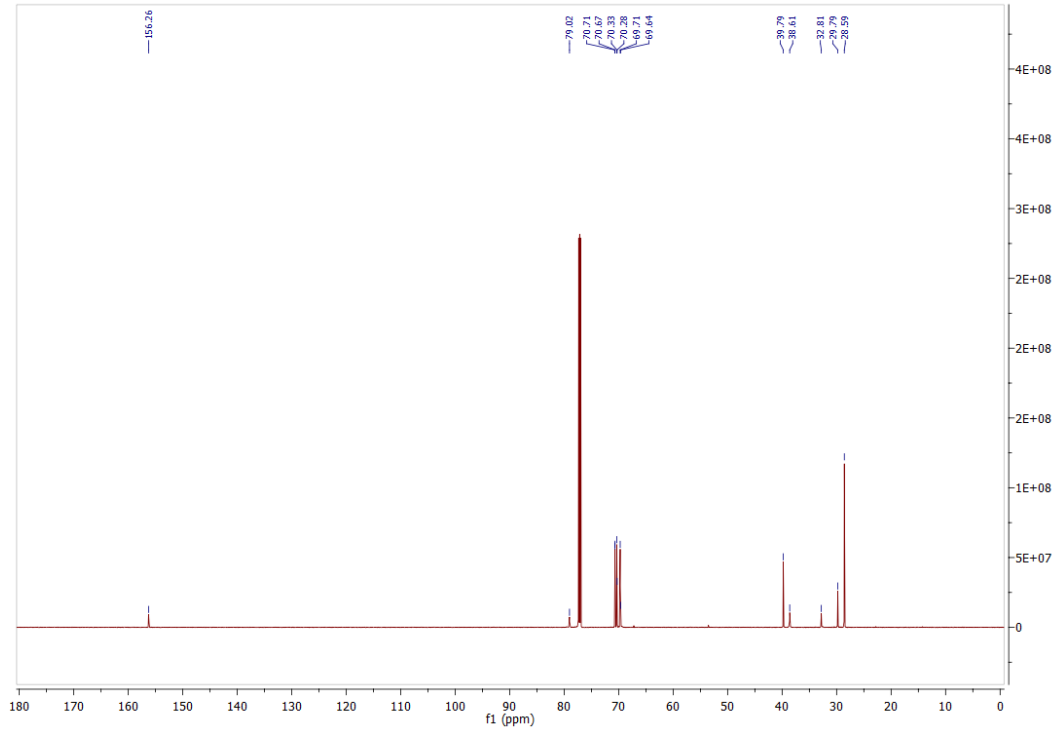
156.26
79.02
70.71
70.67
70.33
70.28
69.71
69.64
39.79
38.61
32.81
29.79
28.59
f1 (ppm)

tert-Butyl (1-(4-(6-methyl-1,2,4,5-tetrazin-3-yl)phenyl)-3,7-dioxo-12,15,18-trioxa-2,8-diazahenicosan-21-yl)carbamate **71**

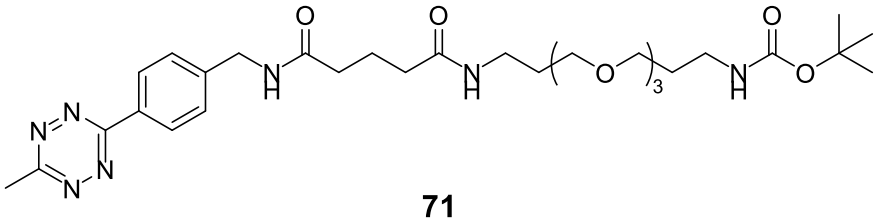

71

To a solution of 5-((4-(6-methyl-1,2,4,5-tetrazin-3-yl)benzyl)amino)-5-oxopentanoic acid **69** (200 mg, 0.63 mmol), HATU (240 mg, 0.63 mmol), and NEt_3 (64 mg, 0.63 mmol) in DCM (5 mL), *tert*-butyl (3-(2-(2-(3-aminopropoxy)ethoxy)ethoxy)propyl)carbamate **70** (220 mg, 0.69 mmol) in DCM (5 mL) was added. The resulting solution was stirred at 21 ºC for 16 h. The solvent was removed *in vacuo*, and the mixture re-dissolved in 1 M HCl solution (20 mL) and washed with DCM (3 × 20 mL) to remove unreacted 5-((4-(6-methyl-1,2,4,5-tetrazin-3-yl)benzyl)amino)-5-oxopentanoic acid **69**. The aqueous phase was then basified with saturated aqueous K_2CO_3 solution, extracted with DCM (3 × 20 mL). The combined organic phases were extracted with 1 M HCl solution (20 mL). The aqueous phase was basified with saturated aqueous K_2CO_3 solution and extracted with DCM (3 × 20 mL). The combined organic phases were washed with brine (20 mL), dried ($MgSO_4$), filtered and the solvent removed *in vacuo*. The crude residue was purified by flash column chromatography (0–10% MeOH in EtOAc) to afford *tert*-butyl (1-(4-(6-methyl-1,2,4,5-tetrazin-3-yl)phenyl)-3,7-dioxo-12,15,18-trioxa-2,8-diazahenicosan-21-yl)carbamate **71** (237 mg, 60%) as a purple oil: ^{1}H NMR (600 MHz, $CDCl_3$) δ 8.49 (d, *J* = 8.4 Hz, 2H), 7.53 (d, *J* = 8.5 Hz, 2H), 4.48-4.45 (m, 2H), 3.63-3.48 (m, 12H), 3.26-3.24 (m, 2H), 3.11-3.09 (m, 2H), 3.02 (s, 3H), 2.31 (t, *J* = 7.5 Hz, 2H), 2.23 (t, *J* = 6.9 Hz, 2H), 1.96 (p, *J* = 6 Hz, 2H), 1.77-1.68 (m, 4H), 1.41 (s, 9H); ^{13}C NMR (150 MHz, $CDCl_3$) δ 175.3 (C), 175.1 (C), 168.6 (C), 165.1 (C), 158.4 (C), 145.0 (C), 132.2 (C), 129.2 (CH), 128.9 (CH), 79.7 (CH_2), 71.4 (CH_2), 71.4 (CH_2), 71.1 (CH_2 × 2), 69.8 (CH_2), 69.8 (CH_2), 43.7 (CH_2), 38.6 (CH_2), 37.7 (CH_2), 36.2 (CH_2), 36.1 (CH_2), 30.8 (CH_2), 30.3 (CH_2), 28.7 (CH_2), 23.1 (CH_3), 23.1 (C) 20.9 (CH_3). IR (thin film) 3281, 3270, 3024, 2973, 2928, 2867,1692, 1628, 1523 cm^{-1}.

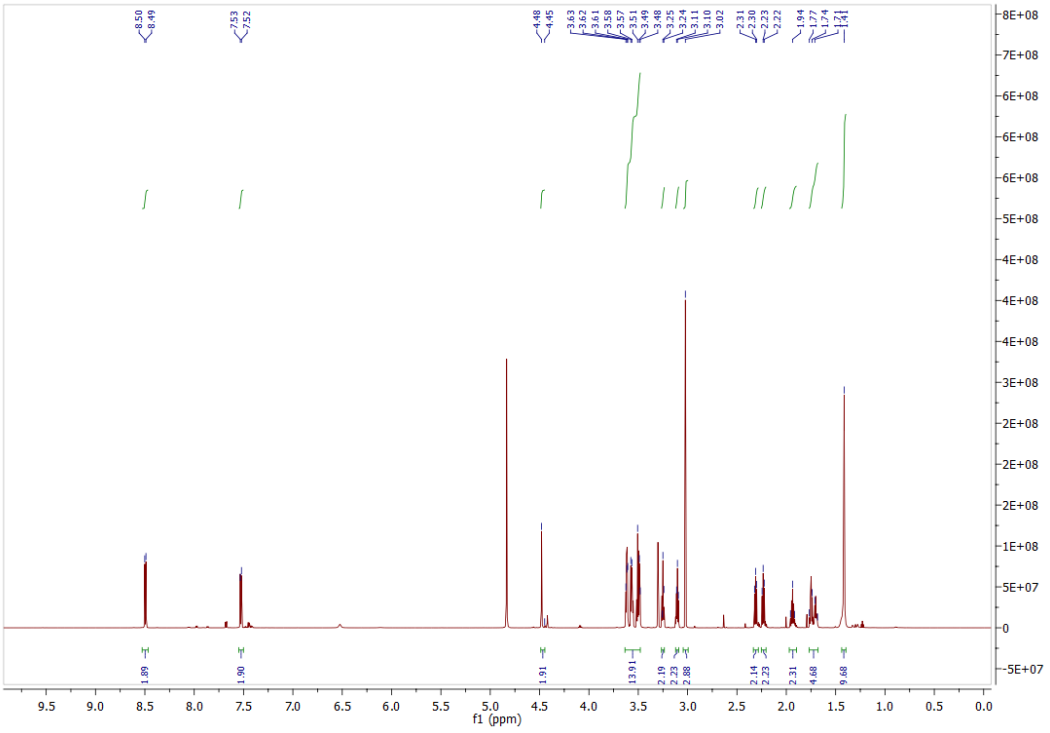
8.50
8.49
7.53
7.52
4.48
4.45
3.63
3.62
3.61
3.58
3.57
3.51
3.49
3.48
3.25
3.24
3.11
3.10
3.02
2.31
2.30
2.23
2.22
1.94
1.77
1.74
1.71
1.41
1.89
1.90
1.91
13.91
2.19
2.23
2.88
2.14
2.23
2.31
4.68
9.68
f1 (ppm)

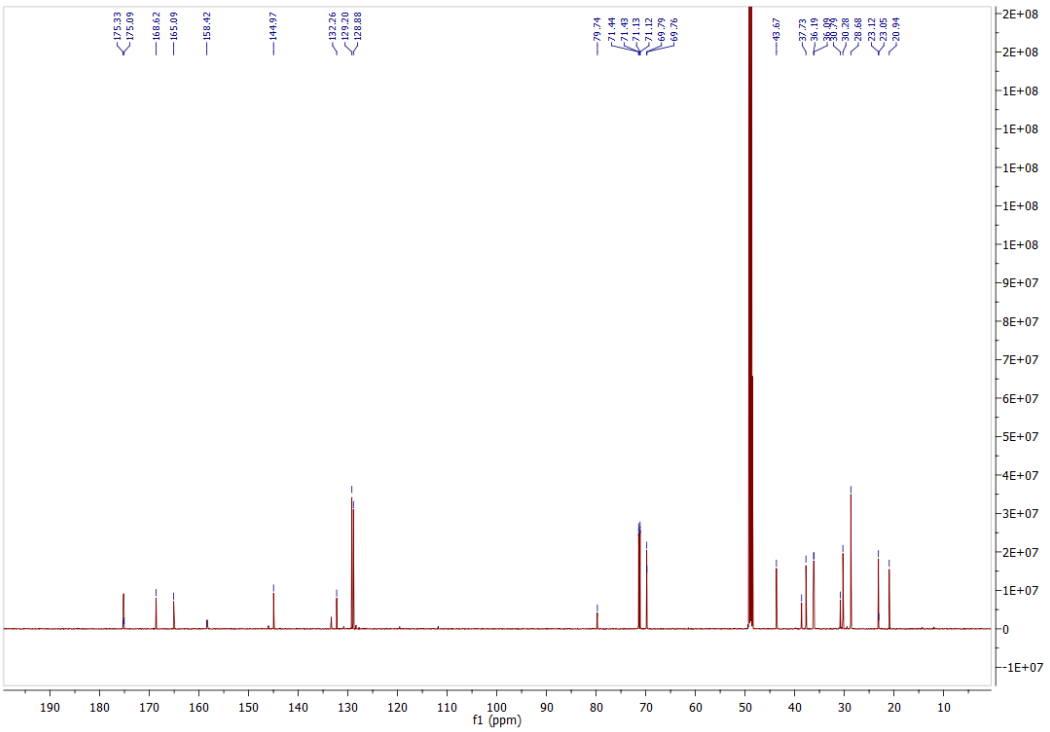
175.33
175.09
168.62
165.09
158.42
144.97
132.26
129.20
128.88
79.24
71.44
71.43
71.13
71.12
69.79
69.76
43.67
37.73
36.19
30.28
28.68
23.12
23.05
20.94
f1 (ppm)

References

1 E. A. Hoyt, P. M. S. D. Cal, B. L. Oliveira and G. J. L. Bernardes, *Nat. Rev. Chem.*, 2019, 3, 147–171.

2 Z. E. Sauna, H. A. D. Lagassé, A. Alexaki, V. L. Simhadri, N. H. Katagiri, W. Jankowski and C. Kimchi-Sarfaty, *F1000Research*, 2017, **6**, 113-130.

3 A. J. de Graaf, M. Kooijman, W. E. Hennink and E. Mastrobattista, *Bioconjug. Chem.*, 2009, **20**, 1281–1295.

4 E. M. Sletten and C. R. Bertozzi, *Angew. Chemie Int. Ed.*, 2009, **48**, 6974–6998.

5 C. D. Spicer and B. G. Davis, *Nat. Commun.*, 2014, **5**, 4740.

6 E. M. Sletten and C. R. Bertozzi, *Angew. Chemie - Int. Ed.*, 2009, **48**, 6974–6998.

7 E. Y. Chi, S. Krishnan, T. W. Randolph and J. F. Carpenter, *Pharm. Res.*, 2003, **20**, 1325–1336.

8 S. Girouard, M. H. Houle, A. Grandbois, J. W. Keillor and S. W. Michnick, *J. Am. Chem. Soc.*, 2005, **127**, 559–566.

9 S. Jevševar, M. Kunstelj and V. G. Porekar, *Biotechnol. J.*, 2010, **5**, 113–128.

10 D. Calarese, H.-K. Lee, C.-Y. Huang, M. D. Best, R. D. Astronomo, R. L. Stanfield, H. Katinger, D. R. Burton, C.-H. Wong and I. Wilson, *Proc. Natl. Acad. Sci. U. S. A.*, 2005, **102**, 13372–13377.

11 L. M. Krug, G. Ragupathi, K. K. Ng, C. Hood, H. J. Jennings, Z. Guo, M. G. Kris, V. Miller, B. Pizzo, L. Tyson, V. Baez and P. O. Livingston, *Clin. Cancer Res.*, 2004, **10**, 916–923.

12 L. Schofield, M. C. Hewitt, K. Evans, M.-A. Siomos and P. H. Seeberger, *Nature*, 2002, **418**, 785–789.

13 Z. Zhang, M. Tan, Z. Xie, L. Dai, Y. Chen and Y. Zhao, *Nat. Chem. Biol.*, 2011, **7**, 58–63.

14 J. M. Goddard and D. Erickson, *Anal. Bioanal. Chem.*, 2009, **394**, 469–479.

15 T. Nakamura, Y. Kawai, N. Kitamoto, T. Osawa and Y. Kato, *Chem. Res. Toxicol.*, 2009, **22**, 536–542.

16 S. Kalkhof and A. Sinz, *Anal. Bioanal. Chem.*, 2008, **392**, 305-312.

17 M. B. Francis and I. S. Carrico, *Curr. Opin. Chem. Biol.*, 2010, **14**, 771–773.

18 Y. Feng, Z. Zhu, W. Chen, P. Prabakaran, K. Lin and D. Dimitrov, *Biomedicines*, 2014, **2**, 1–13.

19 M. J. Matos, B. L. Oliveira, N. Martínez-Sáez, A. Guerreiro, P. M. S. D. Cal, J. Bertoldo, M. Maneiro, E. Perkins, J. Howard, M. J. Deery, J. M. Chalker, F. Corzana, G. Jiménez-Osés and G. J. L. Bernardes, *J. Am. Chem. Soc.*, 2018, **140**, 4004–4017.

20 T. H. Pillow, J. D. Sadowsky, D. Zhang, S.-F. Yu, G. Del Rosario, K. Xu, J. He, S. Bhakta, R. Ohri, K. R. Kozak, E. Ha, J. R. Junutula and J. A. Flygare, *Chem. Sci.*, 2017, **8**, 366–370.

21 Y. Zhang, V. S. Bhatt, G. Sun, P. G. Wang and A. F. Palmer, *Bioconjug. Chem.*, 2008, **19**, 2221–2230.

22 C. Lind, R. Gerdes, Y. Hamnell, I. Schuppe-Koistinen, H. B. Von Lwenhielm, A. Holmgren and I. A. Cotgreave, *Arch. Biochem. Biophys.*, 2002, **406**, 229–240.

23 M. Esmann, P. C. Sar, K. Hideg and D. Marsh, *Anal. Biochem.*, 1993, **213**, 336–348.

24 S. Trapp, *EMBO J.*, 2003, **22**, 2903–2912.

25 R. Bednar, *Biochemistry*, 1990, **29**, 3684–3690.

26 V. Chudasama, A. Maruani and S. Caddick, *Nat. Chem.*, 2016, **8**, 114–119.

27 E. Robinson, J. P. M. Nunes, V. Vassileva, A. Maruani, J. C. F. Nogueira, M. E. B. Smith, R. B. Pedley, S. Caddick, J. R. Baker and V. Chudasama, *RSC Adv.*, 2017, **7**, 9073–9077.

28 M. T. Petersen, P. H. Jonson and S. B. Petersen, *Protein Eng.*, 1999, **12**, 535–548.

29 M. Matsumura, W. J. Becktel, M. Levitt and B. W. Matthews, *Proc. Natl. Acad. Sci. U. S. A.*, 1989, **86**, 6562–6566.

30 S. Shaunak, A. Godwin, J.-W. Choi, S. Balan, E. Pedone, D. Vijayarangam, S. Heidelberger, I. Teo, M. Zloh and S. Brocchini, *Nat. Chem. Biol.*, 2006, **2**, 312–313.

31 A. Maruani, M. E. B. Smith, E. Miranda, K. A. Chester, V. Chudasama and S. Caddick, *Nat. Commun.*, 2015, **6**, 6645-6654.

32 M. T. W. Lee, A. Maruani, J. R. Baker, S. Caddick and V. Chudasama, *Chem. Sci.*, 2016, **7**, 799–802.

33 R. H. Buckley, *J. Clin. Invest.*, 2005, **115**, 2974–2976.

34 P. N. Nelson, G. M. Reynolds, E. E. Waldron, E. Ward, K. Giannopoulos and P. G. Murray, *Mol. Pathol.*, 2000, **53**, 111–117.

35 E. Drewe and R. J. Powell, *J. Clin. Pathol.*, 2002, **55**, 81–85.

36 H. Bouchard, C. Viskov and C. Garcia-Echeverria, *Bioorg. Med. Chem. Lett.*, 2014, **24**, 5357–5363.

37 M. Stern and R. Herrmann, *Crit. Rev. Oncol. Hematol.*, 2005, **54**, 11–29.

38 M. Trikha, L. Yan and M. T. Nakada, *Curr. Opin. Biotechnol.*, 2002, **13**, 609–614.

39 O. Leavy, *Nat. Rev. Immunol.*, 2010, **10**, 297–297.

40 D. A. Richards, A. Maruani and V. Chudasama, *Chem. Sci.*, 2017, **8**, 63–77.

41 G. M. Thurber, M. M. Schmidt and K. D. Wittrup, *Adv. Drug Deliv. Rev.*, 2008, **60**, 1421–1434.

42 K. L. Brogan, K. N. Wolfe, P. A. Jones and M. H. Schoenfisch, *Anal. Chim. Acta*, 2003, **496**, 73–80.

43 I. Buchwalow, V. Samoilova, W. Boecker and M. Tiemann, *Sci. Rep.*, 2011, **1**, 1–6.

44 J. P. M. Nunes, M. Morais, V. Vassileva, E. Robinson, V. S. Rajkumar, M. E. B. Smith, R. B. Pedley, S. Caddick, J. R. Baker and V. Chudasama, *Chem. Commun.*, 2015, **51**, 10624–10627.

45 A. Ritter, *Pharm. Technol.*, 2012, **1**, 42–47.

46 R. S. Zolot, S. Basu and R. P. Million, *Nat. Rev. Drug Discov.*, 2013, **12**, 259–260.

47 P. Bryant, M. Pabst, G. Badescu, M. Bird, W. McDowell, E. Jamieson, J. Swierkosz, K. Jurlewicz, R. Tommasi, K. Henseleit, X. Sheng, N. Camper, A. Manin, K. Kozakowska, K. Peciak, E. Laurine, R. Grygorash, A. Kyle, D. Morris, V. Parekh, A. Abhilash, J. W. Choi, J. Edwards, M. Frigerio, M. P. Baker and A. Godwin, *Mol. Pharm.*, 2015, **12**, 1872–1879.

48 H. Squires, M. Stevenson, E. Simpson, R. Harvey and J. Stevens, *Pharmacoeconomics*, 2016, 34, 673–680.

49 P. A. Szijj, C. Bahou and V. Chudasama, *Drug Discov. Today Technol.*, 2018, 30, 27–34.

50 N. S. Beckley, K. P. Lazzareschi, H. W. Chih, V. K. Sharma and H. L. Flores, *Bioconjug. Chem.*, 2013, **24**, 1674–1683.

51 A. M. Sochaj, K. W. Świderska and J. Otlewski, *Biotechnol. Adv.*, 2015, **33**, 775–784.

52 Q. Zhou, *Biomedicines*, 2017, **5**, 64.

53 R. Van Geel, M. A. Wijdeven, R. Heesbeen, J. M. M. Verkade, A. A. Wasiel, S. S. Van Berkel and F. L. Van Delft, *Bioconjug. Chem.*, 2015, **26**, 2233–2242.

54 M. T. W. Lee, A. Maruani and V. Chudasama, *J. Chem. Res.*, 2016, **40**, 1–9.

55 V. Chudasama, M. E. B. Smith, F. F. Schumacher, D. Papaioannou, G. Waksman, J. R. Baker and S. Caddick, *Chem. Commun.*, 2011, **47**, 8781–8783.

56 V. Chudasama, A. Maruani and S. Caddick, *Nat. Chem.*, 2016, **8**, 114–119.

57 H. C. Kolb and K. B. Sharpless, *Drug Discov. Today*, 2003, **8**, 1128–1137.

58 P. V. Chang, J. A. Prescher, E. M. Sletten, J. M. Baskin, I. A. Miller, N. J. Agard, A. Lo and C. R. Bertozzi, *Proc. Natl. Acad. Sci.*, 2010, **107**, 1821–1826.

59 J. Dommerholt, F. P. J. T. Rutjes and F. L. van Delft, *Top. Curr. Chem.*, 2016, **374**, 16.

60 A. T. Blomquist and F. Jaffe, *J. Am. Chem. Soc.*, 1958, **80**, 3405–3408.

61 S. Bernard, R. A. Kumar, K. Porte, P. Thuéry, F. Taran and D. Audisio, *European J. Org. Chem.*, 2018, **10**, 1–11.

62 C. G. Gordon, J. L. MacKey, J. C. Jewett, E. M. Sletten, K. N. Houk and C. R. Bertozzi, *J. Am. Chem. Soc.*, 2012, **134**, 9199–9208.

63 J. Dommerholt, S. Schmidt, R. Temming, L. J. A. Hendriks, F. P. J. T. Rutjes, J. C. M. Van Hest, D. J. Lefeber, P. Friedl and F. L. Van Delft, *Angew. Chemie - Int. Ed.*, 2010, **49**, 9422–9425.

64 J. Dommerholt, O. van Rooijen, A. Borrmann, C. F. Guerra, F. M. Bickelhaupt and F. L. van Delft, *Nat. Commun.*, 2014, **5**, 5378.

65 K. Chenoweth, D. Chenoweth and W. A. Goddard III, *Org. Biomol. Chem.*, 2009, **7**, 5255.

66 E. M. Sletten and C. R. Bertozzi, *Acc. Chem. Res.*, 2011, **44**, 666–676.

67 C. S. McKay and M. G. Finn, *Chem. Biol.*, 2014, 21, 1075–1101.

68 R. Seigneuric, L. Markey, D. S. Nuyten, C. Dubernet, C. T. Evelo, E. Finot and C. Garrido, *Curr. Mol. Med.*, 2010, **10**, 640–652.

69 C. Saraiva, C. Praça, R. Ferreira, T. Santos, L. Ferreira and L. Bernardino, *J. Control. Release*, 2016, **235**, 34–47.

70 D. Jiang, M. Niwa, A. C. Koong and S. Diego, 2016, **33**, 48–56.

71 M. Wang and M. Thanou, *Pharmacol. Res.*, 2010, **62**, 90–99.

72 K. Donaldson, V. Stone, C. L. Tran, W. Kreyling and P. J. A. Borm, *Occup. Environ. Med.*, 2004, **61**, 727–728.

73 C. Tassa, S. Y. Shaw and R. Weissleder, *Acc. Chem. Res.*, 2011, **44**, 842–852.

74 H. T. Ta, Z. Li, C. E. Hagemeyer, G. Cowin, S. Zhang, J. Palasubramaniam, K. Alt, X. Wang, K. Peter and A. K. Whittaker, *Biomaterials*, 2017, **134**, 31–42.

75 A. Ali, F. T. Hsu, C. L. Hsieh, C. Y. Shiau, C. H. Chiang, Z. H. Wei, C. Y. Chen and H. S. Huang, *Sci. Rep.*, 2016, **6**, 36650.

76 M. Bañobre-López, A. Teijeiro and J. Rivas, *Reports Pract. Oncol. Radiother.*, 2013, **18**, 397–400.

77 S. I. van Kasteren, S. J. Campbell, S. Serres, D. C. Anthony, N. R. Sibson and B. G. Davis, *Proc. Natl. Acad. Sci. U. S. A.*, 2009, **106**, 18–23.

78 J. Lodhia, G. Mandarano, N. Ferris, P. Eu and S. Cowell, *Biomed. Imaging Interv. J.*, 2010, **6**, 12.

79 X. Huang and M. A. El-Sayed, *J. Adv. Res.*, 2010, **1**, 13–28.

80 X. Yang, L.-J. Su, F. G. La Rosa, E. E. Smith, I. R. Schlaepfer, S. K. Cho, B. Kavanagh, W. Park and T. W. Flaig, *Bl. Cancer*, 2017, **3**, 201–210.

81 R. Chapman, Y. Lin, M. Burnapp, A. Bentham, D. Hillier, A. Zabron, S. Khan, M. Tyreman and M. M. Stevens, *ACS Nano*, 2015, **9**, 2565–2573.

82 H. De Jong, *Int. J. Nanomedicine*, 2008, **3**, 133.

83 N. I. Vazquez, Z. Gonzalez, B. Ferrari and Y. Castro, *Boletín la Soc. Española Cerámica y Vidr.*, 2017, **56**, 139–145.

84 Y. Wang, Q. Zhao, N. Han, L. Bai, J. Li, J. Liu, E. Che, L. Hu, Q. Zhang, T. Jiang and S. Wang, *Nanomedicine Nanotechnology, Biol. Med.*, 2015, **11**, 313–327.

85 C. Bharti, N. Gulati, U. Nagaich and A. Pal, *Int. J. Pharm. Investig.*, 2015, **5**, 124.

86 F. Pulizzi, *Nat. Nanotechnol.*, 2015, **10**, 993.

87 E. Groeneveld, L. Witteman, M. Lefferts, X. Ke, S. Bals, G. Van Tendeloo and C. de Mello Donega, *ACS Nano*, 2013, **7**, 7913–7930.

88 M. M. Barroso, *J. Histochem. Cytochem.*, 2011, **59**, 237–251.

89 D. Mo, L. Hu, G. Zeng, G. Chen, J. Wan, Z. Yu, Z. Huang, K. He, C. Zhang and M. Cheng, *Appl. Microbiol. Biotechnol.*, 2017, **101**, 2713–2733.

90 E. Sugawara and H. Nikaido, *Antimicrob. Agents Chemother.*, 2014, **58**, 7250–7257.

91 C. J. Gannon, P. Cherukuri, B. I. Yakobson, L. Cognet, J. S. Kanzius, C. Kittrell, R. B. Weisman, M. Pasquali, H. K. Schmidt, R. E. Smalley and S. A. Curley, *Cancer*, 2007, **110**, 2654–2665.

92 C. A. Poland, R. Duffin, I. Kinloch, A. Maynard, W. A. H. Wallace, A. Seaton, V. Stone, S. Brown, W. MacNee and K. Donaldson, *Nat. Nanotechnol.*, 2008, **3**, 423–428.

93 D. Elgrabli, W. Dachraoui, C. Ménard-Moyon, X. J. Liu, D. Bégin, S. Bégin-Colin, A. Bianco, F. Gazeau and D. Alloyeau, *ACS Nano*, 2015, **9**, 10113–10124.

94 U. Bulbake, S. Doppalapudi, N. Kommineni and W. Khan, *Pharmaceutics*, 2017, **9**, 12.

95 A. L. Klibanov, T. I. Shevchenko, B. I. Raju, R. Seip and C. T. Chin, *J. Control.*

Release, 2010, **148**, 13–17.

96 A. Hussain, S. Singh, D. Sharma, T. J. Webster, K. Shafaat and A. Faruk, *Int. J. Nanomedicine*, 2017, **12**, 5087–5108.

97 H. M. Aliabadi and A. Lavasanifar, *Expert Opin. Drug Deliv.*, 2006, **3**, 139–162.

98 Y. Zhang, Y. Huang and S. Li, *AAPS PharmSciTech*, 2014, **15**, 862–871.

99 Y. Lu and K. Park, *Int. J. Pharm.*, 2013, **453**, 198–214.

100 D. Pandita, N. Poonia, S. Kumar, V. Lather and K. Madaan, *J. Pharm. Bioallied Sci.*, 2014, **6**, 139.

101 E. Abbasi, S. Aval, A. Akbarzadeh, M. Milani, H. Nasrabadi, S. Joo, Y. Hanifehpour, K. Nejati-Koshki and R. Pashaei-Asl, *Nanoscale Res. Lett.*, 2014, **9**, 247.

102 Y. H. Tang, A. Ya Ting Huang, P. Y. Chen, H. T. Chen and C. L. Kao, *Curr. Pharm. Des.*, 2011, **17**, 2308–2330.

103 M. Yan, J. Wen, M. Liang, Y. Lu, M. Kamata and I. S. Y. Chen, *PLoS One*, 2015, **10**, 1–15.

104 C. Scott, Abdelghany, Quinn, Ingram, Gilmore, Donnelly and Taggart, *Int. J. Nanomedicine*, 2012, **7**, 4053.

105 F. Masood, *Mater. Sci. Eng. C*, 2016, **60**, 569–578.

106 K. S. Soppimath, T. M. Aminabhavi, A. R. Kulkarni and W. E. Rudzinski, *J. Control. Release*, 2001, **70**, 1–20.

107 A. Kumari, S. K. Yadav and S. C. Yadav, *Colloids Surfaces B Biointerfaces*, 2010, **75**, 1–18.

108 H. K. Makadia and S. J. Siegel, *Polymers (Basel).*, 2011, **3**, 1377–1397.

109 E. Locatelli and M. Comes Franchini, *J. Nanoparticle Res.*, 2012, **14**, 1316.

110 J. M. Chan, P. M. Valencia, L. Zhang, R. Langer and O. C. Farokhzad, *Methods Mol Biol*, 2010, **624**, 163–175.

111 P. Anand, A. B. Kunnumakara, C. Sundaram, K. B. Harikumar, S. T. Tharakan, O. S. Lai, B. Sung and B. B. Aggarwal, *Pharm. Res.*, 2008, **25**, 2097–2116.

112 A. Pavlopoulou, D. A. Spandidos and I. Michalopoulos, *Oncol. Rep.*, 2015, **33**, 3–18.

113 CancerResearch, Cancer statistics for the UK, http://www.cancerresearchuk.org/health-professional/cancer-statistics.

114 S. D. Steichen, M. Caldorera-Moore and N. A. Peppas, *Eur. J. Pharm. Sci.*, 2013, **48**, 416–427.

115 H. Vriesendorp, R. Vriesendorp and F. Vriesendorp, *Cancer Chemother.*

Pharmacol., 1987, **19**, 273–276.

116 Y. Chen, P. Jungsuwadee, M. Vore, D. A. Butterfield and D. K. St. Clair, *Mol. Interv.*, 2007, **7**, 147–156.

117 S.-S. Feng and S. Chien, *Chem. Eng. Sci.*, 2003, **58**, 4087–4114.

118 R. Solaro, F. Chiellini and A. Battisti, *Materials (Basel).*, 2010, **3**, 1928–1980.

119 C. Fonseca, S. Simoes and R. Gaspar, *J. Control. Release*, 2002, **83**, 273–286.

120 J. Davda and V. Labhasetwar, *Int. J. Pharm.*, 2002, **233**, 51–59.

121 S. E. Gelperina, A. S. Khalansky, I. N. Skidan, Z. S. Smirnova, A. I. Bobruskin, S. E. Severin, B. Turowski, F. E. Zanella and J. Kreuter, *Toxicol. Lett.*, 2002, **126**, 131–141.

122 P. McCarron, D. Woolfson and S. M. Keating, *J. Pharm. Pharmacol.*, 2000, **52**, 1451–1459.

123 A. Z. Wang, *Sci. Transl. Med.*, 2015, **7**, 113-118..

124 K. S. Fountain and G. D. J. Malkasian, *Cancer*, 1981, **47**, 2430–2432.

125 N. F. Steinmetz, *Biomed. Eng. Online*, 2010, **9**, 55.

126 J. Shi, P. W. Kantoff, R. Wooster and O. C. Farokhzad, *Nat. Rev. Cancer*, 2016, **17**, 20–37.

127 R. Bazak, M. Houri, S. El Achy, W. Hussein and T. Refaat, *Mol. Clin. Oncol.*, 2014, **2**, 904–908.

128 K. Ogawara, Y. Yoshizawa, K. Un, T. Araki and T. Kimura, *Biol. Pharm. Bull.*, 2013, **36**, 698–702.

129 F. X. Gu, R. Karnik, A. Z. Wang, F. Alexis, E. Levy-Nissenbaum, S. Hong, R. S. Langer and O. C. Farokhzad, *Nano Today*, 2007, **2**, 14–21.

130 I. Brigger, C. Dubernet and P. Couvreur, *Adv. Drug Deliv. Rev.*, 2002, **54**, 631–651.

131 M. A. Phillips, M. L. Gran and N. A. Peppas, *Nano Today*, 2010, **5**, 143–159.

132 N. Senzer, J. Nemunaitis, D. Nemunaitis, C. Bedell, G. Edelman, M. Barve, R. Nunan, K. F. Pirollo, A. Rait and E. H. Chang, *Mol. Ther.*, 2012, **20**, 21-29.

133 C. Mamot, R. Ritschard, B. Vogel, T. Dieterle, L. Bubendorf, C. Hilker, S. Deuster, R. Herrmann and C. Rochlitz, *J. Clin. Oncol.*, 2011, **29**, 3029–3029.

134 C. Mamot, R. Ritschard, A. Wicki, G. Stehle, T. Dieterle, L. Bubendorf, C. Hilker, S. Deuster, R. Herrmann and C. Rochlitz, *Lancet Oncol.*, 2012, **13**, 1234–1241.

135 W. W. K. Cheng and T. M. Allen, *J. Control. Release*, 2008, **126**, 50–58.

136 R. G. Couston, M. W. Skoda, S. Uddin and C. F. van der Walle, *MAbs*, 2013,

5, 126–139.

137 Y. Li, X. Chen and N. Gu, *J. Phys. Chem. B*, 2008, **112**, 16647–16653.

138 M. Arruebo, M. Valladares and Á. González-Fernández, *J. Nanomater.*, 2009, **2009**, 1–24.

139 M. D. Blanco, C. Teijon, R. M. Olmo and J. M. Teijo, *Recent Adv. Nov. Drug Carr. Syst.*, 2012, **9**, 241–278.

140 R. Bazak, M. Houri, S. El Achy, S. Kamel and T. Refaat, *J. Cancer Res. Clin. Oncol.*, 2015, **141**, 769–784.

141 C. L. Arteaga, M. X. Sliwkowski, C. K. Osborne, E. A. Perez, F. Puglisi and L. Gianni, *Nat. Rev. Clin. Oncol.*, 2011, **9**, 16–32.

142 N. Hu, J. F. Yin, Z. Ji, Y. Hong, P. Wu, B. Bian, Z. Song, R. Li, Q. Liu and F. Wu, *Cell. Physiol. Biochem.*, 2017, **44**, 2158–2173.

143 J. Xiong, S. Han, S. Ding, J. He and H. Zhang, *Oncol. Rep.*, 2018, **39**, 1396–1404.

144 J. Graham, M. Muhsin and P. Kirkpatrick, *Nat. Rev. Drug Discov.*, 2004, **3**, 549–550.

145 H. Yao, F. Jiang, A. Lu and G. Zhang, *Int. J. Mol. Sci.*, 2016, **17**, 194.

146 O. Klykov and M. G. Weller, *Anal. Methods*, 2015, **7**, 6443–6448.

147 A. G. Sorace, C. C. Quarles, J. G. Whisenant, A. B. Hanker, J. O. McIntyre, V. M. Sanchez and T. E. Yankeelov, *Breast Cancer Res. Treat.*, 2016, **155**, 273–284.

148 W. Bou-Assaly and S. Mukherji, *Am. J. Neuroradiol.*, 2010, **31**, 626–627.

149 S. Li, K. R. Schmitz, P. D. Jeffrey, J. J. W. Wiltzius, P. Kussie and K. M. Ferguson, *Cancer Cell*, 2005, **7**, 301–311.

150 J. Huang, S. G. Nair, M. R. Mahoney, G. D. Nelson, A. F. Shields, E. Chan, R. M. Goldberg, S. Gill, M. S. Kahlenberg, J. T. Quesenberry, S. N. Thibodeau, T. C. Smyrk, A. Grothey, F. A. Sinicrope, T. A. Webb, G. H. Farr, B. A. Pockaj, J. L. Berenberg, M. Mooney, D. J. Sargent and S. R. Alberts, *Clin. Colorectal Cancer*, 2014, **13**, 100–109.

151 C. Bahou, D. A. Richards, A. Maruani, E. A. Love, F. Javaid, S. Caddick, J. R. Baker and V. Chudasama, *Org. Biomol. Chem.*, 2018, **16**, 1359–1366.

152 C. Wang, A. Yang, B. Zhang, Q. Yin, H. Huang, M. Chen and J. Xie, *Pancreas*, 2014, **43**, 291–297.

153 R. Gradiz, H. C. Silva, L. Carvalho, M. F. Botelho and A. Mota-Pinto, *Sci. Rep.*, 2016, **6**, 21648.

154 X. Yu, Y. Song, Y. Di, H. He, D. Fu and C. Jin, *Sci. Rep.*, 2016, **6**, 31539.

155 H. Zhang, *Onco. Targets. Ther.*, 2016, **9**, 3001–3007.

156 M. M. Harmsen and H. J. De Haard, *Appl. Microbiol. Biotechnol.*, 2007, **77**, 13–22.

157 L. Huang, S. Muyldermans and D. Saerens, *Expert Rev. Mol. Diagn.*, 2010, **10**, 777–785.

158 S. Zielonka, M. Empting, J. Grzeschik, D. Könning, C. J. Barelle and H. Kolmar, *MAbs*, 2015, **7**, 15–25.

159 T. Yoneya, T. Tahara, K. Nagao, Y. Yamada, T. Yamamoto, M. Osawa, S. Miyatani and M. Nishikawa, *J. Biochem.*, 2001, **129**, 27–34.

160 L. L. Rumfelt, R. L. Lohr, H. Dooley and M. F. Flajnik, *BMC Immunol.*, 2004, **5**, 8-15.

161 E. R. Goldman, J. L. Liu, D. Zabetakis and G. P. Anderson, *Front. Immunol.*, 2017, **8**, 865.

162 H. Dooley, M. F. Flajnik and A. J. Porter, *Mol. Immunol.*, 2003, **40**, 25–33.

163 O. C. Ubah, J. Steven, M. Kovaleva, L. Ferguson, C. Barelle, A. J. R. Porter and C. J. Barelle, *Front. Immunol.*, 2017, **8**, 1780.

164 M. E. Pitulescu, I. Schmidt, B. D. Giaimo, T. Antoine, F. Berkenfeld, F. Ferrante, H. Park, M. Ehling, D. Biljes, S. F. Rocha, U. H. Langen, M. Stehling, T. Nagasawa, N. Ferrara, T. Borggrefe and R. H. Adams, *Nat. Cell Biol.*, 2017, **19**, 915–927.

165 H. E. Elashal and M. Raj, *Chem. Commun.*, 2016, **52**, 6304–6307.

166 J. Nogueira, M. Greene, D. A. Richards, A. Furby, J. Steven, A. Porter, C. Barelle, C. J. Scott and V. Chudasama, *Chem. Commun.*, 2019, **53**, 7671-7674.

167 N. K. Devaraj and R. Weissleder, *Acc. Chem. Res.*, 2011, **44**, 816–827.

168 E. P. Go, G. S. Hewawasam, B. J. Ma, H. X. Liao, B. F. Haynes and H. Desaire, *Int. J. Mass Spectrom.*, 2011, **305**, 209–216.

169 M. K. Greene, D. A. Richards, J. C. F. Nogueira, K. Campbell, P. Smyth, M. Fernández, C. J. Scott and V. Chudasama, *Chem. Sci.*, 2018, **9**, 79–87.

170 J. Schmitz, A. Beckmann, A. Dudic, T. Li, R. Sellier, U. Bartz and M. Gu, *ACS Med. Chem. Lett*, 2014, **5**, 1076–1081.

171 Y. E. Tsvetkov, M. Burg-Roderfeld, G. Loers, A. Ardá, E. V. Sukhova, E. A. Khatuntseva, A. A. Grachev, A. O. Chizhov, H. C. Siebert, M. Schachner, J. Jiménez-Barbero and N. E. Nifantiev, *J. Am. Chem. Soc.*, 2012, **134**, 426–435.

172 K. Lang, L. Davis, S. Wallace, M. Mahesh, D. J. Cox, M. L. Blackman, J. M. Fox and J. W. Chin, *J. Am. Chem. Soc.*, 2012, **134**, 10317–10320.

173 M. T. W. Lee, A. Maruani, D. A. Richards, J. R. Baker, S. Caddick and V. Chudasama, *Chem. Sci.*, 2017, **8**, 2056–2060.